Interpretation of IUE and other spectra of planetary nebulae

Adnan Abdullah Goharji

INTERPRETATION OF IUE AND OTHER SPECTRA OF PLANETARY NEBULAE

BY

Adnan Abdullah Goharji, B.Sc.

(King Abdulaziz University, Jeddah, S.A.)

A thesis submitted to the University of Durham for the degree of Doctor of Philosophy

Department of Physics,

Durham University, U.K.

March, 1986

TO MY SON

"Abdullah"

TABLE OF CONTENTS

Page

Page

Page

Page

ABSTRACT

The current status of observations of planetary nebulae and their central stars is presented. Particular attention is given to ultraviolet observations secured with the IUE satellite. The physical processes occurring in these objects are discussed, with emphasis on the atomic data.

The planetary nebulae SwSt 1, IC 2501, and NGC 4361 have been observed with the IUE satellite. These observations have been combined with observations made by other workers at optical, infrared, and radio wavelengths in order to determine physical conditions in these objects.

The electron density in the compact nebula SwSt 1, determined from the C III λλ1907/1909 line ratio, is high ($\sim 10^5$ cm^{-3}), consistent with the high emission measure determined from radio observations. The C/O abundance ratio in this nebula is found to be < 1, i.e. the envelope is oxygen rich, as suggested by the identification of the silicate feature in the 8-13 μm infrared spectrum. The ultraviolet spectrum of the central star of SwSt 1 shows a few P Cygni Profiles due to a 2000 km s^{-1} stellar wind.

The analysis of observations of IC 2501 suggests that there are two main regions in the nebula: one emitting the [O III] lines, with T_e = 9400 K, the other emitting the [O II] and [N II] lines, with T_e = 9000 K. IC 2501 has a marked SiC feature in its 8-13 μm infrared spectrum and has C/O > 1. The ultraviolet observations are therefore consistent with the interpretation of the infrared observations, namely, that objects with SiC are carbon rich.

An ionization model of NGC 4361 is presented which fits the observed ultraviolet and optical line fluxes well. It is found that the inclusion in the model nebula of charge exchange and dielectronic recombination processes greatly improves the computed ionization and thermal structure of the nebula.

PREFACE

Planetary nebulae are ionized, extended, low-density envelopes of White Dwarf-like stars. The faint green disks of some of these intriguing objects often resemble the plants Uranus and Neptune, hence the name planetary nebulae. They are found at high galactic latitudes and in great numbers towards the centre bulge of our own Galaxy.

A typical planetary nebula has a radius of about 0.1 to 0.5 pc, a gas kinetic temperature in the range 8,000 - 15,000 K, and an electron density in the neighborhood of 10^3 to 10^5 cm^{-3}. The nebular shell is expanding with a velocity of the order of few tens km s^{-1}. The mass of the ionized portion of the nebular shell ranges from less than 10^{-4} to almost 1 $M_\odot$, although values of 0.1 to 0.2 $M_\odot$ have often been adopted. The spectra of planetary nebulae show recombination lines of H and He, and collisionally excited ionic lines of abundant elements such as C, N, O, Ne, Mg, Si, S, and Ar. Neutral atoms as well as molecules, particularly H_2 and CO, may exist in the outer regions of the nebula. The material in these regions is sometimes inhomogeneous and sufficiently cool for solid particles (dust grains) of silicate or SiC to form. Dust is heated by the radiation field of the nebula and its central star to temperatures of the order of 100 K. The dust optical depth is about 0.1.

Many investigators have estimated the total number of planetary nebulae in some Galaxies. There are about 300 and 1000 objects in the Small and Large Magellanic Clouds, respectively, about 750 in M 33, and about 20,000 in M 31. The most likely number in our own Galaxy probably lies between 10,000 and 20,000; the actual number of detected objects is now about 1400. In the solar neighborhood, the spatial density is about 45 to 52 objects kpc^{-3}.

Planetary nebulae are short-lived phenomena on the scale of a stellar life time which may extends over many billions of years. The time interval over which a planetary nebula can be detected seems to be about 20,000 to 30,000 years. Estimates of the local birth rate fall approximately in the range 1.3×10^{-12} to 1.4×10^{-11} pc^{-3} yr^{-1}.

Structures of planetary nebulae can be beautifully symmetric as in the "Red Rectangle" and "Butterfly" M 2-9 bipolar nebulae. IC 418 or the Ring Nebula (NGC 6720) could be represented by a spherically symmetric shell expanding radially from a central star. Examples of double shell planetary nebulae are NGC 2392, 1535, 2022, 3242, 6804, and 7354. There are at least three examples of planetary nebulae with triple shells: NGC 6826, 7009, and 7662. The irregular filamentary, inhomogeneous nebula NGC 40 resembles a truncated ring with a number of fainter wisps. NGC 6543 has been represented by a pair of coiled filaments moving symmetrically away from a central star. Compact, dense objects such as IC 4997, SwSt 1, Hubble 12, and M 1-6 are easily recognized as young planetaries. Planetary nebulae are beautiful art creations.

In a planetary nebula, energy is supplied through photoionization of atoms and ions by ultraviolet radiation from a high-temperature central star, mostly in the range 30,000 - 150,000 K. Only about 1% of known planetary nebulae are excited by ionizing radiation emitted by binary stars. Stars with low temperatures have luminosities between 300 $L_\odot$ and 5000 $L_\odot$. For stellar temperatures greater than 80,000 K much lower luminosities are observed (extending to almost 20 $L_\odot$). The mass distribution of the central stars shows a strong peak around 0.58 $M_\odot$, but extends slightly over 1 $M_\odot$. The progenitor stars have large masses, ranging from about 0.8 to 6 or even 8 $M_\odot$. The mass loss rate from the central stars ranges from about 10^{-6} to 10^{-10} ($M_\odot$ yr^{-1}).

The importance of planetary nebulae in astronomy is well known. At an advanced stage of its life, a star evolves into a Red Giant. The core of the Red Giant becomes very hot and compressed while its outer envelope becomes unstable. At some point the bulk of the outer envelope is torn off to create the luminous shell of a planetary nebula. The core then settles down to form a White Dwarf. Specific details of the physical processes which take place during this relatively rapid (only a few thousand years) phase of stellar evolution are still poorly understood. The understanding of most properties of planetary nebulae and their nuclei is necessary for the study of the previous evolutionary histroy of these objects. Planetary nebulae are also valuable tracers of galactic structure because they are recognizable to great distances from the Sun and because they have much of their visual emission concentrated in a few narrow emission lines.

Planetaries offer outstanding opportunities to atomic physicists for the analysis of forbidden line radiations. At high densities encountered in laboratory plasmas, collisional de-excitations occur sufficiently often that an atom will not remain in a metastable state long enough to make the forbidden transition. Studies of planetary nebulae, particularly in the optical and ultraviolet spectral regions, have led to important advances in certain branches of atomic physics.

It should be mentioned that the material presented above is based mainly on articles given in the IAU Symposium No. 103 "Planetary Nebulae", (1983), edited by D.R. Flower and on Volume 112 of "Physics of Thermal Gaseous Nebulae" [Aller (1984)].

In this thesis, I have tried to interpret the observations of the planetary nebulae SwSt 1, IC 2501, and NGC 4361. Some of the results obtained for the first two objects have been previously reported by Flower, Goharji, and Cohen (1984) and by Goharji and Adams (1984).

After a quick review of the observations of planetary nebulae in general, Chapter 1 summarizes the currently available and our own observations of the planetary nebulae SwSt 1, IC 2501, and NGC 4361. Chapter 2 deals with those aspects of the physics of planetary nebulae which are believed to be responsible for the production of their emission line spectra, with emphasis on the atomic data. Physical conditions and abundances in SwSt 1 and IC 2501 are determined in Chapter 3; the central stars of these two objects are discussed in Chapter 4. A new detailed computer model of NGC 4361 is presented in Chapter 5. In Chapter 6, we summarize the results of this work and draw some conclusions.

ACKNOWLEDGEMENTS

I am heavily indebted to Dr. D.R. Flower for his excellent supervision of this research. I am gratefully acknowledge his guidance, assistance, encouragement, and invaluable suggestions throughout the course of this work.

I wish to thank Prof. A.W. Wolfendale and Prof. B.H. Bransden for the use of the Physics Department's facilities. I am grateful to all the members of the group, both past and present, for their friendly co-operation. In particular I would like to thank Dr. G. Danby and Dr. D. Kirkpatrick for many constructive discussions. Mr. Alan Lotts, the manager of the STARLINK network at Durham node, is thanked for his loyal help.

It is my great pleasure to thank Prof. M.J. Seaton, Dr. S. Adams, Dr. R.E.S. Clegg, Dr. M.J. Barlow, and Drs. C.J. Penn for their generous hospitality at University College London. Stimulating discussions with them have been exteremely useful. I wish to thank them and Dr. D.R. Flower for carrying out the IUE observations for me. I am very grateful to Dr. S. Adams for providing me with copies of his IUE data analysis programmes and Dr. R.E.S. Clegg for copies of Harrington's programmes.

Financial support from King Abdulaziz University, Jeddah, Saudi Arabia, is gratefully acknowledged.

Finally I am substantially indebted to my wife for her help and encouragement during this research.

CHAPTER (1)

OBSERVATIONS AND SPECTRA OF PLANETARY NEBULAE: SwSt 1, IC 2501, AND NGC 4361

1.1 INTRODUCTION

The technological advances which have permitted us to observe planetary nebulae in the optical, infrared, radio, and ultraviolet spectral regions have led to important advances in our knowledge of these objects. The observed features in each spectral region have their own unique properties which make them useful tools for studying the physical conditions in planetary nebulae. It is now possible, by combining these observations, to make a more complete analysis of the excitation and ionization states, and in particular to derive more realistic chemical abundances. An extensive study of the planetary nebula NGC 7662 by Harrington et al. (1982; hereafter abbreviated as HSAL) shows how accurate information can be obtained from these observations.

We shall review briefly the observations, commenting on their importance in the studies of planetary nebulae and the way they have been interpreted. We shall also present the currently available and our own observations of the planetary nebulae SwSt 1, IC 2501, and NGC 4361. These three objects are the main subject of this thesis.

Table (1-1) gives the designations and coordinates of SwSt 1, IC 2501, and NGC 4361.

SwSt 1 is a compact, young, and very low excitation planetary nebula {[O III]/Hβ = 0.3; Aitken et al. (1979)}. It has a nucleus of a spectral type WC 10 [Cohen (1975); Carlson and Henize (1979)]. The angular diameter of the nebula is 0.8 arc sec [Kwok et al. (1981)].

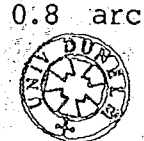

Observations of SwSt 1 have been discussed by Flower, Goharji, and Cohen (1984 ; to be referred to as Paper I). We shall give more detail of these observations.

IC 2501 is an intermediate excitation planetary nebula {[O III]/ Hβ = 10, He II/Hβ = 0; Barlow (1983)} and has an angular diameter of <2 arc sec [Perek and Kohoutek (1967)]. Observations of IC 2501 have been discussed by Goharji and Adams (1984 ; to be referred to as Paper II). These observations will also be discussed here in more detail.

NGC 4361 is an extremely high excitation planetary nebula of relatively low surface brightness. The nebula has an angular diameter of 81 arc sec [Perek and Kohoutek (1967)] and its central star is classified O6 [Cohen and Barlow (1974)].

1.2 THE OPTICAL SPECTRAL REGION

The spectrophotometric measurements of emission-line intensities of planetary nebulae can be made either photographically or photoelectrically. Due to the nonlinear response and limited intensity range of the photographic plate, the photoelectric scanners are preferable. A basic limitation of photoelectric scanning is that although strong emission lines can be measured with accuracy, poor results are often obtained for weak lines, partly because of blending and partly because of the difficulty in estimating the position of the continuum on the tracings. Photographic measurements may still be necessary in order to resolve blends.

In his review, Flower (1983) has illustrated the caution that must be exercised when employing photographic measurements, by discussing the discrepancy between the observed and theoretical intensities of the Balmer lines in NGC 7027. He has showed that the discrepancy could be

resolved if the photoelectric observations of Miller (1971) are used instead of the photographic measurements made by Aller et al. (1955), which systematically overestimated the intensities of the higher members of the Balmer series.

References to early photoelectric spectrophotometric observations of planetary nebulae are given by Aller and Liller (1968). The more recent observations have been made by Peimbert and Torres-Peimbert (1971), Torres-Peimbert and Peimbert (1977; hereafter abbreviated as TPP), Barker (1978), and Kohoutek and Martin (1981; hereafter abbreviated as KM).

Photoelectric detectors are also used to obtain monochromatic images of planetary nebulae. The calibrated monochromatic images are important in establishing the density distribution and overall structure of nebular envelopes. For a review of the currently available data see Reay (1983).

1.2.1 Permitted Lines in The Optical Region

In addition to the strong permitted recombination lines of hydrogen and helium, weak permitted lines of heavy elements (e.g. nitrogen, oxygen carbon, neon) are observed in the optical region of planetary nebulae. Some of these lines are excited by radiative recombination and cascade or by resonance absorption of the stellar ultraviolet continuum and cascade; others are produced by fluorescence (excitation of an atom by absorption of a spectral line). The most spectacular example of fluorescence is provided by the strong O III and N III lines involved in the Bowen fluorescent mechanism. This cycle is induced by the strong He II Ly-α line produced in high-excitation nebulae.

Individual possible excitation mechanisms have to be examined on a case-to-case basis for virtually all permitted lines of heavy elements in

planetary nebulae. As an example, consider the C II λ4267 ($4f\ ^2F^o - 3d\ ^2D$) line, which has been the subject of several observational and theoretical studies.

TPP considered The C II λ4267 line to be excited by radiative recombination and used it to deduce the abundance of C^{+2} ions in planetary nebulae. Their results are significantly larger than that which they adopted for the Sun.

Harrington et al.(1980; hereafter abbreviated as HLSS) and Torres-Peimbert et al.(1980; hereafter abbreviated as TPPD) have analyzed the ultraviolet observations of IC 418 and derived ionic and total abundances. They found that the C^{+2} abundance derived from the strong collisionally excited line C III] λ1908 is much less than deduced by TPP from C II λ4267, but TPPD showed that the discrepancy was reduced using improved photoelectric measurement of λ4267 (previous photographic measurement has overestimated the λ4267 intensity by a factor of 1.5). TPPD suggested that the remaining discrepancy could be due to temperature fluctuations. HLSS, on the other hand, suggested that the dielectronic recombination might contribute to the excitation of λ4267, but this is not supported by the recent work of Storey (1981).

Barker (1982) made ultraviolet observations of the Ring nebula (NGC 6720) at four positions, and also obtained optical (photoelectric) observations of the weak C II λ4267 line. He found that the abundance of C^{+2} derived from the intensity of C II λ4267, assuming recombination theory, is up to 10 times higher than deduced from the intensity of C III] λ1908. Furthermore, he noticed that this discrepancy was greatest near the central star but decreased to agreement with increasing radial distance. This behavior leads him to suggest that resonant absorption

of the stellar ultraviolet continuum radiation may contribute to the excitation of λ4267. This process has been recognised as the principle mechanism of excitation of weak O III lines in the visual spectrum of NGC 7027 [Seaton (1968)], but seems to be an order of magnitude less important than recombination for λ4267 in the Orion nebula [Grandi (1976)]. However, Grandi's calculations considered only a few important levels, while one might expect that excitation of the higher levels, would dominate the resonant absorption process [Seaton (1968)]. At the present time, no satisfactory solution for this interesting problem can be proposed.

1.2.2 Forbidden Lines In The Optical Region

Collisionally excited forbidden lines observed in the visible region of planetary nebulae are due to transitions within the ground configuration of atoms or ions with outer $2p^q$ or $3p^q$ electrons, where q = 1, 2, or 3. Configurations with q even give rise to the ^3P, ^1D, and ^1S terms, and q odd to the ^4S, ^2D, and ^2P terms.

For historical reasons, transitions between ^1S and ^1D or ^2P and ^2D are called auroral transitions and those between ^1D and ^3P or ^2D and ^4S are called nebular transitions. The strongest lines in most planetaries are the λλ4959, 5007 ($^1D - {}^3P_{1,2}$) lines of [O III]. The transition probabilites for forbidden lines are often very low, e.g., 0.007 s^{-1} and 0.020 s^{-1} for λ4959 and λ5007 lines, respectively. Hence, the radiative lifetime of the $^1D_2$ level of [O III] is 36 s, as compared with 10^{-8} s for levels which may decay by optically allowed transitions: if the density of the nebular gas were not extremely low, the intensities of the forbidden lines would be negligible relative to the permitted lines.

The forbidden lines are very important in studies of planetary nebulae because certain of their intensity ratios enable the electron density and temperature of the nebular gas to be determined. We must have this information in order to determine the chemical composition of the nebula.

1.2.3 The Continuum

The most striking evident feature of the continuous spectra of planetary nebulae is the intensity jump at the head of the Balmer series, produced by recombinations of electrons and ions on the second level of hydrogen. The underlying continuum arises mostly from recombinations on the third and higher levels of hydrogen, excited levels of helium, with some contribution from free-free and two-photon emissions.

The ratio of the Balmer continuum to Hβ emission depends on the electron temperature and weakly on the electron density [see eq. 64 of Aller (1984)] so it could give at least a consistency check on electron temperature determinations by other methods. The shape of the continuum is also important when considering the determinations of the central star temperatures.

1.2.4 Optical Spectra of SwSt 1, IC 2501, and NGC 4361.

SwSt 1 was observed on 1976 July 5 with the Lick Observatory 3-m telescope, using the Cassegrain image-tube scanner [Miller, Robinson, and Wampler (1976)]. The observational techniques are discussed in Paper I. Table (1-2) gives the identifications of the nebular emission lines and their measured intensities; the measured continuum fluxes are also listed in the Table.

IC 2501 has been observed by TPP with the 0.91-m telescope at Cerro Tololo Inter-American Observatory (CTIO). It has also been observed by KM with the 1-m telescope at the European Southern Observatory (ESO). The measured line and continuum fluxes are given in Table (1-3). The adopted line intensities are discussed in Paper II.

NGC 4361 has been observed with different entrance slots by Aller (1951), O'Dell (1962), Heap et al. (1969), Kaler (1976a), TPP, Barker (1978), and Aller et al. (1979). The selected line intensities as measured by some of these authors are given in Table (1-4). Martin (1984) has measured the Hβ λ4861, He II λ4686, and [O III] λ5007 lines in NGC 4361 photoelectrically with circular entrance apertures at the ESO - 0.5-m telescope. His data are given in Table (1-5).

Data on the photoelectric U(λ≈3446), B(λ≈4329), and V(λ≈5464) magnitudes of the central stars of the three nebulae are collected in Table (1-6).

1.3 THE INFRARED SPECTRAL REGION

1.3.1 Thermal Infrared Emission

Early observations by Gillett, Low, and Stein (1967) have shown that the infrared continuous emission from the planetary nebula NGC 7027 is much greater than expected from recombination and free-free emission. The infrared excess, which is the most prominent feature of the infrared and radio spectrum of NGC 7027 [Terzian (1978)], has been the subject of several observational and theoretical studies. A variety of observational data are now available for a number of other nebulae. Table 1 of Barlow (1983) summarizes the published ground-based infrared photometry of these objects.

Krishna Swamy and O'Dell (1968) suggested that the infrared excess may be due to the thermal emission of small graphite particles (dust grains) which are heated by Ly-α photons produced by recombination of H^+ ions and electrons in the nebula. It is thus interesting to compare the total thermal infrared (TIR) luminosity with the Ly-α luminosity; the ratio L(TIR)/L(Ly-α) should be ≤ 1 if the dust in the nebula is primary heated by trapped Ly-α.

Moseley (1980) has observed 13 planetaries using photometers with effective wavelengths of 37μm and 70μm (beam 27 arc sec FWHM), and 52μm and 108μm (beam 55 arc sec FWHM). These observations, when combined with middle-infrared (10μm - 19μm) observations [Cohen and Barlow (1974)], completely define the infrared emission from planetary nebulae. The spectral energy distributions were in general similar to that of NGC 7027. IC 418 was found to have a more sharply peaked energy distribution than the other nebulae, and this is due to the presence of a strong emission feature in the 28-52μm passband [Forrest, Houck, and McCarthy (1981)]. Moseley has fitted his observations to theoretical spectra of isothermal dust with emissivity $\epsilon \propto \nu^n$. If n=1, the dust temperature T_d = 105 K, while for n=2, T_d = 90 K. Integration of the theoretical spectrum gives an estimate of L(TIR). The conversion from L(radio) to L(Ly-α) depends only on presumably well-understood recombination theory. He thus obtained the ratio L(TIR)/L(Ly-α) for 11 nebulae. Some of the values of L(Ly-α) used by Moseley were incorrect. The corrected L(TIR)/L(Ly-α) ratios are listed by Barlow (1983), who used the relation of Rubin (1968) to calculate L(Ly-α) values. It is found that the ratios range from 0.4 for NGC 3242 to 7.9 for BD $+30^{\circ}3639$. The predominantly large values of L(TIR)/L(Ly-α) indicate

that the trapped Ly-α radiation alone is insufficient to account for the total infrared continuum emission of most nebulae.

Becklin, Neugebauer, and Wynn-Williams (1973) and Telesco and Harper (1977) argued that the dust in NGC 7027 was heated by direct absorption of stellar ultraviolet continuum and Ly-α radiation.

Bohlin, Marionni, and Stecher (1975) obtained the first rocket ultraviolet spectrum of NGC 7027 and found that the C IV λ1549 resonance doublet, relative to the collisionally excited C III] λ1908, was significantly weaker than predicted by model nebula calculations. They concluded that absorption by internal dust of the resonantly scattered C IV photons is responsible for this discrepancy. Analagous conclusions have been reached regarding the depletion of other resonance lines by internal dust in planetary nebulae (see section 1.5.3).

To decide what is the primary heating source for the dust in a given nebula requires us to examine the total stellar luminosity and spectral energy distribution . With the availability of ultraviolet observations, it is now possible to investigate this problem more fully. For example, Moseley finds NGC 7027, NGC 7662, and IC 418 to have total infrared fluxes of 2.4×10^{-7}, 1.2×10^{-8}, and 3.0×10^{-8} erg cm^{-2} s^{-1}, respectively. Calculations by Barlow (1983) yield total respective fluxes of 2.6×10^{-7} (Ly-α 27%, C IV 32%, other lines 33%, nebular continuum 8%), 1.17×10^{-8} (Ly-α 34%, C IV 5%, other lines 22%, nebular continuum 39%), and 5.0×10^{-8} (Ly-α 42%, stellar continuum 58%). All fluxes are in the same units. It is seen that the calculated fluxes can comfortably supply the observed thermal infrared fluxes in these three nebulae.

1.3.2 Infrared Emission Features

Advances in the infrared spectroscopy have led to the detection of many forbidden lines of heavy elements and recombination lines of hydrogen and helium in planetary nebulae. The collisionally excited forbidden lines are produced in radiative transitions between the fine-structure levels of the ground terms of atoms and positive ions. Ions with ground np^2 and np^4 configurations emit infrared radiation in $^3P_o - {}^3P_1$ and $^3P_1 - {}^3P_2$ transitions; np and np^5 ions emit the $^2P_{1/2} - {}^2P_{3/2}$ transition.

The three major fine-structure lines [Ar III] 9.0μm, [S IV] 10.5μm, and [Ne II] 12.8μm lie within the 8-13μm atmospheric window. Early observations of these lines have been reviewed by Rank (1978). In the last few years, they have been measured in a large number of planetary nebulae by Bregman (1978), Grasdalen (1979), Aitken et al. (1979), Dinerstein (1980), Beck et al. (1981), and Aitken et al. (1982).

The flying Kuiper Infrared Observatory has opened up the spectral regions 5-8μm and 16-100μm. This has enabled the detection of a number of other lines. In Table (1-7), we list the lines which have been measured in planetary nebulae by various observers [see Flower (1983) and Dinerstein (1983)].

The infrared forbidden lines offer the opportunity to sample ions that are difficult or impossible to measure in other spectral regions, and can therefore greatly improve abundance determinations for certain elements. Two of the best examples are Ne II and S IV , which have only been measured in the infrared.

In addition to the transitions mentioned above, other emission features are observed at 3.27μm and 3.4μm [Merrill, Soifer, and Russell (1975); Grasdalen and Joyce (1976)], 6.2μm and 7.7μm [Russell, Soifer, and Willner (1977)], 8.6μm and 11.3μm [Gillett, Forrest, and Merrill (1973)], and at $\lambda > 24\mu m$ [Forrest, Houck, and McCarthy (1981)]. The spectrum of NGC 7027 in the near-to-middle infrared is shown in Figure (1-1) in order to compare the strengths of these features with those of the permitted and forbidden lines. Several suggestions have been made for these spectral features [see for example Barlow (1983)], but no identifications can be given at the present time.

The observations of hydrogen, H_2, and carbon monoxide, CO, molecules in a very few nebulae have been briefly reviewed by Black (1983). Molecular studies of planetary nebulae will yield important new information about their origins, structures, and evolution.

Some planetary nebulae (IC 418, NGC 6572, NGC 6790, IC 2501, M 1-11) show a broad emission feature peaking at 11.2μm [Willner et al. (1979); Aitken et al. (1979); Aitken and Roche (1982)], attributed to silicon carbide (SiC) grains and seen in carbon stars. Other nebulae (SwSt 1, M 1-26, Hb 12, IC 4997, Vy 2-2, He 2-131, He 2-47) display a broad emission feature centred at 9.7μm [Aitken et al. (1979); Aitken and Roche (1982)], attributed to silicate emission and seen in late-type oxygen-rich and H II regions.

Aitken and Roche (1982) fitted the observed 8-13μm continuum spectra of planetary nebulae by linear combinations of four emissivity curves taken to be representative of grain emission. The components were: (1) the silicate or Trapezium feature; (2) the SiC or carbon star feature; (3) a smooth continuum energy distribution appropriate for

graphite grains; and (4) the 8.7μm and 11.3μm features. In this way, they associated SiC emission with a carbon-rich envelope and silicate emission with an oxygen-rich envelope. This relationship has been confirmed by ultraviolet observations of some planetary nebulae [see Chapter 3 ; Table (3-14)].

1.3.3 Infrared Spectra of SwSt 1, IC 2501, and NGC 4361

The multifilter narrow-band photometry between 2.2μm and 22μm of SwSt 1 has been obtained by Cohen and Barlow (1974), who measured the ratio of thermal infrared luminosity to Ly-α luminosity [L(TIR)/ L(Ly-α) = 12] for this object. This large excess of flux was interpreted as being due to thermal emission by cool dust grains (190K).

The 3.3μm emission feature has been observed in IC 2501 by Allen et al. (1982), who reported the possible detection of this feature in SwSt 1. However, Aitken et al. (1979) have mentioned the detection of the 3.3μm emission feature in SwSt 1.

Broad band measurements (1μm - 10μm) of Khromov and Moroz (1972) and of Cohen and Barlow (1974) reveal that NGC 4361 contains possibly very littel dust.

The 8-13μm spectrum of SwSt 1 has been obtained by Aitken et al. (1979). More recently, Aitken and Roche (1982) have obtained the 8-13μm spectra of both SwSt 1 and IC 2501. These spectra are shown in Figure (1-2); the solid lines are the best fits to the continua (see section 1.3.1). The spectra of SwSt 1, which show the energy distribution in the continuum to be similar to that observed from the Trapezium region of the Orion nebula and associated with silicate emission, suggest that the nebula is oxygen rich (C/O < 1), although the central star is classified WC 10 (i.e., carbon rich). The presence of the SiC feature

in the spectra of IC 2501 is taken as evidence that the nebula is carbon rich (C/O > 1).

The measured infrared line intensities in SwSt 1 and IC 2501 are given in Table (1-8). Data on infrared emission lines are not available for NGC 4361 at the present time.

1.4 THE RADIO SPECTRAL REGION

1.4.1 Radio Emission

Radio observations of planetary nebulae have been reviewed by Terzian (1968,1980) and Scott (1983). Reliable data on a total of 397 sources at 14.7 GHz, 332 sources at 5 GHz, 144 sources at 2.7 GHz, and 43 sources at 408 MHz are now available. Observations at many other radio frequencies have also been made for a large number of planetary nebulae [see, e.g., Purton et al. (1982); Kwok et al. (1981)].

These observations have shown that most planetary nebulae are thermal radio sources. Even, most of those originally suspected of being non-thermal have since been found to be thermal sources confused with non-thermal galactic sources of emission. As an example, the planetary nebula NGC 3242 was a candidate of non-thermal sources. However detailed spectroscopic studies in the blue spectral region [Czyzak et al. (1966)] failed to reveal any features which could be attributed to a unique non-thermal cause. Subsequent work [Kaftan-Kassim (1966)] showed that the excess radiation at the longer wavelengths is due to a faint arc of nebulosity about 10' SW of NGC 3242.

The thermal continuum emission arises from free-free transitions (bremsstrahlung) of the electrons in the field of the positive ions (principally of hydrogen and helium). The absorption coefficient for

these free-free transitions varies essentially inversely as the frequency squared [see the expression of Oster (1961)]. Thus, the nebula is optically thin at high frequencies and one may observe emission from all points along the line of sight; at the lower frequencies, the nebula is optically thick and the brightness temperature is equal to that of the blackbody.

If the radio brightness distribution at an optically thin frequency is known, then the emission measure and optical depth may be calculated for an assumed value of the electron temperature [cf. Flower (1983)]. The radio frequency flux may then be calculated and compared with the observed flux distribution; the best fit determines the electron temperature. If any significant structure has not been observed, the derived value of the electron temperature will be underestimated [Scott (1975)].

The ratio of the emission coefficients at a radio frequency ν and at Hβ can be calculated, by assuming the electron temperature and helium abundance in the nebula. Since the nebula is optically thin at Hβ and at a high frequency, this ratio may be compared with the observed fluxes at the corresponding wavelengths and the reddening constant may be derived [Milne and Aller (1975)]. Note that the radio and Hβ fluxes should be refer to the same region, usually the whole nebula.

Radio frequency observations of planetary nebulae can also provide information on the distribution of ionized gas [cf. Salem (1974); HSAL] and radii and distances [cf. Daub (1982)].

In addition to the thermal continuum emission, radio recombination lines have been observed in planetary nebulae [cf. Walmsley et al. (1981)]. From the ratio of line to continuum brightness temperature, the electron temperature may be derived [Shaver et al. (1983)]. A non-LTE analysis

produces electron temperatures substantially in agreement with those derived optically.

1.4.2 Radio Mapping

A large fraction of the known planetary nebulae remain unresolved to the resolution limit of several arc seconds of early radio telescopes. The most recent Very Large Array (VLA) at the National Radio Astronomy Observatory (NRAO) operates at four main frequencies, 23, 15, 5, and 1.5 GHz with achievable resolutions of 0.05, 0.08, 0.25, and 0.8 arc seconds respectively [Bignell (1983)]. This opens the possibility of investigating very compact planetary nebulae.

Eight moderately compact planetary nebulae have been successfully detected with the VLA at 4.9 GHz by Johnson et al. (1979). The VLA maps of a number of "classical" and young planetary nebulae have been obtained by Bignell (1983).

Kwok et al. (1981) have observed 40 stellar planetary nebulae at the Algonquin Radio Observatory (ARO) at a frequency of 10.6 GHz. By comparing their ARO measurements with the 5 GHz measurements previously published, they found that most nebulae were optically thin above 5 GHz. Six of the objects appeared to have a higher turn-over frequency and were subsequently observed with the VLA. The observations were made at 4.885 and 15.036 GHz. SwSt 1 was one of the four nebulae which were detected by the VLA. Figure (1-3) shows the VLA map of SwSt 1 at 4.885 GHz.

The high resolution and high sensitivity of the VLA is currently being utilized to probe the central stars of planetary nebulae. This kind of radio observations will help us to learn more about the mechanisms responsible for the mass loss and early formation of the planetary nebulae.

1.4.3 Radio Spectra of SwSt 1, IC 2501, and NGC 4361

Radio frequency observations of the three nebulae are summarized in Table (1-9). The spectra are shown in Figure (1-4).

Kwok et al. (1981) find that SwSt 1 is optically thick up to ν = 8 GHz indicating an emission measure of 2×10^8 cm^{-6} pc, in exact agreement with the value which they estimated from the angular diameter (0.8 arc sec) of the nebula. The small angular size and high emission measure indicate that SwSt 1 is a compact planetary nebula which may, consequently be young. This conclusion is consistent with the suggestion by Kwok (1980) that the 9.7μm silicate feature (which is observed in the infrared spectrum of SwSt 1; see section 1.3.3), arising from the remnant circumstellar envelope of the red giant progenitor, should only be observable in young planetary nebulae.

The spectral index in the optically thick part of the radio spectrum of SwSt 1 (ν < 7 HGz) is $\alpha = 1.22 \pm 0.12$ according to Kwok et al. (1981), who concluded that the spectrum can not be fitted satisfactorily by a uniform-density model which requires $\alpha = +2$.

A comparison between the 5 and 14.7 GHz flux densities was made for IC 2501 and NGC 4361 by Milne and Aller (1982). They found that both nebulae have an optically thin free-free spectral index of $\alpha \approx -0.1$ between these two frequencies.

The spectrum of NGC 4361 [Figure (1-4)] seems to be optically thin even at low frequencies, indicating that self-absorption is not important. This is consistent with infrared observations which suggest that NGC 4361 may has only very littel dust.

1.5 THE ULTRAVIOLET SPECTRAL REGION

Ultraviolet photometric observations of planetary nebulae were made with the OAO-2 satellite [Holm (1972)]. The TD-1 satellite has also been used to observe the central stars of planetary nebulae [Boksenberg et al. (1975); Lutz and Carnochan (1979)]. Intermediate band measurements of planetary nebulae between 1500 and 3300 Å have been made with ANS [Pottasch et al. (1978a,b)].

The best quality ultraviolet observations of planetary nebulae and of their central stars are obtained by the International Ultraviolet Explorer (IUE) satellite. Observations made with this satellite have been reviewed by Nussbaumer (1980), Peimbert (1981), and Flower (1983). These observations have since been largely superseded by more recent measurements with IUE.

1.5.1 The IUE Satellite

A description of the IUE satellite and its modes of operation is given by Boggess et al. (1978). The satellite was launched from the John F. Kennedy Space Center on 26 January 1978 into an eccentric geosynchronous orbit over the Atlantic Ocean. It is operated for 16 h each day from the NASA ground station at Goddard Space Flight Center near Washington, D.C. and for the remaining 8 h from the ESA Villafranca Satellite Tracking Station located near Madrid.

To achieve adequate resolution, two cameras are required to record the full spectral range: the short wave prime (SWP) camera covers the wavelength range 1150 - 1950 Å and the long wave redundant (LWR) camera the wavelength range 1900 - 3200 Å. The beam is detected photo-electrically, with digitalised read-out of the image (768 × 768 pixels)

in terms of Data Number (DN). Due to the somewhat limited DN range of the cameras, several spectra in each wavelength range, with different exposure times, are required to obtain unsaturated observations of strong lines and good observations of weak lines and of the continuum. Longer exposures are generally necessary for good observations in regions of lower detector sensitivity and in the region, around 2200 Å, of heavy interstellar absorption.

1.5.1.1 Apertures

Two apertures are available for use with each of the cameras: the large aperture is oval with length a and width b; the small aperture is circular with diameter d. According to Bohlin et al. (1980) the values of these parameters, in arc sec (or pixels) projected on to the sky, are :

a = 10.3 (6.8) , b = 23.0 (15.1) , d = 3.21 (2.1) for SWP;

a = 10.2 (6.7) , b = 23.8 (15.6) , d = 3.98 (2.6) for LWR.

1.5.1.2 Resolution

The observations can be made in low or high dispersion modes, the latter being obtained by interposition of an echelle grating in the light path. The resolving power of the echelle spectrograph is 12000 for SWP and 13000 for LWR. Bohlin et al. (1980) give the dispersion at the camera detector to be 1.67 Å per pixel for SWP, 2.65 Å per pixel for LWR. The have-width of the large aperture is therefore corresponds to 5 Å for SWP, 9 Å for LWR. For a point source, the resolution is 6 Å for SWP images and 8 Å for LWR images. For an extended source filling the large aperture, the resolution at low dispersion is degraded to 11 Å for SWP and 17 Å for LWR. The degradation is less serious for the small aperture.

1.5.1.3 Data Extraction and Reduction

The transformation that removes both the camera photometric non-linearities and the spatial sensitivity variations is called the Intensity Transfer Function (ITF). The ITF converts the 8 bit camera response in DN to a linearized 16 bit Flux Number (FN) for each pixel. The net spectrum can then be obtained as the difference between the gross spectrum and the background. It should be noted that the extraction slit must be chosen in such a way that the full width of the spectrum is included. The spectrum is then calibrated to give the observed flux in units of erg cm^{-2} s^{-1} $Å^{-1}$. Standard stars can be used to determine the calibration factors. The fluxes of emission lines in units of erg cm^{-2} s^{-1} are derived by numerical integration over the width of the observed line profile. The degree of uncertainty in fixing the continuum level provides a measure of the error in the line flux.

Software for the interactive extraction, reduction, and analysis of the IUE spectra has been written by S. Adams, J. Giddings, and M.A.J. Snijders of University College London.

1.5.2 IUE Spectral Lines

Most of the lines, listed in Table (1-10), observed in the IUE spectra of planetary nebulae are excited by electron collisions; the intercombination lines such as C III] λ1908 are more prominent than the permitted lines such as C IV λ1549 or the forbidden lines such as [Ne IV] λ2423. The only three dielectronic recombination lines observed in the spectra of planetary nebulae are the C II λ1335, C III λ2297, and C III λ1176 lines. Recombination lines of He II and

Bowen fluorescence lines of O III are also observed in some high-excitation nebulae (e.g., NGC 7009, NGC 7662).

To show how interesting the IUE observations are, consider the spectra of the low-excitation nebula IC 418. In this nebula, much of the carbon is in the form of C^+ and C^{+2}. Reliable measurements of the strong intercombination lines C II] λ2326 and C III] λ1908 will thus lead to the best estimate of the C abundance. The C^+ / C^{+2} ratio in IC 418 obtained from C II] λ2326 and C III] λ1908 (HLSS; TPPD) was found to be significantly greater than had been predicted from model calculations. HLSS suggested that this is might be due to neglect of $C^{+2} \rightarrow C^+$ dielectronic recombination via low-lying autoionization states. Subsequent calculations by Storey (1981) have shown that dielectronic recombination : (1) is important for the calculation of C^+ / C^{+2} and C^{+2} / C^{+3} ionization equilibria (the inclusion of this process in the ionization models of IC 418 will tend to bring the calculated C^+ / C^{+2} ratio in to better agreement with observations); (2) does not give enhanced λ4267 emission (as discussed in section 1.2.1); and (3) leads to the production of a number of spectral lines, including C II λ1335, C III λ2297, and C III λ1176.

Clavel et al. (1981) have observed the C II λ1335 multiplet in high-dispersion spectra of IC 418. By comparing various flux ratios, they confirmed that the C II λ1335 lines are excited by dielectronic recombination. The C II λ1335 is also observed in other nebulae but is usually weak due to absorption by interstellar C II.

The C III λ2297 has been observed in the spectra of many nebulae but is weak and, in low-dispersion spectra, is blended with He II λ2307.

The C III λ1176 is also observed in the spectra of NGC 7662 [Benvenuti and Perinotto (1981); Pena and Torres-Peimbert (1981)].

In low-excitation nebulae, O^+ and O^{+2} are the predominant ionization stages of O. Good IUE and optical measurements of [O II] λ2470 and [O III] λ5007 line intensities give accurate determination of the O abundance in this class of objects; the [O III] λ1663 is generally weak in the spectra of most planetary nebulae.

The N III λ1751, N IV] λ1485, and N V λ1240 lines are clearly very important for the determination of the N abundance in high-excitation nebulae; the only strong nitrogen lines in the visual part of the spectrum are [N II] λλ6548, 6584.

The advent of IUE has also assisted in the abundance determinations of Ne, Ar, Si, and Mg [see Table (1-10) for the relevant lines]. From an analysis of the optical and IUE spectrum of NGC 7662, HSAL found that the abundance of Mg and Si are much less than the solar values. They suggested that both Mg and Si are removed from the gas phase by grain formation. Depletion of gas-phase magnesium has also been found in NGC 6572 [Flower and Penn (1981)].

IUE high-resolution spectra can provide information on the electron densities in planetary nebulae; the C III] λ1907 / λ1909 ratio has proved useful for this purpose.

1.5.3 Depletion of UV Resonance Lines by Internal Dust

The scattering of photons in the C II λ1335 and C IV λ1549 resonance lines enhances the probability of their being absorbed by dust internal to the nebula. A useful review on this subject is given by Seaton (1983a).

From an analysis of the relative intensities of the C II λ1335 and λ4267, Clavel et al. (1981) conclude that the C II λ1335 resonance multiplet is depleted by a factor of about 2 by internal dust in IC 418.

We have already mentioned, in section 1.3.1, the evidence for depletion of C IV λ1549 resonance doublet by internal dust in NGC 7027. For NGC 7662, HSAL compared their model predictions with the relative strengths of C III λ2297 and C IV λ1549 and found that the C IV λ1549 resonance doublet was depleted by a factor of 3 by internal dust.

Ionization models for NGC 6210, NGC 7009, NGC 3242, and IC 2003 have been constructed form optical and IUE spectroscopic data by Koppen and Wehrse (1983). They found that the C IV λ1549 line was depleted by a factor of 10 by dust internal to these objects.

1.5.4 P Cygni Line Profiles

The ultraviolet spectra of the central stars of some planetary nebulae exhibit line profiles consisting of a shortward displaced absorption component and a longward displaced emission component. These profiles are generally called P Cygni profiles. In Table (1-11), we list the transitions which have been observed with P Cygni profiles in the spectra of planetary nebulae.

The study of the unsaturated P Cygni line profiles is the best source of information on the mass-loss rates of the central stars of planetary nebulae. On the other hand, the terminal velocity in the stellar wind of the central star is best found from the extreme width of a saturated P Cygni type line profile (HLSS).

As pointed out by Flower (1983), it is important to couple studies of the ultraviolet spectra of the central stars with the detailed analysis

of the nebular spectra in order to understand the origin and evolution of planetary nebulae.

1.5.5 IUE Spectra of SwSt 1

IUE observations of SwSt 1 have been discussed in Paper I. The images which were obtained using the small (S) and large (L) apertures are listed in Table (1-12). In the column headed resolution, L refers to low; H refers to high.

The low-resolution spectra obtained in the short and long wavelength regions, using the large apertures, are shown in Figures (1-5) and (1-6). Breaks in the plotted curves correspond to fiducial marks and known blemishes in the IUE cameras. The [O II] λ2470 line was saturated on LWR 8734 but well exposed on LWR 10077. The emission feature observed at λ2325 is a blend of C II] λ2326 and [O III] λ2321. A number of P Cygni line profiles (e.g., C IV λ1549, Si IV λ1397) are exhibited in the spectra and are undoubtedly stellar in origin.

Table (1-13) gives the identifications of the nebular emission lines and their measured intensities. Error estimates are based on uncertainties in setting the continuum levels.

1.5.6 IUE Spectra of IC 2501

IUE observations of IC 2501 are discussed in Paper II. In Table (1-12), we list the four images which were obtained using the large apertures. In Figures (1-7) and (1-8), we present the low-dispersion spectra obtained in the short and long wavelength regions. The Mg II λ2800 transition was saturated on LWR 12566 but well exposed on LWR 12567. The C IV λ1549 feature is of stellar origin. The emission at λ2325 is again a blend of C II] λ2326 and [O III] λ2321.

In Table (1-14), we report the measured intensities of the nebular emission lines. The C II λ1335 is weak and may be attributable entirely to noise.

1.5.7 IUE Spectra of NGC 4361

The size of NGC 4361 (whose diameter is 81 arc sec) is larger than the size of the large aperture (approximately 10 × 23 arc sec oval) of the IUE telescope. Ultraviolet spectra may therefore be obtained at a position centred on a guide star or at offset positions. This procedure is generally satisfactory for guide stars brighter than B = 13 (HSAL). The blue magnitude of the central star of NGC 4361 is in the range $12.60 \leqq B \leqq 13.00$ [see Table (1-6)]. It is thus satisfactory to guide on the central star.

We have used the IUE satellite to make observations for two regions:
Region A, large aperture centred on star;
Region B, large aperture offset 28 arc sec (SE) from star.

The central star should not been observed in Region B, since the offset distance was much larger than the dimensions of the aperture. The direction of the long axis of the large aperture was 15 degrees E of N. Region B should therefore be well inside the nebula.

In Table (1-12), we summarize the low dispersion observations which were made; the regions observed are indicated. An IUE high dispersion short wavelength spectrum of NGC 4361 was taken by Adam and Koppen (1985). In their observations, the direction of the long axis of the large aperture was 48 degrees E of N. We have included their image (SWP 13521) in Table (1-12) and we shall make some use of it.

In Figures (1-9) and (1-10), we present the low-dispersion spectra of NGC 4361. The spectra are those of one of the highest excitation planetary nebulae. They do not show low-excitation features such as [O II] and C II] that are exhibited in low-excitation and intermediate-excitation nebulae.

The measured intensities in C IV 1549, He II λ1640, C III] λ1908, and [Ne IV] λ2423 nebular emission lines are given in Table (1-15).

CHAPTER (1)

Tables and Figures

Table (1-1)

Designations and coordinates of the planetary nebulae.

Nebula name	PK	Alternate names (a)	R.A. (1950) H M S	Dec. (1950) o ' "	Ref.
SwSt 1	1 $-6^{o}2$	HD 167362 He 2-377 VV 164 VV' 378 MWC 288 Sa 2-319 Wra 16-397	18 12 58.7	-30 53 12	(b)
IC 2501	281 $-5^{o}1$	He 2-33 VV 53 VV' 92 ARO 510 Sa 2-47 Wra 16-54	09 37 19.4	-59 51 34	(b)
NGC 4361	294 $+43^{o}1$	VV 62 VV' 110 ARO 26	12 21 55.0	-18 30 32	(c)

References : (a) Acker et al. (1982); (b) Purton et al. (1982);

(c) Milne (1973).

Table (1-2)

Visual line (erg cm^{-2} s^{-1}) and continuum (erg cm^{-2} s^{-1} $Å^{-1}$) intensities in SwSt 1. B and V refer to blue and visual magnitude estimates. Numbers in brackets are powers of 10.

Identification	λ(Å)	Transition	Observed flux
Hγ	4340	2 - 5	7.30 ± 0.31 (-12)
[O III]	4363	$2p^2\ ^1D - 2p^2\ ^1S$	6.0 ± 1.7 (-14)
Hβ	4861	2 - 4	2.13 ± 0.06 (-11)
[O III]	5007	$2p^2\ ^3P - 2p^2\ ^1D$	1.12 ± 0.01 (-11)
[N II]	5755	$2p^2\ ^1D - 2p^2\ ^1S$	2.34 ± 0.02 (-12)
He I	5876	$2p\ ^3P - 3d\ ^3D$	2.76 ± 0.04 (-12)
cont.	4300		1.433 (-13)
B	4329		9.550 (-14)
cont.	4800		1.271 (-13)
cont.	5200		1.134 (-13)
V	5464		7.280 (-14)
cont.	5600		9.780 (-14)
cont.	6000		8.830 (-14)
cont.	6400		8.030 (-14)

Table (1-3)

Visual line (10^{-12} erg cm^{-2} s^{-1}) and continuum (10^{-14} erg cm^{-2} s^{-1} Å^{-1}) intensities in IC 2501, as measured by TPP and KM.

Identification	λ(Å)	Observed flux	
		TPP	KM
[O II]	3726,3729	10.06	
[Ne III]	3869	10.59	
N III, Hδ	4098,4102	4.68	
Hγ	4340	8.96	8.71 (± 0.20)
[O III]	4363	1.01	0.65 (± 0.31)
He II	4686	0.91:	
Hβ	4861	22.91	21.38 (± 0.49)
[O III]	5007	188.36	181.97 (± 4.14)
[N II]	5755	0.36:	
He I	5876	4.42	4.37 (± 0.20)
[O I]	6300	1.49	
[S III]	6311	0.32:	
Hα	6563	92.79	91.20 (± 2.08)
[N II]	6584	21.88	18.20 (± 2.35)
He I	6678	1.51	
[S II]	6717,6731	2.02	
He I	7065	3.16	
[Ar III]	7136	6.10	
[O II]	7320,7330	4.05:	
cont.	3246		8.32 (± 0.37)
cont.	3546		9.33 (± 0.42)
cont.	4225		2.51 (± 0.11)
cont.	5306		2.24 (± 0.05)
cont.	6865		2.04 (± 0.14)
cont.	7901		2.24 (± 0.29)

Table (1-4)

Selected visual line intensities, relative to Hβ, in NGC 4361 as measured by different observers.

Ion	λ(Å)	Observed flux				
		TPP (1977)			Barker (1978)	Aller et. al. (1979)
		(a)	(b)	(c)	(d)	(e)
Hδ	4102	<27.5	<26.9	<26.3	28.4	24.6
Hγ	4340	48.6	46.4	48.6	46.6	43.8
Hβ	4861	100	100	100	100	100
Hα	6563	318.8			279	<336
He II	4686	130.5	108.5	116.3	109	103
[O II]	3727,29	7.56	2.94		4.65	
[O III]	4363	8.85	7.03	10.4	9.80	8.20
[O III]	5007	290.4	196.3	325.8	314	288
[Ne III]	3869	24.2	22.0	23.6	27.7	21.8
[Ne IV]	4725		3.0			3.0
[Ne V]	3425	204			67	85
[Ar IV]	4740		6.27	10.64		7.55
[Ar V]	7006	6.2				5.6
log F(Hβ)		-11.65	-12.54	-13.12		

(a) Slit (5.2" × 77.6") 3" S of central star;

(b) Slit (3.5" × 12.2") 4" S of central star;

(c) Slit (3.5" × 12.2") 25" S of central star;

(d) Slit (200" × 8") 10" N of central star;

(e) The intensities are essentially an average over the brighter region of the nebula.

Table (1-5)

Visual line intensities in NGC 4361 , measured through circular entrance apertures [Martin (1984)].

Diameter of aperture	Observed flux (10^{-12} erg cm^{-2} s^{-1}) Hß λ4861	He II λ4686	[O III] λ5007
10"	0.6 (± 0.3):	1.0 (± 0.5):	1.9 (± 0.3):
21"	3.2 (± 0.4)	4.4 (± 0.2)	8.1 (± 0.5)
40"	11.0 (± 1.0)	14.1 (± 0.6)	30.9 (± 1.4)
80"	25.7 (± 2.3):	28.8 (± 1.3):	77.6 (± 3.5):

Table (1-6)

Photoelectric U, B, and V magnitudes of the central stars.

Nebula	U	B	V	Reference
SwSt 1	--	--	11.00	Aller (1976)
	--	--	11.80	Carlson & Henize (1979)
	--	12.1	11.90	Acker et al. (1982)
IC 2501	--	--	10.00	Campbell & Moore (1918)
NGC 4361	11.30	12.60	12.90	Liller & Shao (1968)
	--	12.93±0.07	13.60±3	Kaler (1976b)
	11.66	13.00	13.40	Drummond (1980)
	11.43	12.74	13.04	Shao & Liller (1982)

Table (1-7)

Recombination and forbidden lines observed in the infrared spectra of planetary nebulae [see Flower (1983); Dinerstein (1983)].

Identification	λ(μm)	Transition
H	2.17	7 - 4
H	3.74	8 - 5
H	4.05	5 - 4
[Mg IV]	4.49	$^2P_{3/2}$ - $^2P_{1/2}$
[Mg V]	5.61	$^3P_2$ - $^3P_1$
[Ni II]	6.62	$^2P_{1/2}$ - $^2P_{3/2}$
[Ar II]	6.98	$^2P_{1/2}$ - $^2P_{3/2}$
[Ar III]	8.99	$^3P_1$ - $^3P_2$
[S IV]	10.52	$^2P_{3/2}$ - $^2P_{1/2}$
[Cl IV]	11.76	$^3P_1$ - $^3P_2$
[Ne II]	12.81	$^2P_{1/2}$ - $^2P_{3/2}$
[S III]	18.71	$^3P_2$ - $^3P_1$
[Ne V]	24.28	$^3P_1$ - ^3P_o
[O IV]	25.87	$^2P_{3/2}$ - $^2P_{1/2}$
[O III]	51.81	$^3P_2$ - $^3P_1$
	88.36	$^3P_1$ - ^3P_o
[N III]	57.33	$^3P_{3/2}$ - $^3P_{1/2}$
[O I]	63.17	$^3P_1$ - $^3P_2$

Table (1-8)

Infrared line intensities (10^{-11} erg cm^{-2} s^{-1}) in SwSt 1 and IC 2501.

Nebula	Beam (arcsec)	[Ar III] 8.99μm	[Ne II] 12.81μm	[S IV] 10.52μm	Reference
SwSt 1	3.5	1.58 ± 0.42	5.50 ± 0.27		Aitken & Roche (1982)
	3.4	0.44 ± 0.12	7.00 ± 0.30	0.23 ± 0.15	Aitken *et al.* (1979)
IC 2501	5.3			1.15 ± 0.12	Aitken & Roche (1982)
	6.0	1.30 ± 0.20	1.80 ± 0.30	3.60 ± 0.60	Beak *et al.* (1981)

Table (1-9)

Radio fluxes from the planetary nebulae SwSt1, IC 2501, and NGC 4361.

Frequency	Flux density (mJy)†			Telescope	Ref.
	SwSt 1	IC 2501	NGC 4361		
408 MHz	<70	<100	190	Molonglo	(1)
2.7 GHz	---	310±25	170±60	Parkes	(2,3)
2.7	63±1	---	---	NARO-3 element	(4)
4.885	130±3	---	---	NARO-VLA	(5)
5.0	148	261	207	Parkes	(6,7)
8.1	202±3	---	---	NARO-3 element	(4)
8.9	---	180±20	---	Parkes	(2)
10.6	171±20	---	---	ARO	(2)
14.7	240	236	206	Parkes	(8)
15.035	207±11	---	---	NARO-VLA	(5)
22	128±93	---	---	ARO	(2)

† Jy = 10^{-26} W m^{-2} Hz^{-1} = 10^{-23} erg cm^{-2} s^{-1} Hz^{-1}.

References: (1) Calabretta (1982); (2) Purton et al. (1982);
(3) Aller & Milne (1972); (4) Marsh, Purton, & Feldman (1976);
(5) Kwok, Purton, & Keenan (1981); (6) Milne (1979);
(7) Milne & Aller (1975); (8) Milne & Aller (1982).

Table (1-10)

Emission lines observed in IUE spectra of planetary nebulae.

Ion	λ(Å)	Transition
C II]	2326	$2s^2\ 2p\ ^2P^o - 2s\ 2p^2\ ^4P$
C II	1335	$2s^2\ 2p\ ^2P^o - 2s\ 2p^2\ ^2D$
C III]	1908	$2s^2\ ^1S - 2s\ 2p\ ^3P^o$
C III	2297	$2s\ 2p\ ^1P^o - 2p^2\ ^1D$
C III	1176	$2s\ 2p\ ^3P^o - 2p^2\ ^3P$
C IV	1549	$2s\ ^2S - 2p\ ^2P^o$
[O II]	2470	$2p^3\ ^4S^o - 2p^3\ ^2P^o$
[O III]	1663	$2s^2\ 2p^2\ ^3P - 2s\ 2p^3\ ^5S^o$
O IV]	1402	$2s^2\ 2p\ ^2P^o - 2s\ 2p^2\ ^4P$
N III]	1751	$2s^2\ 2p\ ^2P^o - 2s\ 2p^2\ ^4P$
N IV]	1485	$2s^2\ ^1S - 2s\ 2p\ ^3P^o$
N V	1240	$2s\ ^2S - 2p\ ^2P^o$
[Ne IV]	2423	$2p^3\ ^4S^o - 2p^3\ ^2P^o$
Mg II	2800	$3s\ ^2S - 3p\ ^2P^o$
Si III]	1883	$2s^2\ ^1S - 2s\ 2p\ ^3P^o$
Si IV	1397	$3s\ ^2S - 3p\ ^2P^o$
[Ar IV]	2855	$3p^3\ ^4S^o - 3p^3\ ^2P^o$

Table (1-11)

P Cygni line profiles observed in the IUE spectra of the central stars of some planetary nebulae [see Castor et al. (1981); Clavel et al. (1981)].

Ion	SL	S'L'	J	J'	λ(Å)
N V	$2s\ ^2S$	$2p\ ^2P^o$	1/2	1/2	1242.80
			1/2	3/2	1238.82
C II	$2s^2 2p\ ^2P^o$	$2s2p^2\ ^2D$	1/2	3/2	1334.53
			3/2	3/2	1335.66
			3/2	5/2	1335.71
O IV	$2s2p^2\ ^2P$	$2p^3\ ^2D^o$	1/2	3/2	1338.60
			3/2	3/2	1342.98
			3/2	5/2	1343.51
O V	$2s2p\ ^1P^o$	$2p^2\ ^1D$	1	2	1371.29
Si IV	$3s\ ^2S$	$3p\ ^2P^o$	1/2	1/2	1402.73
			1/2	3/2	1393.73
C IV	$2s\ ^2S$	$2p\ ^2P^o$	1/2	1/2	1550.77
			1/2	3/2	1548.20
He II	n = 2	n = 3			1640.50
N IV	$2s2p\ ^1P^o$	$2p^2\ ^1D$	1	2	1718.55

Table (1-12)

IUE observations of SwSt 1 , IC 2501, and NGC 4361.

Nebula name	Date	Image	Aperture	Exposure time (min)	Resolution
SWST 1	1980 September 6	SWP 10035	L	20	L
		SWP 10034	L	10	L
		SWP 10034	S	10	L
		LWR 8734	L	20	L
		LWR 8734	S	20	L
	1981 March 6	LWR 10077	L	7	L
	1982 May 30	SWP 17068	L	130	H
IC 2501	1982 February 12	SWP 16320	L	15	L
		SWP 16319	L	25	L
		LWR 12567	L	27	L
		LWR 12566	L	55	L
NGC 4361	1980 January 26	SWP 7779 (A)	L	5	L
		SWP 7780 (B)	L	25	L
		LWR 6779 (A)	L	11	L
		LWR 6780 (B)	L	55	L
	1981 March 17	SWP 13521(A)	L	180	H

Table (1-13)

Ultraviolet line identifications and observed absolute intensities in SwSt 1. Error estimates are based on uncertainties in setting the continuum levels.

Ion	λ(Å)	Observed flux (10^{-13} erg cm^{-2} s^{-1})				
		SWP 10035 (20 min)	SWP 10034 (10 min)	LWR 8734 (20 min)	LWR 10077 (7 min)	Adopted
O III]	1663	2.2±1.4	2.6±1.8			2.4±1.8
C III]	1908	34.0±4.0	30.0±4.0			32.0±4.0
[O III]	2321			41.0±3.0	39.0±3.0	40.0±3.0
C II]	2326					
[O II]	2470			saturated	46.0±4.0	46.0±4.0

Table (1-14)

Ultraviolet line identifications and observed absolute intensities in IC 2501. Error estimates are based on uncertainties in setting the continuum levels.

Ion	λ(Å)	Observed flux (10^{-13} erg cm^{-2} s^{-1})				
		SWP 16319 (25 min)	SWP 16320 (15 min)	LWR 12566 (55 min)	LWR 12567 (27 min)	Adopted
C II	1335	2.6±2.0	2.2±1.6			2.4±1.8
N III]	1751	3.7±1.6	3.3±1.6			3.5±1.6
C III]	1908	71.0±2.0	68.0±2.0	64.0±6.0	62.0±6.0	69.5±2.0
[O III]	2321			21.0±1.0	19.0±1.0	20.0±1.0
C II]	2326					
[O II]	2470			7.7±1.0	7.3±1.0	7.5±1.0
Mg II	2800			saturated	12.0±1.0	12.0±1.0

Table (1-15)

Ultraviolet line identifications and observed absolute intensities in NGC 4361. Error estimates are based on uncertainties in setting the continuum levels.

Ion	λ(Å)	Observed flux (10^{-12} erg cm^{-2} s^{-1})				
		Region (A)			Region (B)	
		SWP 7779 (5 min)	SWP 13521 (180 min)	LWR 6779 (11 min)	SWP 7780 (25 min)	LWR 6780 (55 min)
He II	1640	6.0±1.0	7.7±1.8		3.4±0.2	
C III]	1908	>1.1	2.2±0.4	2.0±0.6	>1.4	1.8±0.4
C IV	1549	20.0±2.0	15.6±3.0		8.5±0.4	
[Ne IV]	2423			3.1±0.3		1.3±0.2

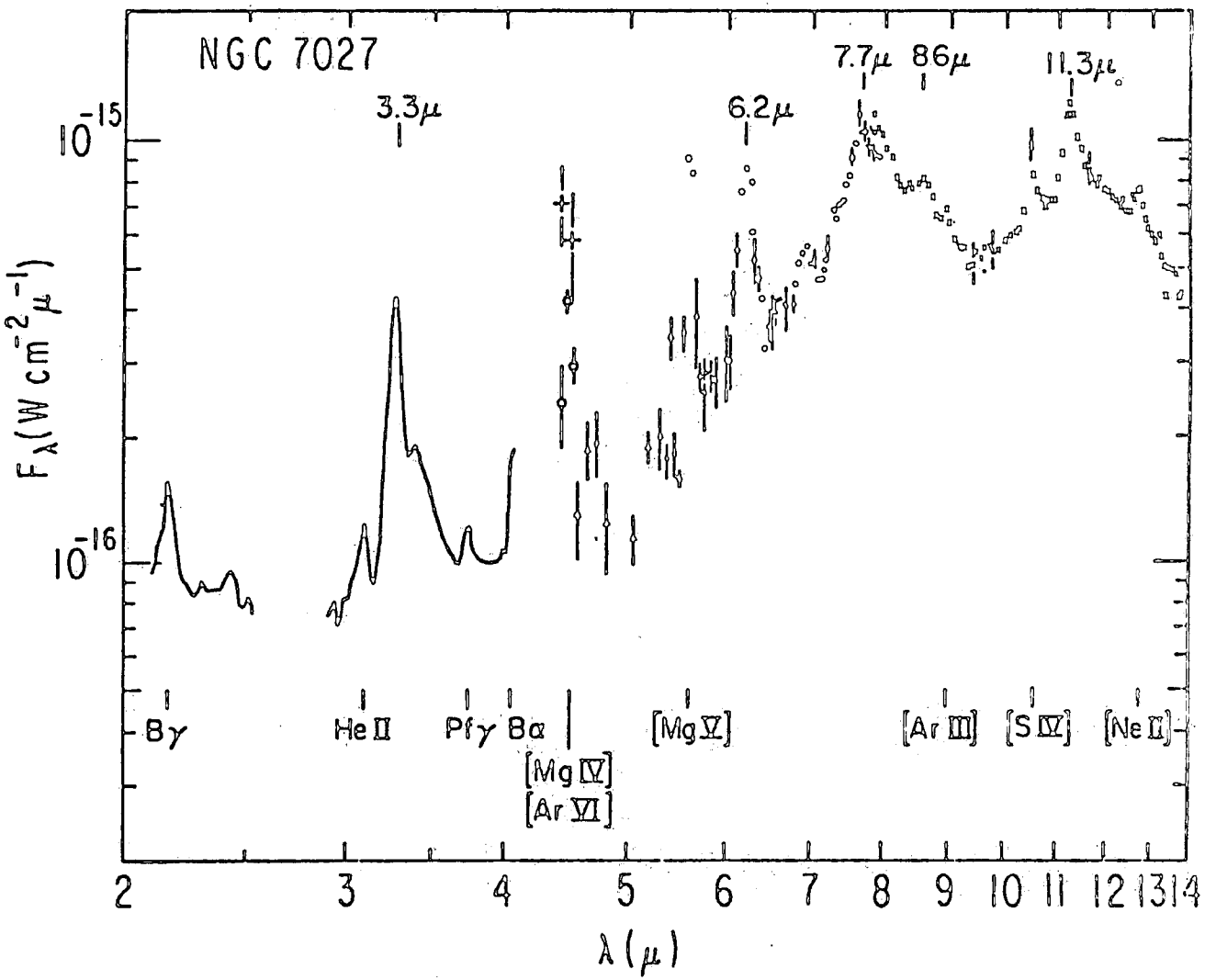

Figure (1-1): The near-to-middle infrared spectrum of NGC 7027, showing : the unidentified features at 3.27, 3.4, 6.2, 7.7, 8.6, and 11.3 μm; the strong continuous infrared spectrum; and both forbidden and permitted nebular lines. The figure has been taken from Russel, Soifer, and Willner (1977).

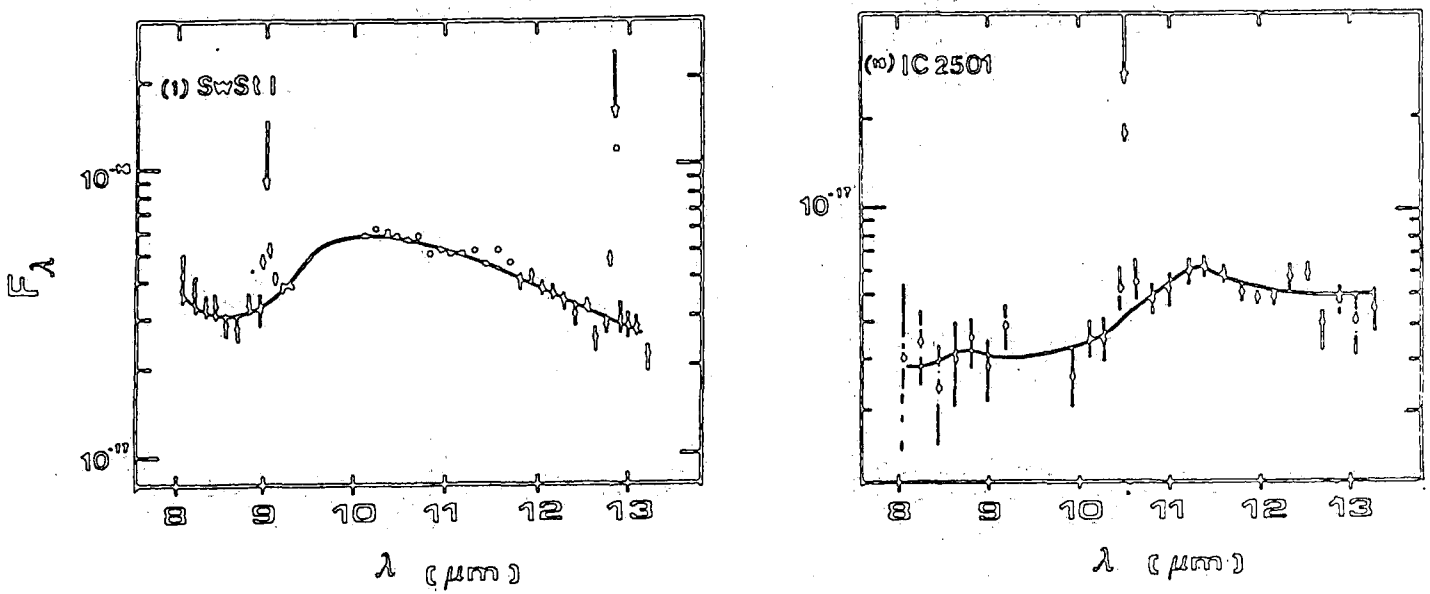

Figure (1-2): The 8 - 13 μm spectra of SwSt 1 and IC 2501. The solid lines are best fits to the continua (see text). Arrows indicate the positions of [Ar III] 9.0 μm, [S IV] 10.52 μm, and [Ne II] 12.81 μm. Note the silicate feature (centred at 9.7 μm) in the spectrum of SwSt 1, and SiC feature (peaking at 11.2 μm) in the spectrum of IC 2501. All figures have been taken from Aitken and Roche (1982).

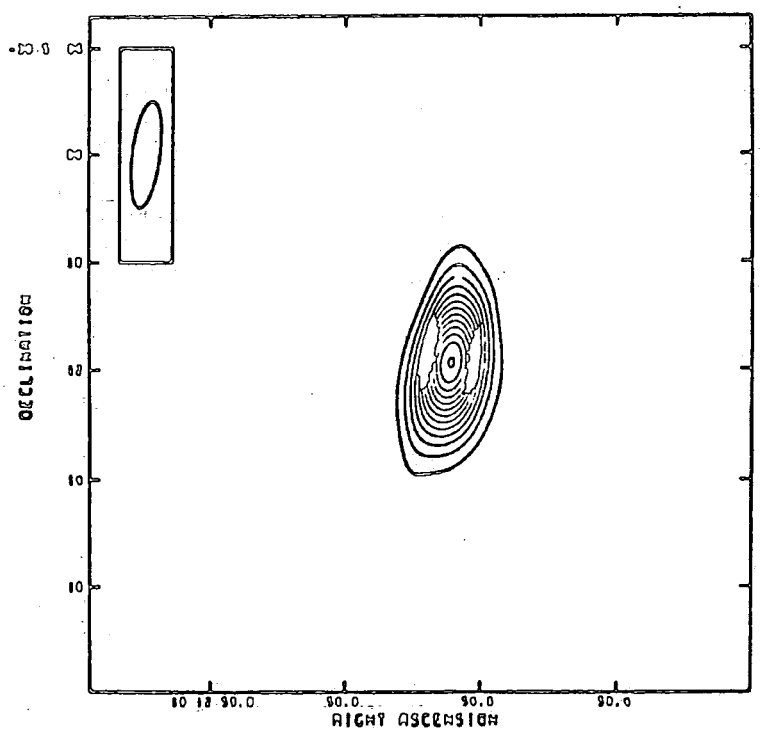

Figure (1-3): The 4.885 GHz map of SwSt 1 obtained with the VLA. The figure has been taken from Kwok, Purton, and Keenan (1981).

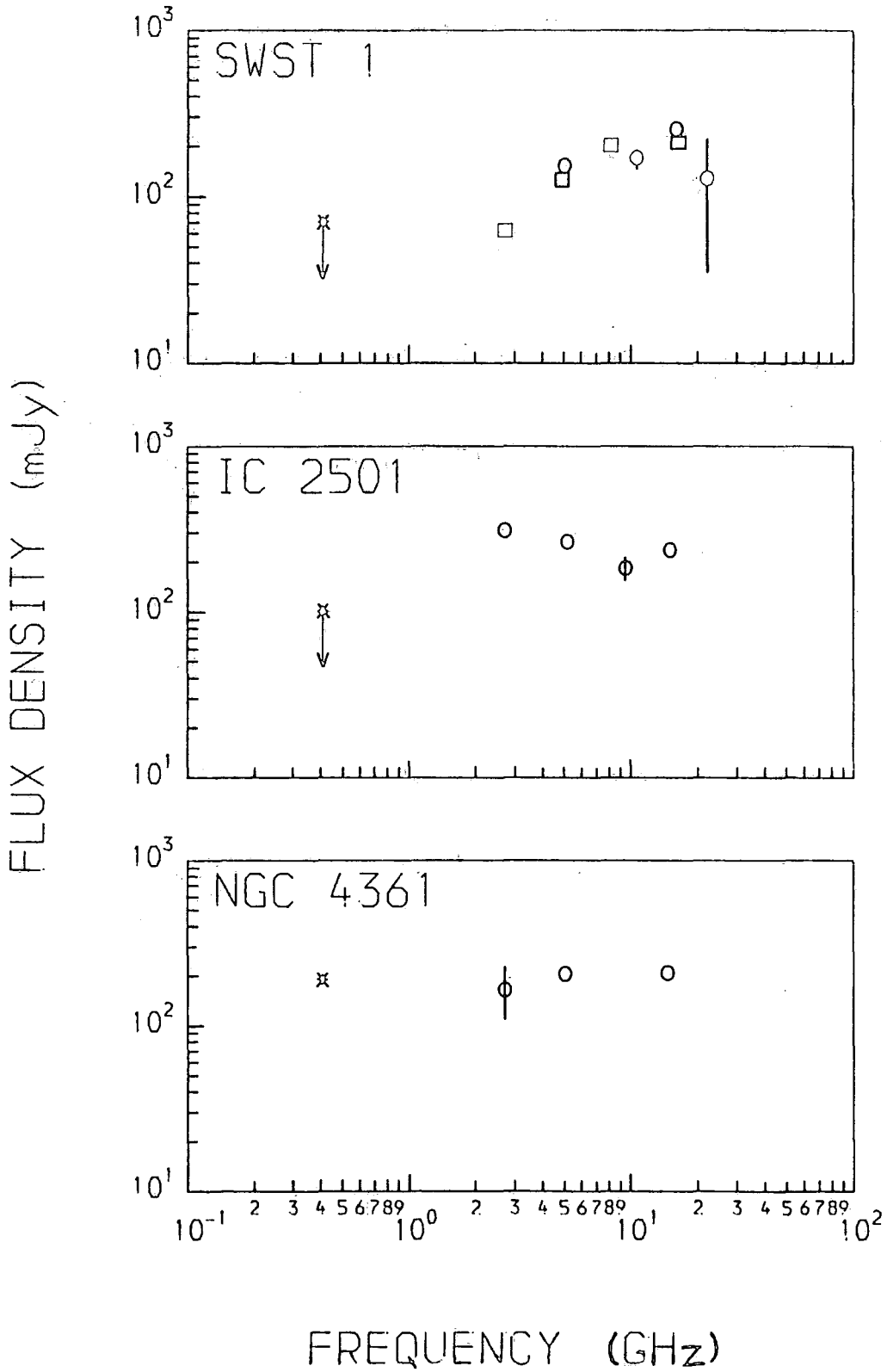

Figure (1-4): Radio spectra of SwSt 1, IC 2501, and NGC 4361. Data obtained using the Molonglo (*), Parkes (O), ARO (O), NARO-VLA (⊡), and NARO-3 element (□). telescopes. See Table (1-9).

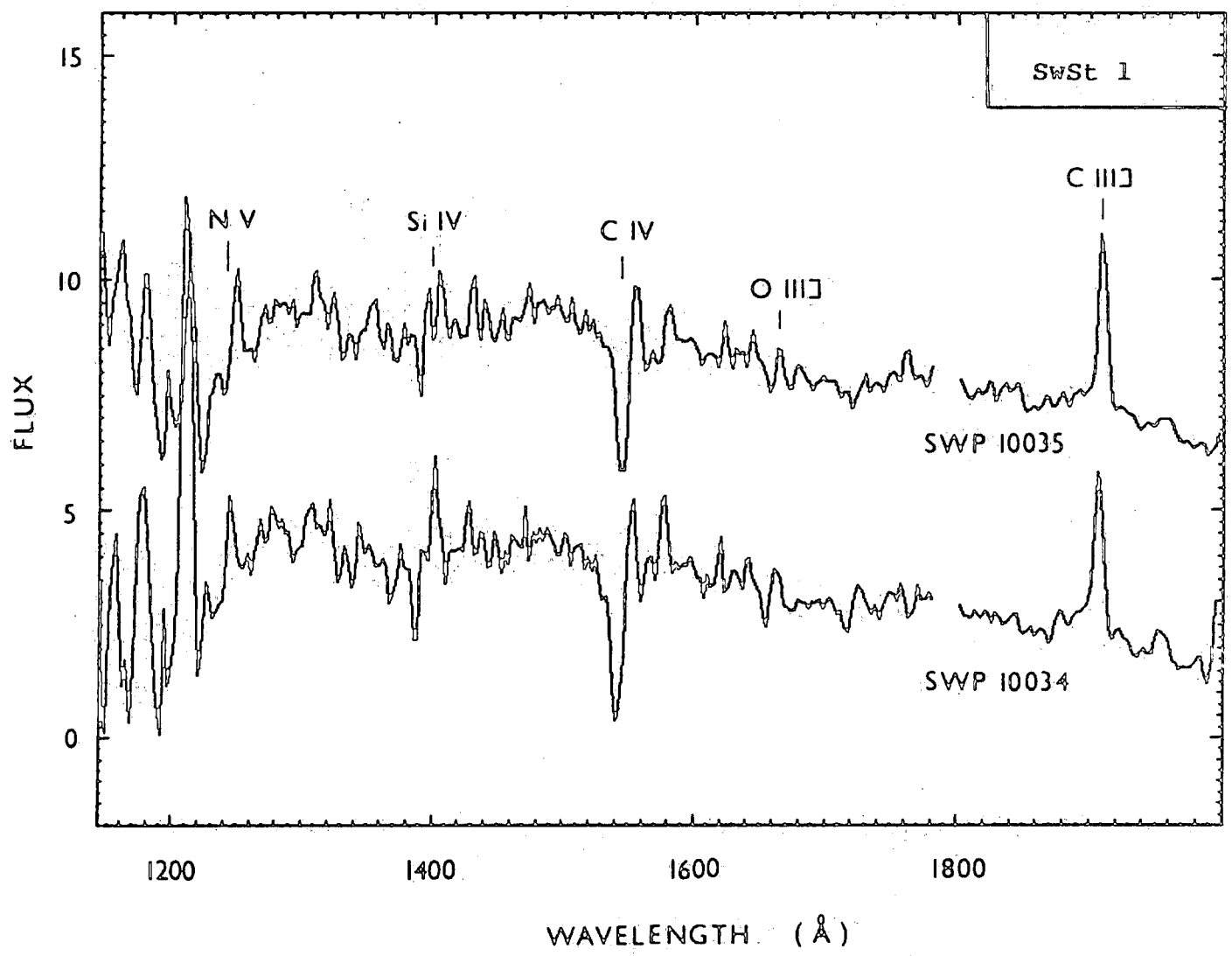

Figure (1-5): IUE low-dispersion (SWP) spectra of SwSt 1. The observed flux is in units of 10^{-13} erg cm^{-2} s^{-1} Å^{-1} (a value of 5 is added to the upper curve).

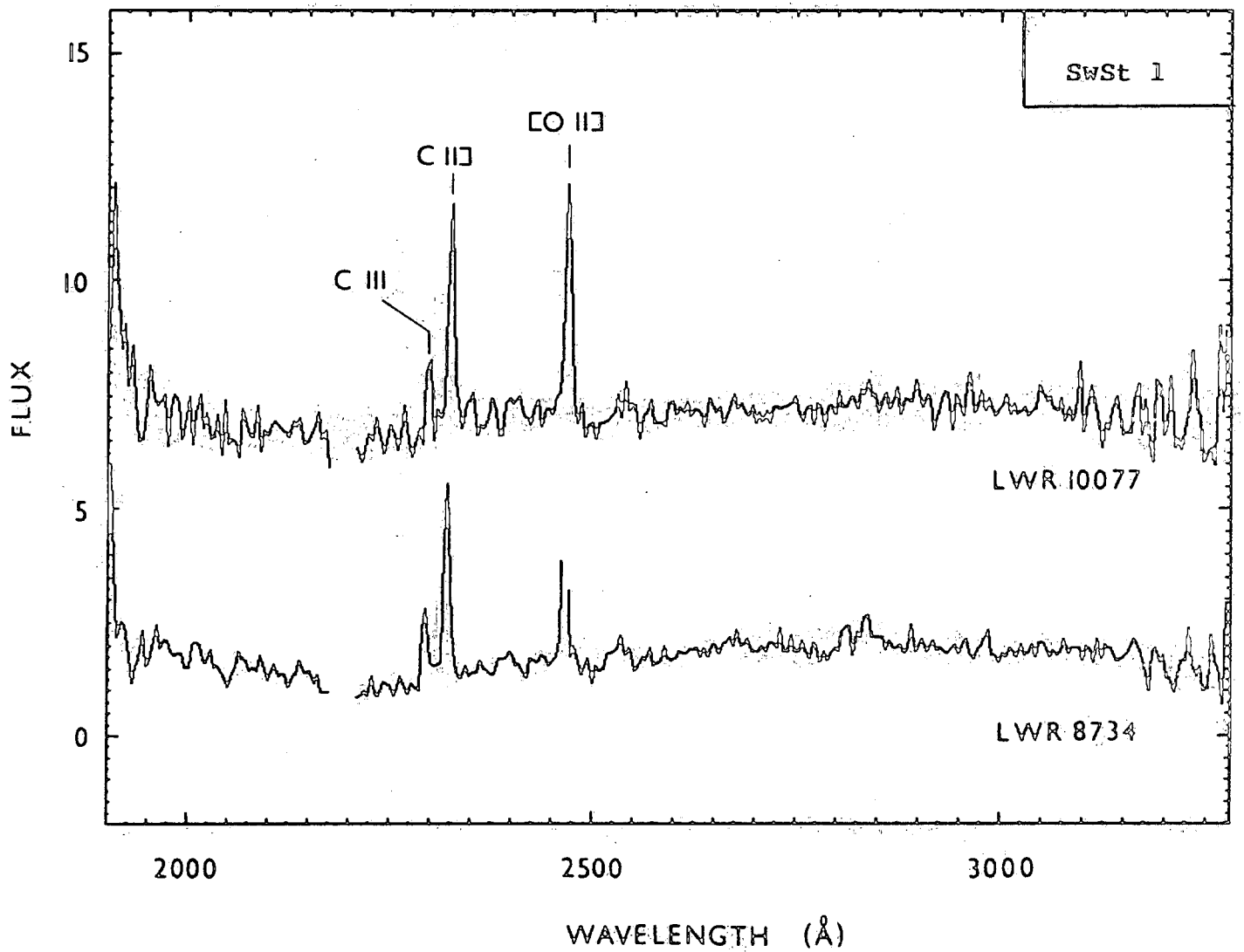

Figure (1-6): IUE low-dispersion (LWR) spectra of SwSt 1. The observed flux is in units of 10^{-13} erg cm^{-2} s^{-1} Å^{-1} (a value of 5 is added to the upper curve).

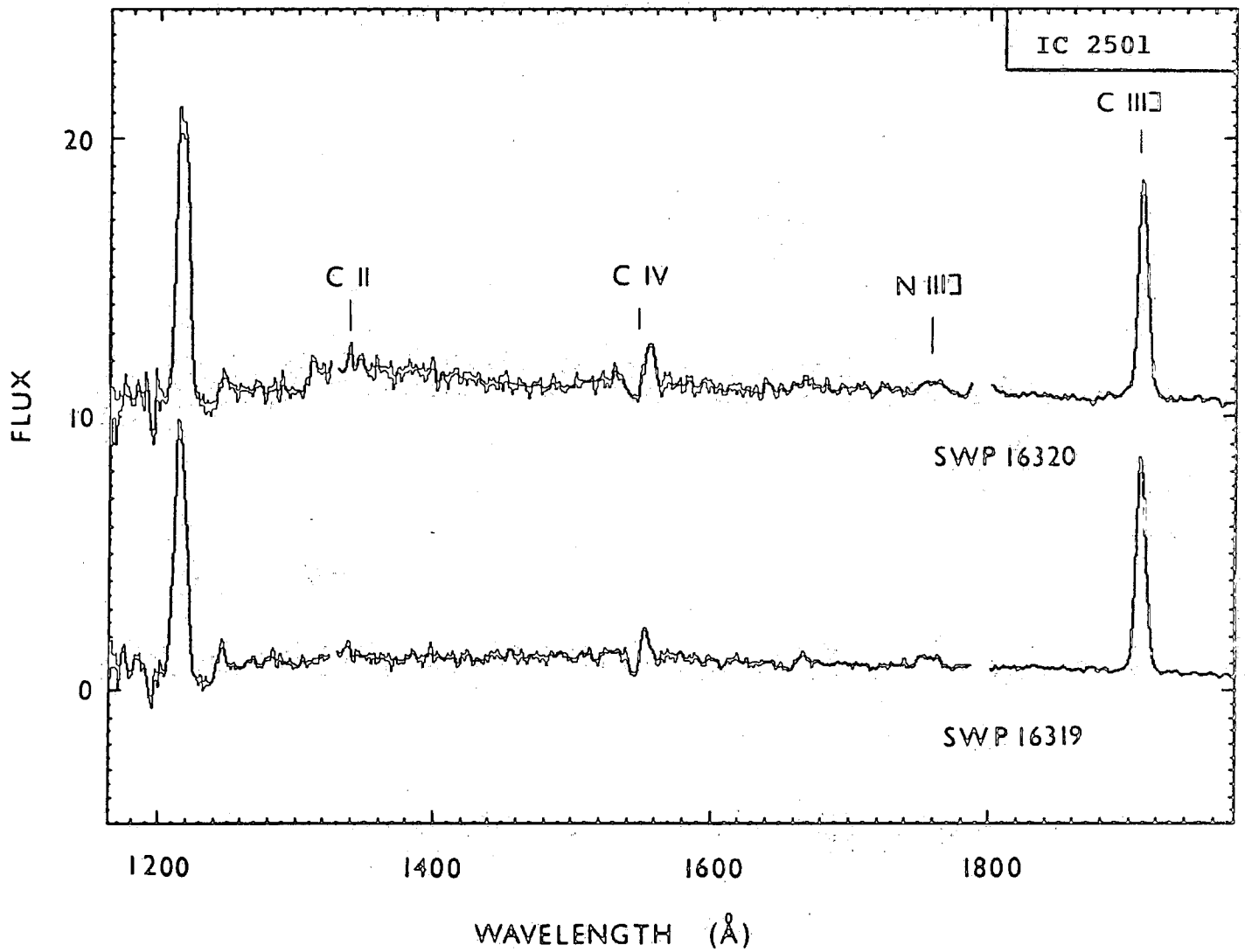

Figure (1-7): IUE low-dispersion (SWP) spectra of IC 2501. The observed flux is in units of 10^{-13} erg cm^{-2} s^{-1} $Å^{-1}$ (a value of 10 is added to the upper curve).

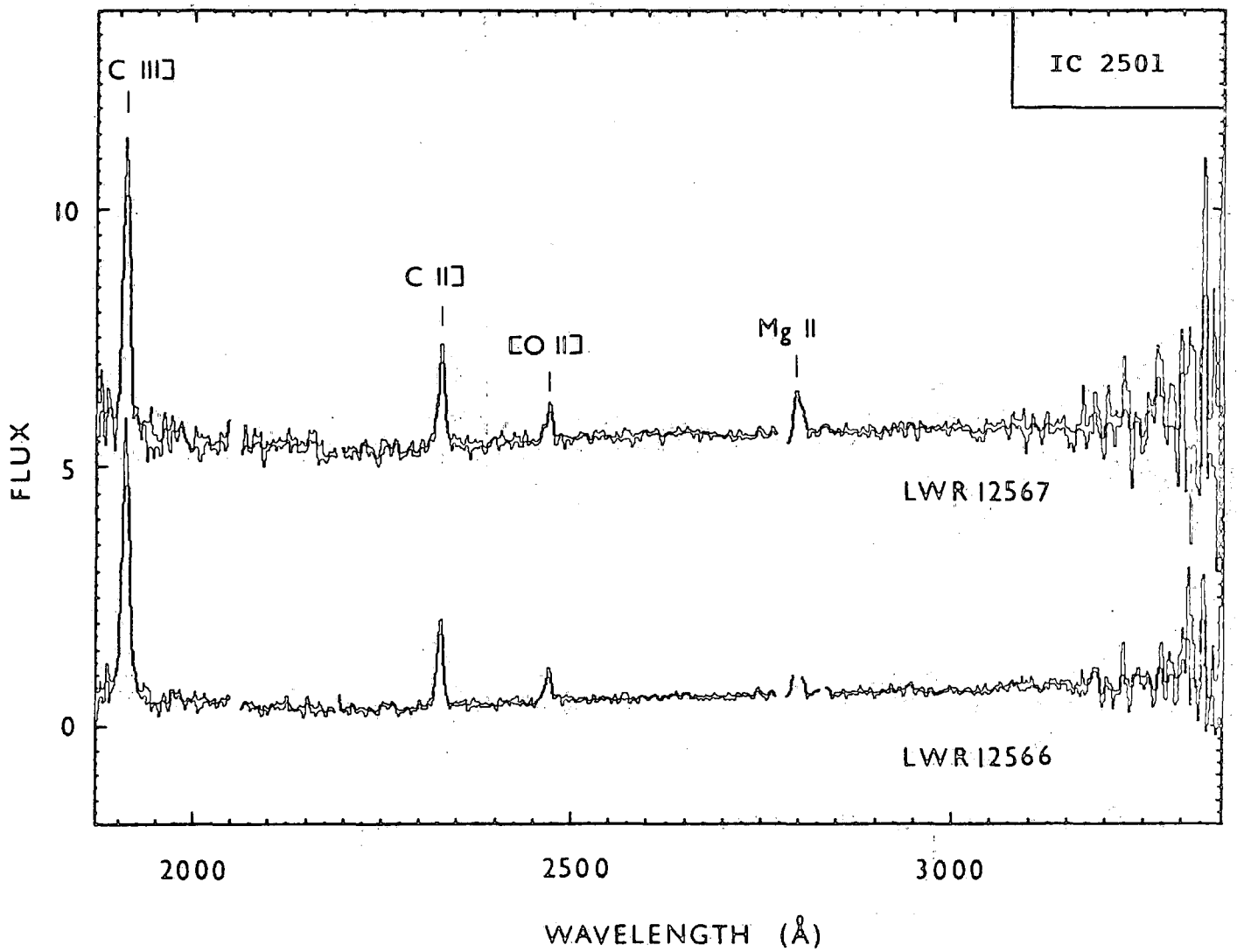

Figure (1-8): IUE low-dispersion (LWR) spectra of IC 2501. The observed flux is in units of 10^{-13} erg cm^{-2} s^{-1} $Å^{-1}$ (a value of 5 is added to the upper curve).

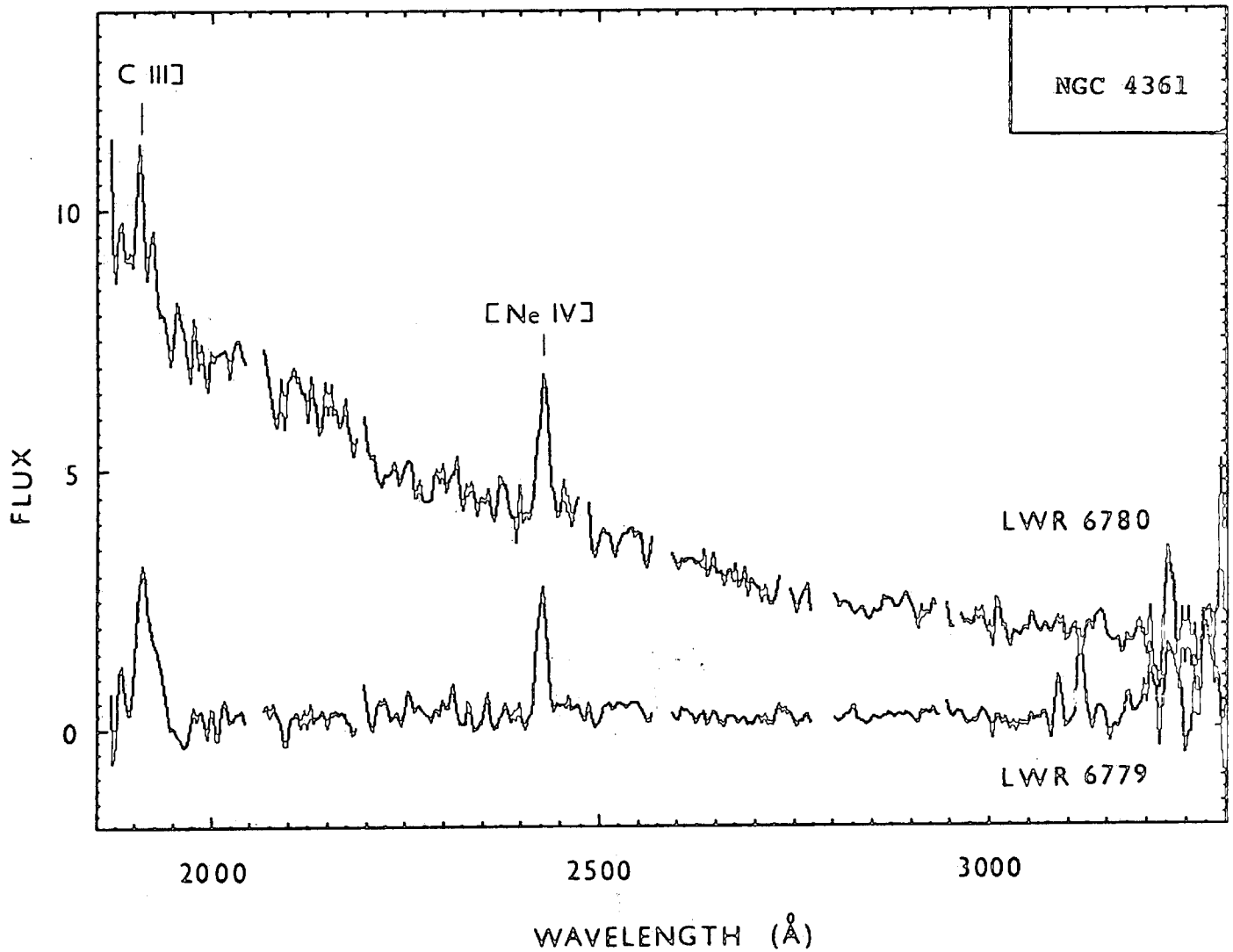

Figure (1-10): IUE low-dispersion (LWR) spectra of NGC 4361. The observed flux is in units of 10^{-13} erg cm^{-2} s^{-1} Å^{-1} (the lower curve is multiplied by 3).

CHAPTER (2)

PHYSICAL PROCESSES AND RELATED ATOMIC DATA

2.1 PHOTOIONIZATION

Photoionization of atoms or ions by absorption of the stellar ultraviolet radiation is the primary physical process in planetary nebulae. Let $N(X^{+m})$ be the number of ions per unit volume of element X in the m^{th} stage of ionization. The number of photoionization from an initial level i,

$$X_i^{+m} + h\nu \longrightarrow X^{+(m+1)} + e , \tag{2.1}$$

per unit volume per unit time is

$$\Phi_{PH} = N(X_i^{+m}) \int_{\nu_i}^{\infty} \frac{4\pi J_\nu}{h\nu} \, a(\nu, X_i^{+m}) \, d\nu . \tag{2.2}$$

where a is the photoionization cross-section, ν_i the threshold frequency, and the mean photon intensity of the local radiation field J_ν is less than Planck function,

$$B_\nu(T_e) = \frac{2 h \nu^3}{c^2} \left[\exp (h\nu/KT_e) - 1 \right]^{-1}, \tag{2.3}$$

by a factor of order 10^{-13} (this being the geometrical dilution factor). In equation (2.3); h is the Planck constant, K the Boltzmann constant, c the velocity of light, and T_e the electron temperature.

The major difficulty in the determination of the photoionization cross-section lies in the calculation of the matrix element $|M_{if}|^2$, resulting in the expression [Burgess and Seaton (1960a)]

$$a(\nu, X_i^{+m}) = \frac{4\pi\alpha a_o}{3} \frac{(I_i + k^2)}{\omega_i} |M_{if}|^2. \tag{2.4}$$

where α is the fine structure constant, a_o the Bohr radius, and ω_i the statistical weight of level i. Both the energy of the photon in excess of the ionization threshold k^2 and the ionization threshold energy I_i are expressed in Rydberg unit (13.60 ev or 109737 cm^{-1}), and $|M_{if}|^2$ is in atomic units.

2.1.1 Hydrogen Like

Exact analytic expressions for the matrix elements necessary for the calculation of the photoionization cross-section for atomic hydrogen and for hydrogen-like ions have been given by Gordon (1929). These expressions are complicated and difficult to evaluate directly for some ranges of parameters due to cancellation.

The quantum-mechanical treatment for hydrogen-like systems has been carried out by Gaunt (1930) and more completely by Menzel and Pekeris (1935). For many practical purposes, it is sufficiently accurate to calculate the photoionization cross-sections using the asymptotic expansion of the Kramers-Gaunt g-factor, as derived by Menzel and Pekeris (1935) and corrected by Burgess (1958) [see for example Seaton (1959)].

Burgess (1964a) introduced a method involving simple recurrence relations satisfied by the exact matrix elements which enable them to be calculated rapidly and to high accuracy. With this method, he calculated the photoionization cross-sections for all levels $n\ell$, where n and ℓ are the principal and orbital angular momentum quantum numbers, with $n \leq 20$ and for a wide range of energies of the ejected electron. Thus, photoionization cross-sections for hydrogenic ions are, in principle, known exactly.

2.1.2 Complex Ions

Application of equation (2.4) to non-hydrogenic atomic systems requires the use of approximate wave functions for the initial and final states. The most frequently used approximations are the Central Potential approximation [Reilman and Manson (1979)] and Quantum Defect theory [Burgess and Seaton (1960a); Peach (1967); Seaton (1983b)], the latter has been extensively applied in astrophysics [Flower (1968); Hidalgo (1968)]. Calculations based on methods like these give a very good picture about the general behavior of the cross-section over a broad energy range. To obtain the complicated resonance structure and features of the cross-section, methods such as the Close-Coupling approximation [Eissner and Seaton (1972); Mendoza (1983)] and Many Body Perturbation theory [Kelly (1964)] should be used. Figure (2-1) shows the theoretical photoionization cross-section of the ground state of the N^{+3} ion [Mendoza (1983)]. It can be seen that the resonance structure is well determined by the Close-Coupling approximation. The background of the cross-section is also obtained satisfactorily by the Quantum Defect theory.

References to the calculated photoionization cross-sections for ions of interest in planetary nebulae studies and to the type of approximation used in each case are given in Table 10 of Mendoza (1983). Aller (1984) gives two interpolation formulae based on the calculations by Henry (1970) and Chapman and Henry (1971, 1972). He also gives the parameters which are necessary for calculating the the photoionization cross-sections for the ground terms of ions of C, N, O, Ne, Si, S, and Ar. Fits for the photoionization cross-sections of N^{+2}, N^{+3}, O^{+4}, Al^{+}, Si^{+2}, and S^{+4} ions are given by Butler, Mendoza, and Zeippen (1985).

For most ions of astrophysical interest, photoionization cross-section calculations which incorporate resonance effects have been made only for the ground and some low-lying metastable states. There remains a lot of work to be done in order to extend this type of calculation.

2.2 RECOMBINATION PROCESSES

In a nebular gas of electron density N_e (cm^{-3}), and temperature T_e (K), the total number of captures,

$$X^{+(m+1)} + e \longrightarrow X^{+m} \tag{2.5}$$

per unit volume per unit time is

$$\Phi_{REC} = N_e \, N[X^{+(m+1)}] \; \alpha(T_e, X^{+m}). \tag{2.6}$$

where the total recombination coefficient $\alpha(cm^3 \; s^{-1})$ is given by

$$\alpha(T_e, X^{+m}) = \alpha^R(T_e, X^{+m}) + \alpha^D(T_e, X^{+m}). \tag{2.7}$$

α^R and α^D being respectively the total radiative and dielectronic recombination coefficients.

When an electron is captured in a highly excited level j, it may cascade to a lower level i,

$$X_j^{+m} \longrightarrow X_i^{+m} + h\nu_{ji} \, , \tag{2.8}$$

with the emission of a recombination line. The prominent H and He lines are produced in this manner, as are the permitted lines of C, N, O, and Ne, which are much weaker because of the lower abundances of these elements in planetary nebulae. The number of photons emitted in the $j \rightarrow i$ transition is

$$\mathcal{N}_{ji} = N_e \, N[X^{+(m+1)}] \; \alpha^{eff}_{j \rightarrow i}(T_e, X^{+m}). \tag{2.9}$$

where $\alpha^{eff}_{j \rightarrow i}$ is called the effective recombination coefficient.

2.2.1 Radiative Recombination Coefficients

Consider the radiative recombination on level i of an ion X^{+m},

$$X^{+(m+1)} + e \longrightarrow X_i^{+m} + h\nu \, . \tag{2.10}$$

The cross-section for radiative capture, $\sigma(v, X_i^{+m})$, can be found from the standard relation of Milne, involving the equilibrium condition for processes (2.1) and (2.10). The relation can be written as

$$\sigma(v, X_i^{+m}) = \frac{\omega_i}{\omega_e \, \omega_+} \, \frac{h\nu}{m \, c^2} \, \frac{h\nu}{1/2 \, m \, v^2} \, a(\nu, X_i^{+m}). \tag{2.11}$$

where v and m are respectively the free electron velocity and mass, ω_+ the statistical weight of the recombining ion, and the statistical weight of the free electron ω_e is 2. The rate coefficient for radiative recombination is obtained by integrating $\sigma(v, X_i^{+m})$ over the Maxwellian distribution of v :

$$\alpha^R(T_e, X_i^{+m}) = (1/c^2) \, (2/\pi)^{1/2} \, [m \, K \, T_e]^{-3/2} \, (\omega_i/\omega_+) \, \exp[I_i/(KT_e)] \times$$
$$\times \int_{I_i}^{\infty} (h\nu)^2 \, a(\nu, X_i^{+m}) \, \exp[-h\nu/(KT_e)] \, d(h\nu) \, . \tag{2.12}$$

where I_i is the threshold ionization energy of level i of the X^{+m} ion.

Because of the low density of the nebular gas and diluteness of the radiation field, it may be assumed that photoionization occurs only from the ground state, whereas recombinations may occur on all states [see for example Zanstra (1926)]. The total radiative recombination coefficient is therefore given by

$$\alpha^R(T_e, X^{+m}) = \sum_{i=n_o} \alpha^R(T_e, X_i^{+m}). \tag{2.13}$$

where n_o is the principal quantum number of the ground state of the X^{+m} ion.

Hydrogenic radiative recombination coefficients can, in practice, be calculated to any required precision [Seaton (1959); Burgess (1964a)]. A FORTRAN programme which computes them is also available through Computer Physics Communications [Flower and Seaton (1969a)]. For recombination to excited states with $i > n_o$ of complex ions, the coefficients can be calculated assuming the hydrogenic approximation, since these states with increasing i approach hydrogenic ones and give the principal contribution to the sum in equation (2.13). For recombination to the ground state ($i = n_o$), the coefficient must be calculated from the corresponding photoionization cross-section.

Burgess and Seaton (1960b) have evaluated the recombination coefficients for

$$He^+ + e \longrightarrow He(n\,{}^{2S+1}L) + h\nu, \qquad (2.14)$$

using hydrogenic data for $L \geq 2$ and allowing for the non-hydrogenic character of the He nS and nP states.

Tarter (1971, 1973), Aldrovandi and Pequignot (1973, 1974), and Gould (1978) have given expressions for calculating radiative recombination coefficients of complex ions. In all cases, a hydrogenic formulation is used, but the results of Gould are corrected for non-hydrogenic effects. In Table (2-1), we summarize these results.

The effect of resonances in the photoionization cross-sections, which have been used to evaluate the recombination coefficients, have not been considered in all of the above compilations. In He and Li-like ions, the formation of resonance states involves the excitation of an electron from the 1S shell and free electron energies which are not available at nebular temperatures. Resonance effects can therefore be neglected for these ions [Storey (1983)]. For other ions of astrophysical interest, a great deal of work remains to be done.

2.2.2 Dielectronic recombination coefficients

Consider an ion $X^{+(m+1)}$ which collides with an electron whose energy is E. Suppose that this total energy E corresponds to the ion X^{+m} in which two electrons in the outer shell are excited simultaneously (the electron excited to the higher level is held in a state above the first ionization potential). Then we may have the reaction

$$X^{+(m+1)} + e \longrightarrow X_a^{+m} \tag{2.15}$$

where a stands for an autoionizing state. We refer to this process as dielectronic capture, and to its inverse as autoionization. In thermodynamic equilibrium (TE), the principle of detailed balance applies and the number of dielectronic captures will equal the number of autoionizations:

$$N_e\, N_{TE}[X^{+(m+1)}]\ \alpha^C(T_e, X_a^{+m}) = N_{TE}(X_a^{+m})\ \Gamma_a^{(A)}\ . \tag{2.16}$$

where $\Gamma_a^{(A)}$ is the autoionization transition probability (s^{-1}), α^C is the capture coefficient, and N_{TE} are the thermodynamic populations given by Saha equation:

$$N_{TE}(X_a^{+m}) = \frac{\omega_a}{2\,\omega_{+(m+1)}} \left[\frac{h^2}{2\,\pi\, m\, K\, T_e}\right]^{3/2} \exp\left[\frac{-E_a}{K\, T_e}\right] N_e\, N_{TE}[X^{+(m+1)}]. \tag{2.17}$$

where E_a is the energy of the autoionizing state relative to the ground state of $X^{+(m+1)}$. Under nebular conditions, ions escape from X_a^{+m} not only by autoionization transitions but also by radiative decays,

$$X_a^{+m} \longrightarrow X^{+m} + h\nu\ . \tag{2.18}$$

In the non TE conditions which prevail in nebulae, the radiative decay of X^{+m} with total probability $\Gamma_a^{(R)}$ (s^{-1}) must also be included, so that

$$N_e\, N[X^{+(m+1)}]\ \alpha^C(T_e, X_a^{+m}) = N(X_a^{+m})\ [\Gamma_a^{(A)} + \Gamma_a^{(R)}]\ . \tag{2.19}$$

By combining equations (2.16) and (2.19), we obtain

$$\frac{N(X_a^{+m})}{N_e\ N[X^{+(m+1)}]} = \frac{N_{TE}(X_a^{+m})}{N_e\ N_{TE}[X^{+(m+1)}]}\ b(X_a^{+m}) \ . \qquad (2.20)$$

The factor $b(X_a^{+m})$ is a measure of the departure of the population of X_a^{+m} from its TE value, given by

$$b(X_a^{+m}) = \frac{\Gamma_a^{(A)}}{\Gamma_a^{(A)} + \Gamma_a^{(R)}} \ . \qquad (2.21)$$

The recombination rate will equal the rate of recombined ions strickling down to a common bound state b in stabilizing transitions, i.e.,

$$N_e\ N[X^{+(m+1)}]\ \alpha^D(T_e, X_a^{+m}) = N(X_a^{+m})\ \Gamma_{ab}^{(R)} \ . \qquad (2.22)$$

From (2.17), (2.20), and (2.22), we obtain

$$\alpha^D(T_e, X_a^{+m}) = \frac{\omega_a}{2\ \omega_{+(m+1)}} \left[\frac{h^2}{2\ \pi\ m\ K\ T_e}\right]^{3/2} \exp\left[\frac{-E_a}{K\ T_e}\right]\ b(X_a^{+m})\ \Gamma_{ab}^{(R)} \ . \qquad (2.23)$$

for the dielectronic recombination coefficient. The total coefficient can be obtained from

$$\alpha^D(T_e, X^{+m}) = \sum_{n_a} \alpha^D(T_e, X_a^{+m}) \ . \qquad (2.24)$$

where n_a is the effective quantum number of the autoionizing state.

2.2.2.1 High Temperatures

A general formula which enables dielectronic recombination coefficients to be calculated is given by Burgess (1964b). The main assumptions of Burgess are :

(1) the mean thermal energies $3/2\ (K\ T_e)$ of the free electrons are comparable with E_R , where E_R is the excitation energy of the first resonance transition of the recombining ion;

(2) dielectronic recombination proceeds via large numbers of doubly excited autoionizing states with a high principal quantum number of the captured electron; and

(3) core relaxation is the principal mechanism of radiative stabilization.

In a following paper, Burgess (1965) introduced a fit to the dielectronic recombination coefficient, intended for use at high temperatures ($KT_e > E_R$). The general formula shows that the coefficient of dielectronic recombination greatly exceeds that of direct radiative recombination.

At the lower temperatures ($\approx 10^4$K) more typical of planetary nebulae, the Burgess general formula, employed for example by Aldrovandi and Pequignot (1973), gives the dielectronic contribution to the recombination coefficient to be negligible [see Figure (2-2)].

2.2.2.2 Low Temperatures

Recent calculations by Beigman and Chichkov (1980) and Storey (1981) have shown that dielectronic recombination is also important at nebular temperatures. The use of the general formula is incorrect at these temperatures because of the following. In most ions, terms of the same parity as the ground term lie between the ground and the first excited state of opposite parity. Series of autoionizing states converge on these terms and become accessible at nebular temperatures. These terms were not included in the general formula. In addition, some ions have low-lying metastable states. The corresponding autoionizing states have not been considered in the dielectronic process described by Burgess. Furthermore, for low-lying autoionizing states, radiative stabilization through transitions of the captured electron must be taken into account.

It is shown by Seaton and Storey (1976) that, in atomic units, $\Gamma_a^{(A)} = C / n_a^3$ where C is of order unity. As a function of increasing orbital angular momentum quantum number ℓ, C generally at first increases, then decreases rapidly. Thus $\Gamma_a^{(A)}$ tends to zero for ℓ, n_a large. Since $\Gamma_a^{(A)}$ is independent of a, the sum in equation (2.24) converges since $b(X_a^{+m}) \longrightarrow 0$ as $\Gamma_a^{(A)} \longrightarrow 0$ for ℓ, n_a large. In practice at high temperatures, states with $n_a \approx 100$ and $\ell \leq 10$ are important. For the outer electron decay we have, in atomic units, $\Gamma_a^{(R)} = R\, \alpha^3\, Z^4 / n_a^3$ where α is the fine structure constant, R is of order unity, and Z is the recombining ion charge. Hence, if Z, ℓ, n_a are small, $\Gamma_a^{(A)} >> \Gamma_a^{(R)}$ so that $b(X_a^{+m}) = 1$. It follows from equation (2.23) that to obtain α^D at low temperatures where only low-lying resonances are accessible, only knowledge of $\Gamma_{ab}^{(R)}$ is necessary.

Low temperature dielectronic recombination coefficients which take account of the above effects have been given by Nussbaumer and Storey (1983a) for ions of C, N, and O. In Table (2-2), we summarize these results. From Tables (2-1) and (2-2), we see that the coefficients for dielectronic recombination of most ions exceed the corresponding radiative recombination coefficients over a wide range of nebular temperatures.

It is recommended by Nussbaumer and Storey (1983a) that the total recombination coefficient be calculated from

$$\alpha(T_e, X^{+m}) = \alpha^R(T_e, X^{+m}) + \alpha^D(T_e, X^{+m}) + \alpha^B(T_e, X^{+m}) \qquad (2.25)$$

rather than from equation (2.7); α^B is the high temperature dielectronic recombination coefficient as derived from the general formula of Burgess.

2.2.2.3 Recent Work

The most recent and more rigorous theory of the dielectronic recombination process has been developed by Bell and Seaton (1985). Their derived formulae differ from those which have been derived earlier using intuitive arguments, but the differences are not such as to give important differences in the calculated values of the dielectronic recombination rates for astronomical plasma conditions (cf. their figure 2).

The theory of Bell and Seaton has resolved one of the most interesting problems which have been encountered in earlier work. We refer to the work by Seaton and Storey (1976), who found difficulties in attempts to use the theory of Davies and Seaton (1969) for the case of Rydberg series of resonances. Seaton (1983b) thought that the method used by Davies and Seaton to solve the time-dependent equations for interactions with the radiation field was in error. It is shown by Bell and Seaton that:

(a) the method used by Davies and Seaton is correct and it gives results in agreement with those obtained using the method described by Bell (1979);

(b) the point concerning the validity of an interchange of limiting processes in solving the time-dependent equations, which was questioned by Seaton, can be justified rigorously using methods described by Titchmarsh (1948); and

(c) the treatment of Seaton and Storey was unsatisfactory in that they attempted to consider separately the resonances belonging to definite values of the principal quantum number while, in order to obtain correct results for any one energy in the case of Rydberg series of resonances, it is necessary to evaluate summations for the complete series of autoionization resonances.

2.2.3 Effective Recombination Coefficients

Extensive calculations of the effective recombination coefficients for Cases A and B (nebulae optically thin in all spectrum lines or optically thick for transitions to the ground state) of Baker and Menzel (1938) have been made by Pengelly (1963, 1964) for an infinite number of levels, assuming no collisional redistribution of angular momentum or of energy. These calculations are valid in the limit of zero density.

The most complete calculations, which allow fully for such collisional processes, of recombination coefficients for hydrogen and helium are those of Brocklehurst (1970, 1971, 1972). The first of these three papers deals with highly excited states ($n \geq 40$) of hydrogen, making the assumption that collisional processes of the type

$$H(n, \ell) + H^+ \longrightarrow H(n, \ell \pm 1) + H^+ \qquad (2.26)$$

are much faster than radiative processes. Pengelly and Seaton (1964) have discussed the validity of this assumption, which results in the individual n,ℓ states being populated according to their statistical weights $\omega_{n\ell} = 2(2\ell+1)$,

$$N_{n,\ell} = N_n \, (2\ell+1) \, / \, n^2 \, . \qquad (2.27)$$

In the second paper, the low states ($n \leq 40$) of hydrogen and singly ionized helium are treated, and the populations of ℓ states are calculated explicitly. The recombination coefficients for neutral helium are calculated in the last paper.

Table (2-3) gives the effective radiative recombination coefficients for the most important lines of H and He, which have been observed in the spectra of planetary nebulae. Data are from Brocklehurst (1971, 1972) and for the case $N_e = 10^4$ cm^{-3}. The dependence of the

coefficients on N_e is shown explicitly by Brocklehurst's calculations. The values given in Table (2-3) for He I are for Case A. All other values are for Case B.

Effective dielectronic recombination coefficients for ions of C , N , and O have been calculated by Storey (1981), assuming that $\Gamma_a^{(A)} >> \Gamma_a^{(R)}$. His results for C III λ1176 and C II λ1335 lines are given in Table (2-4). Nussbaumer and Storey (1983b) have calculated the coefficients for C III λ2297 transition, using improved bound-bound radiative data. Their results, given in Table (2-4), are approximately 25% lower than the results of Storey (1981).

2.3 CHARGE TRANSFER

Ionization of a planetary nebula depends not only on the photoionization, but also on the phenomenon of charge exchange. The most important charge exchange reactions are

$$X^{+(m+1)} + H^{o} \rightleftharpoons X^{+m} + H^{+} + \Delta E, \qquad (2.28)$$

and

$$X^{+(m+1)} + He^{o} \rightleftharpoons X^{+m} + He^{+} + \Delta E. \qquad (2.29)$$

where ΔE is the energy defect. In most cases, the ion X^{+m} is produced in an excited state. As a result, the inverse reaction of charge transfer is not usually of importance since the excited state decays rapidly by spontaneous radiative emission. However, if charge transfer can proceed via the ground state of the X^{+m} ion, then the inverse process can also take place. The effect of this process on the ionization equilibrium of Si is discussed by Baliunas and Butler (1980).

In general, charge transfer reaction may proceed more rapidly than radiative and dielectronic recombination as a mechanism for reducing the state of ionization and more rapidly than electron impact ionization and photoionization as a mechanism for increasing the state of ionization.

if β denotes the coefficient of the charge transfer process $X^{+(m+1)} + Y^{o} \longrightarrow X^{+m} + Y^{+}$ while β' the coefficient of the inverse process $X^{+(m+1)} + Y^{+} \longrightarrow X^{+m} + Y^{o}$, then the corresponding rates ($cm^3\ s^{-1}$) are

$$\Phi_{CT} = N(Y^{o})\ N[X^{+(m+1)}]\ \beta\ , \tag{2.30}$$

and

$$\Phi'_{CT} = N(Y^{+})\ N(X^{+m})\ \beta'\ . \tag{2.31}$$

where Y stands for H or He.

In the analysis of Pequignot et al. (1978) of the the planetary nebula NGC 7027, the rate coefficients for charge transfer reactions were regarded as empirical parameters to be determined by the observations of the emission spectrum. This analysis led them to conclude that charge transfer reactions with neutral hydrogen and helium are important for certain doubly and more highly charged ions. Pequignot (1980a) assumed reasonable empirical estimates of the charge exchange reaction rates and obtained excellent agreement between the calculated and observed fluxes produced by ions of C , N , O , Ne , and S. On the basis of models of of NGC 7662 [Pequignot (1980b)] and NGC 6720 [Ulrich and Pequignot (1980)], these conclusions were confirmed.

Recent developments in the calculations of the adiabatic potential energy surfaces and the coupling matrix elements [Butler (1979)] and in the solution of the coupled equations describing the scattering [Heil and Dalgrano (1979)] have allowed quantal calculations of charge

transfer rate coefficients at nebular temperatures. In Table (2-5), we compile the most recent results of calculations of charge transfer rate coefficients. For strong reactions, the calculated rate coefficients are in substantial agreement with the predicted ones. For weaker reactions, the problem is more confused. For example, Pequignot et al. (1978) have predicted a rate coefficient of 8×10^{-10} cm^3 s^{-1} for the reaction

$$O^{+2} + H^{o} \longrightarrow O^{+} + H^{+} . \qquad (2.32)$$

Quantum mechanical calculations by Butler et al. (1980) yield a rate coefficient of about the same as the predicted value. On the other hand, the reaction

$$Ne^{+2} + H^{o} \longrightarrow Ne^{+} + H^{+} \qquad (2.33)$$

was predicted to be fast, with a rate coefficient of 3×10^{-10} cm^3 s^{-1} (Pequignot et al.). Quantal calculations (Butler et al.) show that this reaction must be slow. Butler et al. concluded that radiative charge transfer,

$$Ne^{+2} + H^{o} \longrightarrow Ne^{+} + H^{+} + h\nu , \qquad (2.34)$$

will proceed more rapidly, with a rate coefficient between 10^{-15} and 10^{-14} cm^3 s^{-1}.

The best known of charge transfer reactions is that between ground level of O^{+} and H^{o},

$$O^{+} (^4S_{3/2}) + H^{o} (^2S_{1/2}) \rightleftharpoons O^{o} (^3P) + H^{+} . \qquad (2.35)$$

The importance of this process in the planetary nebula IC 418 was first demonstrated by Williams (1973). The interaction here is almost resonant ($\Delta E << KT_e$) and is sufficiently rapid for detailed balance to be established. Under these conditions, the reaction rate coefficients

[$\beta=1.04\times10^{-9}$ cm^3 s^{-1}, $\beta'=0.91\times10^{-9}$ cm^3 s^{-1} ; Field and Steigman (1971)] are in the ratios of statistical weights, i.e., $[\omega(O^o)\ \omega(H^+)] / [\omega(O^+)\ \omega(H^o)] = \omega(^3P) / [\omega(^4S)\ \omega(^2S)] = 9/8$. So that

$$\frac{N(O^o)}{N(O^+)} = \frac{9}{8}\ \frac{N(N^o)}{N(H^+)}\ , \qquad (2.36)$$

and the ionization of O^o is bound to that of H^o. Chambaud et al. (1980) have performed quantum mechanical calculations of the rate coefficients for $10 \leq T_e \leq 1000$ K. Their results differ from those calculated by Field and Steigman (1971), using the orbiting approximation, by less than 40% at $T_e = 1000$ K. In planetary nebulae, where $T_e \approx 10000$ K, the exact value of the rate coefficient is unimportant.

In planetary nebulae of moderate-to-high excitation, ions may be found in zones where there is an appreciable concentration of H^o, so the production of O^+ ions by charge exchange can become significant. It is thus important to consider charge exchange when calculating the ionization equilibria and structural models of planetary nebulae. Perinotto (1977) concluded that inclusion in the model nebulae of charge transfer reactions will help to reconcile the computed line intensities with the observed ones.

2.4 ELECTRON COLLISIONAL EXCITATION

Electron collisional excitation is responsible for the production of the strong forbidden and intercombination lines observed in the spectra of planetary nebulae. This process is also responsible for the excitation of some of the permitted lines in the ultraviolet (e.g., C IV λλ1548, 1551).

Consider the electron collisional excitation of an ion X^{+m} from a lower level i to an upper level j. The direct process is

$$X_i^{+m} + e \longrightarrow X_j^{+m} + e \,. \tag{2.37}$$

It is also important to consider processes of the type

$$X_i^{+m} + e \longrightarrow X_a^{+(m+1)} \longrightarrow X_j^{+m} + e \,. \tag{2.38}$$

in which an autoionizing state, a , is excited during the collision.

Hebb and Menzel (1940) noted that the cross-section, $Q_v(i \Rightarrow j)$, for collisional excitation varied almost as v_i^{-2} , where v_i is the velocity of the incident electron. Hence, they introduced the parameter $\Omega(i,j)$, which Seaton (1955a,b) subsequently suggested should be termed the collision strength. It is defined by the expression

$$Q_v(i \rightarrow j) = \frac{\pi \, \Omega(i,j)}{\omega_i \; K_i^2} \tag{2.39}$$

where $K_i = m \, v_i \, / \, \hbar$. Since K_i^2 has the dimensions of a reciprocal length, $\Omega(i,j)$ is dimensionless. From the principle of detailed balance it follows that Ω is symmetrical in lower and upper states, $\Omega(i,j)=\Omega(j,i)$.

In the calculation of the collision rate, the collision strength must be determined. For the low temperatures found in planetary nebulae, the collision strength must be calculated at low energies where it is dominated by threshold effects such as resonances. To reproduce these effects, full quantum mechanincal calculations are necessary. Calculations of collision strengths have been carried out by a variety of theoretical techniques. Czyzak (1968) gives a discussion of the "Exact Resonance method" [Seaton (1953)] and the "Distorted Wave method" [Seaton (1955a,b)]. The most recent "Close Coupling approximation" mentioned in section (2.1.2) has also been employed. In this approximation, the coupled integro-diffrential equations are solved numerically by methods such as the linear algebraic [Seaton (1974)], the R-matrix [Burke et al. (1971)], and the

non-iterative integral equation [Smith and Henry (1973)] methods. For a review of most of these methods and description of the major computer programme packages that are available and widely used in this field, see Burke and Eissner (1983).

In Figure (2-3), we present the results of the calculations of the collision strength for the $^4S^o - {}^2P^o$ transition of S^+ [Mendoza (1983)]. Given the complexity of the calculations, the results obtained by different methods are in good agreement.

In the more rigorous theory of Bell and Seaton (1985), expressions have been derived for detailed resonance profiles allowing for radiative decays (dielectronic recombination) as well as for collision strengths averaged over resonances. Pradhan and Seaton (1985) have used these expressions to calculate collision strengths for the $1\ {}^1S - 2\ {}^1S$ transitions in O^{+6} ion at energies below the $2\ {}^1P$ threshold. They found that there are no large differences between their results and the results obtained by Pradhan (1981) using an intuitive argument. This conclusion is analogous to that encountered in our discussion of the dielectronic recombination rates (section 2.2.2.3).

Pradhan and Seaton have also shown that allowance for radiative decays leads to modifications of autoionizing resonance profiles and substantial reduction in collision strengths averaged over resonances. The effects of radiative decays on collision strengths for collisional excitation of positive ions, particularly the more highly ionized systems, were first discussed by Presnyakov and Urnov (1974) and by Pradhan (1981).

In astrophysical applications, one generally requires the number of collisional excitation ($cm^{-3}\ s^{-1}$)

$$\Psi_{ij} = N_e \, N(X_i^{+m}) \quad q(i \rightarrow j) \, , \tag{2.40}$$

where $q(i \rightarrow j)$ is the collisional excitation rate coefficient ($cm^3 \, s^{-1}$). Put $E_i = m \, v_i^2 / 2$ and $E_j = m \, v_j^2 / 2$, where v_j is the velocity of the scattered electron. The rate coefficient for de-excitation is

$$q(j \rightarrow i) = \frac{8.63 \times 10^{-6} \quad T(j,i)}{\omega_j \quad T_e^{1/2}} \tag{2.41}$$

where

$$T(j,i) = \int_0^{\infty} \Omega(j,i) \quad \exp(-E_i/KT_e) \quad d(-E_j/KT_e) \tag{2.42}$$

is called the effective collision strength. If Ω is independent of energy, $T = \Omega$. In thermodynamic equilibrium, $N(X_i^{+m})$ and $N(X_j^{+m})$ are related by the Boltzmann equation

$$\frac{N(X_j^{+m})}{N(X_i^{+m})} = \frac{\omega_j}{\omega_i} \quad \exp(-h\nu/KT_e) \, . \tag{2.43}$$

From the principle of detailed balance, it follows that

$$q(i \rightarrow j) = \frac{8.63 \times 10^{-6} \quad T(i,j)}{\omega_i \quad T_e^{1/2}} \quad \exp(-\Delta E_{ij}/KT_e) \tag{2.44}$$

where $\Delta E_{ij} = (E_j - E_i)$ is the excitation energy of the $i \rightarrow j$ transition.

A compilation of effective collision strengths for ions of interest in planetary nebulae studies is presented by Mendoza (1983). Table (2-6) gives the values of $T(SL, S'L')$ for some important ultraviolet transitions.

A very useful relation holds for collision strengths between a term consisting of a single level and one consisting of several levels:

$$T(SLJ, S'L'J') = \frac{(2J'+1)}{(2S'+1) \, (2L'+1)} \quad T(SL, S'L') \tag{2.45}$$

where (2S'+1) (2L'+1) is the statistical weight of the term while (2J'+1) is the statistical weight of the level under consideration. For example, if we denote by T(SL, S'L') the total collision strength for the $^3P - {}^1D$ transition in a p^2 or p^4 configuration, then $T(^1D_2, {}^3P_J) = (2J+1)\ T(^1D, {}^3P)/9$.

2.5 RADIATIVE TRANSITION PROBABILITIES

Early theoretical transition probabilites, $A(s^{-1})$, have been compiled by Garstang (1968), Czyzak and Krueger (1963), and McKim-Malville and Berger (1965) for forbidden lines and by Laughlin and Victor (1974, 1979) for intercombination lines. More elaborate calculations have since been performed for a number of important ions. The most recent and reliable transition probabilities have been compiled by Mendoza (1983). Some values of A are given in Table (2-7).

The most significant recent theoretical development made in connection with transition probabilities relevant to planetary nebulae is the resolution of a long standing discrepancy between the observed and theoretical values of the electron density sensitive line intensity ratio

$$R(N_e) = I(^2D_{5/2} - {}^4S_{3/2}) \ / \ I(^2D_{3/2} - {}^4S_{3/2}). \qquad (2.46)$$

In the low-density limit ($N_e \rightarrow 0$), the intensity ratio is given by the ratio of statistical weights; R(0) = 3/2. At high density ($N_e \rightarrow \infty$), the radiative de-excitation can be neglected and the level populations are determined by the Boltzmann distribution. In these conditions, the intensity ratio is given by [Flower and Seaton (1969b); see also Chapter 3]

$$R(\infty) = (3/2)\ [A(^2D_{5/2} \rightarrow {}^4S_{3/2}) \ / \ A(^2D_{3/2} \rightarrow {}^4S_{3/2})]. \qquad (2.47)$$

Seaton and Osterbrock (1957) reported a best-calculated value of $R(\infty) = 0.43$ for [O II], obtained with partly empirical methods, as compared

with the value $R(\infty) = 0.35$ observed in high-density planetary nebulae [Kaler et al. (1976)]. A similar discrepancy is found for [N I]: Dopita et al. (1976) calculated a value of $R(\infty) = 0.65$, while the observed value, according to them, is $R(\infty) \leq 0.51$. The transition probabilities compiled by Garstang (1968) for [S II] give $R(\infty) = 0.24$ compared with an observed value of $R(\infty) = 0.45$ [Kaler et al. (1976)].

Seaton and Osterbrock (1957) suggested that such discrepancies could be reduced by taking configuration interaction wave functions explicitly into account, but later calculations [Zeippen (1977)] showed that this was not the case. Zeippen (1977) suggested that one way to improve the theoretical method was to allow for relativistic magnetic dipole transitions. This point of view was later confirmed by Zeippen (1980) and Eissner and Zeippen (1981). Recent calculations have been made by Zeippen (1982) and Mendoza and Zeippen (1982). The values obtained by these authors, listed in Table (2-8), are in excellent agreement with observations.

2.6 EXCITATION BY ABSORPTION OF STELLAR RADIATION IN SPECTRUM LINES

The weak permitted lines of oxygen and carbon ions have excitation energies which are much too large for collisional excitation to be of importance. It has generally been assumed that these lines are excited by the mechanism of radiative recombination.

The abundance of O can be determined from the analysis of the strong forbidden lines of O^0, O^+, and O^{+2} and of the weak recombination lines of O^{+3}, O^{+4}, and O^{+5}, observed in the spectra of planetary nebulae. Burgess and Seaton (1960c) obtained a chemical abundance ratio $N(O)/N(H) = 12 \times 10^{-4}$ for NGC 7027. Gebbie (1969) has used the forbidden lines and

an ionization equilibrium equation to obtain N(O)/N(H) abundance ratios for a number of planetary nebulae. She derived values of 2 to 3 × 10^{-4} both for high excitation nebulae, such as NGC 7027, and for low excitation objects, and this figure was confirmed by Flower (1969) from a detailed study of the planetary nebula NGC 7662.

It was shown by Seaton (1968) that the discrepancy between the values of the oxygen abundance derived by Burgess and Seaton and by Gebbie is due to the assumption that the permitted lines are excited by radiative recombination. The alternative excitation mechanism which was proposed by Seaton is resonant absorption of the stellar ultraviolet continuum radiation.

Let $\mathcal{N}_{abs}(X^{+m})$ be the total number of ions X^{+m} populating excited states per unit time due to absorption of stellar radiation in spectrum lines :

$$\mathcal{N}_{abs}(X^{+m}) = \sum_i \left[\frac{L_\nu}{h\nu} \Delta\nu \right]_i \tag{2.48}$$

where the sum is over all lines from the ground state, L_ν is the stellar luminosity (erg s^{-1} Hz^{-1}), and $\Delta\nu$(Hz) is the equivalent width of the absorption line. Let $\mathcal{N}_{capt}(X^{+m})$ be the total number of ions X^{+m} populating excited states per unit time due to radiative capture:

$$\mathcal{N}_{capt}(X^{+m}) = \int N_e \, N[X^{+(m+1)}] \, \alpha_B(T_e, X^{+m}) \, dV \tag{2.49}$$

where α_B is the radiative recombination coefficient summed over all excited states and the integration is over the nebular volume. The relative importance of resonant absorption and recombination in populating the excited states is then defined by the ratio

$$R(X^{+m}) = \mathcal{N}_{abs}(X^{+m}) \, / \, \mathcal{N}_{capt}(X^{+m}) \, . \tag{2.50}$$

Seaton calculated the ratio $R(O^{+2})$ for NGC 7027, assuming the central star to be radiated as a blackbody at a temperature T_S. The calculated values of $R(O^{+2})$, as a function of the adopted values of the temperature parameter $t = 10^{-5} T_S(K)$, are :

16.1 ($t = 1.0$), 11.6 ($t = 1.2$), 7.9 ($t = 1.5$), and 5.8 ($t = 1.82$). These results show that resonant absorption of the stellar ultraviolet continuum radiation is about an order of magnitude more important than radiative recombination in exciting the weak O III lines observed in the spectrum of NGC 7027. Allowing for excitation by resonant absorption, both permitted and forbidden O^{+2} line intensities are found to be consistent with N(O) / N(H) values derived by Gebbie.

2.7 BOWEN FLUORESCENT MECHANISM

In the spectra of high-excitation planetary nebulae with strong He II λ4686 line, certain permitted lines of O III and N III appear to be much stronger than predicted by recombination theory and subsequent cascade. Other lines, equally strong (or even stronger) under conditions of laboratory excitation, are missing or extremely weak in these objects.

Bowen (1935) noticed that all the O III lines could originate from a single upper level, 2p 3d $^3P^o$, either directly or by cascade; the N III lines are originated from the 3d ^2D term by cascade. In order for these levels to be excited, some remarkable coincidences must occur.

Figure (2-4) shows a schematic partial energy level diagram of O III. An O^{+2} ion in the $2p^2\ ^3P_2$ level of the ground term requires a photon of wavelength $\lambda = 303.779$ Å to reach the 2p 3d $^2P^o_2$ level. The He II Ly-α photon has a wavelength of $\lambda = 303.780$ Å . Small kinematical and Doppler

shifts could easily bring the two wavelengths into coincidence. Hence, in a high-excitation nebulae where helium is doubly ionized and the He II Ly-α attains great strength, the O^{+2} ion could easily be excited to the 2p 3d $^3P^o$ level from which it could cascade through the 2p 3p configuration with the production of the observed Bowen fluorescence lines. The wavelengths of these lines are included in Figure (2-4)

An equally surprising coincidence is that the final transition of the O III fluorescent cycle, 2p 3s $^3P^o_1$ - $2p^2$ $^3P_2$, has a wavelength λ374.436 so nearly coincident with N III 2p $^2P_{3/2}$ - 3d $^2D_{5/2}$ line at λ374.434. The other, N III 2p $^2P_{3/2}$ - 3d $^2D_{3/2}$ line, falls also near at λ374.442. Small Doppler shifts produce a somewhat similar fluorescent cycle in this ion. The prominent N III λ4634, λ4641, λ4642, λ4097, and λ4103 lines are produced by this mechanism.

2.7.1 The Efficiency of the Bowen Mechanism

He II Ly-α photons produced in a high-excitation planetary nebula are resonantly scattered many times in the vicinity of their origin and eventualy :

(i) are destroyed by photoionization of H^o and He^o during scattering;

(ll) escape through Doppler shift ;

(iii) are absorbed in the nearly coincident O III $2p^2$ $^3P_2$ - 2p 3d $^3P^o_2$ λ303.79 transition.

Process (iii) results in the emission of

(a) the resonant transition at 303.779 Å , or

(b) the O III $2p^2$ $^3P_1$ - 2p 3d $^3P^o_2$ line at 303.621 Å , or

(c) the Bowen fluorescence lines.

The fraction of He II Ly-α photons which leads to case (c) is called the efficiency of the Bowen mechanism.

The intensity of any He II recombination line, usually He II λ4686, provides a measure of the rate at which He II Ly-α photons are being created. Neglecting other means of populating O III levels, we can measure the efficiency factor , R , from the intensity ratio I(λ)/I(λ4686), where λ is the wavelength of any Bowen line: Thus [cf. Aller (1984)]

$$R = \frac{\lambda(\text{Å})}{4686} \; \frac{I(\lambda)}{I(\lambda 4686)} \; \frac{P(\text{cascade})}{P(\lambda)} \; \frac{\alpha^{\text{eff}}(T_e, \text{ He II P-}\alpha)}{\alpha^{\text{eff}}(T_e, \text{ He II Ly-}\alpha)} \qquad (2.51)$$

where P(cascade) = 0.0187; P(λ) is the probability for the emission of a particular line. The values of P(λ), listed in Table (2-9), have been calculated by Saraph and Seaton (1980). The ratio α^{eff}(He II P-α) / α^{eff}(He II Ly-α) is 0.328 and 0.277 for $T_e = 1.0\times10^4$ K and 2.0×10^4 K, respectively. In NGC 7662, Saraph and Seaton have measured a value of $R \approx 0.32 \pm 0.10$ for λ3133.

The theoretical value of R can be obtained by solving the complex He II Ly-α line transfer problem. This problem has been solved by Weymann and Williams (1969) and by Harrington (1972). Based on the numerical results of Harrington, 50% of the He II Ly-α photons undergo Bowen conversion, while 30% result in escaping λ303.621 photon. Hence, the efficiency of the Bowen mechanism is $R \approx 0.50$. In these computations, the effect of the two electron transition $2s^2\ 2p\ 3p\ ^3S$ - $2s\ 2p^3\ ^3P^o$ on the population of the $2s^2\ 2p\ 3p\ ^3S$ level has not been taken into account.

Dalgrano and Sternberg (1982) have showed that the $2s^2\ 2p\ 3p\ ^3D_1$ level is populated almost entirely by charge exchange $O^{+3} + H^o \longrightarrow O^{+2}(2p\ 3p\ ^3D_1) + H^+$. The Bowen fluorescent mechanism makes a negligible contribution since λ2809, which feeds $2p\ 3p\ ^3D_1$, has a very

low transition probability. Transitions from this level (λ3774, λ3757) are indicated by dashed lines in Figure (2-4). This effect must also be considered when evaluating the efficiency of the Bowen fluorescent mechanism. By this means, the intensities of the Bowen lines can be calculated with better accuracy.

CHAPTER (2)

Tables and Figures

Table (2-1)

Total radiative recombination coefficients for the process $X^{+(m+1)} + e \longrightarrow X^{+m} + h\nu$. Data are from Gould (1978). The values given between brackets are from Aldrovandi and Pequignot (1973, 1974).

X^{+m}	α^R (10^{-12} cm^3 s^{-1})			
$T_e(10^4$ K) =	0.5	1.0	1.5	2.0
C^o	0.74	0.466 (0.47)	0.35	0.29
C^+	3.78	2.45 (2.3)	1.90	1.58
C^{+2}	7.84	5.05 (3.2)	3.89	3.22
C^{+3}	13.2	8.45 (7.5)	6.48	5.35
N^o	0.64	0.392 (0.41)	0.29	0.24
N^+	3.55	2.28 (2.2)	1.76	1.46
N^{+2}	8.41	5.44 (5.0)	4.20	3.49
N^{+3}	14.8	9.55 (6.5)	7.37	6.11
O^o	0.55	0.331 (0.31)	0.24	0.19
O^+	3.23	2.05 (2.0)	1.56	1.29
O^{+2}	8.41	5.43 (5.1)	4.19	3.48
O^{+3}	15.9	10.30 (9.6)	7.97	6.63
Ne^o	0.49	0.282 (0.22)	0.20	0.16
Ne^+	2.76	1.71 (1.5)	1.28	1.04
Ne^{+2}	6.97	4.44 (4.4)	3.39	2.80
Ne^{+3}	15.2	9.81 (9.1)	7.57	6.28
Mg^o	0.41	0.261 (0.14)	0.18	0.14
Mg^+	2.33	1.35 (0.88)	0.97	0.75
Mg^{+2}	6.86	4.19 (3.5)	3.11	2.51
Mg^{+3}	13.5	8.44 (7.7)	6.36	5.18
Si^o	0.97	0.648 (0.59)	0.49	0.41
Si^+	2.39	1.44 (1.0)	1.06	0.85
Si^{+2}	5.91	3.65 (3.7)	2.73	2.22
Si^{+3}	12.0	7.32 (5.5)	5.43	4.37
S^o	0.71	0.465 (0.41)	0.33	0.27
S^+	3.79	2.42 (1.8)	1.86	1.54
S^{+2}	5.77	3.53 (2.7)	2.63	2.12
S^{+3}	11.3	7.03 (5.7)	5.28	4.29
Ar^o	0.52	0.330 (0.377)	0.22	0.18
Ar^+	3.84	2.45 (1.95)	1.88	1.55
Ar^{+2}	6.92	4.31 (3.23)	3.25	2.65
Ar^{+3}	11.9	7.40 (4.01)	5.57	4.54

Table (2-2)

Total dielectronic recombination coefficients for the process $X^{+(m+1)} + e \longrightarrow X_a^{+m} \longrightarrow X^{+m} + h\nu$. Data are from Nussbaumer and Storey (1983a).

X^{+m}	α^D (10^{-12} cm^3 s^{-1})			
$T_e(10^4$ K) =	0.5	1.0	1.5	2.0
C^o	0.52	0.29	0.22	0.18
C^+	8.79	6.06	4.79	4.10
C^{+2}	23.38	13.11	9.19	7.18
N^o	0.85	0.52	0.36	0.27
N^+	1.34	2.04	2.14	2.10
N^{+2}	20.38	21.62	19.56	17.57
N^{+3}	15.17	15.38	13.72	12.09
O^o	0.07	0.08	0.08	0.08
O^+	2.42	1.66	1.29	1.07
O^{+2}	7.81	11.39	11.01	10.07
O^{+3}	51.48	34.53	30.26	28.83
O^{+4}	1.17	5.93	8.62	9.65

Table (2-3)

Effective radiative recombination coefficients. Data are from Brocklehurst (1971, 1972) and for the case $N_e = 10^4$ cm^{-3}.

Ion	λ(Å)	α_R^{eff} (10^{-14} cm^3 s^{-1})		
	$T_e(10^4$ K) =	0.5	1.0	2.0
Hα	6563	22.07	11.67	5.963
Hβ	4861	5.443	3.036	1.612
Hγ	4340	2.234	1.271	0.685
Hδ	4102	1.160	0.665	0.360
He I	4471	2.638	1.367	0.6633
He I	5876	10.44	4.966	2.247
He II	1640	143.8	80.68	44.08
He II	4686	65.15	34.92	16.90

Table (2-4)

Effective dielectronic recombination coefficients. Data are from Storey (1981) and Nussbamer and Storey (1983b).

Ion	λ(Å)	α_D^{eff} (10^{-12} cm^3 s^{-1})								
	$T_e(10^4$ K) =	0.7	0.8	0.9	1.0	1.1	1.2	1.3	1.4	1.5
C^+	1335	.....	6.06	5.45	4.93	4.50	4.14	3.83	3.56	3.33	3.13
C^{+2}	1176	.....	4.25	3.75	3.35	3.03	2.76	2.53	2.34	2.18	2.04
C^{+3}	2297	.....	3.90	3.43	3.04	2.73	2.47	2.26	2.07	1.91	1.77

Table (2-5) - A

Rate coefficients for charge transfer reactions $X^{+(m+1)} + H^{o} \longrightarrow X^{+m} + H^{+}$. Numbers in brackets are powers of 10.

$X^{+(m+1)}$	β (10^{-9} cm^3 s^{-1})			Reference
$T_e(10^4$ K) =	0.5	1.0	2.0	
C^{+2}	1.00(-3)	1.00(-3)	1.35(-3)	(a)
C^{+3}	3.09	3.58	4.22	(a)
	1.6	1.6	1.6	(b)
C^{+4}	2.16	2.13	2.28	(c)
	0.29	0.76	2.17	(d)
N^{+}	1.23(-3)	1.00(-3)	0.84(-3)	(e)
N^{+2}	0.78	0.86	0.97	(a)
N^{+3}	1.54	2.93	5.14	(a)
	1.82	3.41	5.97	(c)
N^{+4}	0.06	0.16	0.49	(d)
O^{+}		1.04		(f)
O^{+2}	0.60	0.77	1.03	(a)
O^{+3}	6.34	8.63	11.81	(a)
O^{+4}	0.21	0.26	0.38	(d)
Ne^{+3}	4.00	5.68	8.28	(a)
Ne^{+4}	6.09	6.60	9.10	(d)
S^{+2}	1.00(-5)	1.00(-5)	1.00(-5)	(d)
S^{+3}	2.59	2.30	2.35	(d)
S^{+4}	7.60	6.50	6.96	(d)
Si^{+2}	4.26	6.16	6.09	(g)
Si^{+3}	0.40	0.41	0.42	(d)
Si^{+4}	2.23	2.30	2.48	(d)
Mg^{+2}	8.60(-5)	8.60(-5)	8.60(-5)	(d)
Mg^{+3}	4.96	6.50	9.04	(d)
Mg^{+4}	6.06	6.50	9.04	(d)
Ar^{+3}	3.38	4.40	5.23	(d)
Ar^{+4}	6.00	6.50	11.36	(d)

Table (2-5) - B

Rate coefficients for charge transfer reactions $X^{+(m+1)} + He^{o} \longrightarrow X^{+m} + He^{+}$. Numbers in brackets are powers of 10.

$X^{+(m+1)}$	β (10^{-9} cm^3 s^{-1})			Reference
$T_e(10^4$ K) =	0.5	1.0	2.0	
C^{+3}	0.02	0.05	0.19	(d)
N^{+2}	0.32	0.33	0.39	(d)
N^{+3}	0.17	0.11	0.15	(d)
N^{+4}	2.58	2.00	1.86	(d)
O^{+2}	0.10	0.20	0.39	(a)
O^{+3}	1.15	1.00	1.00	(d)
O^{+4}	0.81	0.65	0.65	(d)
Ne^{+4}	1.70	1.70	2.35	(d)
S^{+3}	0.68	1.10	1.65	(d)
S^{+4}	8.40(-4)	7.60(-4)	9.17(-4)	(d)
Si^{+3}	0.54	0.96	1.44	(d)
Si^{+4}	1.13	1.20	1.25	(d)
Mg^{+3}	0.83	0.74	0.75	(d)
Mg^{+4}	1.91	2.20	2.66	(d)
Ar^{+2}	0.13	0.13	0.13	(d)
Ar^{+4}	1.29	0.98	0.91	(d)

References :

(a) Butler, Heil, & Dalgarno (1980);
(b) Watson & Christensen (1979);
(c) Gargaud, Hanssen, McCarroll, & Valiron (1981);
(d) Butler & Dalgarno (1980);
(e) Butler & Dalgarno (1979);
(f) Field & Steigman (1971);
(g) McCarroll & Valiron (1976).

Table (2-6)

Effective collision strengths for some important ultraviolet transitions. Data are from the compilation of Mendoza (1983).

Ion	SL	S'L'	λ(Å)	$T_e(10^4$ K)	T(SL,S'L')
C^+	^4P	$^2P^o$	2326	0.4	3.25
				1.0	3.17
				1.5	3.09
				2.0	2.97
C^{+2}	$^3P^o$	^1S	1908	0.5	1.12
				1.0	1.01
				1.5	0.996
				2.0	0.990
C^{+3}	$^2P^o$	^2S	1549	1.0	8.88
				2.0	8.95
N^{+2}	^4P	$^2P^o$	1751	0.4	2.00
				1.0	2.03
				1.4	2.07
				2.0	2.11
O^+	$^2P^o$	$^4S^o$	2470	0.5	0.398
				1.0	0.405
				1.4	0.411
				2.0	0.420
O^{+2}	$^5S^o$	^3P	1663	0.5	1.05
				1.0	1.18
				1.5	1.22
				2.0	1.24
Si^{+2}	$^3P^o$	^1S	1892	0.5	6.90
				1.0	5.43
				1.5	4.80
				2.0	4.41
Si^{+3}	$^2P^o$	^2S	1397	0.5	16.9
				1.0	17.0
				1.5	17.0
				2.0	17.1
Mg^+	$^2P^o$	^2S	2800	0.5	15.6
				1.0	16.5
				1.5	17.2
				2.0	17.7

Table (2-7)

Transition probabilities for some selected forbidden lines. Data are form the compilation of Mendoza (1983).

Ion	SL	S'L'	J	J'	λ(Å)	A(S^{-1})
O^{+}	$^2P^o$	$^4S^o$	1/2	3/2	2470	7.96 (-2)
			3/2	3/2		
O^{+2}	^1S	^1D	0	2	4363	1.78
	^1D	^3P	2	2	5007	1.96 (-2)
			2	1	4959	6.74 (-3)
N^{+}	^1S	^1D	0	2	5755	1.12
	^1D	^3P	2	2	6584	2.99 (-3)
			2	1	6548	1.01 (-3)
Ne^{+}	$^2P^o$	$^2P^o$	1/2	3/2	12.82μm	8.55 (-3)
Ne^{+2}	^1D	^3P	2	2	3869	1.71 (-1)
S^{+}	$^2D^o$	$^4S^o$	5/2	3/2	6717	2.60 (-4)
			3/2	3/2	6731	8.82 (-4)
S^{+2}	^1S	^1D	0	2	6311	2.22
	^1D	^3P	2	2	9534	5.76 (-2)
			2	1	9069	2.21 (-2)
S^{+3}	$^2P^o$	$^2P^o$	1/2	3/2	10.52μm	7.73 (-3)
Ar^{+2}	^3P	^3P	1	2	8.99μm	3.08 (-2)
	^1D	^3P	2	2	7136	3.14 (-1)

Table (2-8)

Observed and theoretical values of intensity ratio high-density limit $R(\infty) = I(^2D_{5/2} - {}^4S_{3/2} ; \lambda_1) / I(^2D_{3/2} - {}^4S_{3/2} ; \lambda_2)$. See the text for references.

Ion	λ_1(Å)	λ_2(Å)	R(∞)	
			Observed	Theoretical
[N I]	5201	5199	≤0.51	0.54
[O II]	3729	3727	0.35±0.04	0.35
[S II]	6717	6731	≤0.45	0.44
[Ne IV]	2425	2422		0.13

Table (2-9)

Probabilities, $P(\lambda)$, for emission of photons in lines, following excitation O III 2p 3d $^3P^o_2$. Numbers in brackets are powers of 10. From Saraph and Seaton (1980).

Transition	J	J'	λ(Å)	P(λ)
2p 3d $^3P^o_J$ - 2p 3p $^3P_{J'}$	2	2	3444.10	3.74 (-3)
	2	1	3428.67	1.25 (-3)
- 2p 3p $^3S_{J'}$	2	1	3132.86	1.23 (-2)
- 2p 3p $^3D_{J'}$	2	3	2837.17	1.16 (-3)
	2	2	2819.57	2.08 (-4)
	2	1	2808.77	1.38 (-5)
2p 3p ^3P_J - 2P 3S $^3P^o_{J'}$	2	2	3047.13	2.14 (-3)
	2	1	3023.45	7.12 (-4)
	1	2	3059.30	3.95 (-4)
	1	1	3035.43	2.37 (-4)
	1	0	3024.57	3.17 (-4)
2p 3p ^3S_J -	1	2	3340.74	1.79 (-3)
	1	1	3312.30	1.07 (-3)
	1	0	3299.36	3.57 (-4)
2p 3p ^3D_J -	3	2	3759.87	5.39 (-4)
	2	2	3791.26	2.41 (-5)
	2	1	3754.67	7.22 (-5)
	1	2	3810.96	1.80 (-7)
	1	1	3774.00	2.67 (-6)
	1	0	3757.21	3.57 (-6)

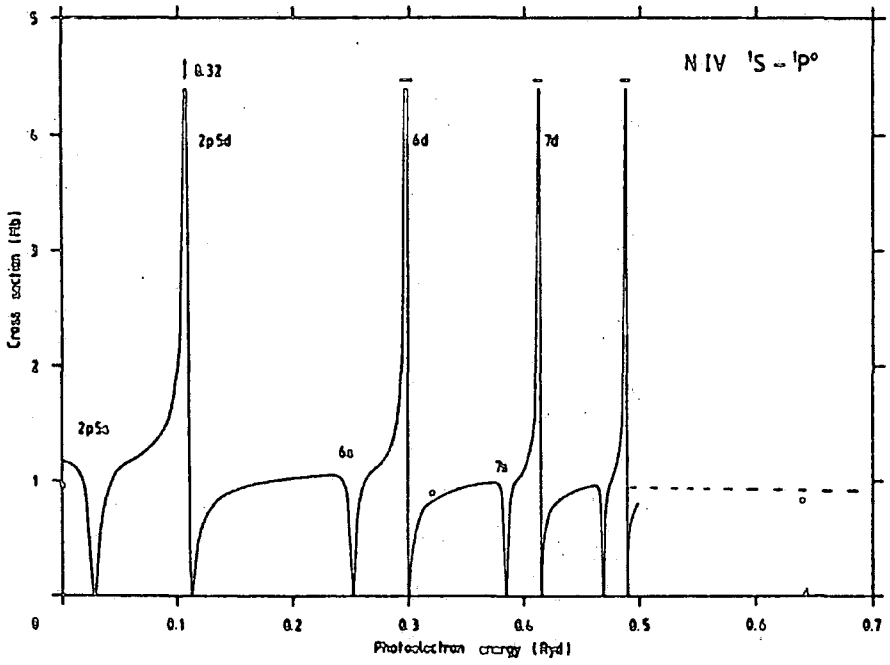

Figure (2-1): Photoionization cross-section of the ground state of N^{+3} [Mendoza (1983)]. The figure shows the Close-Coupling (solid curve), Quantum Defect (filled circles), and averaged over resonances (dashed curve) results.

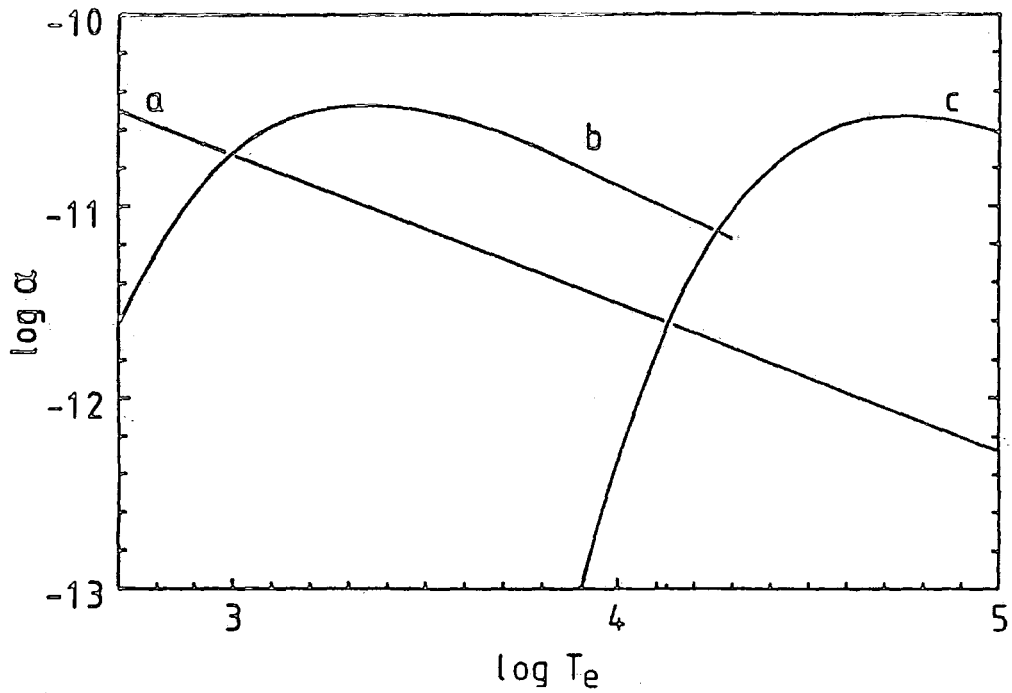

Figure (2-2): Total recombination rate coefficients for C^{+3} + e as a function of electron temperature [Storey (1983)]. The curves (a), (b), and (c) represent α^R, α^D, and α^B (see text), respectively.

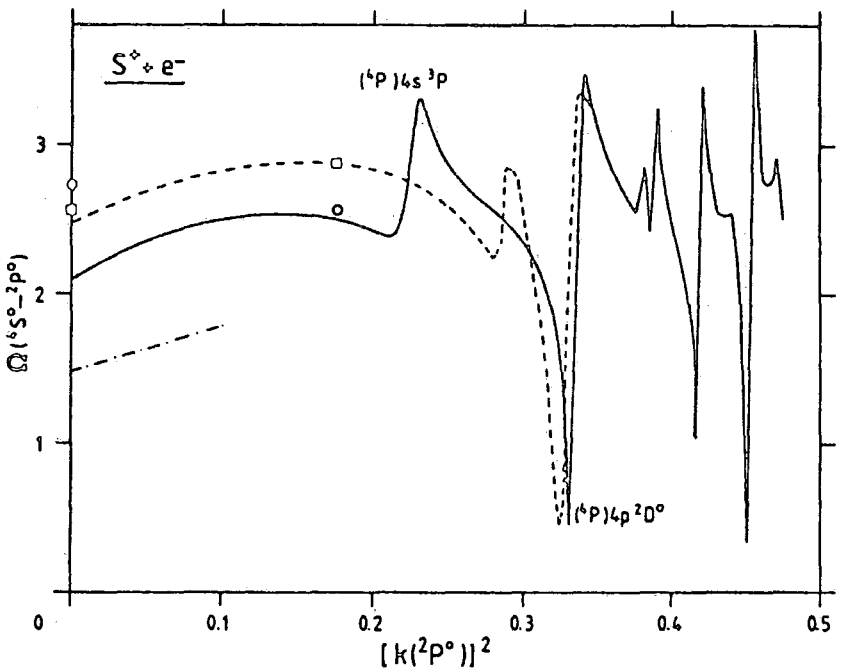

Figure (2-3): Total collision strength for the $^4S^o$ - $2p^o$ transition of S^+ [Mendoza (1983)]. The curves shown are: the results by Pradhan (1976) in 3CC+CI (filled circles) and DW (filled squares) approximations; the DW (dot-dashed curve) results by Krueger and Czyzak (1970); and the results by Mendoza (1982) in a 6CC+CI using the R-matrix method (solid curve) and Linear Algebraic method (dashed curve).

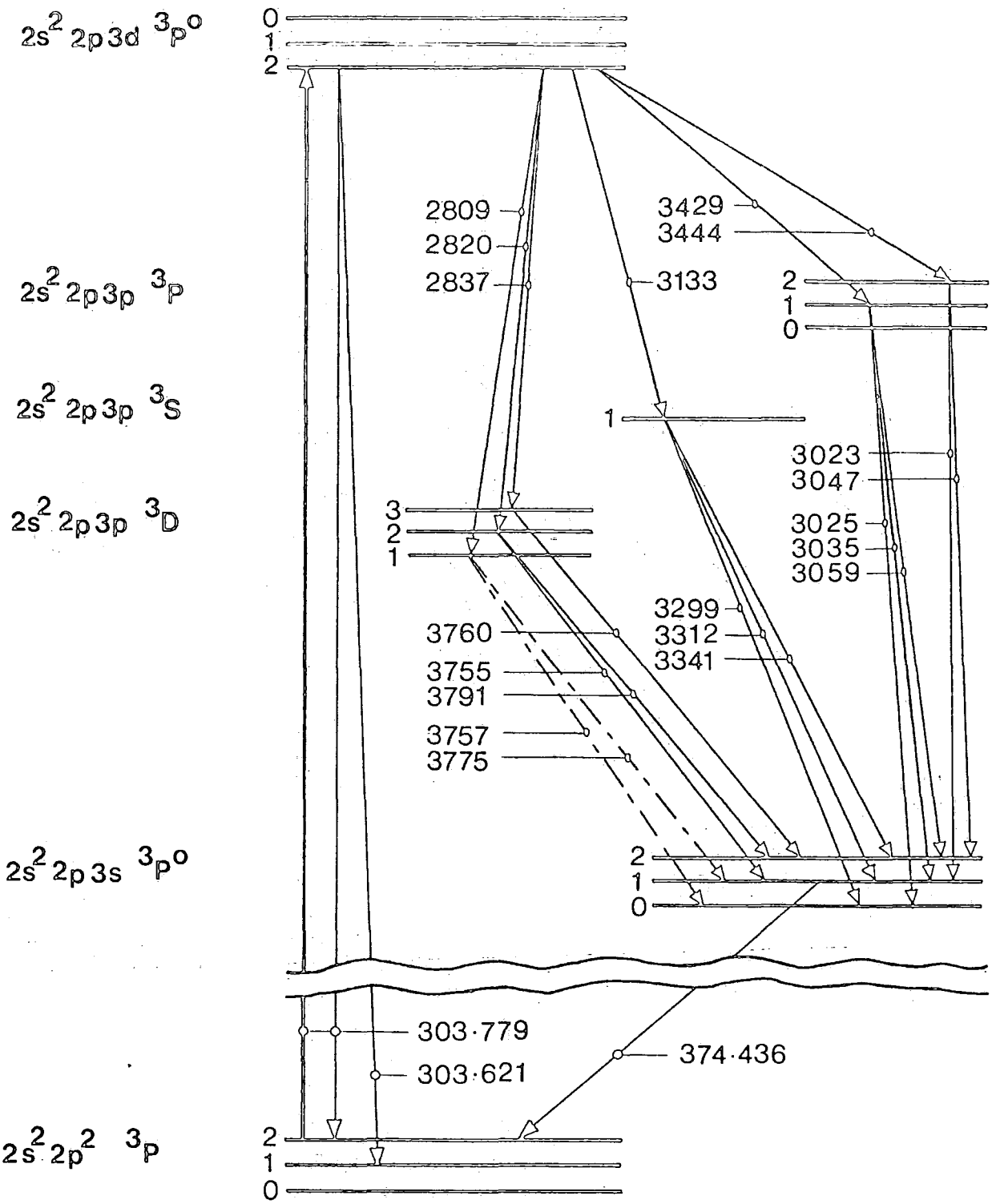

Figure (2-4): Partial energy-level diagram of O III. The positions and separations of the levels are not drawn to scale. The wavelengths of the lines are given in angstroms. See the text for explanation.

CHAPTER (3)

PHYSICAL CONDITIONS IN PLANETARY NEBULAE: SwSt 1 AND IC 2501

3.1 THE INTERSTELLAR EXTINCTION

The importance of the interstellar extinction has long been recognized by Trumpler (1930), who compared the distances of clusters determined from spectral types and photographic photometry with those estimated from apparent diameters of clusters. He found a systematic increase of apparent angular diameters with distances, unless a correction of 0.67 mag./kpc was made to photometric spectroscopic data. Trumpler concluded that only the existence of interstellar extinction (absorption by dust) could explain this behavior. He also showed that this extinction is accompained by reddening because interstellar dust does not dim the starlight identically at all wavelenghts; more light is absorbed in the blue than in the red.

The extinction at any wavelength may be obtained by comparing the radiation of a reddened star with that of an unreddened star of the same spectral and luminosity class. However, investigations of the nature and amount of reddening indicated that most of the reddening, which is observed with increasing luminosity, in many spectral classes (such as G and K) is intrinsic and can not be accounted for by interstellar causes. But in the case of O and B stars, a considerable part of the reddening is due to interstellar material [see, however, Morgan (1938)]. Furthermore, O and B stars posses the characteristics of high luminosity and nearly featureless spectra. Indeed, the more luminous stars are also the more distant and will be more likely to be affected by interstellar reddening. Because all of that, O and B

stars have been the major objects for studies of the interstellar extinction.

Investigations [Hall (1937); Stebbins et al.(1939)] into wavelength dependence of the interstellar extinction showed that the extinction is proportional to $1/\lambda$ over a wide spectral range. However, this is only a rough approximation of the real law of reddening and is not valid in some spectral regions. Furthermore, direct evaluation of the absolute value of the extinction requires data at extremely long wavelengths.

An alternative indirect method of investigating the nature of the interstellar extinction is the ratio of total to selective extinction method. The principle behind the method is illustrated by the assumption that the form of the wavelength dependence of the interstellar extinction is the same for all stars or nebulae, and only the amount of extinction varies from one object to another.

If A_λ is the extinction in magnitudes at wavelength λ, the color excess is then defined by

$$E_{\lambda_1 - \lambda_2} = A_{\lambda_1} - A_{\lambda_2} \quad ; \lambda_1 < \lambda_2 \quad . \tag{3.1}$$

In the UBV system, we have

$$E_{B-V} = A_B - A_V \, . \tag{3.2}$$

where A_B and A_V are the extinctions at the wavelenghts of the B and V filters; $1/\lambda_B = 2.31$ and $1/\lambda_V = 1.83$, with λ in μm. At wavelength $\lambda < \lambda_V$, the extinction is

$$A_\lambda = E_{\lambda-V} + A_V \, . \tag{3.3}$$

We can express interstellar extinction as $E_{\lambda-V} / E_{B-V}$ versus $1/\lambda$. Thus:

$$A_\lambda / E_{B-V} = E_{\lambda-V} / E_{B-V} + R \quad . \tag{3.4}$$

where R is the ratio of total to selective extinction on the UBV system given by

$$R = A_V / E_{B-V} \quad . \tag{3.5}$$

We must find the exact value of R to determine the absolute extinction scale. In fact, the determination of R depends on accurate extrapolation of the reddening curve at all spectral regions. Many determinations of this value by different authors, different methods, and in different regions of the sky have been published [cf. Johnson (1968)]. Seaton (1979) adopted $R = 3.2$ and wrote

$$X(x) = A_\lambda / E_{B-V} \quad \text{where} \quad x = 1 / \lambda(\mu m) \quad . \tag{3.6}$$

The extinction at any wavelength is $10^{-c[1+f(\lambda)]}$ where

$$f(\lambda) = [X(x)/X(H\beta)] - 1 \quad ; \quad X(H\beta) = X(1/0.4861) = 3.68. \tag{3.7}$$

$$\text{Thus,} \quad f(H\beta) = 0 \ , \quad \text{and} \quad c = 0.4 \, X(H\beta) \, E_{B-V} = 1.47 \, E_{B-V} \ . \tag{3.8}$$

It can be seen from equation (3.7) that the function $f(\lambda)$ that gives the form of the wavelength dependence of the interstellar extinction is normalized to Hβ, the usual nebular standard reference line. The reddening correction c is thus defined as the logarithmic extinction at Hβ.

Seaton (1979) has given some empirical formulae for $X(x)$, where $2.70 \leq x \leq 10$, based on fitting the observational data obtained by the OAO-2, Copernicus and TD-1 satellites. He also listed the published values of $X(x)$ for $1.0 \leq x \leq 2.70$, re-normalized to $R = 3.2$. Figure (3-1) illustrates the behavior of $X(x)$. We have used the expression $X(x) = 1.36 \, x^2$ for $0 \leq x \leq 1.0$. Note the broad interstellar absorption feature centred at $\lambda \approx 2200$ Å ($x \approx 4.6$). This feature is generally attributed to extinction by small graphite grains [cf. Mathis et al. (1977)].

The values of $f(\lambda)$, listed in Table (3-1), are the same for all

nebulae, but c varies from one object to another. In order to correct the observations of any given nebula for the effect of the interstellar extinction, we must determine the reddening correction c.

3.2 DETERMINATION OF THE REDDENING CORRECTION

3.2.1 Methods Involving Line Intensity Ratios

The principle is to use the observed ratio of fluxes of two nebular lines, $F(\lambda_{ji})/F(\lambda_{u\ell})$, for which the relative intensity ratio, $I(\lambda_{ji})/I(\lambda_{u\ell})$, as emitted in the nebula, is known independently. Thus, in the expression

$$\mathrm{Log}[I(\lambda_{ji})/I(\lambda_{u\ell})] - \mathrm{Log}[F(\lambda_{ji})/F(\lambda_{u\ell})] = c\,[f(\lambda_{ji})-f(\lambda_{u\ell})] \,. \qquad (3.9)$$

only c is unknown and can be solved for. It should be noticed that the ratio $I(\lambda_{ji})/I(\lambda_{u\ell})$ must be completely independent of physical conditions and easy to measure in planetary nebulae.

Consider a line for which there is no scattering and no absorption within the nebula. The intensity of the line, as emitted in the nebula, is

$$I(\lambda) = \frac{L(\lambda)}{4\,\pi\,r^2} = \frac{1}{4\,\pi\,r^2} \int \varepsilon(\lambda)\, dV \,. \qquad (3.10)$$

where L is the luminosity (erg s^{-1}), r is the distance to the nebula, ε is the emissivity (erg cm^{-3} s^{-1}), and where the integral is over the observed volume. For a line with scattering, but no absorption, equation (3.10) is strictly valid only if the whole nebula is observed. If the emission originates in an optically thin homogenous shell, then the intensity ratio of any two lines is given by

$$\frac{I(\lambda_{ji})}{I(\lambda_{u\ell})} = \frac{\varepsilon(\lambda_{ji})}{\varepsilon(\lambda_{u\ell})} \,. \qquad (3.11)$$

Let $N(X_j^{+m})$ be the number density of ions X^{+m} in an upper level j. The rate for spontaneous radiative transition to a lower level i and the corresponding emissivity are

$$F_{ji} = N(X_j^{+m}) \quad A(j \longrightarrow i), \tag{3.12}$$

and

$$\epsilon_{ji} = h\nu_{ji} \, N(X_j^{+m}) \quad A(j \longrightarrow i), \tag{3.13}$$

respectively. It follows from equations (3.11) and (3.13) that

$$\frac{I(\lambda_{ji})}{I(\lambda_{u\ell})} = \frac{\lambda_{u\ell}}{\lambda_{ji}} \quad \frac{A(j \longrightarrow i)}{A(u \longrightarrow \ell)} \quad \frac{N(X_j^{+m})}{N(X_u^{+m})} \; . \tag{3.14}$$

If both lines are emitted by the same ion and from a single upper level, the ratio of the two lines is then given by

$$\frac{I(\lambda_1)}{I(\lambda_2)} = \frac{\lambda_2}{\lambda_1} \quad \frac{A(\lambda_1)}{A(\lambda_2)} \; . \tag{3.15}$$

This ratio depends only on the transition probabilities (i.e., constant), and it is therefore the best to be used for the determination of the reddening constant.

Table (3-2) gives the intensity $I(\lambda_1)/I(\lambda_2)$ ratios for some lines, calculated using equation (3.15) and transition probabilites referenced in Chapter 2. In practice, all of these ratios are difficult to use for one or more of the following reasons: (i) both lines are very weak in most nebulae; (ii) the line at λ_2 is usually weak and difficult to observe; (iii) the line at λ_2 is usually badly blended with other lines; (iv) the wavelengths λ_1 and λ_2 represent almost a single point on the reddening curve and small errors in the measurements of the weak line at λ_2 can lead to large errors in the evaluated values of c.

Since the results of Table (3-2) are not effective in determining the reddening correction (their importance in separating blends will be discussed later), it is necessary to make some approximations for those intensity ratios which depend, but slightly, on the physical conditions. Various approximations do exist and can be used to determine the reddening constant with high precision. Below, we discuss the methods most frequently used in practice to detrmine c.

3.2.1.1 The [O II] Intensity Ratio

The [O II] $^2P^o \longrightarrow {}^2D^o$ λ7325 and $^2P^o \longrightarrow {}^4S^o$ λ2470 lines are emitted from a double upper term rather than from a single level, and the populations of the two levels depend slightly on the electron density N_e. Following HLSS, for $T_e \approx 10^4$ K and $N_e < 7 \times 10^7$ cm^{-3}, we can neglect collisional de-excitation of $^2P^o$ and population of $^2D^o$ by cascade from $^2P^o$. Under these conditions, the ratio of the number of $^2P^o \longrightarrow {}^4S^o$ quanta to the total number of quanta emitted in the $^2P^o \longrightarrow {}^4S^o$ and $^2P^o \longrightarrow {}^2D^o$ transitions is

$$r = \frac{A(^2P^o_{1/2} \longrightarrow {}^4S^o)}{3\,A(^2P^o_{1/2})} + \frac{2\,A(^2P^o{}_{3/2} \longrightarrow {}^4S^o)}{3\,A(^2P^o_{3/2})} \quad . \tag{3.16}$$

where

$$A(^2P^o_J) = A(^2P^o_J \longrightarrow {}^2D^o) + A(^2P^o_J \longrightarrow {}^4S^o) \quad . \tag{3.17}$$

With the transition probabilites of Zeippen (1982), we obtain r = 0.2018 and hence

$$\frac{I(\lambda 7325)}{I(\lambda 2470)} = \frac{2470}{7325}\,\frac{(r-1)}{r} = 1.334. \tag{3.18}$$

From Table (3-1) and equations (3.9) and (3.18), we finally obtain

$$c = 0.696 \log[F(\lambda 7325)/F(\lambda 2470)] - 0.087. \qquad (3.19)$$

from which the reddening constant can be determined directly from the observed fluxes of the two multiplets of [O II].

The [O II] ratio method is excellent for those nebulae with the oxygen being mostly in the form of O^+ and where the electron density is sufficiently high for the $^2D^o$ levels to approach a Boltzmann distribution, so that excitation of $^2P^o$ is enhanced due to transitions via $^2D^o$. In High-excitation objects, the [O II] lines are very weak or absent and the [O II] ratio method is not applicable. For these objects, the He II ratio method discussed in the following subsection is interesting.

3.2.1.2 The He II Intensity Ratio

The He II-Baα λ1640 and He II-Pα λ4686 recombination lines are strong in high-excitation planetary nebulae. The relative intensity of these two lines is given by [see equation (2.9)]

$$\frac{I(\lambda 1640)}{I(\lambda 4686)} = \frac{4686}{1640} \frac{\alpha^{eff}(T_e, \text{ He II-Ba}\alpha)}{\alpha^{eff}(T_e, \text{ He II-P}\alpha)}. \qquad (3.20)$$

With the effective recombination coefficients of Table (2-3), this ratio is 6.307, 6.602, and 7.453 for $T_e = 5\times10^3$, 10^4 , and 2×10^4 K, respectively. Though the upper levels are not the same for the two lines, the relative insensitivity of the line ratio to the electron temperature means that the reddening constant can be determined with high precision. If an estimate of T_e is available, then the reddening constant can be derived from the following interpolated formula :

$$c = 0.914 \{\log[t^{-1/2}(33.491\ t^{1/3} - 15.835 \log(t) - 26.889)] - \log[F(\lambda 1640)/F(\lambda 4686)]\}. \qquad (3.21)$$

where

$$t = T_e(K) / 10^4 . \qquad (3.22)$$

3.2.1.3 The H I Intensity Ratios

According to the discussion of section (3.2.1), it is important to note that the [O II] and He II ratio methods are valid only if the IUE and optical observations are made for the same region in the nebula. Hence, the method most frequently used to determine c is the Balmer decrements method.

The H I Balmer lines are strong in most nebulae and occur in the part of the spectrum that is ordinarily observed. By measuring the ratios of two or more H I Balmer lines, the reddening constant can be determined with high accuracy. Since different upper levels are involved, the relative strengths depend slightly on excitation conditions, but as Brocklehurst's (1971) calculations show, the variation in H I Balmer line ratios is very small over the range $0.5 \leq t \leq 2.0$. Within this range, the predicted intensity ratios may be fitted almost exactly by

$$I(H\alpha)/I(H\beta) = t^{-1/2} [567.657\ t^{1/3} - 148.662 \log(t) - 282.957]; \quad (3.23)$$

$$I(H\gamma)/I(H\beta) = t^{-1/2} [112.706\ t^{1/3} - 29.492 \log(t) - 65.806]; \quad (3.24)$$

$$I(H\delta)/I(H\beta) = t^{-1/2} [58.826\ t^{1/3} - 13.138 \log(t) - 32.826]; \quad (3.25)$$

$$I(H\epsilon)/I(H\beta) = t^{-1/2} [41.249\ t^{1/3} - 11.859 \log(t) - 25.349]. \quad (3.26)$$

where I(Hβ) is scaled to 100. The reddening constant can thus be derived from these equations and equation (3.9).

In addition to the Balmer decrements method, the reddening constant can also be obtained from the comparison of an H I Paschen line and a Balmer line from the same upper set of levels. This Paschen-to-Balmer ratio method has the problems of contamination by infrared OH atmospheric emission lines and the relative insensitivity of the IR detectors.

3.2.2 Radio Continuum and Hβ Fluxes

The radio continuum flux is not attenuated by interstellar extinction, and a comparison of the flux in the optically thin part of the radio spectrum with the flux in the Hβ line yields the reddening constant directly.

The free-free radio emission (erg cm^{-3} s^{-1} Hz^{-1}) at frequency ν in the optically thin part of the radio spectrum is [Oster (1961)]

$$\varepsilon_\nu = \frac{N_e\, N_{ion}\, 32\, z^2\, e^6}{3\, m^2\, c^2} \left[\frac{2\,\pi\, m}{K\, T_e}\right]^{1/2} \ln\left[\left[\frac{2\, K\, T_e}{\gamma\, m}\right]^{3/2} \frac{m}{\pi\, \gamma\, z\, e^2\, \nu}\right] . \qquad (3.27)$$

where N_{ion} and z are the ionic density and charge, respectively; $\gamma = 1.78$ is Euler's constant. K, m, c, and e have their usual meanings. Consider a plasma that consists of ions of H^+, He^+, and He^{2+}. Then :

$$N_{ion}(z^2) = N(H^+) + N(He^+) + 4\, N(He^{2+}). \qquad (3.28)$$

Substituting numerical values in equation (3.27) yields

$$\varepsilon_\nu = 3.77 \times 10^{-38}\, N_e\, T_e^{-1/2} \{[N(H^+) + N(He^+)]\, [17.72 + \ln(T_e^{3/2}/\nu)] + 4\, N(He^{2+})\, [17.03 + \ln(T_e^{3/2}/\nu)]\} . \qquad (3.29)$$

The rate of emission in the Hβ line (erg cm^{-3} s^{-1}) is

$$\varepsilon_\beta = h\nu_\beta\, N_e\, N(H^+)\, \alpha^{eff}(T_e, H\beta). \qquad (3.30)$$

where the effective recombination coefficients for a nebula which is optically thick to Lyman radiation (case B) are given in Table (2-3). These values may be fitted to within 2 per cent over the range $5 \times 10^3 \leq T_e \leq 2 \times 10^4$ K by

$$\alpha^{eff}(T_e, H\beta) = 9.692 \times 10^{-11}\, T_e^{-0.878} . \qquad (3.31)$$

The relative intensity of Hß and radio radiation at an optically thin frequency is given by

$$I(H\beta)/I(\nu) = 1.05 \times 10^{16}\ T_e^{-0.378}\ K_{He}^{-1}\ ,\ \text{Hz}. \qquad (3.32)$$

where

$$K_{He} = \{(1+y')[17.72+\ln(T_e^{3/2}/\nu)] + 4y''[17.03+\ln(T_e^{3/2}/\nu)]\}\ , \qquad (3.33)$$

with

$$y' = N(He^{+})/N(H^{+})\ ;\ \ y'' = N(He^{2+})/N(H^{+}). \qquad (3.34)$$

The reddening constant may then be derived from

$$c = \log\ [1.05 \times 10^{16}\ \ T_e^{-0.378}\ \ K_{He}^{-1}\ ] - \log[F(H\beta)/F(\nu)]\ . \qquad (3.35)$$

Since K_{He} is well determined in planetary nebulae, we would expect that the value of c found by comparing radio frequency and Hß fluxes to be consistent with the values obtained by the methods of section (3-2-1). Actually, the former is larger in many nebulae. The reason may be because the radio frequency flux is measured in an optically thick part of the spectrum. It should also be recalled that the reddening correction is based on a mean interstellar extinction curve and that variations from object to object may be expected.

3.2.3 The 2200 Å Absorption Feature

The interstellar reddening curve [Figure (3-1)] displays a broad maximum at $\lambda \approx 2200$ Å. An estimate of the reddening constant may be made by determining the value required to remove the corresponding dip in the observed ultraviolet continuum.

To illustrate the method, we use the merged SWP and LWR spectra of IC 2501 as an example. Figure (3-2) gives the logarithms of the observed flux $F_o(\lambda)$ and the flux $F(\lambda)$ corrected for reddening using

the relation

$$\log F(\lambda) = \log F_o(\lambda) + c\,[1+f(\lambda)]\,, \qquad (3.36)$$

with $c = 0.40$, 0.45, and 0.50. It is clear that the 2200 Å absorption feature is discernible for $c > 0.5$ or $c < 0.4$. The value $c = 0.45$ seems to be the best.

The 2200 Å absorption feature method is to be recommended for objects where we anticipate the continuous spectrum to be well-defined.

3.3 EXTINCTIONS FOR SwSt 1 AND IC 2501

SwSt 1 and IC 2501 differ from NGC 4361 in that the angular sizes of SwSt 1 and IC 2501 are such that the entire objects are observed at all wavelengths. This fact makes it possible to use most of the methods discussed in section (3-2) to determine the reddening constant.

The results of papers I and II which we obtained using some of these methods and the observed fluxes of Chapter 1 are summarized in Table (3-3).

For IC 2501, the values of c as determined by different independent methods are consistent to within their combined error bars. Paper II (see also Chapter 4) shows that the adopted value of $c = 0.5$ ($\pm$ 0.08) is consistent with ultraviolet and visual continuum measurements. It also gives consistent results for the colour and Zanstra temperatures of the central star.

In the case of SwSt 1, the values of c are not compatible to within their error bars. The point concerning the use of a mean interstellar extinction curve, discussed in section (3-2-2), may be important for this nebula. It is clear from Figure (3-3) that the larger value of the reddening constant, $c = 0.5$, leads to a distinct over-correction of the

λ2200 dip in the ultraviolet continuum of SwSt 1. On the other hand, as shown in paper I (see also Chapter 4), it gives better agreement between the calculated nebular continuum and the optical continuum measurements. Consistent results for the Zanstra temperature of the central star are also obtained with $c = 0.5$.

3.4 ADOPTED FLUXES IN SwSt 1 AND IC 2501

Given the extinctions to the nebulae, the ultraviolet and visual fluxes may be corrected for reddening and put on a common scale. Table (3-4) gives adopted fluxes for SwSt 1 and IC 2501, corrected for extinction using the relation

$$\frac{I(\lambda)}{I(H\beta)} = \frac{F(\lambda)}{F(H\beta)} \; 10^{[c\, f(\lambda)]} . \qquad (3.37)$$

where $I(H\beta) = 100$. The observed fluxes have been taken from Chapter 1. The infrared line fluxes of Aitken et al.(1979) and of Beck et al. (1981) are also included in Table (3-4). The intensity of λ2321 was determined from the theoretical I(λ4363)/I(λ2321) ratio of Table (3-2).

3.5 RELATIVE LEVEL POPULATIONS

The rate of change of the population density of level i of an ion X^{+m} with time , t, is given by the difference between the rates of population and depopulation. For ions which emit forbidden lines, the most important processes that need to be considered are electron collisions and spontaneous emission of radiation. Thus, we can write for the i^{th} level

$$\frac{d\, N(X_i^{+m})}{dt} = \sum_{j \neq i} \left[\Psi_{ji} + F_{ji} \right] - \sum_{j \neq i} \left[\Psi_{ij} + F_{ij} \right] . \qquad (3.38)$$

where Ψ and F are the rates for electron collision and spontaneous radiative transition, respectively. These are defined by equations (2.40) and (3.12). Note that $F_{ij} = 0$ for $i < j$. The condition of statistical equilibrium expresses the fact that $d\,N(X_i^{+m})/dt = 0$ (all i), and equation (3.38) may be rewritten as

$$N_e \sum_{j<i}^{i-1} N(X_i^{+m})\, q(j\rightarrow i) + \sum_{j>i}^{L} N(X_j^{+m}) \left[A(j\rightarrow i) + N_e\, q(j\rightarrow i)\right]$$

$$= N(X_i^{+m}) \left[\sum_{i>j}^{L} A(i\rightarrow j) + N_e \sum_{j\neq i}^{L} q(i\rightarrow j)\right] . \qquad (3.39)$$

where L = 5 for p^2, p^3, and p^4 configurations, but if higher terms are involved as in considerations of many ultraviolet lines, L is often of the order of 15.

Equations (3.39), together with the condition

$$\sum_i N(X_i^{+m}) = N(X^{+m}) , \qquad (3.40)$$

where $N(X^{+m})$ is the ion number density, form a set of linear, inhomogenous equations which may be solved for the relative level population,

$$n(X_i^{+m}) = \frac{N(X_i^{+m})}{N(X^{+m})} , \qquad (3.41)$$

by matrix inversion at any given values of the electron temperature and density.

We have computed the values of n for O^{+2} and N^+ (L=6), O^o, O^+, S^+, S^{+2}, S^{+3}, and Ar^{+2} (L=5), and Ne^+ (L=2) ions for conditions found in SwSt 1 and IC 2501 [see section (3.6)]. The results are given in Table (3-5). Some of these values are necessary for determining the abundances of the above ions. Detail is given in section (3.7).

Nussbaumer and Storey (1981) have computed the values of n for $^5S_2^o$, ^1S_o , $^1D_2$, $^3P_2$, $^3P_1$, and ^3P_o levels of O^{+2} for an extensive set of N_e and T_e . Their values should be more accurate, since they have employed a model consisting of the 15 energetically lowest levels (L=15) corresponding to the 9 lowest terms. Furthermore, proton-ion collision rates among the ^3P levels are included in their model. Among the most important levels is the $^1D_2$ level; it is the upper level of the strong forbidden transitions at λλ5007, 4959. For $0.75 \leq t \leq 2.0$ and $3.0 \leq \text{Log } N_e \leq 5.5$, the values of $n(O^{+2} , {}^1D_2)$ may be fitted by

$$n(O^{+2} , {}^1D_2) = 10^{[\delta(T_e) + \Delta(N_e)]} . \qquad (3.42)$$

where

$$\delta(T_e) = \text{Log} \{ 10^{-6} \; t^{-1/2} \; [a_1 \; t^{1/3} - a_2 \; \text{Log}(t) - a_3]\} , \qquad (3.43)$$

and

$$\Delta(N_e) = a_4 \; \text{Log}(N_e) - a_5 . \qquad (3.44)$$

The parameters a_1, a_2, a_3, a_4, and a_5 are given in Table (3-6).

In Table (3-7), we list the values of $n(O^{+2} , {}^1D_2)$ obtained with L = 15 [Nussbaumer and Storey (1981)], L = 6, and using equation (3.42). These results call for the following comments:

(i) There are no large differences between the values of n computed with L = 15 and L = 6. This indicates that the populations of the higher levels (above $^5S_2^o$) are negligible at the electron densities and temperatures considered in Table (3-7).

(ii) The values of n obtained using equation (3.42) are slightly larger than those calculated with L = 6, but similar or very close to those computed with L = 15. This may means that if we can fit the relative

level populations of all ions of interest by simple equations, our computing time will be reduced, especially when making models for planetary nebulae.

3.6 DETERMINATION OF THE ELECTRON DENSITIES AND TEMPERATURES FROM THE OBSERVED LINE INTENSITY RATIOS

Once the relative level populations have been computed for all ions of interest by the method of section (3.5), the de-reddened observed intensity ratio of any two forbidden lines originating from an ion X^{+m} ,

$$\frac{I(\lambda_{ji})}{I(\lambda_{u\ell})} = \frac{\lambda_{u\ell}}{\lambda_{ji}} \frac{A(j\longrightarrow i)}{A(u\longrightarrow \ell)} \frac{n(X_i^{+m})}{n(X_u^{+m})} , \qquad (3.45)$$

may be calculated as a function of N_e and T_e . The corresponding observed ratio, corrected for interstellar reddening, may then be used to determine the electron density and temperature. Below, we discuss this method in detail.

3.6.1 Electron Density

The ratio $R(N_e) = I(^2D^o_{5/2} - {}^4S^o_{3/2}) \,/\, I(^2D^o_{3/2} - {}^4S^o_{3/2})$ in a p^3 configuration depends only weakly on T_e and much more strongly on N_e . This behavior is of practical importance for establishing electron densities in planetary nebulae.

In order to understand how the electron density plays this very important role, let us examine the following simplified situation in which we consider the [O II] ion as an example. As Figure (3-4) shows, this ion has a ground $^4S^o_{3/2}$ level and $^2D^o_{5/2,3/2}$ and $^2P^o_{3/2,1/2}$ excited levels. Let us assume that processes involving the $^2P^o$ term have only a second-order influence on the population of the $^2D^o$ term. In effect,

the five-level problem reduces to a three-level problem for which the statistical equilibrium equations can easily be solved (see Appendix A). Denote the $^4S^o_{3/2}$, $^2D^o_{5/2}$, and $^2D^o_{3/2}$ levels by 1, 2, and 3. Since the excitation difference between levels 2 and 3 is extremely small ($\Delta E_{23} << KT_e$) and the transition probability $A(3 \longrightarrow 2) = 1.20 \times 10^{-7}\ s^{-1}$ is very small, the results of Appendix B are valid. Hence, in the limit of high density, equations (3.45) and (B2) give

$$\frac{I(3-1)}{I(2-1)} = \frac{\omega_3}{\omega_2}\,\frac{A(3\longrightarrow 1)}{A(2\longrightarrow 1)} \quad ; \quad (N_e \longrightarrow \infty), \tag{3.46}$$

since $\lambda_{21} \approx \lambda_{32}$ for the close doublet considered. Note that the collision strengths do not enter at all. The relative level populations are sufficiently determined from the Boltzmann's law. Some numerical values of ratio (3.46) have already been given in Table (2-8). In the low density limit, we find from equations (3.45) and (B3) that

$$\frac{I(3-1)}{I(2-1)} = \frac{\Omega_{13}}{\Omega_{12}} \quad ; \quad (N_e \longrightarrow 0). \tag{3.47}$$

Here, collisional excitations alone determine the ratio; the transition probabilities are not involved at all.

Between these two extreme cases, the ratio $R(N_e)$ changes rapidly with density. In actual practice, this ratio does depend slightly on T_e because the values of $n(^2D^o)$ are influenced by interchanges with the $n(^2P^o)$ values. As we shall see now, the temperature effect is relatively minor.

In Figures (3-5) to (3-8), we plot the ratio $R(N_e)$ in [O II], [S II], [Ar IV], and [Ne IV] as a function of $Log(N_e)$ for some values of T_e. These curves enable the electron density to be accurately determined.

The [O II] λλ3729/3727 ratio [Figure (3-5)] has extensively been used to determine the electron densities in planetary nebulae. The great

advantage of line ratios of this type is that we do not have to worry about the effect of the interstellar extinction. The [S II] λλ6717/6731 ratio [Figure (3-6)] has the advantage of good observations, since the lines are well separated in wavelength. Care must be taken when using the [Ar IV] λλ4711/4740 ratio [Figure (3-7)] because the λ4711 line is often blended with He I λ4713 at moderate dispersions. On the scale I(He I; λ4471) = 1, the ratio I(He I; λ4713)/I(He I; λ4471) is 0.065, 0.092, and 0.139 for t = 0.5, 1.0, and 2.0, respectively [Brocklehurst (1970)]. This He I ratio may be used to obtain the contribution of [Ar IV] λ4711 to the blend. The [Ne IV] λλ2425/2422 ratio [Figure (3-8)] is important in high-excitation objects. The lines are strong and can be measured accurately by the IUE satellite. Flower, Penn, and Seaton (1982) have shown that the relative intensity of close doublets can be determined to an accuracy of about 10 per cent on well exposed IUE high-dispersion spectra.

In addition to the above diagnostic line intensity ratios, the ratio of the magnetic quadrupole transition, $2s^2\ {}^1S_o$ - $2s2p\ {}^3P_2^o$ λ1907, and the electric dipole transition, $2s^2\ {}^1S_o$ - $2s2p\ {}^3P_1^o$ λ1909, in C III is again insensitive to T_e but dependent, over an important range, on N_e. The theoretical computations for the line ratio C III] λλ1907/1909 as a function of electron density for various electron temperatures have been made by Loulergue and Nussbaumer (1976). More recent computations for this ratio have been made by Nussbaumer and Schild (1979) and are shown in Figure (3-9). In their computations, Nussbaumer and Schild have employed a model C^{+2} consisting of the 10 energetically lowest levels corresponding to the three lowest configurations $2s^2$, 2s2p, and $2p^2$. The proton-ion collision rates for the $2s2p\ {}^3P_J^o$ - ${}^3P_J^o$, transitions are also included in

the model. They found that the proton collisions have practically no influence on the populations for $T_e \leq 40{,}000$ K.

The C III] λ1907 and λ1909 lines are common to both SWP and LWR cameras of the IUE satellite, but the former is much more sensitive at these wavelengths. Feibelman et al. (1981) claim agreement to within 5 per cent in measurements of the λλ1907/1909 ratio from SWP and LWR spectra of a number of planetary nebulae. We would expect this ratio, as measured by the SWP camera, to provide the most accurate determination of the electron density.

Other IUE line intensity ratios such as N III] I(λ1752)/I(λ1749) and N IV] I(λ1486)/I(λ1483) are important for nebulae with high electron densities. Computations of the N III] line intensity ratio are to be found in Nussbaumer and Storey (1979).

3.6.2 Electron Temperature

In a nebula with a moderately low density, $N_e < 5 \times 10^4$ cm^{-3}, the ratio $R(T_e) = I(^1S_o - {}^1D_2) \,/\, I(^1D_2 - {}^3P_{2,1})$, in a p^2 or p^4 configuration, is sensitive to T_e and enables this parameter to be accurately determined. The behavior of $R(T_e)$ may be understood easily by examining the following simplified situation.

Consider the [O III] ion as an example of the p^2 configuration. As Figure (3-10) shows, in this ion there is a ground ^3P term and $^1D_2$ and ^1S_o metastable levels. Due to the magnetic spin-orbit interactions in the ion (in pure LS coupling), the ^3P term is split into $^3P_2$, $^3P_1$, and ^3P_o fine-structure levels. Since the separation of the metastable levels is much larger than the fine-structure separations, equations (2.44) and (2.45) allow us to assume that the fine-structure levels are

degenerate. In other words, we can treat the ^3P term as a single "level" in equations of statistical equilibrium. Let us now denote the ^3P, $^1D_2$, and ^1S_o levels by 1, 2, and 3. At the low densities postulated, we can usually make the following approximations :

(i) collisional excitations from level 1 to levels 2 and 3 are much more important than collisional 2 to 3 excitations.

(ii) the number of ions entering level 3 by collisional excitations equals the number escaping by spontaneous radiative transitions (collisional de-excitations of level 3 are unimportant).

(iii) the number of ions entering level 2 by collisional excitations equals the number escaping by collisional de-excitation and radiative transitions (an error, but not significant, will be introduced due to the neglect of the radiative 3 to 2 transition which populates level 2).

Under these conditions, equation (C5) of Appendix C is valid. From equations (3.45) and (C5), we obtain

$$R(T_e) = \frac{I(\lambda 4363)}{I(\lambda\lambda 5007,4959)} = 0.129\ [1 + 1.42\times10^{-6}\ N_e\ t^{-0.5}]\ 10^{-1.432/t}\ . \quad (3.48)$$

It is clear that ratio (3.48) depends only weakly on N_e (due to the factor 1.42×10^{-6}) and much more strongly on T_e which enters as a power of 10.

At high densities, collisional de-excitations of level 3 are important. If we replace Ω's by T's, we find from equations (3.45) and (C2) that

$$\frac{I(2-1)}{I(3-2)} = \frac{I(^1D_2 - {}^3P_{2,1})}{I(^1S_o - {}^1D_2)} = a_t \left[\frac{1 + a_2\ x}{1 + a_1\ x}\right] 10^{(a_{23}/t)}\ , \quad (3.49)$$

degenerate. In other words, we can treat the P term as a single "level" in equations of statistical equilibrium. Let us now denote the ^3P, $^1D_2$, and ^1S_o levels by 1, 2, and 3. At the low densities postulated, we can usually make the following approximations :

(i) collisional excitations from level 1 to levels 2 and 3 are much more important than collisional 2 to 3 excitations.

(ii) the number of ions entering level 3 by collisional excitations equals the number escaping by spontaneous radiative transitions (collisional de-excitations of level 3 are unimportant).

(iii) the number of ions entering level 2 by collisional excitations equals the number escaping by collisional de-excitation and radiative transitions (an error, but not significant, will be introduced due to the neglect of the radiative 3 to 2 transition which populates level 2).

Under these conditions, equation (C5) of Appendix C is valid. From equations (3.45) and (C5), we obtain

$$R(T_e) = \frac{I(\lambda 4363)}{I(\lambda\lambda 5007,4959)} = 0.129\,[1 + 1.42\times10^{-6}\, N_e\, t^{-0.5}]\, 10^{-1.432/t} \quad . \qquad (3.48)$$

It is clear that ratio (3.48) depends only weakly on N_e (due to the factor 1.42×10^{-6}) and much more strongly on T_e which enters as a power of 10.

At high densities, collisional de-excitations of level 3 are important. If we replace Ω's by T's, we find from equations (3.45) and (C2) that

$$\frac{I(2-1)}{I(3-2)} = \frac{I(^1D_2 - {}^3P_{2,1})}{I(^1S_o - {}^1D_2)} = a_t \left[\frac{1 + a_2\, x}{1 + a_1\, x}\right] 10^{(a_{23}/t)} , \qquad (3.49)$$

where x is defined by equation (A8). The constants a_t, a_1, a_2, and a_{23} for [O III], [N II], and [S III] ions are given in Table (3-8). If only the strong $^1D_2 - {}^3P_2$ transition is to be used, the values of a_t must be multiplied by the factor $[R/(R+1)]$. The relevant values of the ratio $R = I(^1D_2 - {}^3P_2;\ \lambda_1) \ / \ I(^1D_2 - {}^3P_1;\ \lambda_2)$ are listed in Table (3-2).

It is seen from Table (3-8) that the constants a_t, a_1, and a_2 change only slowly with t. In practice, we use the values tabulated for $t = 1$ and find the electron temperature by iteration, providing that the electron density is known.

For accurate determination of the electron temperature, we need to solve the full equations of statistical equilibrium. Using the method of Section (3.5), we can compute the relative level populations and hence the intensity ratios for all ions of interest. In Figures (3-11), (3-12), and (3-13), we plot the ratio $I(^1D_2 - {}^3P_2) \ / \ I(^1S_o - {}^1D_2)$ in [O III], [N II], and [S III] as a function of T_e for a number of values of N_e in the range $10^3 \leq N_e \leq 10^6$ cm^{-3}. The relative level populations of [O III] computed by Nussbaumer and Storey (1981) are used. These curves enable the electron temperature to be determined in objects with low electron densities.

Electron temperatures, T_e(O III) and T_e(N II), are available for a large number of planetary nebulae. TPP found that for objects of high degree of ionization, T_e(O III) is about 1.25 times higher than T_e(N II); while for those of low degree of ionization, T_e(O III) = T_e(N II). This relationship may be used to find T_e(N II) in objects where the weak [N II] λ5755 line is not observed.

Due to the weakness of the $^1S_0 - {}^1D_2$ transition, line ratios of other ions (such as [Ne III], [Ne V], [Ar III], [Ar V]) are difficult to use for temperature determinations.

The electron temperature may also be determined from the intensity ratio of the collisionally excited line C III] λ1908 to the dielectronic recombination line C II λ1335 :

$$\frac{I(\lambda 1908)}{I(\lambda 1335)} = \frac{1335}{1908} \frac{q(\lambda 1908;\, T_e)}{\alpha_D^{eff}(\lambda 1335;\, T_e)} \quad . \tag{3.50}$$

Using the relevant atomic data from Tables (2-4) and (2-6), this ratio is plotted in Figure (3-14). If the weak C II λ1335 line is measured accurately, the electron temperature can be derived directly from this figure; the C III] λ1908 is strong in low and intermediate-excitation planetary nebulae, but weak in high-excitation objects.

3.6.3 Electron Density and Temperature

The theoretical ratio I(λλ3727,3729) / I(λ2470) of [O II] is shown in Figure (3-15). This ratio depends on both N_e and T_e . Several other optical and ultraviolet region line ratios are dependent on both of these two parameters. By combining two or more line ratios of this type, the electron density and temperature can be estimated.

Suppose that the [O III] λ5007, λ4363, and λ1663 lines are all observed in the nebula. The electron density and temperature at the region where these lines are emitted can be estimated directly from Figure (3-16). Similarly, Figure (3-17) allows the determination of N_e and T_e at the region where [O II] λ3727, λ3729, and λ2470 lines are emitted. By combining optical (λ5007 and λ4363) and infrared (at 88μm) measurements, Dinerstein (1983) was able to find T_e(O III) and N_e(OIII)

for four nebulae. She also found that the (O III) densities are similar to those found from [O II] lines in these objects.

For any given nebula, we usually plot various diagnostic line intensity ratios in a (N_e, T_e) diagram to obtain estimates of N_e and T_e. Note that each observed ratio defines a curve in the (N_e, T_e) plane. If the nebular gas were of uniform density and temperature and all atomic data were accurate, all curves would intersect at a single point. An example which illustrates this method is given below.

3.6.4 Applications to SwSt 1 and IC 2501.

In Table (3-9), we summarize the determinations of the electron densities and temperatures in SwSt 1 and IC 2501. These results have been discussed in Papers I and II. Below, we confirm our conclusions and discuss these results again in connection with the various diagnostic curves given in the previous sections.

3.6.4.1 SwSt 1

The observed value of the [O II] I(λ3729)/I(λ3727)=0.39 (Paper I) is close to the high density limit of 0.35 [see Figure (3-5)]. Allowing for observational uncertainties, this ratio implies only a lower limit to the electron density.

The C III] I(λ1907)/I(λ1909) ratio has been measured accurately from the high-dispersion IUE spectrum of SwSt 1 (see Figure 2 of Paper I). We consider that the best quantitative estimate of N_e derives from this ratio and Figure (3-9). the derived value ($N_e = 1.1 \times 10^5$ cm^{-3}) is consistent with the high emission measure determined from the radio spectrum of this object [see section (1.4.3)].

With this estimate of N_e , T_e is derived from [O III] I(λ5007)/I(λ4363) and I(λ5007)/I(λ1663) ratios [see Figure (3-11) and Figure 4 of Paper I]. Clearly, the two estimates are not consistent. Even if we use the upper limit of λ4363 [see Table (1-2)] and lower limit of λ1663 [see Table (1-13)], the intersection point in Figure (3-16) is still far away from the plotted area. We conclude that the feature observed at λ1663 may be attributable entirely to noise. The feature at λ4363 lies in the wing of Hγ λ4340 and contributes only about 1 per cent of the blend. However, consistent values of I(λ4363) are obtained using different extraction procedures (see Paper I). We consider that the value of T_e derived from the λλ5007/4363 ratio to be more reliable than that deduced from I(λ5007)/I(λ1663); the former also has the advantage of being less sensitive to the reddening than the latter. We thus adopt $T_e = T_e(\lambda 5007/\lambda 4363)$.

3.6.4.2 IC 2501

Using the diagnostic forbidden line intensity ratios [O III] I(λ5007)/I(λ4363) [see Figure (3-11)] , [N II] I(λ6584)/I(λ5755) [see Figure (3-12)], and [O II] I(λλ3727,3729)/I(λ2470) [see Figure (3-15)], we obtain Figure (3-18). From this figure we estimate the electron density and temperatures in IC 2501.

As Table (3-9) shows, the value of T_e derived from C III] λ1908/C II λ1335 intensity ratio [see Figure (3-14)] is higher than that obtained from the [O III] forbidden lines. However, we note that the feature observed at λ1335 is weak and may be attributable entirely to noise. We consider that T_e(O III) to be more relaible than T_e(C III).

3.7 CHEMICAL COMPOSITIONS

3.7.1 Ionic Abundances

Once the line intensities relative to Hβ and the electron temperature and density are determined in the nebula, the abundance ratio $N(X^{+m}) / N(H^+)$ may be calculated for each observed ion. Below, we discuss the determination of ionic abundances from recombination and collisionally-excited permitted and forbidden lines.

3.7.1.1 Abundances From Recombination Lines

The number of quanta emitted in the j→i recombination line, $\mathcal{N}_{ji}$, is given by equation (2.9). The emission rate per unit volume is just $\mathcal{N}_{ji}$ times $h\nu_{ji}$. Assuming equation (3.11) to be satisfied, we find

$$\frac{I(\lambda_{ji})}{I(H\beta)} = \frac{4861}{\lambda_{ji}} \frac{\alpha_{eff}(\lambda_{ji})}{\alpha_{eff}(H\beta)} \frac{N(X^{+m})}{N(H^+)} . \qquad (3.51)$$

Since the effective recombination coefficients are relatively insensitive to the electron density, we can use the values computed with $N_e=10^4$ cm^{-3}. Ionic abundances may then be calculated from

$$\frac{N(X^{+m})}{N(H^+)} = K(\lambda_{ji}, T_e) \frac{I(\lambda_{ji})}{I(H\beta)} , \qquad (3.52)$$

where

$$K(\lambda_{ji}, T_e) = T_e^{-1/2} [a T_e^{1/3} - b \log(T_e) + c] . \qquad (3.53)$$

The constants a, b, and c for the strongest He I and He II lines are given in Table (3-10).

In principle, recombination lines of other ions (such as O III, N III, C II,....) can be used, but the difficulty is that these lines are very weak in the spectra of planetary nebulae.

3.7.1.2 Abundances From Collisionally-Excited Permitted Lines

To obtain the abundances of ions that are represented by collisionally-excited permitted and intercombination lines, we simply equate the number of collisional excitations to the number of quanta emitted (collisional de-excitation is negligible). If i and j denote ground and excited levels, respectively, then the rate of emission from ions X^{+m} in the j→i transition per unit volume is

$$\epsilon(\lambda_{ji}) = N(X_j^{+m})\ A(j\rightarrow i)\ h\nu_{ji} = N(X_i^{+m})\ N_e\ q(i\rightarrow j)\ h\nu_{ji}. \qquad (3.54)$$

Using equation (3.30), we find

$$\frac{I(\lambda_{ji})}{I(H\beta)} = \frac{4861}{\lambda_{ji}}\ \frac{q(i\rightarrow j)}{\alpha_{eff}(H\beta)}\ \frac{N(X_i^{+m})}{N(H^+)}\ . \qquad (3.55)$$

Since $N(X_i^{+m}) \approx N(X^{+m})$, we can rewrite equation (3.55) as

$$\frac{N(X^{+m})}{N(H^+)} = K(\lambda_{ji}, T_e)\ T_e^{1/2}\ 10^{(d/T_e)}\ \frac{I(\lambda_{ji})}{I(H\beta)}\ . \qquad (3.56)$$

where $K(\lambda_{ji}, T_e)$ is given by equation (3.53). Table (3-10) gives the constants a, b, c, and d for some IUE lines. Note that the O^+ ion is represented by the forbidden transition at λ2470. If equation (3.56) and Table (3-10) are used to derive the $N(O^+)/N(H^+)$ ratio, $K(\lambda2470, T_e)$ must be devided by $K_{eff}(\lambda2470)$, where

$$K_{eff}(\lambda2470) = 0.2018\ [(1+15.25x+39.3x^2)/(1+8.06x+7.56x^2)], \qquad (3.57)$$

to correct for the effects of collisional de-excitation (cf. HLSS).

The evidence for the depletion of C IV λ1549 resonance doublet by internal dust is discussed in Chapter 1 (section 1.5.3). We must consider this effect when determining ionic abundances from resonance lines.

3.7.1.3 Abundances From Collisionally-Excited Forbidden Lines

For determining the abundances of ions that are represented by forbidden transitions, correction must be made for the effects of collisional de-excitation. If the statistical equilibrium equations are solved for the relative level populations, ionic abundance may be calculated from

$$\frac{N(X^{+m})}{N(H^{+})} = \frac{\lambda_{ji}}{4861} \frac{N_e \ \alpha_{eff}(H\beta)}{n(X_j^{+m}) \ A(j\rightarrow i)} \frac{I(\lambda_{ji})}{I(H\beta)} . \qquad (3.58)$$

where $n(X_j^{+m})$ is the relative population of the upper level j of the X^{+m} ion. For consistent abundance determinations, we fit $\alpha_{eff}(H\beta)$ by equation (3.53) with $a=4.890\times10^{-14}$, $b=3.422\times10^{-12}$, and $c=1.567\times10^{-11}$. This fit gives results better than those obtained by equation (3.31).

3.7.2 Total Abundances

To derive total chemical abundances it is necessary to estimate the fraction of atoms in the unobserved stages of ionization. Two methods are frequently used to establish the ionization correction factors, ICF = $N(X) / N(X^{+m})$, and hence total abundances: (i) theoretical models employed as interpolation devices ; (ii) simple empirical formulae based on the similarity of the ionization potentials. The first method is discussed in Chapter 5. Here, we consider the second method which has been used by numerous investigators, including Peimbert and Costero (1969), TPP, Stasinska (1978), and Barker (1983). First of all, we discuss the He abundance which seems to be well established in planetary nebulae.

3.7.2.1 Helium

For nebulae containing a negligible amount of neutral helium, we may calculate the He/H abundance ratio from

$$\frac{N(He)}{N(H)} = \frac{N(He^{+}) + N(He^{+2})}{N(H^{+})} \quad . \tag{3.59}$$

TPP have shown that this expression is reasonably valid for the high degree of ionization objects, defined as $Log[N(O)/N(O^{+})] > 0.4$, while Harman and Seaton (1966) concluded that it gives satisfactory results for all nebulae with measured He II lines. Based on the recombination coefficients, the absence of He I lines does not mean that the content of He^{+} is negligible. By contrast, the absence of He II lines suggests that the He^{+2} content is negligibly small.

In nebulae of low degree of ionization, a considerable amount of helium is expected to be in the neutral stage. To estimate the fraction of He^{o} it is necessary to make observations at different distances from the ionizing star.

3.7.2.2 Carbon

For high-excitation nebulae, in which C is expected to be only in the form of C^{+2} to C^{+4}, it is difficult to obtain accurate C abundances. Simply because the C IV] λ1549 resonance doublet is often depleted and the C II λ2297 dielectronic recombination line is usually weak; the ratio $N(C^{+3}) / N(H^{+})$ is poorly determined. However, an estimate of the total C abundance may be derived from (TPP)

$$\frac{N(C)}{N(H)} = \frac{N(C^{+2})}{N(H^{+})} \; \frac{N(He^{+}) + N(He^{+2})}{N(He^{+})} \left[1 + \frac{3\, N(O^{+2})}{10\, N(O^{+}) + N(O^{+2})} \right] . \tag{3.60}$$

This relation is based on the ionization potentials of C and He and theoretical models by Flower (1969) and Rodriguez (1973).

In low-excitation nebulae, $N(He^{+2}) << N(He^{+})$ and much of the O is in the form of O^{+}. It follows from equation (3.60) that the contributions of ionization stages higher than C^{+2} to the total carbon abundance are negligible. Hence, for this type of objects , the total C/H abundance ratio may be derived accurately from

$$\frac{N(C)}{N(H)} = \frac{N(C^{+}) + N(C^{+2})}{N(H^{+})} , \qquad (3.61)$$

since C II] λ2326 and C III] λ1908 lines are strong and can be measured with high accuracy.

3.7.2.3 Oxygen and Nitrogen

For nebulae where observational data are limited, the O/H and N/H abundance ratios are satisfactory determined from the following formulae:

$$\frac{N(O)}{N(H)} = \frac{N(O^{+}) + N(O^{+2})}{N(H^{+})} \quad \frac{N(He^{+}) + N(He^{+2})}{N(He^{+})} , \qquad (3.62)$$

$$\frac{N(N)}{N(H)} = \frac{N(N^{+})}{N(H^{+})} \quad \frac{N(O)}{N(O^{+})} . \qquad (3.63)$$

Equation (3.62) is a good approximation for planetary nebulae, even if [O I] lines are measured, a similar fraction of oxygen and hydrogen is expected to be in the neutral stage. Hawley and Grandi (1978) and Kaler (1979) find that for nebulae without neutral helium, equations (3.62) and (3.63) are reasonably valid.

3.7.2.4 Neon, Argon, and Sulphur

The elemental abundances of Ne, Ar, and S may be calculated from the following formulae:

$$\frac{N(Ne)}{N(H)} = \frac{N(Ne^{+2})}{N(H^{+})} \quad \frac{N(O)}{N(O^{+2})} \tag{3.64}$$

$$\frac{N(Ar)}{N(H)} = \frac{N(Ar^{+2}) + N(Ar^{+3}) + N(Ar^{+4})}{N(H^{+})} \quad \frac{N(S^{+}) + N(S^{+2})}{N(S^{+2})} \tag{3.65}$$

$$\frac{N(S)}{N(H)} = \frac{N(S^{+}) + N(S^{+2})}{N(H^{+})} \quad \{ 1 - [1 - N(O^{+})/N(O)] \}^{-1/3} \tag{3.66}$$

The expressions for Ne and Ar are unsatisfactory for low-excitation nebulae. Equation (3.64) also appears to fail at high excitation where we have observational data from Ne^{+3} and Ne^{+4}. The S^{+3} ion usually contains most of the sulphur in typical planetaries. Equation (3.66) seems to underestimate the S abundance.

3.7.2.5 Silicon and Magnesium

Accurate determinations of the Si and Mg abundances can only be made by model nebulae. These elements appear to be depleted in most planetary nebulae. This depletion suggests that most of the Si and Mg are removed from the gas phase by grain formation.

3.7.3 Effect of The Temperature Fluctuation on Abundance Determinations

The evaluation of ionic abundances depends on whether or not we assume temperature fluctuations in the radiating gas. Following Peimbert (1971), for a spherically symmetric nebula, we define the mean square fluctuation t^2 with respect to the X^{+m} ion as

$$t^2(X^{+m}) = \frac{\int N_e \, N(X^{+m}) \, [T - T_o(X^{+m})]^2 \, r^2 \, dr}{[T_o(X^{+m})]^2 \int N_e \, N(X^{+m}) \, r^2 \, dr} \tag{3.67}$$

where r is the radial distance, T is the local value of T_e, and

$$T_o(X^{+m}) = \frac{\int N_e\, N(X^{+m})\, T\, r^2\, dr}{\int N_e\, N(X^{+m})\, r^2\, dr} \qquad (3.68)$$

is the mean temperature [temperatures obtained from particular line ratios do not represent the entire nebula; T_e(O III), for example is a mean weighted by $N_e\, N(O^{+2})$].

An effect of the temperature fluctuation is that recombination lines tend to originate in cooler regions [since, for hydrogenic ions, the emission of these lines is proportional to $N_e\, N[X^{+(m+1)}]\, T_e^{-3/2} \times \exp(I_H\, z^2/\, n^2 KT_e)$, where I_H (=13.60 ev) is the threshold ionization energy of hydrogen], while collisionally-excited lines are favored in the hotter regions [collisional excitation rates for these lines go as $N_e\, N(X^{+m})\, T_e^{-1/2} \exp(-E_j/\, KT_e)$, where E_j is the energy of the upper level of the transition]. This means that to obtain accurate abundances from emission lines produced by collisional excitation relative to lines produced by recombination, it is necessary to derive the $t^2(X^{+m})$ value corresponding to the observed region.

Both $t^2(X^{+m})$ and $T_o(X^{+m})$ can be obtained using the computer models of planetary nebulae (cf. Chapter 5). In deriving chemical abundances without the aid of models, the mean square temperature fluctuation has to be adopted. TPP suggested a mean value of t^2=0.035 for all ions of nebulae of both low and high excitation. This large value of t^2 has been questioned by HSAL, who employed two models to find that t^2=0.02 in NGC 7662. In Chapter 5, we shall see that t^2 is about 0.01 in NGC 4361. In HII regions, Chaver et al. (1983) adopted an upper limit of $t^2 < 0.015$. We feel that the mean value of t^2, which should be

adopted for planetary nebulae, is much lower than the value adopted by TPP. With a reasonable adoption of the value of t^2, T_o may be derived for all ions emitting the forbidden transitions from [Peimbert (1967)]

$$T_e(X^{+m};\lambda_{ji}/\lambda_{u\ell}) = T_o(X^{+m}) \left[1 + \frac{1}{2} \left(\frac{\Delta E_{ji} + \Delta E_{u\ell}}{K\, T_o(X^{+m})} - 3 \right) t^2 \right]. \quad (3.69)$$

In practice, we can measure T_e(O III) and T_e(N II) in many nebulae. Electron temperatures for other ions are difficult to obtain in most nebulae. However, as already done by TPP, we can assume two different temperatures corresponding to the regions of low and high ionization degree given by $T_o(\text{low}) = T_o(\text{N II})$ and $T_o(\text{high}) = T_o(\text{O III})$, respectively.

Once T_o has been derived, electron temperatures approporiate for abundance determinations (section 3.7.2) can be obtained from the following relations [Peimbert and Costero (1969)]:

$$T_e^{1/2}(\lambda)\, \exp(-\Delta E/KT_e) = T_o^{1/2}\, \exp(-\Delta E/KT_o) \times$$

$$\times \left[1 + \frac{1}{2} \left((\Delta E/KT_o)^2 - 3\, (\Delta E/KT_o) + \frac{3}{4} \right) t^2 \right] \quad (3.70)$$

and

$$T_e(H\beta) = T_o\, (1 - 0.92\, t^2). \quad (3.71)$$

Equation (3.70) is valid for collisionally-excited lines; $T_e(H\beta)$ may be used for all recombination lines.

Table 8 of TPP illustrates the effect of the temperature fluctuation on abundance determinations. In summary, the relative abundances derived only from recombination lines or collisionally-excited lines are almost independent of t^2. The values of $N(X^{+m})/N(H^+)$, derived from the collisionally-excited lines, increase as t^2 increases.

3.7.4 Mean Abundances in Planetary Nebulae

Table (3-11) gives the mean abundances in planetary nebulae, obtained primary by models. For comparisons, the solar abundances are also given. All of these data have been taken from the compilation of Aller (1983,1984). The assignment of population types is that of Kaler (1978). High-excitation objects are those showing the He II λ4686 line in their spectra. The N-rich objects are those with log[N(N)/N(H)] > 8.0 on the scale log N(H) = 12. The C-rich objects are those for which N(C)/N(O) > 1.

A comparison between the nebular and solar abundances shows a number of close similarities, but also some differences. The He abundance seems to be well established in planetary nebulae; the solar He abundance is poorly known. Carbon tends to be enhanced, while Nitrogen shows a considerable spread in abundance. Oxygen appears to be less abundant in planetary nebulae than in the sun. In population I, high-excitation, N-rich, and C-rich objects, the abundance of Ne appears to be solar. S, Cℓ, and Ar seem to have similar abundances in population I, high-excitation, and C-rich objects. The abundances of F, S, and K appear to be essentially solar. Other elements such as Ca, Mg, Si, and Fe seem to be depleted by grain formation; the abundances of the last three elements have not been given in Table (3-11).

3.7.5 Abundances in SwSt 1 and IC 2501

Having adopted a set of line intensities [Table (3-4)] and derived the electron densities and temperatures [Table (3-9)] we now employ the methods of section (3.7.1) to evaluate the ionic abundances in SwSt 1 and IC 2501.

We consider that both nebulae have a constant density distribution; $N_e = 1.1\times10^5$ cm^{-3} in SwSt 1 and $N_e = 2.1\times10^4$ cm^{-3} in IC 2501. Regarding the temperature fluctuations, we shall assume that $t^2 = 0.0$. Since SwSt 1 is a very low-excitation object, we shall assume that $T_e = T_e$(O III) in all regions in the nebula. For IC 2501, we use $T_e = T_e$(O III) for regions of high degree of ionization and $T_e = T_e$(N II) for regions of low degree of ionization.

Using equation (3.52) for He^+ and He^{+2}, equation (3-56) for C^+, C^{+2}, O^+, N^{+2}, and Mg^+, and equation (3.58) for O^{+2}, N^+, S^+, S^{+2}, S^{+3}, Ne^+, and Ar^{+2}, the abundances of these ions have been derived. The transition probabilites have been taken from Table (2-7). In the case of $O^{+2}(\lambda5007)$, the relative level populations have been computed from equation (3.42). Relative level populations for other ions have been taken from Table (3-5). In Table (3-12), we present the derived ionic abundances.

The results in Table (3-12) differ only slightly from those given in Papers I and II, due to the more accurate fits to the recombination coefficients and collision strengths employed in the present calculations. The only exception to this is the values of $N(S^+)/N(H^+)$ ratio in IC 2501. The value given in Paper II was 8.12×10^{-8}, while Table (3-12) shows that the correct value is 8.22×10^{-7}; the value of the ratio $I(\lambda\lambda6717,31)/I(H\beta) = 5.9$ was mistakenly taken to be 0.59 when calculating the S^+ abundance in Paper II.

Table (3-13) gives the total element abundances and the C/O abundance ratio in SwSt 1 and IC 2501. The total carbon, oxygen, and nitrogen abundances have been obtained by summing the abundances of the X^+ and X^{+2} ions. The contributions of higher ionization stages

to the total element abundances are negligible, since $N(He^{+2}) << N(He^{+})$ [see, however, section (3.7.2)]. Similarly, the total S abundance is obtained by summing the abundances of S^{+}, S^{+2}, and S^{+3} ions. The amount of neutral helium in IC 2501 is expected to be small. This contribution to the total helium abundance has been neglected.

3.7.5.1 Discussion of Abundance Determinations

The results in Tables (3-11), (3-12), and (3-13) call for the following comments :

(i) Ionic abundances relative to hydrogen are more reliably determined in IC 2501 than in SwSt 1, owing to remaining uncertainties in the reddening constant and electron temperature in the latter object.

(ii) The absence of nebular He II recombination lines in the spectra of SwSt 1 suggest that $N(He^{+2})/N(H^{+}) = 0$ in this object. The total He abundance is well determined in IC 2501.

(iii) Carbon is more abundant in both nebulae than in the sun.

(iv) The value of the total oxygen abundance in SwSt 1 is higher than the average values found in different types of planetary nebulae but in agreement with the solar value.

(v) There is little doubt that SwSt 1 is an oxygen-rich (C/O < 1) object, while IC 2501 is a carbon-rich (C/O > 1) object.

(vi) The value of the total nitrogen abundance in IC 2501 is in good agreement with the average value found in carbon-rich nebulae.

(vii) The value of the total S abundance in IC 2501 is below the solar value, but close to the average value found in planetary nebulae.

(viii) The ratio $N(Mg^{+})/N(H^{+})$ is 8.58×10^{-7} in IC 2501, 3.0×10^{-6} in IC 418 (HLSS), and 1.3×10^{-8} in NGC 6572 [Flower and Penn (1981)]. There is no strong evidence for Mg depletion in IC 2501.

(ix) Neon is mostly in the form of Ne^{+} in SwSt 1, while argon is mostly in the form of Ar^{+2} in IC 2501.

3.7.5.2 The C/O Abundance Ratio

As mentioned in Chapter 1 (section 1.3.2), Aitken and Roche (1982) classify planetary nebulae as carbon-rich (C/O>1) or oxygen-rich (C/O<1) according to the presence of SiC or silicate features, respectively, in their infrared spectra. Table (3-14) gives the C/O abundance ratio in nebulae which exhibit SiC or silicate infrared features. These results confirm the correlation proposed by Aitken and Roche (1982).

CHAPTER (3)

Tables and Figures

Table (3-1)

Values of the wavelength dependent reddening function.

Ion	λ(Å)	f(λ)	Ion	λ(Å)	f(λ)
Hα	6563	-0.323	O IV]	1402	1.307
Hβ	4861	0.000	[Ne II]	12.80μm	-0.998
Hγ	4340	0.129	[Ne III]	3869	0.223
Hδ	4102	0.171	[Ne IV]	1575	1.168
Hε	3970	0.207	[Ne IV]	2972	0.534
He I	4471	0.096	[Ne IV]	2423	1.118
He I	5876	-0.216	[Ne IV]	4720	0.034
He II	1640	1.136	[Ne V]	3346	0.370
He II	4686	0.042	[Ne V]	3426	0.344
C II	1335	1.416	Mg II	2800	0.646
C II]	2326	1.354	Si III]	1883	1.196
C II	4267	0.142	Si IV	1397	1.312
C III]	1908	1.227	[S II]	4073	0.178
C III	1176	1.845	[S II]	6725	-0.344
C III	2297	1.431	[S III]	3722	0.256
C IV	1549	1.184	[S III]	6311	-0.289
[N II]	5755	-0.191	[S III]	9069	-0.607
[N II]	6548	-0.321	[S IV]	10.52μm	-0.997
[N II]	6584	-0.326	[Ar III]	7751	-0.451
N III]	1751	1.120	[Ar III]	7136	-0.391
N IV]	1487	1.229	[Ar III]	8.99μm	-0.995
N V	1240	1.639	[Ar IV]	2855	0.606
[O I]	6300	-0.285	[Ar IV]	4711	0.337
[O I]	6364	-0.294	[Ar IV]	4740	0.030
[O II]	2470	1.025	[Ar IV]	7171	-0.394
[O II]	3727	0.255	[Ar V]	7006	-0.376
[O II]	7325	-0.411			
O III]	1663	1.128			
[O III]	2321	1.323	U	3446	0.337
[O III]	4363	0.124	B	4329	0.131
[O III]	5007	-0.034	V	5464	-0.127

Table(3-2)

Some theoretical line intensity ratios that are independent of physical conditions in planetary nebulae.

Ion	λ_1 / λ_2	$I(\lambda_1) / I(\lambda_2)$
[O III]	4363 / 2321	4.246
[O III]	5007 / 4959	2.880
[N II]	6584 / 6548	2.944
[Ne V]	1575 / 2972	2.787
[Ne V]	3425 / 3346	2.722
[S III]	6311 / 3722	1.645
[S III]	9532 / 9069	2.480
[Ar III]	7736 / 7751	4.145
[Ar IV]	2855 / 7171	6.717
[Ar IV]	7005 / 6435	2.143

Table(3-3)

Values of the reddening constants, c , for SwSt 1 and IC 2501.

Method	SwSt 1	IC 2501
[O II] ratio		0.42 ± 0.08
Balmer decrements		0.49 ± 0.09
Hβ - radio continuum	0.50 ± 0.05	0.58 ± 0.07
The λ2200 feature	0.35 ± 0.05	0.45 ± 0.05

Table (3-4)

The line intensities, I(λ), in SwSt 1 and IC 2501, corrected for interstellar extinction and expressed relative to Hβ.

Ion	λ(Å)	SwSt 1		IC 2501
		c = 0.35	c = 0.50	c = 0.50
Hα	6563			279.5
Hβ	4861	100	100	100
Hγ	4340	37.4	38.8	45.4
He I	5876	10.9	10.1	15.1
He II	4686			0.9
C II	1335			5.4
C II]	2326	55.8	89.1	40.5
C III]	1909	40.4	61.8	124.9
[N II]	5755	9.43	8.83	1.3
[N II]	6584			65.7
N III]	1749			5.54
[O I]	6300			4.68
[O II]	2470	49.3	70.3	10.7
[O II]	3727,29			58.9
[O II]	7320,30			11.0
O III]	1663	2.79	4.11	
[O III]	2321	0.099	0.103	1.1
[O III]	4363	0.31	0.33	4.53
[O III]	5007	51.2	50.6	791.0
[NeII]	12.80μm	147.0	104.2	24.9
Mg II	2800			11.0
[S II]	6717,31			5.9
[S III]	6312			1.0
[S IV]	10.52μm	4.84	3.43	49.7
[Ar III]	7136			17.0
[Ar III]	8.99μm	9.26	6.57	18.0

Table (3-5)

Relative level populations, computed for physical conditions found in the planetary nebulae SwSt 1 and IC 2501.

X^{+m}	Log(N_e)	T_e(K)	$n(X_i^{+m})$					
		i ≡	$^5S_2^o$	^1S_o	$^1D_2$	$^3P_1$	$^3P_2$	^3P_o
O^{+2}	4.322	9000	2.51-11	3.52-8	6.77-4	5.11-1	3.65-1	1.23-1
		9400	3.73-11	4.65-8	7.64-4	5.11-1	3.65-1	1.23-1
	5.041	8800	1.06-10	1.90-7	2.94-3	5.40-1	3.42-1	1.15-1
		8900	1.18-10	2.05-7	3.04-3	5.40-1	3.42-1	1.15-1
N^{+}	4.322	9000	1.12-9	4.76-7	9.89-3	5.49-1	3.32-1	1.09-1
		9400	1.50-9	5.79-7	1.08-2	5.50-1	3.31-1	1.08-1
	5.041	8800	4.90-9	2.89-6	2.60-2	5.40-1	3.26-1	1.08-1
		8900	5.31-9	3.04-6	2.67-2	5.40-1	3.26-1	1.08-1
S^{+2}	4.322	9000		1.37-6	3.87-3	3.99-1	4.38-1	1.59-1
		9400		1.61-6	4.06-3	3.98-1	4.38-1	1.59-1
	5.041	8800		7.66-6	1.68-2	4.97-1	3.63-1	1.24-1
		8900		8.00-6	1.71-2	4.97-1	3.62-1	1.23-1
		i ≡		^1S_o	$^1D_2$	^3P_o	$^3P_1$	$^3P_2$
Ar^{+2}	4.322	9000		1.25-7	2.73-4	1.97-2	2.58-2	9.54-1
		9400		1.54-7	2.93-4	1.95-2	2.55-2	9.55-1
	5.041	8800		6.11-7	1.37-3	4.62-2	9.70-2	8.55-1
		8900		6.45-7	1.40-3	4.62-2	9.68-2	8.56-1
O^{o}	4.322	9000		2.59-8	5.49-4	7.91-2	1.84-1	7.36-1
		9400		3.30-8	6.30-4	7.83-2	1.87-1	7.34-1
	5.041	8800		1.62-7	2.60-3	9.34-2	2.83-1	6.21-1
		8900		1.71-7	2.69-3	9.31-2	2.83-1	6.21-1

Table (3-5) - continued -

X^{+m}	$Log(N_e)$	$T_e(K)$		$n(X_i^{+m})$				
			i ≡	$^2P^o_{1/2}$	$^2P^o_{3/2}$	$^2D^o_{3/2}$	$^2D^o_{5/2}$	$^4S^o_{3/2}$
O^+	4.322	9000		2.15-6	3.44-6	9.51-3	1.56-2	9.75-1
		9400		2.75-6	4.41-6	1.13-2	1.86-2	9.60-1
	5.041	8800		1.15-5	1.84-5	1.12-2	1.72-2	9.72-1
		8900		1.23-5	1.97-5	1.18-2	1.80-2	9.70-1
			i ≡	$^2P^o_{3/2}$	$^2P^o_{1/2}$	$^2D^o_{5/2}$	$^2D^o_{3/2}$	$^4S^o_{3/2}$
S^+	4.322	9000		1.07-4	8.64-5	8.43-2	5.38-2	8.62-1
		9400		1.21-4	9.80-5	9.12-2	5.82-2	8.50-1
	5.041	8800		5.87-4	4.48-4	9.56-2	6.45-2	8.39-1
		8900		6.07-4	4.74-4	9.76-2	6.59-2	8.35-1
			i ≡	$^4P_{5/2}$	$^4P_{3/2}$	$^4P_{1/2}$	$^2P^o_{3/2}$	$^2P^o_{1/2}$
S^{+3}	4.322	9000		2.69-13	4.55-13	5.75-14	3.28-1	6.72-1
		9400		4.27-13	7.23-13	9.12-14	3.26-1	6.74-1
	5.041	8800		1.20-12	1.85-12	2.22-13	5.37-1	4.63-1
		8900		1.36-12	2.10-12	2.52-13	5.37-1	4.63-1
			i ≡				$^2P^o_{1/2}$	$^2P^o_{3/2}$
Ne^+	4.322	9000					1.71-2	9.83-1
		9400					1.68-2	9.83-1
	5.041	8800					7.27-2	9.27-1
		8900					7.25-2	9.28-1

The notation a-b signifies $a \times 10^{-b}$.

Table (3-6)

Parameters for calculating $n(O^{+2}, {}^1D_2)$.

Range of t	a_1	a_2	a_3	Range of $Log(N_e)$	a_4	a_5
≧ 0.75 to < 1.25	24977	16055	24537	≧ 3.0 to ≦ 4.0	1.0000	4.0000
				> 4.0 to ≦ 4.5	0.9738	3.8952
				> 4.5 to ≦ 5.0	0.9236	3.6693
				> 5.0 to ≦ 5.5	0.7946	3.0243
≧ 1.25 to ≦ 2.00	21452	12930	21043	≧ 3.0 to ≦ 4.0	1.0000	4.0000
				> 4.0 to ≦ 4.5	0.9712	3.8848
				> 4.5 to ≦ 5.0	0.9286	3.6931
				> 5.0 to ≦ 5.5	0.8036	3.0681

Table (3-7)

Values of $n(O^{+2}, {}^1D_2)$ computed with L=15 [Nussbaumer & Storey (1981)], L=6, and equation (3.42).

$Log(N_e)$		$T_e(K)$								
		7500	9000	10000	11500	12500	13500	15000	17500	20000
4.0	L = 15	1.87-4		4.40-4		7.27-4		1.01-3		1.48-3
	L = 6	1.84-4	3.27-4	4.35-4	6.04-4	7.18-4	8.31-4	9.97-4	1.25-3	1.47-3
	Fit	1.87-4	3.30-4	4.40-4	6.12-4	7.27-4	8.44-4	1.01-3	1.26-3	1.48-3
4.25	L = 6	3.24-4	5.76-4	7.65-4	1.06-3	1.26-3	1.46-3	1.76-3	2.20-3	2.59-3
	Fit	3.28-4	5.77-4	7.71-4	1.07-3	1.27-3	1.48-3	1.77-3	2.20-3	2.59-3
4.5	L = 15	5.72-4		1.35-3		2.24-3		3.09-3		4.55-3
	L = 6	5.64-4	1.00-3	1.34-3	1.86-3	2.21-3	2.56-3	3.07-3	3.84-3	4.53-3
	Fit	5.74-4	1.01-3	1.35-3	1.88-3	2.22-3	2.58-3	3.09-3	3.85-3	4.53-3
4.75	L = 6	9.68-4	1.73-3	2.30-3	3.19-3	3.80-3	4.41-3	5.29-3	6.63-3	7.82-3
	Fit	9.77-4	1.72-3	2.30-3	3.20-3	3.79-3	4.41-3	5.27-3	6.57-3	7.73-3
5.0	L = 15	1.64-3		3.91-3		6.49-3		9.00-3		1.33-2
	L = 6	1.62-3	2.89-3	3.86-3	5.37-3	6.40-3	7.43-3	8.93-3	1.12-2	1.32-2
	Fit	1.66-3	2.93-3	3.91-3	5.44-3	6.47-3	7.52-3	9.00-3	1.12-2	1.32-2

The notation a-b signifies $a \times 10^{-b}$.

Table (3-8)

Parameters for temperature determinations [see equation (3.49)]. Numbers in brackets are powers of 10.

Ion	t	a_t	a_1	a_2	a_{23}
[O III]	0.5	8.028	4.08(-2)	3.29(-4)	1.432
	1.0	7.750	4.60(-2)	3.85(-4)	
	1.5	7.582	4.72(-2)	4.04(-4)	
	2.0	7.502	4.73(-2)	4.08(-4)	
[N II]	0.5	6.773	2.45(-1)	5.66(-4)	1.086
	1.0	6.876	2.51(-1)	5.71(-4)	
	1.5	6.842	2.54(-1)	5.81(-4)	
	2.0	6.754	2.55(-1)	5.91(-4)	
[S III]	0.5	7.233	4.37(-2)	7.36(-4)	0.990
	1.0	6.522	4.69(-2)	8.75(-4)	
	1.5	6.338	4.79(-2)	9.21(-4)	
	2.0	6.117	4.75(-2)	9.47(-4)	

Table (3-9)

Electron temperatures and densities in SwSt 1 and IC 2501. The values listed with a colon are unreliable.

Ion	The diagnostic ratio R	Value of R	T_e(K)	N_e(cm^{-3})
			SwSt 1	
[O II]	I(λ3729)/I(λ3727)	0.39		1.6×10^{-4}:
C III]	I(λ1907)/I(λ1909)	0.30		1.1×10^{-5}
[O III]	Log[I(λ5007)/I(λ4363)]	2.218(c=0.35)	8800	
		2.186(c=0.50)	8900	
[O III]	Log[I(λ5007)/I(λ1663)]	1.264(c=0.35)	15000:	
		1.090(c=0.50)	17000:	
			IC 2501	
[O III]	Log[I(λ5007)/I(λ4363)]	2.242	9400	
[N II]	Log[I(λ6584)/I(λ5755)]	1.704	9000	
[O II]	Log[I(λλ3727,29)/I(λ2470)]	0.741		2.1×10^{-4}
C III	Log[I(λ1908)/I(λ1335)]	1.364	12000:	

Table (3-10)

Coefficients for calculation of ionic concentrations in planetary nebulae.

X^{+m}	transition	λ(A)	a	b	c	d
He^{+}	$2\ ^3P^o - 4\ ^3D$	4471	3.615+1	3.009+2	6.292+2	
He^{+}	$2\ ^3P^o - 3\ ^3D$	5876	1.679+1	1.505+2	3.141+2	
He^{+2}	2 - 3	1640	9.410-2	1.716-1	-7.127-2	
He^{+2}	3 - 4	4686	1.676	1.582+1	3.557+1	
C^{+}	$2s^22p\ ^2P^o - 2s2p^2\ ^4P$	2326	1.047-8	4.049-7	1.713-6	2.686+4
C^{+2}	$2s^2\ ^1S - 2s2p\ ^3P^o$	1908	-1.074-8	-9.349-8	-5.929-9	3.275+4
C^{+3}	$2s\ ^2S - 2p\ ^2P^o$	1550	2.785-10	2.658-8	1.256-7	4.031+4
O^{+}	$2p^3\ ^4S^o - 2p^3\ ^2P^o$	2470	2.153-8	2.019-6	9.377-6	2.530+4
O^{+2}	$2s^22p^2\ ^3P - 2s2p^3\ ^5S^o$	1663	1.106-7	2.928-6	1.025-5	3.758+4
O^{+3}	$2s^22p\ ^2P^o - 2s2p^2\ ^4P$	1406	3.526-8	1.086-6	4.023-6	4.444+4
N^{+2}	$2s^22p\ ^2P^o - 2s2p^2\ ^4P$	1749	2.964-9	4.001-7	1.911-6	3.573+4
N^{+3}	$2s^2\ ^1S - 2p2p\ ^3P^o$	1487	-3.828-10	7.608-8	4.389-7	4.202+4
Mg^{+}	$3s\ ^2S - 3p\ ^2P^o$	2800	8.683-10	4.063-8	1.684-7	2.234+4
Si^{+2}	$3s^2\ ^1S - 3s3p\ ^3P^o$	1892	-1.698-9	-2.527-8	-3.928-8	3.303+4
Si^{+3}	$3s\ ^2S - 3p\ ^2P^o$	1397	2.236-10	1.418-8	6.378-8	4.473+4

The notation $a \pm b$ signifies $a \times 10^{\pm b}$.

Table (3-11)

Mean abundances in planetary nebulae [as compiled by Aller (1983,1984)].

X	log[N(X)/N(H)] + 12					
	Population I	Population II	High Excitation	N-rich	C-rich	Solar
He	11.06	11.03	11.04	11.13	11.03	11.0:
C	8.82	8.72	8.89	8.50	8.99	8.66
N	8.12	7.94	8.39	8.88	8.15	7.98
O	8.68	8.58	8.66	8.71	8.69	8.91
Ne	8.08	7.88	8.02	8.05	8.05	8.05
S	6.96	6.88	7.03	6.98	7.09	7.23
Cl	5.28	5.13	5.27	5.40	5.27	5.50
Ar	6.42	6.22	6.48	6.65	6.46	6.57
F			4.60			4.60
Na			6.18			6.31
K			5.00			5.15
Ca			5.00			6.34

Table (3-12)

Ionic abundances in SwSt 1 and IC 2501. Numbers in brackets are powers of 10.

X^{+m}	λ(A)	$N(X^{+m})/N(H^+)$		
		SwSt 1		IC 2501
	c =	0.35	0.50	0.50
He^+	5876	0.078	0.072	0.109
He^{+2}	4686	0.0:	0.0:	7.51(-4)
C^+	2326	2.09(-4)	3.07(-4)	1.29(-4)
C^{+2}	1908	3.01(-4)	4.16(-4)	5.29(-4)
O^+	2470	6.92(-4)	9.13(-4)	1.55(-4)
O^{+2}	5007	3.39(-5)	3.21(-5)	3.64(-4)
N^+	5755	1.29(-4)	1.13(-4)	
N^+	6584			2.10(-5)
N^{+2}	1749			1.35(-4)
S^+	6717,31			8.22(-7)
S^{+2}	6312			2.44(-6)
S^{+3}	10.52μm	9.41(-7)	6.61(-7)	2.87(-6)
Mg^+	2800			8.58(-7)
Ne^+	12.82μm	2.33(-4)	1.64(-4)	3.14(-5)
Ar^{+2}	8.99μm	2.14(-6)	1.51(-6)	2.85(-6)

Table (3-13)

Total abundances and the C/O abundance ratio in SwSt 1 and IC 2501. Numbers in prackets are powers of 10.

X	N(X)/N(H)		log[N(X)/N(H)] + 12	
	SwSt 1	IC 2501	SwSt 1	IC 2501
He		0.110		11.04
C	6.17±1.1(-4)	6.58(-4)	8.79±0.07	8.82
O	8.36±1.1(-4)	5.19(-4)	8.92±0.06	8.72
N		1.56(-4)		8.19
S		6.13(-6)		6.79
$\frac{N(C)}{N(O)}$	0.7±0.1	1.3		

Table (3-14)

The C/O abundance ration in nebulae displying SiC or silicate features in their infrared spectra.

Objects with SiC feature			Objects with silicate feature		
Nebula	C/O	References	Nebula	C/O	Reference
IC 2501	1.3	see Table (3-13)	SwSt 1	0.7	see Table (3-13)
IC 418	1.3	(a)	He 2-131	0.3	(a)
NGC 6572	1.1	(b)	Hb 12	0.3	(d)
NGC 6790	0.8:	(c)	IC 4997	0.4	(e)
			M 1-26	0.5	(g)

References: (a) Adams and Seaton (1982)

(b) Flower and Penn (1981)

(c) Adams (1982)

(d) Flower and Penn (1983)

(e) Flower (1980)

(g) Adams and Barlow (1983)

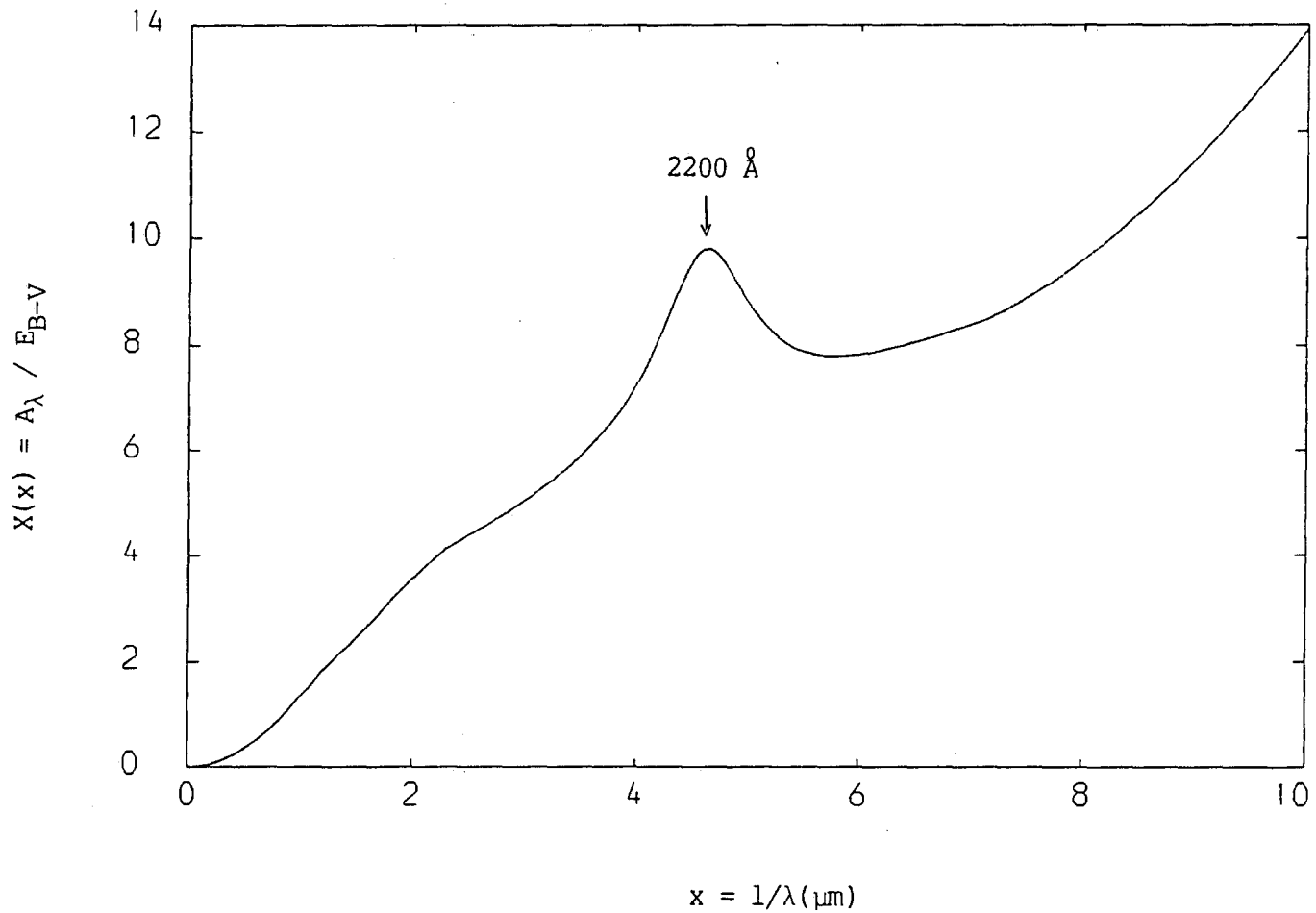

Figure (3-1): The interstellar extinction curve. See the text for explanation

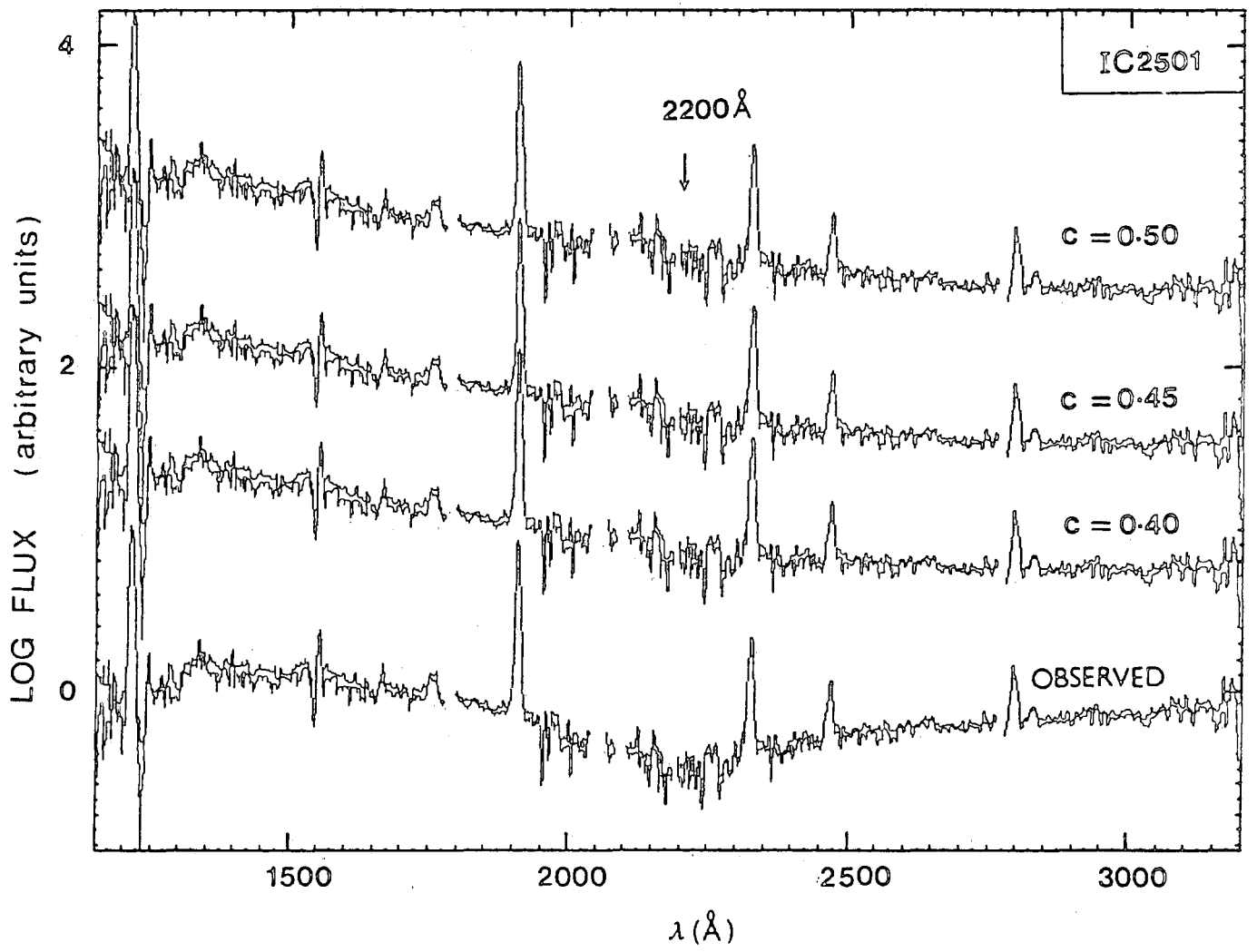

Figure (3-2): This figure demonstrates the use of the 2200 Å absorption feature in determining the reddening constant c. See the text for explanation.

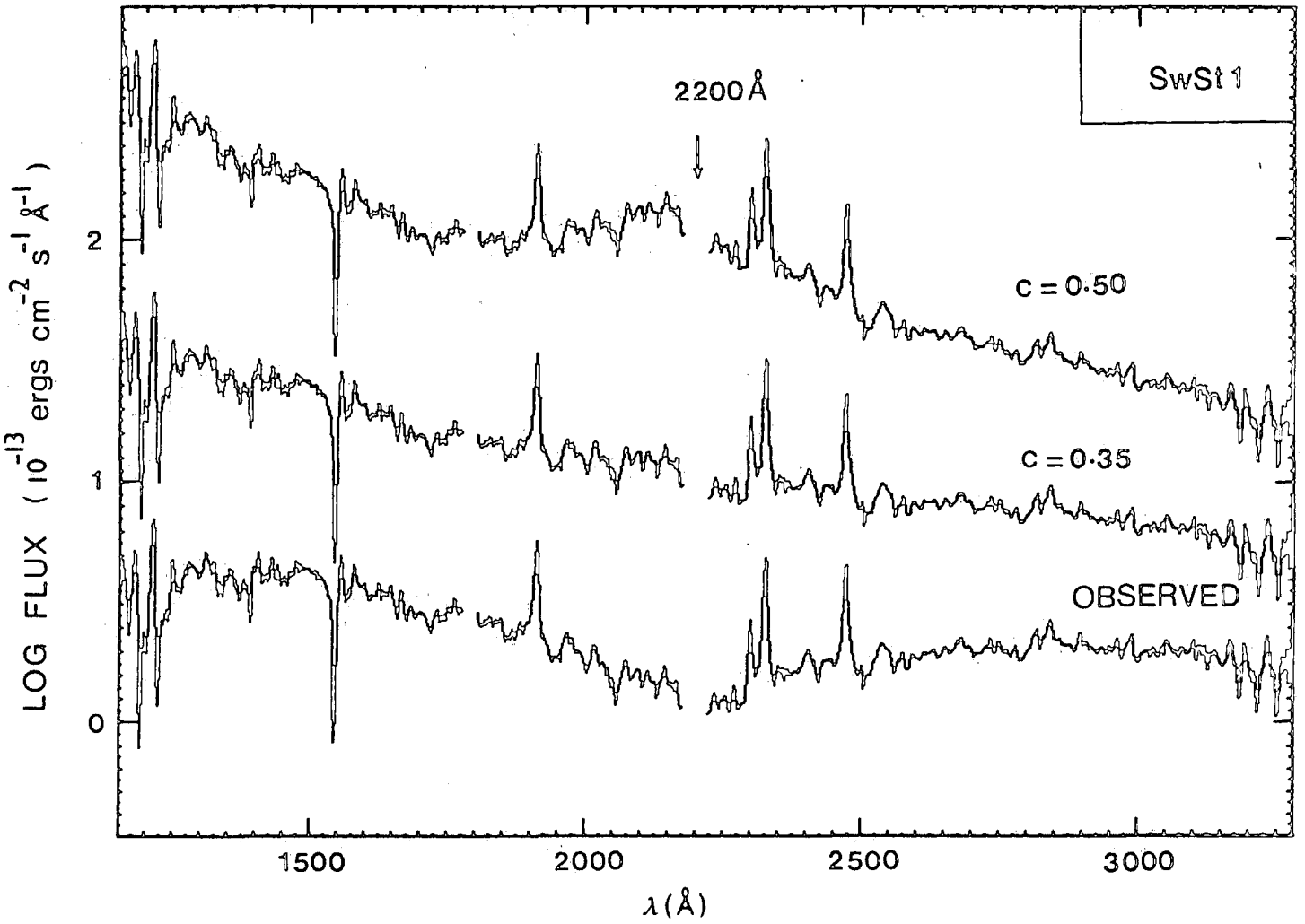

Figure (3-3): Same as figure (3-2), but for SwSt1.

[O II]

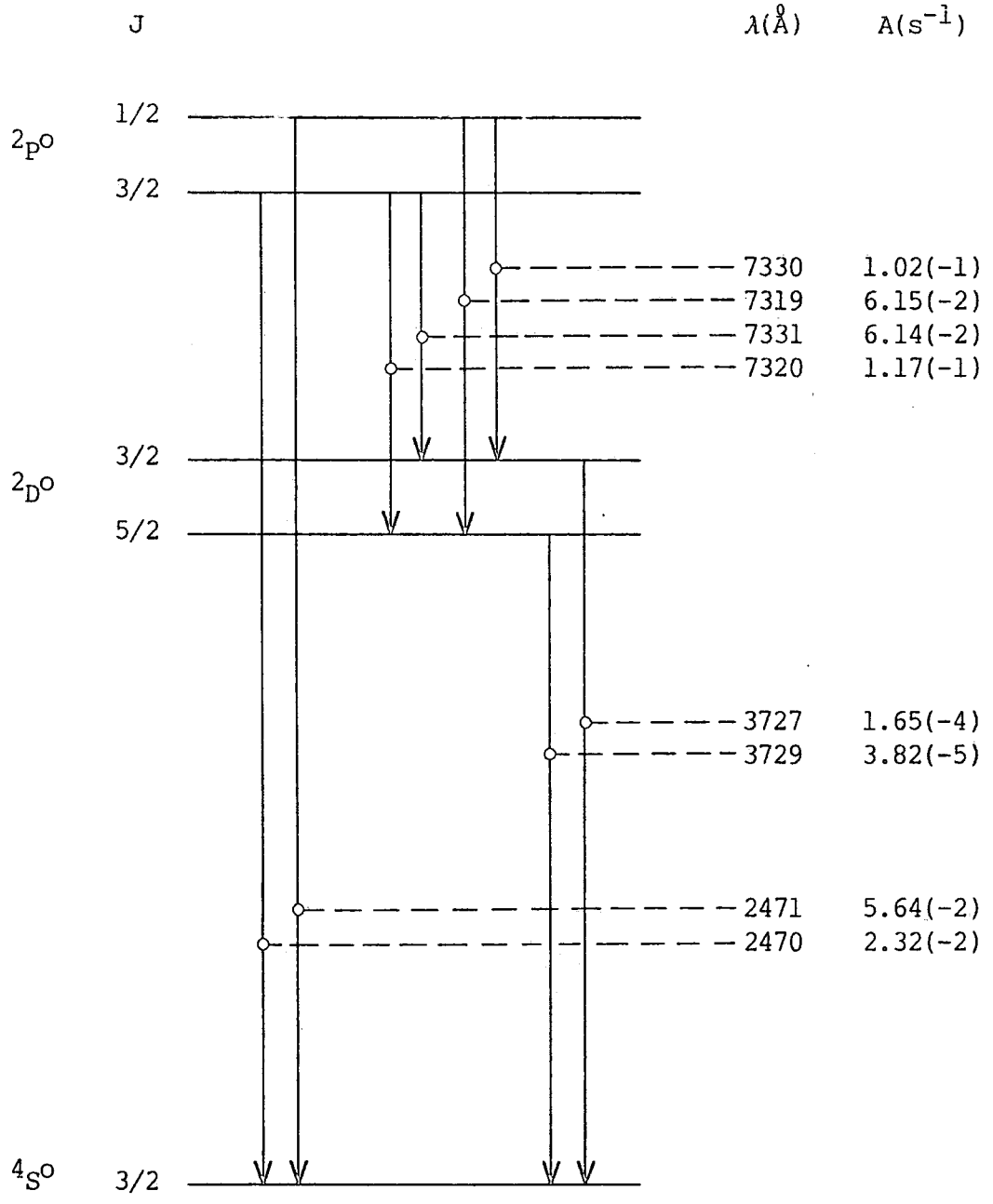

Figure (3-4): Energy level diagram for the $2p^3$ configuration of [O II]. The level separations are not drawn to scale. Wavelengths and transition probabilities for all observed lines are given. Powers of ten are given in parnetheses.

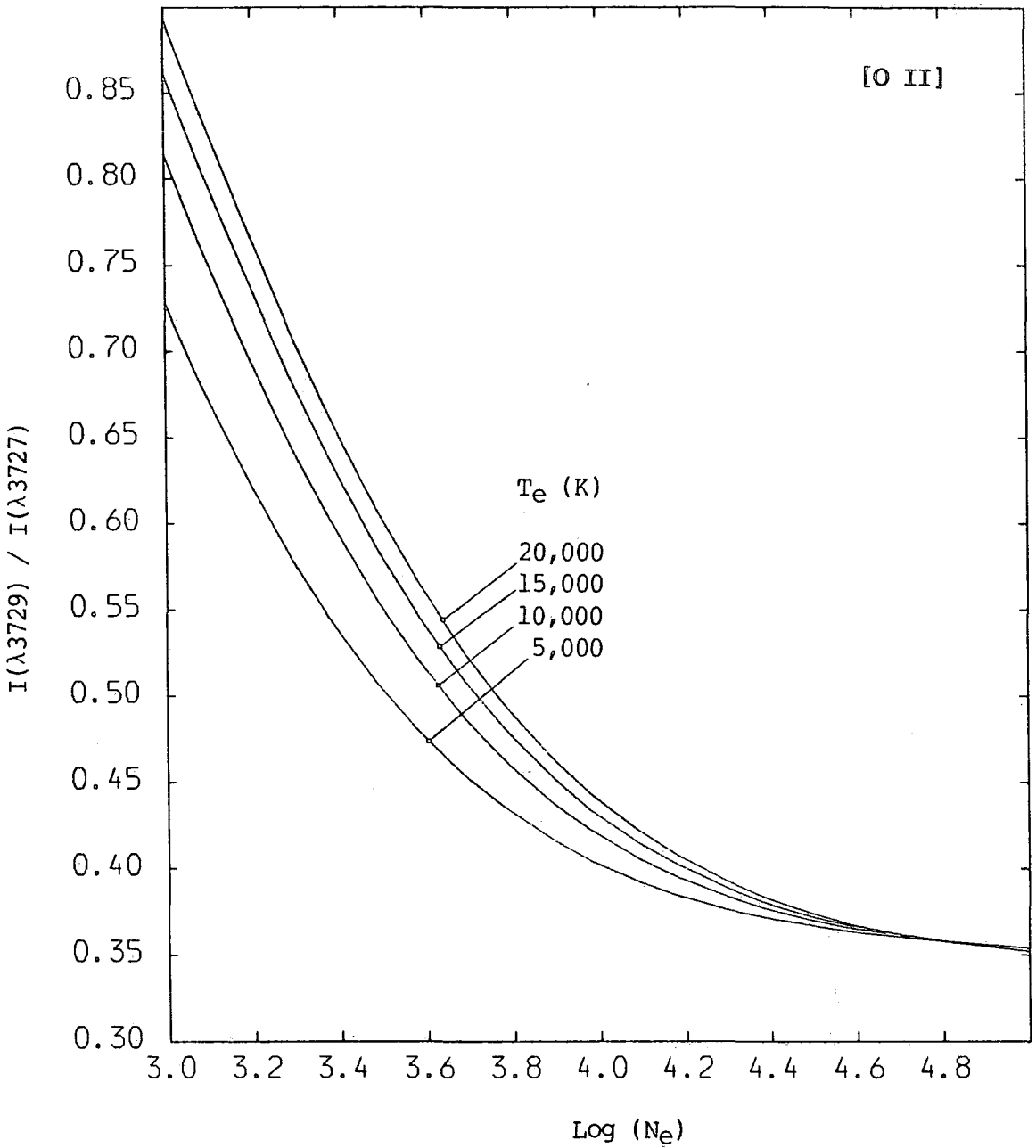

Figure (3-5): Computed dependence of the [O II] λλ 3729 / 3727 intensity ratio on electron density and temperature.

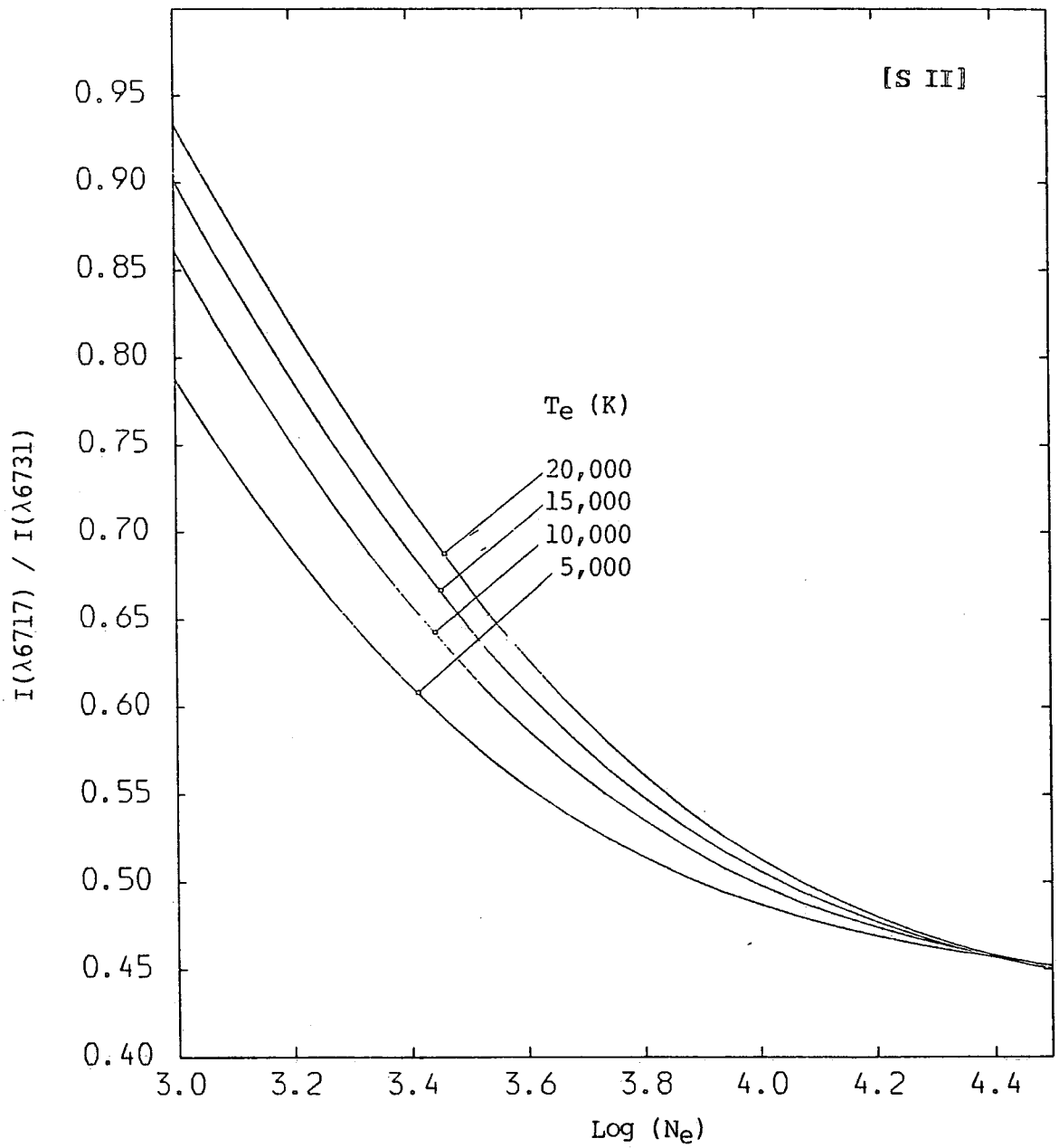

Figure (3-6): Computed dependence of the [S II] λλ 6717 / 6731 intensity ratio on electron density and temperature.

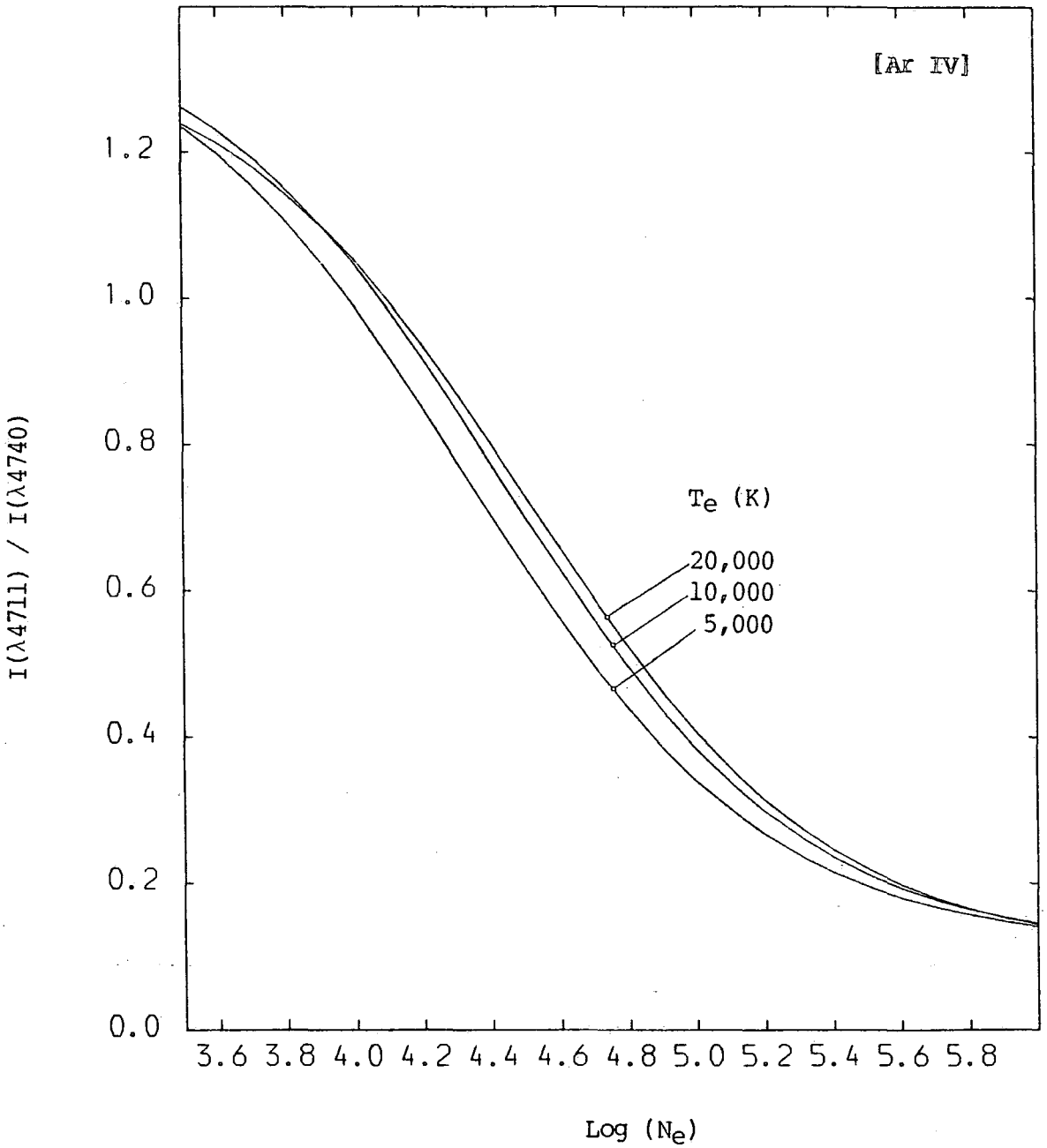

Figure (3-7): Computed dependence of the [Ar IV] λλ 4711 / 4740 intensity ratio on electron density and temperature.

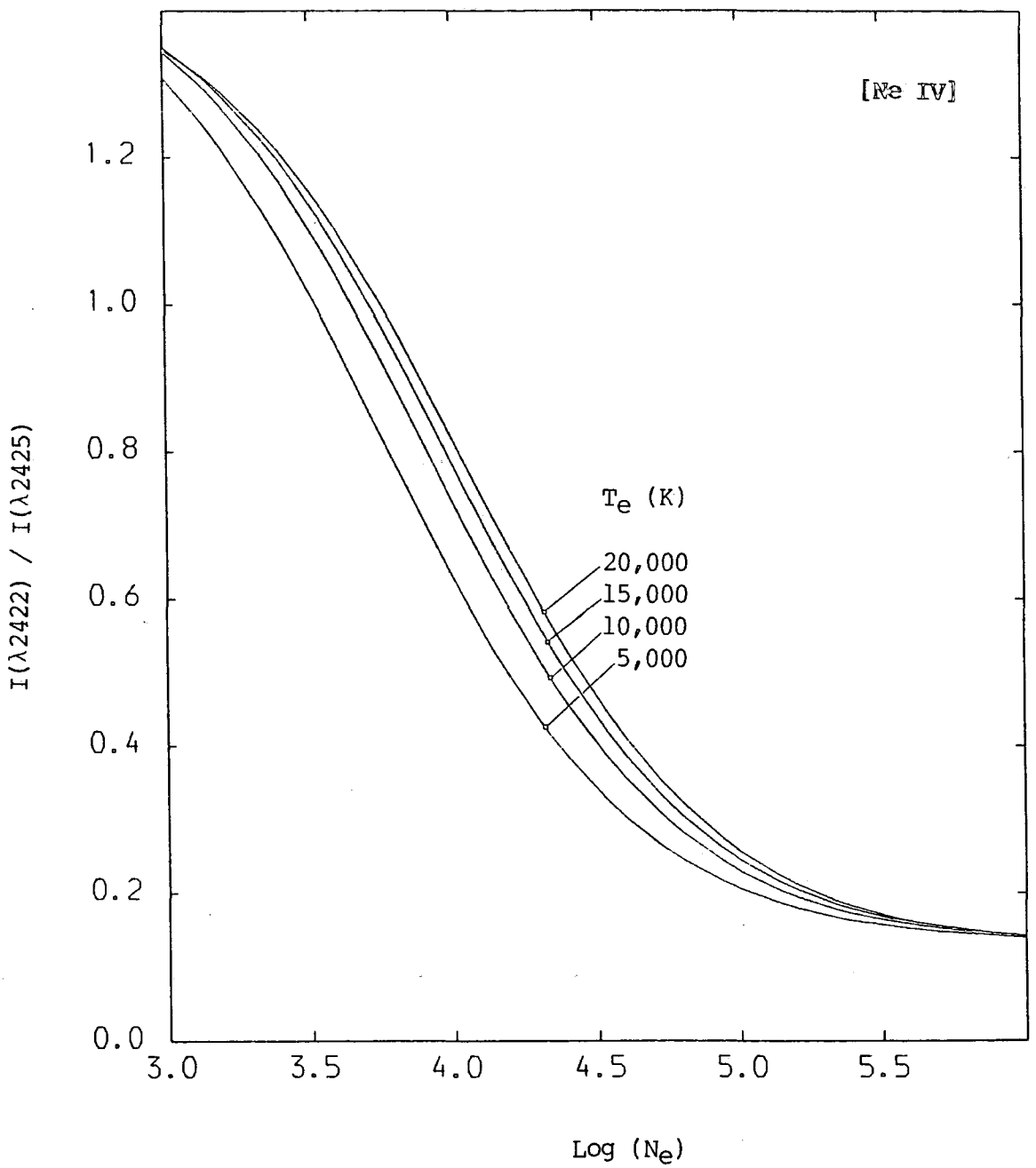

Figure (3-8): Computed dependence of the [Ne IV] λλ 2422 / 2425 intensity ratio on electron density and temperature.

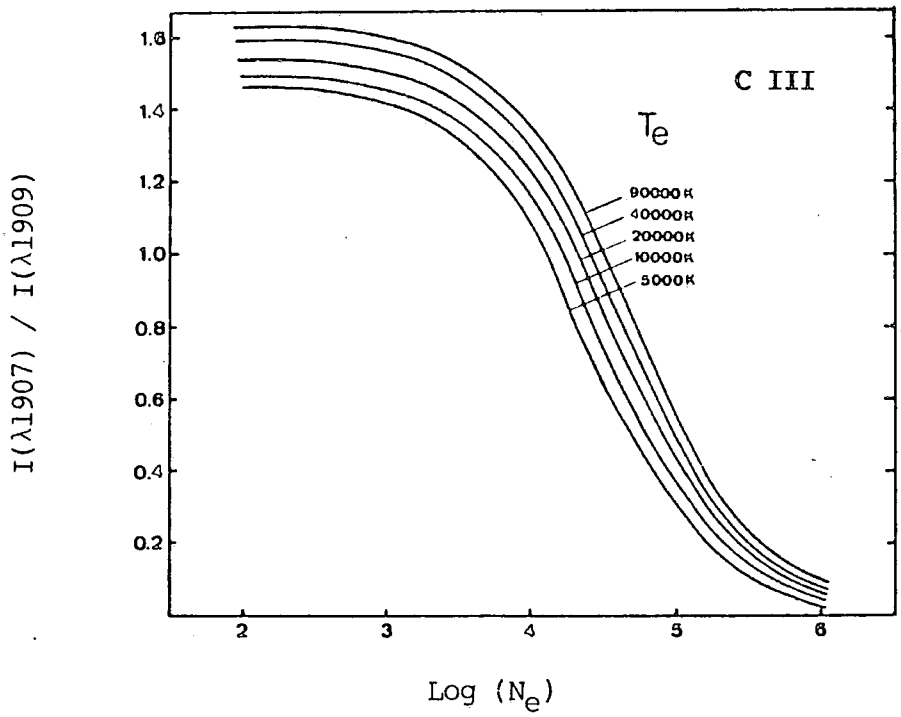

Figure (3-9): Computed dependence of the C III λλ1907/1909 intensity ratio on electron density and temperature [Nussbaumer and Schild (1979)].

[O III]

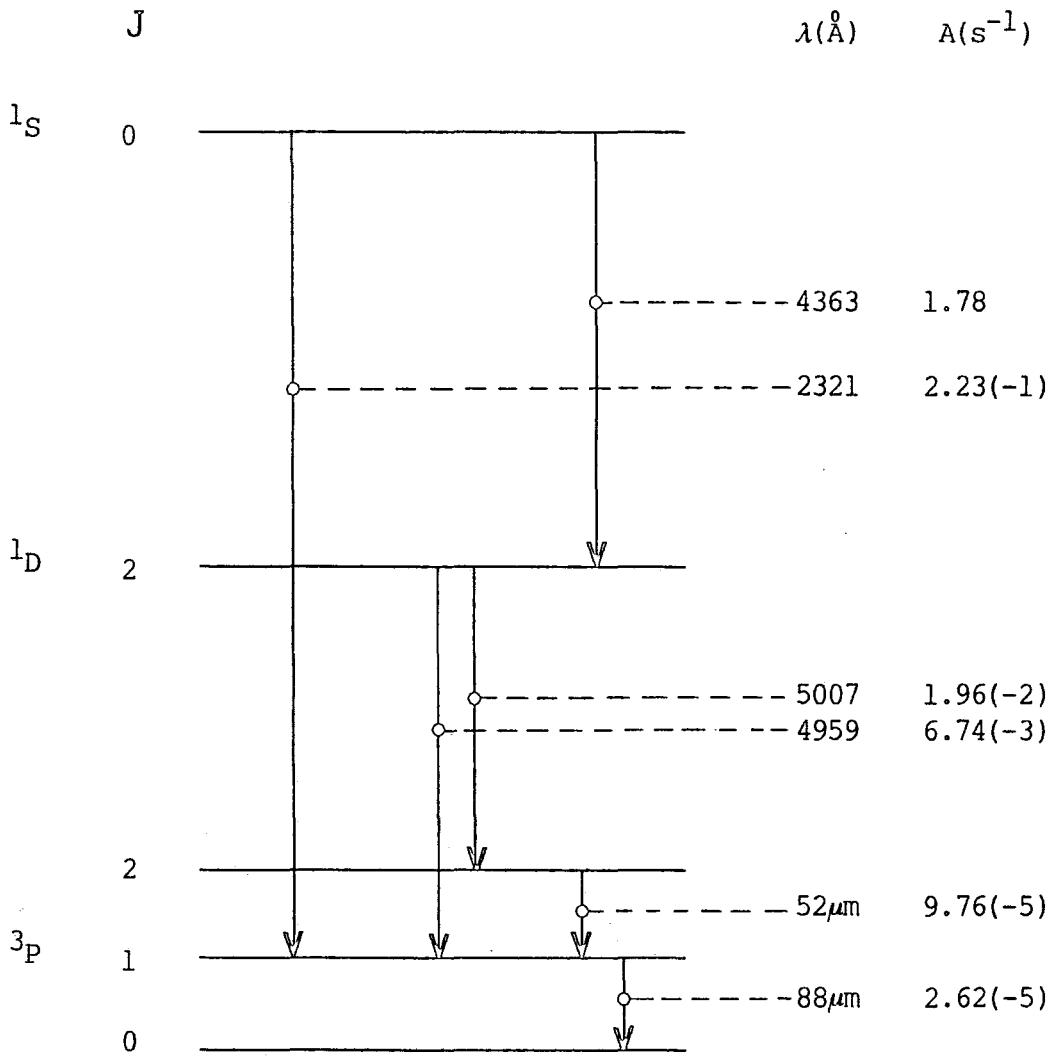

Figure (3-10): Energy level diagram for the $2p^2$ configuration of [O III]. The level separations are not drawn to scale. Wavelengths and transition probabilities for all observed lines are given. Powers of ten are given in parnetheses.

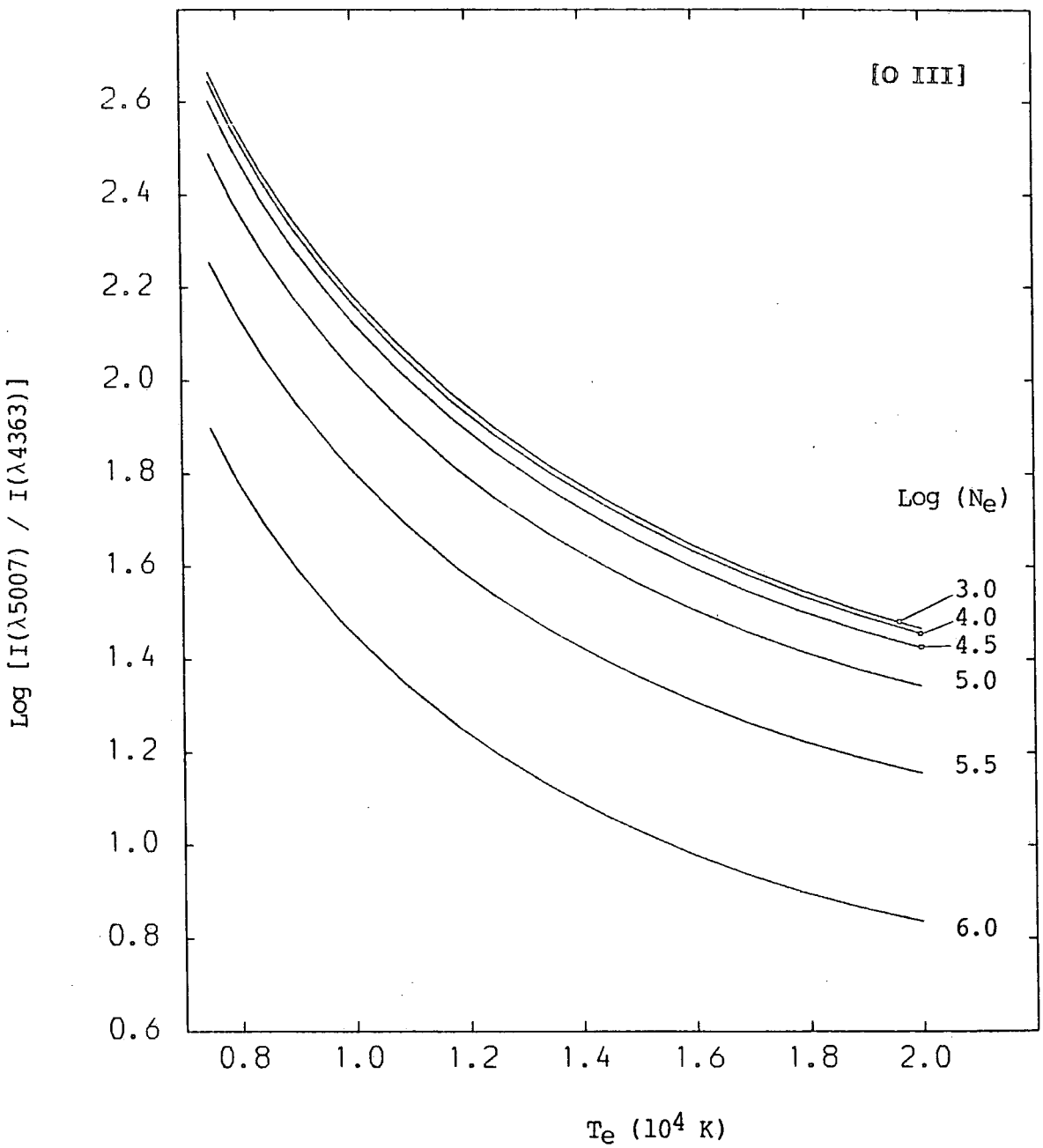

Figure (3-11): Computed dependence of the [O III] λλ 5007 / 4363 intensity ratio on electron temperature and density.

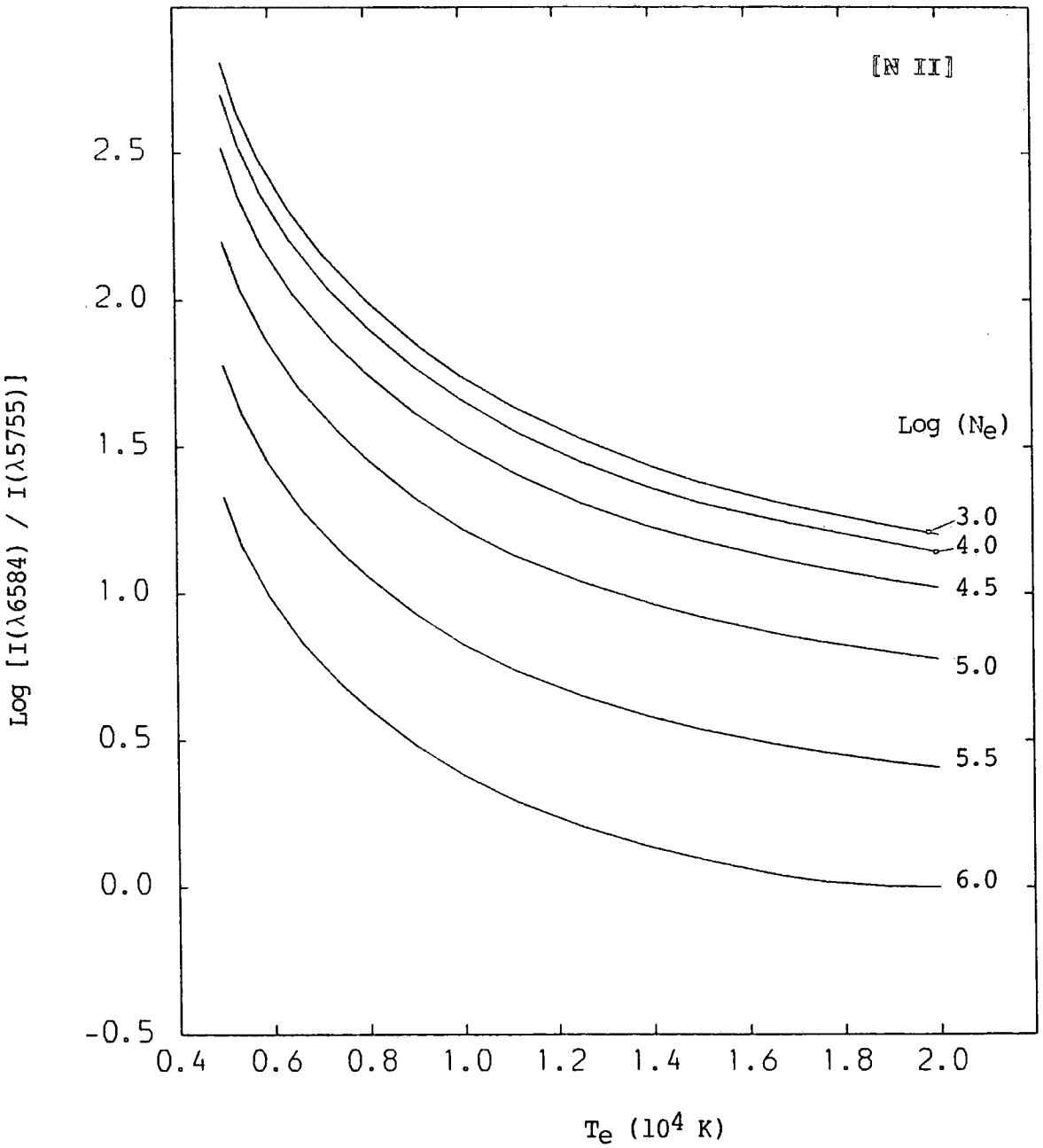

Figure (3-12): Computed dependence of the [N II] λλ 6584 / 5755 intensity ratio on electron temperature and density.

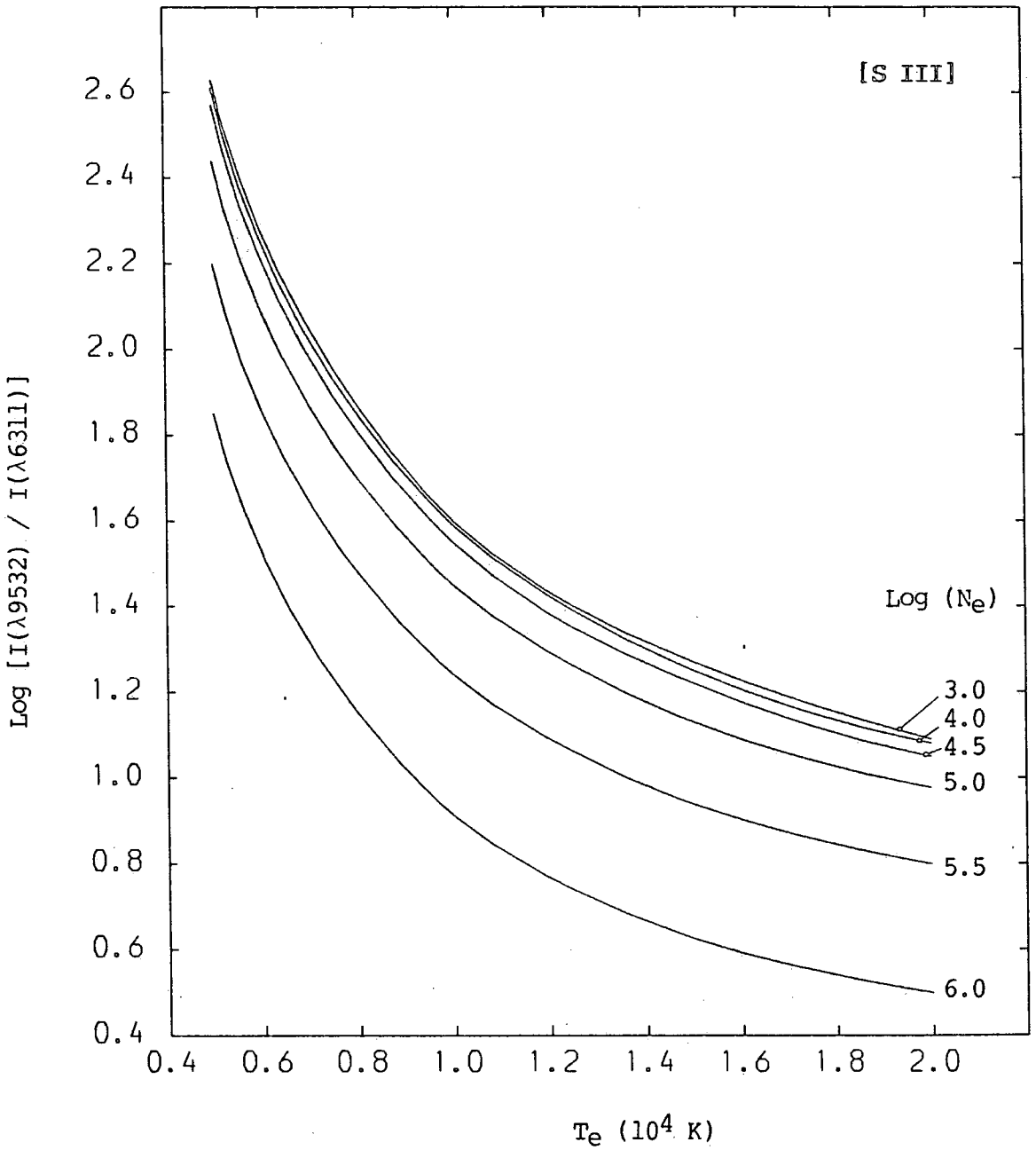

Figure (3-13): Computed dependence of the [S III] λλ 9532 / 6311 intensity ratio on electron temperature and density.

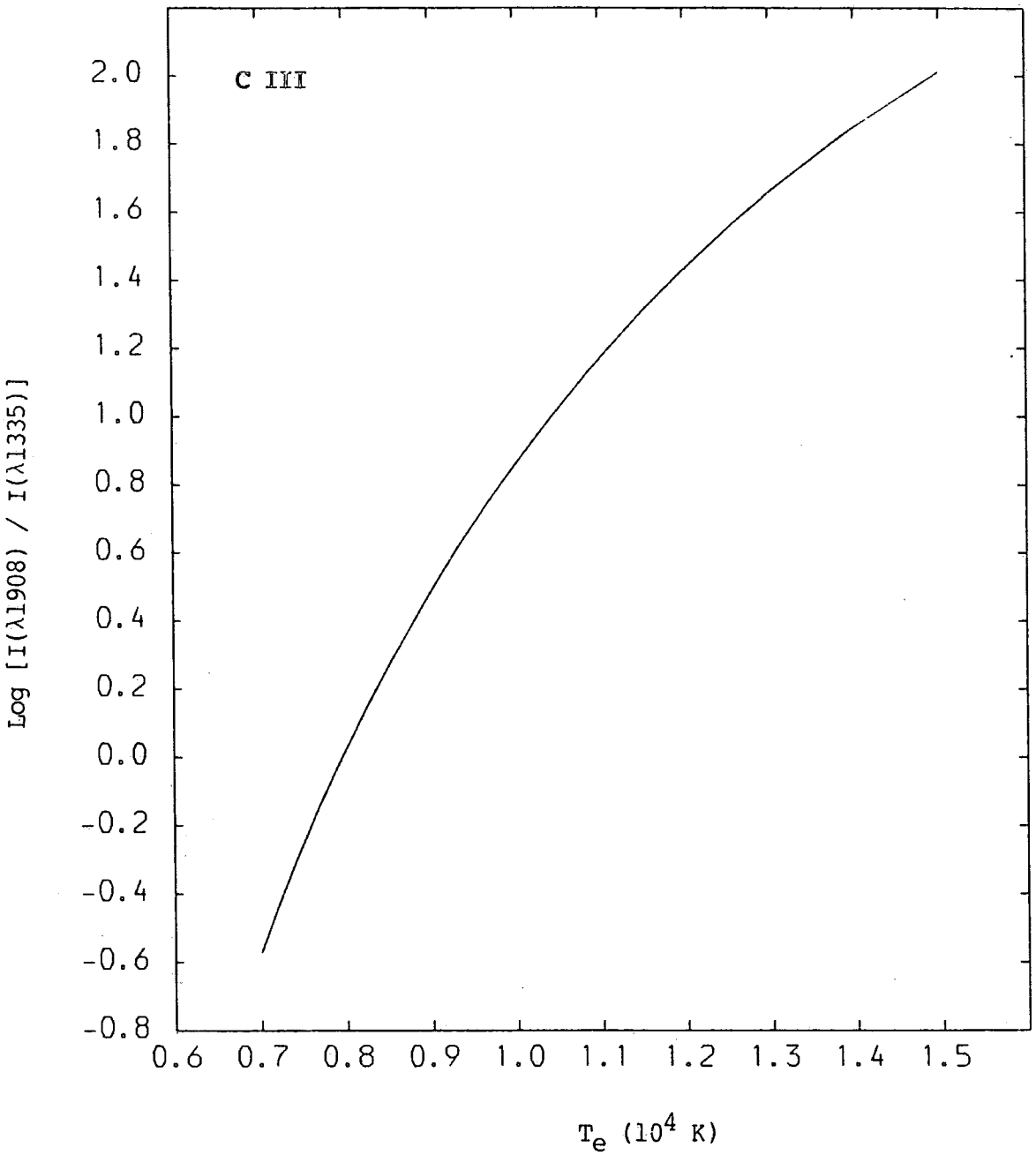

Figure (3-14): The ratio I(C III; λ1908) / I(C II; λ1335) as a function of the electron temperature.

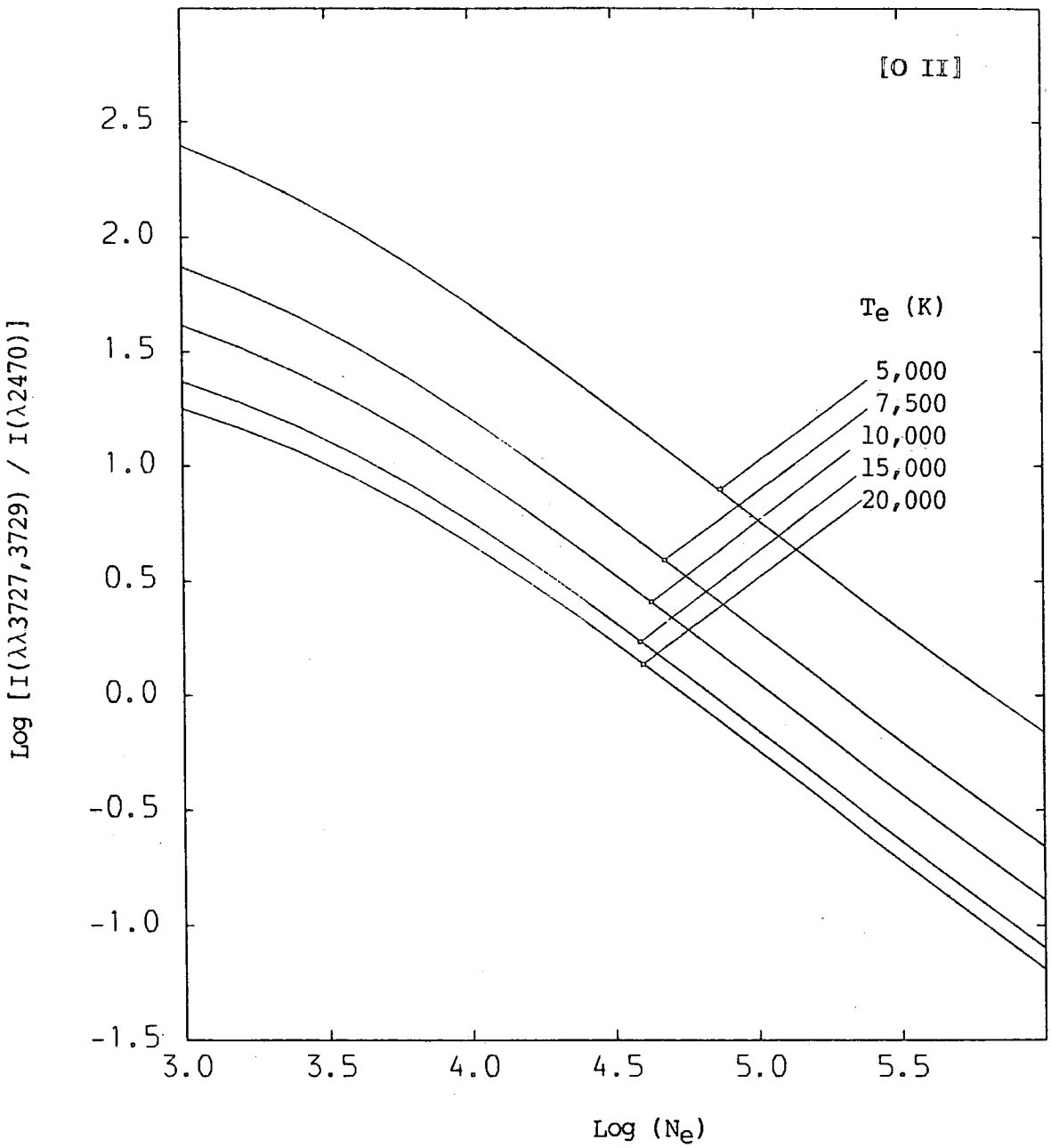

Figure (3-15): Computed dependence of the [O II] λλ3727,3729/λ2470 intensity ratio on electron density and temperature.

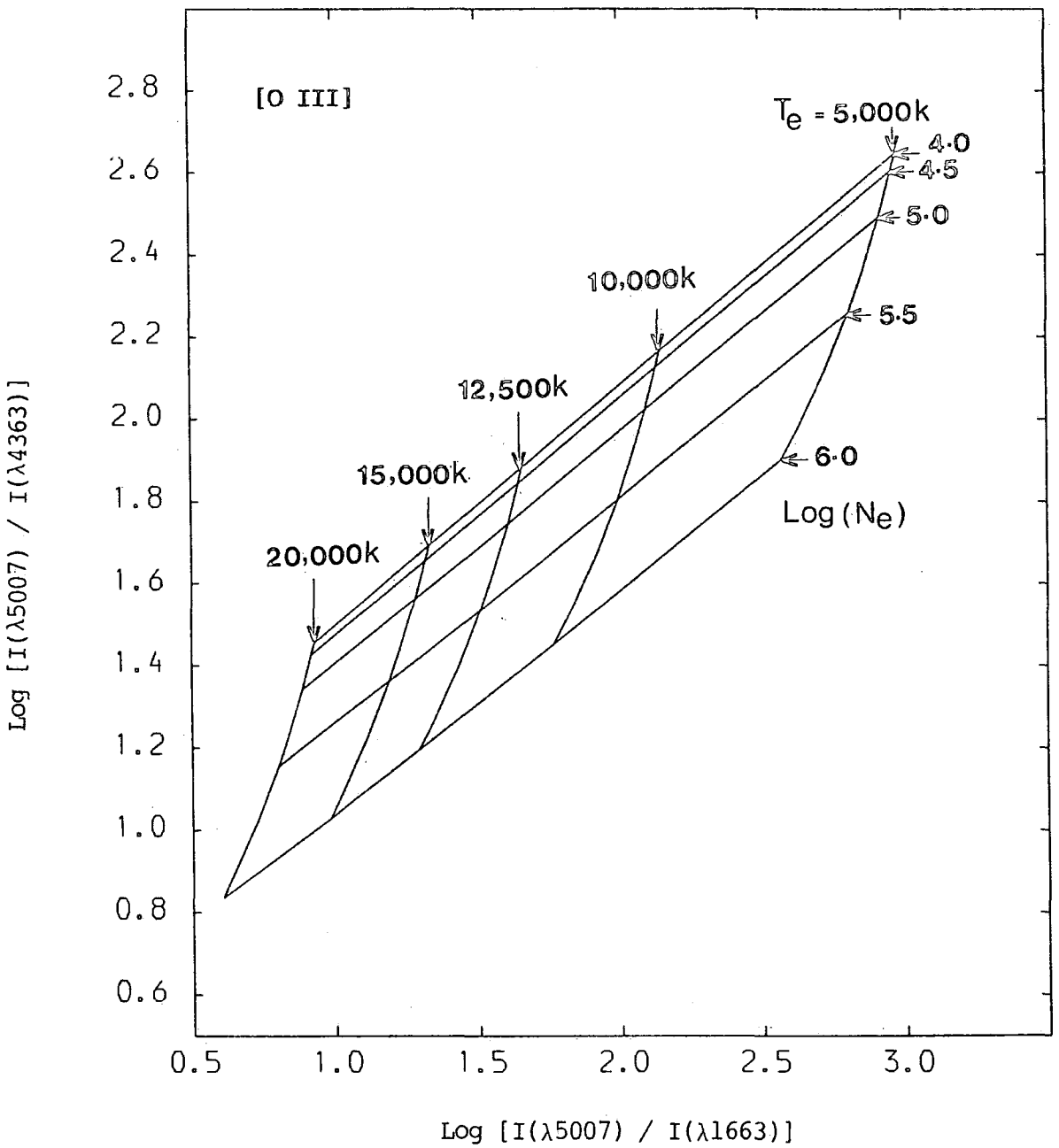

Figure (3-16): I(λ5007)/I(λ4363) versus I(λ5007)/I(λ1663) in [O III] as a density and temperature discriminate.

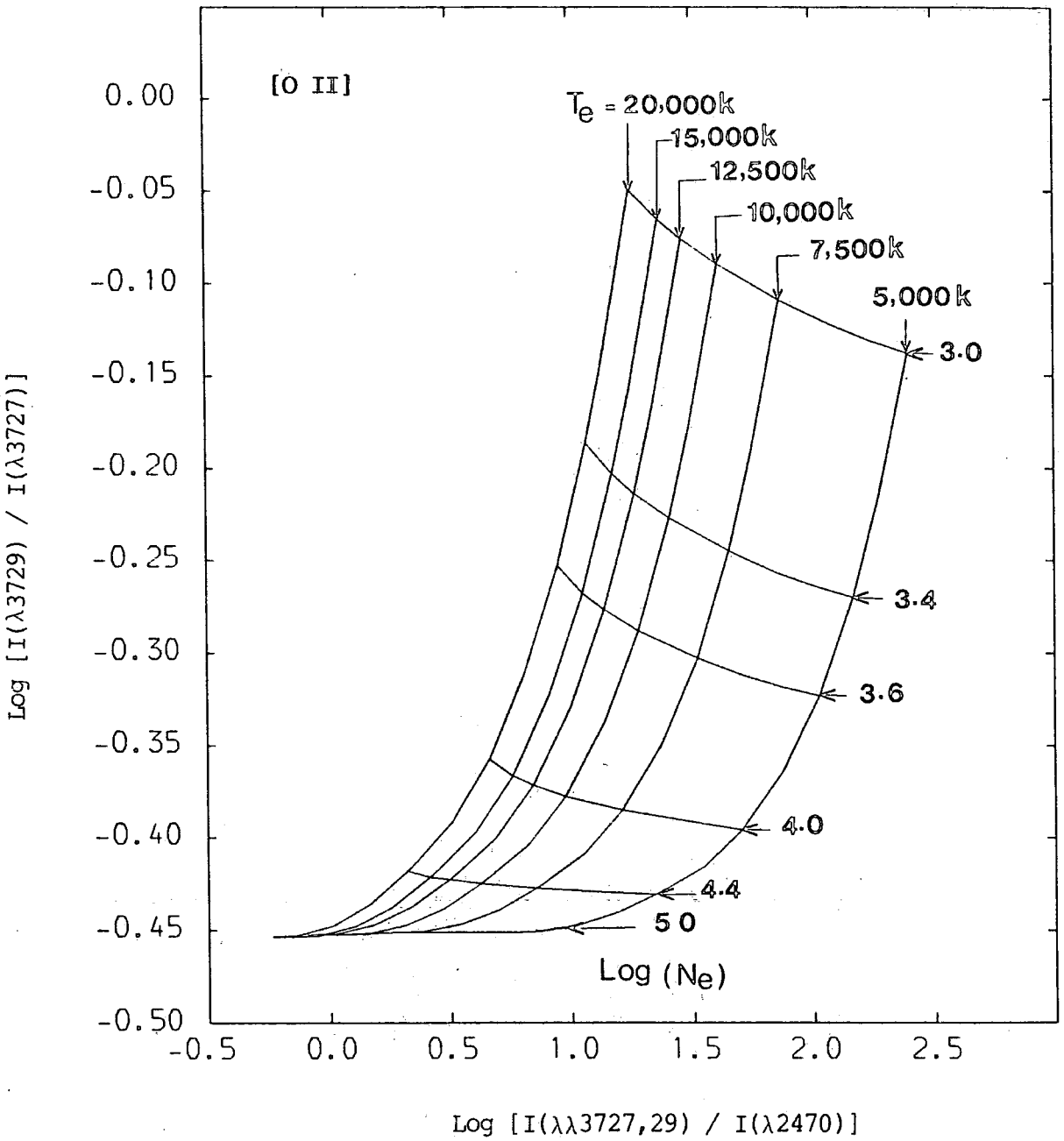

Figure (3-17): I(λ3729)/I(λ3727) versus I(λλ3727,29)/I(λ2470) in [O II] as a density and temperature discriminate.

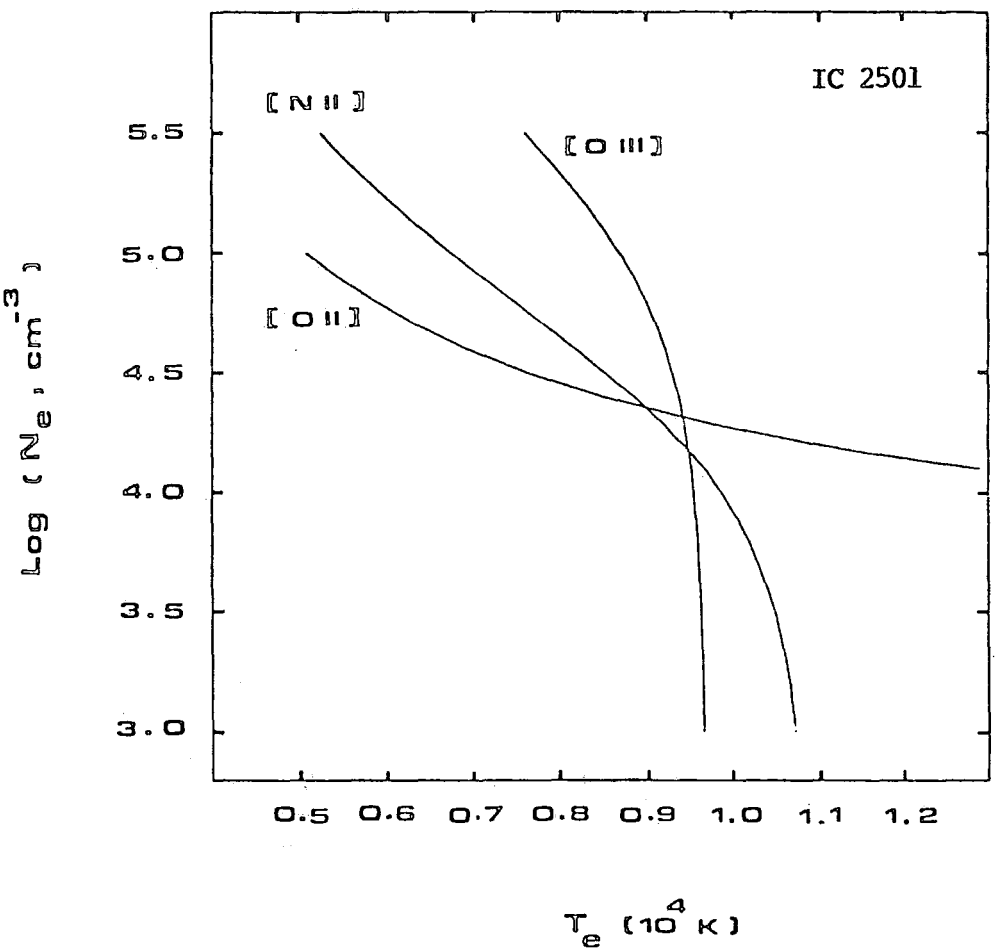

Figure (3-18): Diagram for density and temperature diagnostics. Figure from Paper II.

CHAPTER (4)

CENTRAL STARS OF THE PLANETARY NEBULAE SwSt 1 AND IC 2501

4.1 NEBULAR CONTINUUM EMISSION COEFFICIENTS

In Chapter 1, we have measured the sum of the nebular emission and the emission from the central stars of SwSt 1 and IC 2501. In this section we shall compute the nebular continuum emission coefficients. This will enable us, in the next section, to determine the stellar continuum fluxes. From these fluxes we can gain some information on the central stars.

In the ultraviolet and optical spectral regions, the most important processes that produce quanta in the continuum are : (1) recombination of electron and ions to the second and higher levels of hydrogen and excited levels of helium; (2) free-free emissions; and (3) the H I two-photon emission.

Following Brown and Mathews (1970), we define an effective emission coefficient $\gamma_{eff}(cm^3\ s^{-1})$ by the expression

$$\varepsilon(\text{nebcont})\ d\nu = N_e\ N(H^+)\ \gamma_{eff}\ d(h\nu)\ , \qquad (4.1)$$

where ε(nebcont) is the nebular continuum emission per cm^3 in all directions. Let γ(H I), γ(He I), γ(He II), and γ(2q,H I) denote, respectively, the coefficients for H I, He I, He II, and two-photon emissions. Then

$$\gamma_{eff} = \gamma(\text{H I}) + \gamma(\text{2q,H I}) + y'\ \gamma(\text{He I}) + y''\ \gamma(\text{He II})\ , \qquad (4.2)$$

where y' and y" are defined by equation (3.34).

For hydrogenic ions, the total emission coefficient for bound-free and free-free transitions is [Seaton (1960); Aller (1984)]

$$\gamma(\text{bf+ff}) = \frac{K_o\, Z^4}{T_e^{3/2}} \exp(h\nu/kT_e) \left[\sum_{n_o}^{\infty} g_{II} \exp(X_n)/n^3 + \bar{g}_{III}\, kT_e/2hR_oZ^2 \right]. \qquad (4.3)$$

where $K_o = 3.261 \times 10^{-6}$ ($cm^3\ s^{-1}\ K^{3/2}$), $R_o = 3.288 \times 10^{15}$ (s^{-1}), $X_n = Z^2\ h\ R_o\ /\ n^2\ k\ T_e$, and n_o is the lowest level to which one can observe recombination at a frequency ν [it is such that $\nu_n (= R_o\ Z^2/\ n^2)$ is less than ν]. g_{II} and $\bar{g}_{III}$ are of order unity and may be represented by the asymptotic expansions [eqs. (2.4) and (2.38) of Seaton (1960)].

Equation (4.3) can be used to calculate γ(H I) by setting Z=1 and γ(He II) by setting Z=2. To a first approximation, we may replace γ(He I) by γ(H I). In order to obtain the correct values of γ(He I), we must consider the ℓ degeneracy (because the He I levels are nonhydrogenic). For each (n,ℓ) level, we may express γ(He I) in terms of the atomic absorption coefficient that can be calculated by equations given by Peach (1967). Such calculations have been made by Aller (1984) for $T_e(10^4K)$ = 0.5, 1.0, 1.5, and 2.0.

The H I two-photon emission process has been discussed by Seaton (1960). The emission coefficient for case B of Baker and Menzel is

$$\gamma(2q,\text{H I}) = \frac{\gamma_o(2q,\text{H I})}{1 + 0.6 \times 10^{-4}\ N_e}\ , \qquad (4.4)$$

where $\gamma_o(2q,\text{H I})$ may be approximated by the expression

$$\gamma_o(2q,\text{H I}) = 4.59 \times 10^{-0.68}\ (\nu/\nu_H) \left[\ 0.75\ (\nu/\nu_H) - (\nu/\nu_H)^2\ \right]^{0.55} \qquad (4.5)$$

(ν_H being the frequency at the H I Lyman limit).

Table (4-1) gives the values of γ(H I), $\gamma(2q,\text{H I})$, γ(He I), γ(He II), and γ_{eff} computed for physical conditions found in SwSt 1 (T_e = 8900 K; $N_e = 1.1 \times 10^5\ cm^{-3}$; y' = 0.072; y" = 0.0). Similar computations could be made for IC 2501.

In general, the H I Balmer continuum emission is the most important contributor at longest wavelengths; the HI two-photon emission becomes more important at shortest wavelengths. The contribution of Helium to the nebular continuum emission is of second order. The most interesting feature in the nebular continuum emission is the jump at the head of the Balmer limit ($\lambda \approx 3646$ Å), produced by recombinations of electrons and ions on the second level of hydrogen.

4.2 CONTINUUM FLUXES

Tables (4-2) and (4-3) give the observed total flux $I_\lambda(tot)$, corrected for reddening (using c = 0.50 for both nebulae), for the wavelengths at which ultraviolet and optical observations have been made. The UV fluxes have been measured from the averaged and merged IUE spectra (the spectra are weighted by their exposure times) by means of visual inspection. The optical continuum measurements are from Tables (1-2) and (1-3). In the case of SwSt 1, the fluxes at $\lambda=\lambda_B$ =4329Å and $\lambda=\lambda_V$ =5464Å have been derived from measurements of the B and V magnitudes using the relations of Allen (1973):

$$\text{Log } [I_{\lambda_B}(tot)] = - 0.4\ B + 1.131\ c - 8.18\ , \qquad (4.6)$$

and

$$\text{Log } [I_{\lambda_V}(tot)] = - 0.4\ V + 0.876\ c - 8.42. \qquad (4.7)$$

The corresponding nebular, $I_\lambda(nebcont)$, and stellar, $I_\lambda(star)$, continuum fluxes are also given in Tables (4-2) and (4-3). The nebular fluxes have been computed using the relation

$$I_\lambda(nebcont) = (\lambda_\beta / \lambda^2)\ [\gamma_{eff} / \alpha_{eff}(H\beta)]\ \ I(H\beta)\ , \qquad (4.8)$$

with $I(H\beta) = 6.74 \times 10^{-11}$ in SwSt 1 and 7.24×10^{-11} in IC 2501 (all fluxes are in units of ergs $cm^{-2}\ s^{-1}$). When computing the values of γ_{eff} , we include the contributions of the heavy elements. The effect

of the heavy elements is in fact negligible. The stellar continuum fluxes are derived from

$$I_\lambda(\text{star}) = I_\lambda(\text{tot}) - I_\lambda(\text{nebcont}) \qquad (4.9)$$

These continuum fluxes have been shown in Figure (5) of Paper I and Figure (2) of Paper II. It is seen that the nebular continuum dominates in the optical region, the stellar in the ultraviolet region.

4.3 EFFECTIVE TEMPERATURES

The determination of the effective temperature of the central stars of planetary nebulae is still a controversial subject, although substantial progress has been made in recent years. At present time, there are a number of methods of determining the effective temperatures. The most important are : (1) the colour temperature; (2) Zanstra method; and (3) Energy-Balance method (or Stoy temperature).

Method (3) has been generalized by Preite-Martinez and Pottasch (1983). It may be applied for those objects in which most of the collisionally-excited lines are seen in their spectra. For application to SwSt 1 and IC 2501, we shall consider only methods (1) and (2).

4.3.1 Colour

The colour temperature, T_c, of the central star of the nebula is determined by comparing the shape of the stellar continuum flux between the ultraviolet and visual spectral regions with either a blackbody or a model atmosphere. However, a blackbody and the three series of model atmospheres in the literature [Hummer and Mihalas (1970); Wesemael et al. (1980); Mendez et al. (1981)] all predict approximately the same shape between λ = 1300 Å and λ = 6000 Å. We shall consider the central star to radiate like a blackbody.

For a star of radius R_S the stellar flux per unit wavelength observed at the distance D of the Earth is, after correction for reddening,

$$I_\lambda(\text{star}) = 3.74 \times 10^{27} (R_S/D)^2 \lambda^{-5} [\exp(1.43883 \times 10^8/\lambda T_c) - 1]^{-1} \quad (4.10)$$

with λ in Å and T_c in K.

In Figures (4-1) and (4-2), we compare the measured continuum fluxes from the central stars of SwSt 1 [Table (4-2)] and IC 2501 [Table (4-3)] with those calculated using equation (4.10). The stellar values are :

$$T_c = 30{,}000 \text{ K} \; ; \; (R_S/D)^2 = 2.31 \times 10^{-22} \quad \text{(in SwSt 1)} \quad (4.11)$$

and

$$T_c = 60{,}000 \text{ K} \; ; \; (R_S/D)^2 = 9.94 \times 10^{-24} \quad \text{(in IC 2501)} \quad (4.12)$$

The ratios $(R_S/D)^2$ have been determined by normalizing $I_\lambda(\text{star})$ at $\lambda = \lambda_1 = 1400$ Å :

$$\lambda_1 I_{\lambda_1}(\text{star}) = 7.56 \times 10^{-9} \text{ erg cm}^{-2} \text{ s}^{-1} \quad \text{(in SwSt 1)} \quad (4.13)$$

$$\lambda_1 I_{\lambda_1}(\text{star}) = 2.13 \times 10^{-9} \text{ erg cm}^{-2} \text{ s}^{-1} \quad \text{(in IC 2501)} \quad (4.14)$$

We shall see below that the Zanstra temperatures of the central stars of SwSt 1 and IC 2501 are consistent with these values of T_c.

4.3.2 Zanstra

The Zanstra method [Zanstra (1931)] has been discussed by Harman and Seaton (1966) and HSAL. The principle of this method is to count the number of ionizing photons from the central star by measuring the nebular flux in a single recombination line or in the radio continuum. This number of photons may then be interpreted in terms of a temperature if the continuum flux from the central star in a given wavelength band is known.

Let $I(\lambda_\ell)$ be the observed flux, corrected for reddening, in a nebular line at wavelength λ_ℓ due to recombination of an ion $X^{+(m+1)}$. Let $I_\lambda(\text{star})$ be measured at $\lambda=\lambda_1$, and assume that all stellar photons with $\nu \geq \nu_o$, where $h\nu_o$ is the ionization potential of X^{+m}, are absorbed in ionization of X^{+m}. Then

$$\frac{I(\lambda_\ell)}{\lambda_1 \, I_{\lambda_1}(\text{star})} \; \frac{\lambda_\ell}{\lambda_1 \, \xi} \; \frac{\alpha_B(X^{+m})}{\alpha_{\text{eff}}(\lambda_\ell)} = G[T_z(X^{+m})] \tag{4.15}$$

where the geometrical factor ξ ($= \Omega/4\pi$, here Ω is the solid angle filled by the nebula as seen from the central star) is 1 for a shell nebula and about 0.3 for a ring nebula, $\alpha_B(X^{+m})$ is the coefficient for recombination to all excited states of X^{+m}, $\alpha_{\text{eff}}(\lambda_\ell)$ is the effective recombination coefficient for λ_ℓ, and

$$G[T_z(X^{+m})] = \frac{\int_{\nu_o}^{\infty} \nu^{-1} \, I_\nu(\text{star}) \, d\nu}{I_{\nu_1}(\text{star})} \tag{4.16}$$

is a dimensionless number which depends on the spectral distribution of the stellar radiation and hence on the temperature T_z of the star. If the star radiates like a blackbody, then (cf. HSAL)

$$G[T_z(X^{+m})] = \frac{\exp(u_1) - 1}{(u_1)^3} \sum_{n=1}^{\infty} n^{-3} \exp(-nu_o) \, [nu_o(nu_o+2)+2] \, . \tag{4.17}$$

where

$$u_1 = h\nu_1/KT_z = 1.43883 \times 10^8 / \, [\lambda_1(\text{Å}) \; T_z(\text{K})]. \tag{4.18}$$

These formulae may be applied to nebulae which are optically thick in the H I (λ_o=911.8Å) and He I (λ_o=504.6Å) or He II (λ_o =227.9Å) continua using the lines Hβ and He I λ5876 or He II λ4686. Table (4-4)

gives the values of $G[T_z(H\ I)]$, $G[T_z(He\ I)]$, and $G[T_z(He\ II)]$ calculated using equation (4.17) with $\lambda_1 = 1400$ Å. In equation (4.15), the ratios of the recombination coefficients depend only weakly on N_e and change slowly with T_e. For $N_e = 10^4$ cm^{-3}, they are represented fairly well by the expressions:

$$\alpha_B(H^o) / \alpha_{eff}(H\beta\ \lambda4861) = 8.498\ [T_e/10^4]^{0.062} \qquad (4.19)$$

$$\alpha_B(He^o) / \alpha_{eff}(He\ I\ \lambda5876) = 5.477\ [T_e/10^4]^{0.323} \qquad (4.20)$$

$$\alpha_B(He^+) / \alpha_{eff}(He\ II\ \lambda4686) = 4.410\ [T_e/10^4]^{0.274} \qquad (4.21)$$

According to Harman and Seaton (1966), the criteria for deciding whether or not the nebula is optically thick to the ionizing radiation are as follows :

(1) the nebula is optically thick in the H I continuum if the [O I] nebular lines are measurable.

(2) the nebula is optically thick in the He I continuum if monochromatic He I images are smaller than H I images. An alternative criterion is that He II lines are absent and that $N(He^+)/N(H^+) \leq 0.11$.

(3) the nebula is optically thick in the He II continuum if He I lines are measurable and $N(He^{+2}) / [N(He^{+2}) + N(He^+)] \leq 3/4$. If He I lines have not been observed, then the criterion is that $N(He^{+2})/N(H^+) \leq 0.12$.

When temperature determinations are carried out by this method, it is found that $T_z(HI)$ and $T_z(He\ I)$ are consistent to within the observational uncertainties, but the values of $T_z(H\ I)$ and $T_z(He\ II)$ are often different; the latter value is consistently higher than the former.

The most straightforward explanation of the discrepancy between the values of T_z(H I) and T_z(He II) is that the nebula may be optically thin in the H I Lyman continuum. If this is the case, then T_z(H I) will only be a lower limit and T_z(He II) will be a better approximation. An alternative explanation is that the blackbody assumption may be not valid for calculating the total number of quanta emitted beyond the He II ionization limit. The use of a model atmosphere with emission in excess of that of a blackbody shortward of λ227.8 would result in T_z(H I) being the more correct value and T_z(He II) being excessively high.

Pottasch (1983) has shown that whether a blackbody or a model atmosphere is assumed, the same temperature T_z(H I) is obtained; but the use of the atmospheric models of Hummer and Mihalas give a higher value of T_z(He II) than a blackbody atmosphere, while the models of Wesemael et al. and of Mendez et al. give much lower value of T_z(He II). Until more reliable model atmospheres become available, it would be better to avoid use of T_z(He II).

The Zanstra temperature may also be determined from a comparison of the radio flux at a frequency, ν_R, at which the nebula is optically thin and the stellar continuum flux at any wavelength. Equating the number of stellar quanta with $\lambda \leq 911.8$ Å absorbed by the nebula to the number of recombination to all excited states of H^o, He^o, and He^+ and using equation (3.29), we obtain

$$\frac{I_{\nu_R}(\text{f.u.})}{\lambda_1 \, I_{\lambda_1}(\text{star})} \; \frac{2.06 \times 10^{-3} \, A_{He}}{\xi \, \lambda_1} = G[T_z(\text{Radio})] = G[T_z(H^o)] \, , \qquad (4.22)$$

where

$$A_{He} = \frac{T_e^{-0.3} \; [\, 1 + 1.05\, y' + 5.97\, y'' \,]}{(1+y') \, [17.72 + \ln(T_e^{3/2}/\nu_R)] + 4y'' \, [17.03 + \ln(T_e^{3/2}/\nu_R)]} \, . \qquad (4.23)$$

with T_e in K and ν_R in Hz. If y" = 0.0, then

$$[A_{He}]^{-1} \approx T_e^{0.3} [\ 17.72 + \ln(T_e^{3/2}/\nu_R)\ ] . \qquad (4.24)$$

We take T_e = 8900K in SwSt 1 and T_e = 9400K in IC 2501. For both nebulae we use c=0.5, ξ=1, and $\lambda_1 I_{\lambda_1}$(star) from (4.13) and (4.14), with λ_1 = 1400Å. The line fluxes (erg cm^{-2} s^{-1}), corrected for reddening, are : I(Hβ) = 6.74×10^{-11} and I(He I λ5876) = 6.81×10^{-12} in SwSt 1; I(Hβ) = 7.24×10^{-11} and I(He II λ4686) = 6.31×10^{-13} in IC 2501. The radio fluxes are: 0.207 (f.u.) at 15.035 GHz for SwSt 1 and 0.236 (f.u.) at 14.7 GHz for IC 2501. We obtain:
G(H I) = 0.261, G(He I) = 0.020, and G(Radio) = 0.333 for SwSt 1, and G(H I) = 1.000, G(He II) = 0.0043, and G(Radio) = 1.314 for IC 2501. Comparing these values with those given in Table (4-4), we obtain the Zanstra temperatures of the central stars of SwSt 1 and IC 2501. The results are listed in Table (4-5).

Due to small differences in the measured values of the stellar continuum fluxes, the results in Table (4-5) differ slightly from those given in Papers I and II; the present values are more accurate. SwSt 1 appears to satisfy criteria for complete absorption in the continua of H I and of He I. IC 2501 is optically thick in the H I and He II continua. The values of T_c and T_z obtained for IC 2501 are in good agreement. In the case of SwSt 1, the Zanstra temperatures are slightly higher than the colour temperature obtained from the best fit to the stellar ultraviolet continuum flux.

4.3.3 Adopted Temperatures

For the temperature of the central star of SwSt 1 we adopt a mean value of T_s = 35,000 K. This value conforms with the "very low excitation" (VLE) classification of the nebula. However, in subsequent discussion, we shall recognize the uncertainties involved. For the exciting star of IC 2501, we adopt T_s = 62,000 K.

4.4 DISTANCES

The determination of the distances of planetary nebulae has been discussed in many papers [Shklovsky (1956); Seaton (1966); Cahn and Kaler (1971); and others]. In all of these, it is assumed that all planetary nebulae are optically thin to Lyman continuous radiation from the central stars, so that the ionized hydrogen mass M_i is equal to the total nebular mass M_n, and that they are all have the same value of M_n. Figure (4) of Pottasch (1983) shows the distribution of M_i with electron density. It is clear that M_i ranges from about 6×10^{-4} $M_\odot$ for NGC 4997 to almost 1 $M_\odot$ for NGC 6781. The assumption of a constant ionized mass is therefore a poor approximation. According to the discussion of section (4-3), both SwSt 1 and IC 2501 are optically thick to H I Lyman continuum. This is confirmed by the fact that M_i(SwSt 1 or IC 2501) << M_i(optically thin PN) (see below). We should therefore avoid use of these methods which seem to give reasonable distances only to optically thin planetary nebulae.

From the proper motion statistics, Gudworth (1974) obtained a distance scale for optically thick nebulae. We consider this scale to be only a rough approximation, since Gudworth assumed that the absolute Hβ flux is constant. Assuming uniform nebular luminosities, Acker (1978) has computed distances of optically thick nebulae. Daub (1982) has pointed out that Acker's distances have been inaccurately determined.

We consider that the most reliable distance scale, at least for the present time, for both optically thin and thick planetary nebulae is that of Daub (1982). He finds satisfactory data for 14 nebulae and uses them to establish the relation between M_i and the observed quantity θ^2/S, where θ(arc-sec) is the angular diameter of the nebula and S(f.u.) the flux density at 5 GHz. For optically thick planetary nebulae, with Log $(\theta^2/S) < 3.65$, he gives the following relations:

$$\log \left[(M_i/M_\odot) \{f(t)/\epsilon\}^{1/2} \right] = \log (\Theta^2/S) - 4.50 \; ; \tag{4.25}$$

$$f(t) = t^{-1/2} \left[1 + 0.110 \ln(t^{3/2}) \right] \; ; \tag{4.26}$$

$$D = 324 \left[\Theta/S^3 \right]^{1/5} \text{(pc)} \; ; \tag{4.27}$$

$$R_i = 7.85 \times 10^{-4} \left[\Theta^2/S \right]^{3/5} \text{(pc)} \; . \tag{4.28}$$

where ϵ is the filling factor , $t = T_e(10^{-4}$ K) , D is the distance to the nebulae, pc = 3.086×10^{18} cm, and R_i is the radius of the ionized nebular shell; $R_i \approx 0.12$ pc when a nebula first becomes optically thin. For a typical optically thin nebula, $M_i/M_\odot \approx 0.14$.

We take Θ = 0.8(arc-sec), S = 0.148(f.u.), t = 0.89, and ϵ = 1 for SwSt 1 and Θ = 2.0(arc-sec), S = 0.261(f.u.), t = 0.94, and ϵ = 1 for IC 2501. We then obtain:

D(pc) = 975, R_i(pc) = 0.002 , and $M_i(M_\odot)$ = 0.0001 for SwSt 1, and

D(pc) = 833, R_i(pc) = 0.004 , and $M_i(M_\odot)$ = 0.0005 for IC 2501.

We note that the values of M_i are very small. In the case of SwSt 1, the reason could be due to the fact that the nebula is optically thick at 5 GHz for which equation (4.25) can not be expected to give correct results. Use of the expression

$$M_i(M_\odot) = 11.06 \; I(H\beta) \; D^2 \; t^{0.88} \; / \; N_e(cm^{-3}) \tag{4.29}$$

[Pottasch (1983)], where I(Hβ) is expressed in units of 10^{-11} erg cm^{-2} s^{-1} and D in Kpc, yields $M_i(M_\odot)$ = 0.0006 for SwSt 1 and $M_i(M_\odot)$ = 0.003 for IC 2501. We conclude that the ionized hydrogen mass is small in both nebulae. The very small value of M_i, obtained for SwSt 1, is probably due to the fact that the nebula is very young; a substantial amount of its mass has not yet been ejected. Fortunately, our subsequent analysis does not require a determination of the ionized hydrogen mass.

4.5 ANALYSIS OF THE Si IV P CYGNI LINE PROFILE OBSERVED IN THE IUE SPECTRA OF SwSt 1

The IUE spectra of SwSt 1 [Figures (1-5) and (1-6)] show P Cygni type profiles of N V λ1240, Si IV λ1397, C IV λ1549, and C III λ2297. These profiles provide a strong evidence for the presence of a stellar wind. Consequently, the central star of SwSt 1 is ejecting material into the interstellar medium. Information on the mass-loss rate from the central star of SwSt 1 may be obtained from the analysis of the unsaturated Si IV resonance doublet profile. We shall try to analyse this feature assuming it to be produced in a stellar wind with no underlying photospheric absorption using the Sobolev approximation of line formation for a two-level atom in a rapidly expanding atmosphere. Since our analysis requires the determination of the stellar radius, we first estimate this parameter.

4.5.1 The Stellar Radius

If we know the absolute bolometric magnitude, M_{bol}, of the central star of SwSt 1, we can use the following relations to determine the star's luminosity, L, and radius, R_S :

$$\log (L/L_\odot) = 0.4 \left[M_{\odot,bol} - M_{bol}\right] \ ; \qquad (4.30)$$

$$R_S/R_\odot = (L/L_\odot)^{1/2} \ / \ (T_S/T_\odot)^2 \ . \qquad (4.31)$$

The solar values are : $M_{\odot,bol} = +4.76$ [Code et al.(1976)]; $T_\odot = 5770K$, $L_\odot = 3.82 \times 10^{33}$ erg s^{-1}, and $R_\odot = 6.96 \times 10^{10}$ cm [Allen (1973)]. From section (4.3.1) we have $T_S = 35000K$.

The bolometric magnitude is not directly observed, but it can be estimated from the absolute visual magnitude, M_V, and visual bolometric correction, BC_V :

$$M_{bol} = M_V + BC_V \ . \qquad (4.32)$$

According to Bradley and Morton (1969), the bolometric correction of a star is related to that of the sun by the expression

$$BC = BC_{\odot} - 10 \log(T_S/T_{\odot}) + 2.5 \log\left[\int I_\lambda(\text{star}) S_\lambda \, d\lambda \Big/ \int I_\lambda(\text{sun}) S_\lambda \, d\lambda\right] \quad (4.33)$$

where $BC_{\odot} = -0.07$ [Code et al. (1976)] and the filter sensitivity function S_λ has been tabulated by Matthews and Sandage (1963). M_V can be found from the unreddend visual magnitude, V_o, and distance D:

$$V_o - M_V = 5 \log[D(pc)] - 5. \quad (4.34)$$

With a reddening constant c = 0.5, we have $E_{B-V} = 0.34$ and $A_V = 1.09$. The observed visual magnitude is V = 11.9, so that $V_o = V - A_v = 10.81$, and with a distance D = 975 pc, we have $M_V = 0.86$. For a star with $T_S = 35000K$, the bolometric correction is $BC_V = -3.10$, so $M_{bol} = -2.23$. The estimated luminosity is $L = 630\ L_{\odot}$ and hence $R_S = 0.68\ R_{\odot}$. It is seen that the ratio $(R_S/D)^2 = 2.47 \times 10^{-22}$ is in good agreement with the value (2.31×10^{-22}) used to obtain the colour temperature of the central star. The luminosity and temperature may be checked by the theoretical evolutionary tracks. Renzini (1979) gives a discussion of the tracks calculated by Paczynski (1971). From Renzini's Figure 1, we see that the central star of SwSt 1 can be located close to the region expected for a central star with mass $M_S = 0.55\ M_{\odot}$. We conclude that the derived values of T_S, L, and R_S are reasonable.

4.5.2 Profile Fitting

The full lines of Figure (4-3) show the profile of the Si IV feature observed in the spectrum of SwSt 1 (SWP 10035). We plot the ratio F_λ/F_c as a function of λ, where F_λ is the observed flux and F_c a smoothed flux for the continuum. The wavelength scale was taken to be such that the measured

wavelength of the nebular emission in CIII] is at λ=1907.4Å (this being the weighted mean for the CIII] doublet at $\lambda\lambda$ 1906.7 and 1908.7). The SiIV feature is due to the transition 3s ^2S - 3p $^2P^o$ and has a blue component ($^2S_{1/2}$ - $^2P^o_{3/2}$) at λ_b = 1393.73Å and a red component ($^2S_{1/2}$ - $^2P^o_{1/2}$) at λ_r = 1402.73Å. The corresponding oscillator strengths are f_b = 0.447 and f_r = 0.223, so that f_d = 0.67 and λ_d = 1396.73Å for the doublet [Castor et al. (1981); to be refered to as CLS]. The positions and relative gf values of the two components are indicated in Figure (4-3). It is seen that the components of the doublet are partially resolved. The overall shape of the feature is identical to the unsaturated SiIV profile observed in NGC 6543 (CLS).

In order to compute the theoretical profile it is necessary to know the velocity law and radial optical depth of the expanding envelope. Let r be the distance from the centre of the star, $x = r/R_s$, V(r) the velocity in the stellar wind, $V_\infty = V(r=\infty)$ the terminal velocity, and $w = V(r)/V_\infty$. Following Castor and Lamers (1979), we use

$$w(x) = (1 - 1/x)^\beta \tag{4.35}$$

for the variation of velocity with radius, and

$$\tau_{rad}(w) = \tau_{tot}\ (1+\gamma)\ (1-w)^\gamma \tag{4.36}$$

for the variation of radial optical depth with velocity. β, γ, and τ_{tot} are parameters.

Calculations have been made for each component of the doublet using the Sobolev approximation and numerical method described by Castor (1970) and CLS. This method gives results in excellent agreement with those obtained by the method of Lucy (1971). Since the radiation scattered by the blue component in the direction of the observer can be scattered again by the red component, simple addition or superposition

of the two separately calculated components does not give the correct doublet profile. We, therefore, use the method of Castor and Lamers (1979) to treat the interaction between the two components. To compare the computed doublet profiles with the observed one, we take the terminal velocity V_∞ as a parameter.

A large number of profiles were computed and the following parameters were finally adopted:

$$\left.\begin{aligned} V_\infty &= 2000(\pm 100)\ \text{Km/s} \\ \tau^b_{tot} &= 1.2 \quad ; \quad \tau^r_{tot} = 0.4 \\ \beta &= 1.0 \quad ; \quad \gamma = 1.0 \end{aligned}\right] \qquad (4.37)$$

(τ^b_{tot} is for the blue component and τ^r_{tot} for the red component). The dashed curves in Figure (4-3) show the profile computed with these parameters. It is seen that the observed and theoretical profiles are in good agreement. The adopted velocity law , $\beta = 1$, and optical depth, $\gamma = 1$, are those of CLS.

4.5.3 Column and Number Densities

The column density N_i (cm^{-2}) and number density n_i (cm^{-3}) of the absorbing ions in the lower state of the transition are related to τ_{tot} by (see CLS)

$$N_i = \int_{R_S}^{\infty} n_i \, dr = \frac{mc}{\pi e^2} \frac{V_\infty}{f\lambda_o} \tau_{tot}$$

$$= 3.77 \times 10^{14} \frac{V_\infty(\text{Km/s})}{f\ \lambda_o(\text{Å})} \tau_{tot} \qquad (4.38)$$

where f is the oscillator strength of the transition and λ_o the rest wavelength of the line. Taking the values of f and λ_o from section (5.4.2)

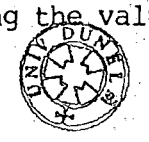

and parameters V_∞ and τ_{tot} from (4.37), we obtain $N_i = 1.5 \times 10^{15}$ cm^{-2} for the blue component of the Si IV doublet, and $N_i = 1.0 \times 10^{15}$ cm^{-2} for the red component.

For our adopted velocity law and optical depth, CLS have shown that at a representative point in the atmosphere taken to be at x = 2, corresponding to w = 0.5, one has $\tau_{tot} = W_1 / 0.3$, where

$$W_1 = [c/\lambda_o V_\infty]^2 \int [(F_\lambda/F_c)-1] \, (\lambda-\lambda_o) \, d\lambda \qquad (3.39)$$

is the observed first order moment. In the case of optically thin lines, Surdej (1982) shows that the moment W_1 for an unresolved doublet is the same as that for a single line transition provided that λ_o and f are replaced by λ_d and f_d in equations (4.38) and (4.40). From the observed Si IV profile we estimate $W_1 = 0.28$ and hence $\tau_{tot} = 0.93$. Use of equation (3.38) yields $N_i = 0.75 \times 10^{15}$ cm^{-2}. To allow for all possible uncertainties in the fitting procedure and measurement of W_1, we adopt

$$N_i = (1.1 \pm 0.4) \times 10^{15} \text{ cm}^{-2}. \qquad (3.40)$$

The optical depth used in Sobolev theory [see Castor (1979)] is

$$\tau_{rad}(V) = \frac{\pi e^2}{mc} (f\lambda_o) \, n_i \, / \, (dV/dr) \, , \qquad (4.41)$$

or, using equation (4.35),

$$\tau_{rad}(w) = \frac{\pi e^2}{mc} (f\lambda_o) \, n_i \, \frac{R_s \, x^2 \, w}{V_\infty \, \beta \, w^{2-1/\beta}} \qquad (4.42)$$

Eliminating $\tau_{rad}(w)$ between (4.35) and (4.42) and using (4.38), we obtain

$$n_i = \frac{N_i}{6.96 \times 10^{10}} \, \frac{(1+\gamma) \, (1-w)^\gamma \, \beta \, w^{2-1/\beta}}{(R_s/R_\odot) \, x^2 \, w} \, . \qquad (4.43)$$

With our adopted parameters and for the case x = 2 (w = 0.5), we obtain

$$n_i = (5.8 \pm 2.0) \times 10^3 \text{ cm}^{-3}. \qquad (4.44)$$

4.5.4 Mass-Loss Rate

The mass-loss rate, $\dot{M}$, is given by the equation of mass continuity,

$$\dot{M} = 4\pi r^2 V(r) \rho(r)$$

$$= 4\pi R_S^2 x^2 w V_\infty \mu M_H n(H) \qquad (4.45)$$

where $\rho(r)$ is the mass density in gram/cm^3, μ is the mean atomic weight per H atom, and M_H and $n(H)$ are, respectively, the mass and number density of H atoms. For Si IV ^2S - $^2P^o$ transition, the lower level is the ground level. We may define

$$n(Si^{+3}) = n_i = I A n(H) , \qquad (4.46)$$

where $I = n(Si^{+3})/n(Si)$ is an ionization factor and $A = n(Si)/n(H)$ is an abundance factor. From (4.45) and (4.46), we have

$$\dot{M}(M_\odot/yr) = \frac{2.20\times10^{-22}}{I\ A} (\mu/1.42) (R_S/R_\odot)^2 x^2 w V_\infty(Km/s) n_i(cm^{-3}). \qquad (4.47)$$

Taking x=2 (w=0.5), μ = 1.42, $R_S/R_\odot$ = 0.68, V_∞ = 2000 Km/s, and the value of n_i from equation (4.35), we obtain

$$\dot{M} = \frac{(2.4\pm0.8) \times 10^{-15}}{I\ A} (M_\odot/yr) . \qquad (4.48)$$

Assuming the abundances in the stellar wind to be the same as those in the solar photosphere, we have $A=4.27\times10^{-5}$ [Lambert and Luck (1978)]. For the central star of NGC 6543, CLS estimate $I=8.0\times10^{-4}$ and T_S=43,000K. For ζ Puppis, Lamers and Morton (1976) estimate $I=2.0\times10^{-3}$ while Remie and Lamers (1982) obtain T_S=35,500K. Adopting $I=2.0\times10^{-3}$ for SwSt 1 (T_S=35,000K) , we obtain

$$\dot{M} = (2.8\pm1.0) \times 10^{-8} (M_\odot yr^{-1}). \qquad (4.49)$$

If our assumptions about the factors A and I are valid then the mass

loss rate from the central star of SwSt 1 is probably correct to within the included error bar.

4.5.5 Discussion of the Terminal Velocity and Mass-Loss Rate

It is of interest to compare our estimated values of V_∞ and $\mathring{M}$ for the central star of SwSt 1 with those obtained for early-type stars. Castor, Abbott, and Klein (1975) have shown that the outflow of material observed in many early-type stars is a result of direct momentum input into the gas through the absorption of radiation by strong resonance and subordinate lines of representative ions. In their theory " radiation-driven stellar winds ", some analytical expressions for the velocities and mass-loss rates have been derived. The expression for the terminal velocity may be written as [Abbott (1978)]

$$V_\infty = K\, V_{esc} = K\, [2GM_S(1-\Gamma_e)/R_S]^{1/2} \qquad (4.50)$$

where $\Gamma_e = 2.45 \times 10^{-5}\ (L/L_\odot) / (M_S/M_\odot)$ is the ratio of radiation to gravity force in the case of free electron scattering and V_{esc} is the effective surface escape velocity [the standard gravitational binding energy is reduced by the factor $(1-\Gamma_e)$ to account for the outward force of the continuum radiation pressure]. Abbott (1978) estimated the K factor to be ~3 for O, B, A, and WR stars, while Lamers (1983) adopted K = 2.5 and 3.5 for O and early B stars, respectively.

Assuming 0.55 $M_\odot$ for the central star of SwStl and taking K=3.5, we obtain $\Gamma_e = 0.028$ and $V_\infty = 1912$ Km/s; if $M_S = 1\ M_\odot$ and K=3.0, then $V_\infty = 2225$ Km/s . We conclude that our adopted value of $V_\infty = 2000$ Km/s, derived from the best fit to the observed Si IV P Cygni line profile, is probably correct.

Abbott (1982) concluded that the mass-loss rate for a stellar wind driven by radiation pressure depends only on stellar luminosity: $\dot{M}=1.3\times10^{-16}(L/L_{\odot})^{1.77}(M_{\odot}/yr)$. Other workers [cf. Aller (1984)] suggested that the mass-loss rate also depends on surface gravity $g = GM_S/R_S^2$:

$$\dot{M} = 3.9 \times 10^{-13} \, (L/L_{\odot})^{1.42} \, [g(cm\ s^{-2})]^{-0.31} \, (M_{\odot}/yr). \qquad (4.51)$$

Use of equation (4.51) with log(g)=4.51 yields $\dot{M} = 6.5 \times 10^{-10}$ $(M_{\odot}/yr)$ for the mass-loss rate from the central star of SwSt 1. We conclude that the actual mass-loss rate (2.8×10^{-8} $M_{\odot}/yr$) is large compare with the rate for a wind driven by radiation pressure. The radiation-driven stellar wind theory seems to be attractive for early-type stars of high luminosity, but for those stars which can hardly be considered luminous, it likely fails to apply. The reason could be due to the fact that the physical parameters employed in the theory are applicable to Of stars which possess the characteristics of high luminosity.

The most exciting result of our analysis is that the actual mass-loss rate, $\dot{M} = 2.8(\pm1.0) \times 10^{-8}$ $(M_{\odot}/yr)$, is larger than the "maximum" rate, $\dot{M}_{max} = L/(V_{\infty}\, c) = 6.4 \times 10^{-9}$ $(M_{\odot}/yr)$, which can be produced by radiation pressure. Any reasonable increase in the stellar temperature or luminosity will not reverse the situation. We should, however, remember that the largest uncertainties in the estimated value of $\dot{M}$ arise from uncertainties in our assumptions about the abundance, A, and ionization, I, factors. If these assumptions are valid then there may be a real discrepancy, i.e., $\dot{M}/\dot{M}_{max} > 1$. Analogous conclusions have been reached regarding the mass-loss rate from the central star of the planetary nebula NGC 6543 (CLS). A similar situation is also revealed in galactic Pop. I Wolf-Rayet stars [Barlow (1979)], which constitutes a problem for stellar wind theories.

CHAPTER (4)

Tables and Figures

Table (4-1)

Continuous emission coefficients, computed for physical conditions found in SwSt 1. Tabulated is log [10^{14} γ].

λ(Å)	(H I)	(2q,H I)	(He I)	(He II)	effective
1400	-1.39	0.25	-0.65	0.77	0.25
2051	0.21	0.27	0.76	2.37	0.59
2052	0.21	0.27	0.76	0.55	0.59
2599	0.94	0.17	1.28	1.27	1.06
2600	0.94	0.17	1.04	1.27	1.04
3121	1.39	0.08	1.47	1.72	1.45
3122	1.39	0.08	1.43	1.73	1.44
3421	1.59	0.03	1.60	1.92	1.63
3422	1.59	0.03	0.84	1.92	1.61
3646	1.72	0.00	0.95	2.05	1.73
3648	0.25	0.00	0.95	1.18	0.53
3679	0.27	-0.01	0.97	1.19	0.54
3680	0.27	-0.01	0.30	1.19	0.47
5698	0.95	-0.26	1.03	1.87	1.01
5699	0.95	-0.26	1.03	1.40	1.01
7848	1.29	-0.46	1.24	1.74	1.32
7849	1.29	-0.46	1.19	1.74	1.32
8193	1.33	-0.49	1.14	1.78	1.35
8194	1.33	-0.49	1.10	1.78	1.35
8197	1.33	-0.49	0.95	1.78	1.35
8198	1.33	-0.49	0.91	1.78	1.34
8205	1.33	-0.49	0.89	1.78	1.34
8206	0.80	-0.49	0.89	1.49	0.86
8265	0.81	-0.50	0.89	1.50	0.86
8266	0.81	-0.50	0.88	1.50	0.86
10000	0.96	-0.62	0.96	1.65	1.00

Table (4-2)

Ultraviolet and visual continuum fluxes (10^{-13} erg cm^{-2} s^{-1} Å^{-1}) from SwSt 1 and its central star.

λ(Å)	I_λ(tot)	I_λ(nebcont)	I_λ(star)
1300	71.77	0.82	70.95
1400	54.95	0.94	54.02
1500	52.48	0.92	51.56
1600	41.02	0.89	40.13
1700	32.51	0.85	31.66
1800	30.41	0.83	29.58
1900	29.92	0.85	29.07
2000	28.77	0.90	27.88
2100	30.83	0.97	29.86
2200	24.10	1.08	23.02
2300	22.49	1.21	21.28
2400	20.75	1.36	19.39
2500	16.90	1.53	15.37
2600	15.17	1.62	13.55
2700	14.55	1.85	12.71
2800	13.58	1.85	11.73
2900	12.71	2.32	10.38
3000	11.07	2.57	8.49
3100	10.64	2.82	7.82
3200	9.16	3.07	6.09
4300	5.32	0.25	5.08
4329(B)	3.51	0.25	3.26
4800	4.07	0.28	3.79
5200	3.29	0.29	2.99
5464(V)	1.99	0.31	1.68
5600	2.58	0.33	2.25
6000	2.12	0.32	1.80
6400	1.80	0.33	1.47

Table (4-3)

Ultraviolet and visual continuum fluxes (10^{-13} erg cm^{-2} s^{-1} Å^{-1}) from IC 2501 and its central star.

λ(Å)	I_λ(tot)	I_λ(nebcont)	I_λ(star)
1300	21.00	2.95	18.05
1400	18.58	3.37	15.21
1500	16.00	3.26	12.73
1600	12.71	3.03	9.67
1700	11.22	2.78	8.44
1800	10.07	2.56	7.51
1900	9.12	2.41	6.71
2000	7.36	2.32	5.05
2100	8.09	2.23	5.86
2200	6.08	2.24	3.84
2300	5.68	2.28	3.39
2400	5.22	2.36	2.87
2500	4.87	2.46	2.41
2600	4.69	2.46	2.23
2700	4.21	2.65	1.56
2800	4.21	2.65	1.56
2900	4.10	2.70	1.40
3000	3.95	2.90	1.05
3100	4.00	3.00	1.00
3200	4.10	3.20	0.90
3246	4.34	3.35	0.99
3546	4.32	3.52	0.80
4225	0.95	0.42	0.53
5306	0.63	0.41	0.22
6865	0.43	0.38	0.05
7901	0.41	0.38	0.03

Table (4-4)

Values of $G[T_Z(X^{+m})]$, calculated from eq.(4.17) for λ_1=1400Å

$T_Z(10^3$ K)	$G(H^O)$	$G(He^O)$	$G(He^+)$
25	0.085	0.0015	6.424(-9)
30	0.155	0.0061	2.612(-7)
35	0.244	0.017	3.755(-6)
36	0.265	0.021	5.866(-6)
37	0.286	0.024	8.950(-6)
38	0.307	0.028	1.336(-5)
39	0.330	0.033	1.955(-5)
40	0.353	0.038	2.808(-5)
45	0.479	0.072	1.355(-4)
50	0.620	0.120	4.806(-4)
55	0.777	0.185	0.0014
60	0.949	0.267	0.0033
61	0.985	0.286	0.0038
62	1.021	0.305	0.0044
63	1.058	0.325	0.0052
69	1.292	0.459	0.011
70	1.333	0.484	0.013
71	1.374	0.509	0.015
75	1.545	0.618	0.023
80	1.769	0.771	0.037
85	2.006	0.940	0.057
90	2.256	1.125	0.084
95	2.517	1.327	0.119
100	2.791	1.545	0.163
110	3.375	2.027	0.283
120	4.006	2.568	0.451
130	4.683	3.167	0.671
140	5.408	3.821	0.949
150	6.179	4.529	1.287

Table (4-5)

Values of the colour and Zanstra temperatures (Kelvin) of the exciting stars of SwSt1 and IC2501.

	SwSt 1	IC 2501
T_C	30 000	60 000
T_Z(H I)	36 000	62 000
T_Z(He I)	36 000	----
T_Z(He II)	----	62 000
T_Z(Radio)	39 000	70 000

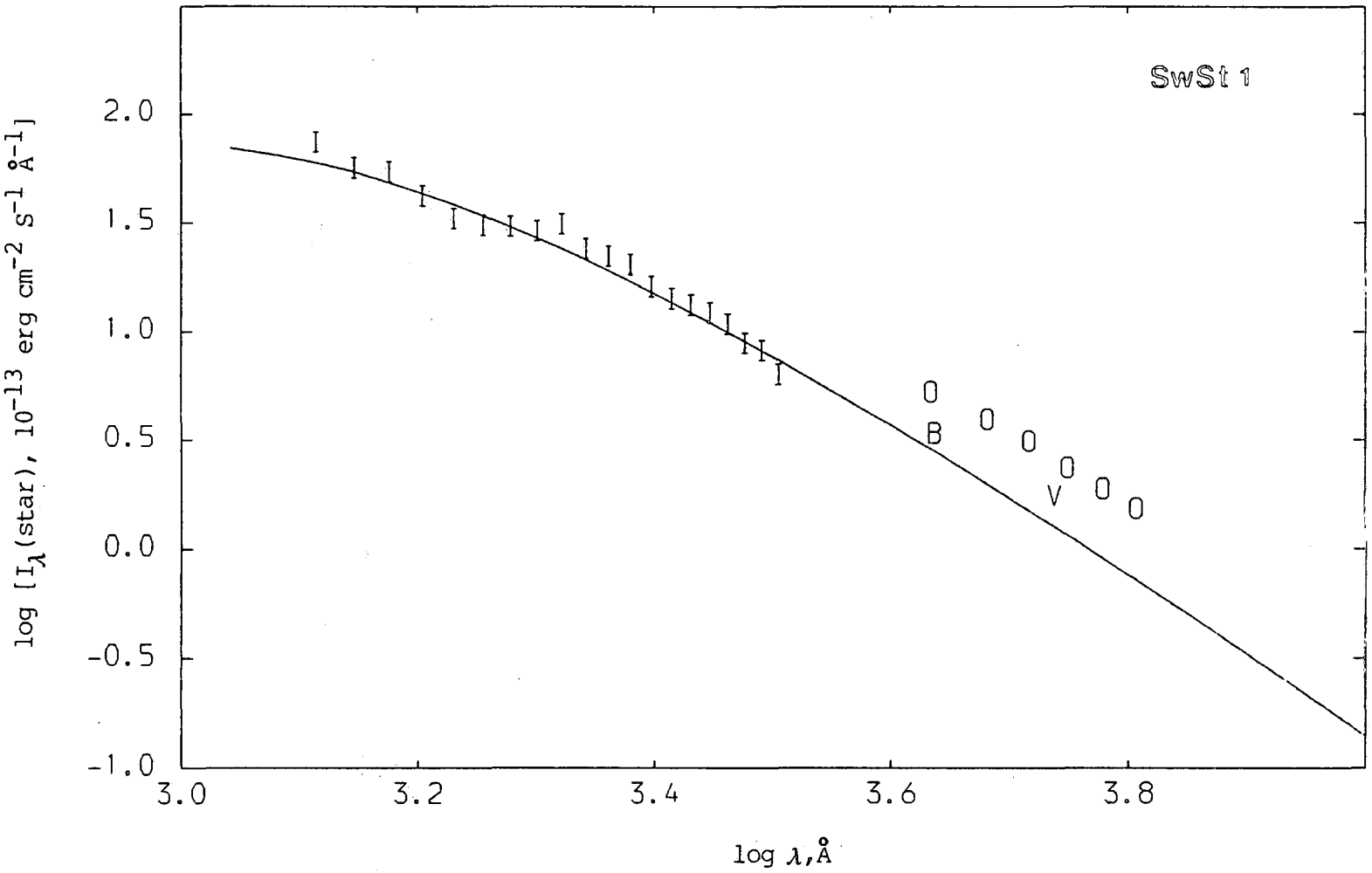

Figure (4-1): Ultraviolet (I) and optical (O) continuum fluxes from the central star of SwSt1; B refers to blue and V to visual magnitude estimates. The solid curve is the flux for a blackbody star with T_c = 30,000 K and total flux at the distance of the earth normalized such that $\lambda I_\lambda(\text{star}) = 7.56 \times 10^{-9}$ erg cm^{-2} s^{-1} at λ = 1400 Å.

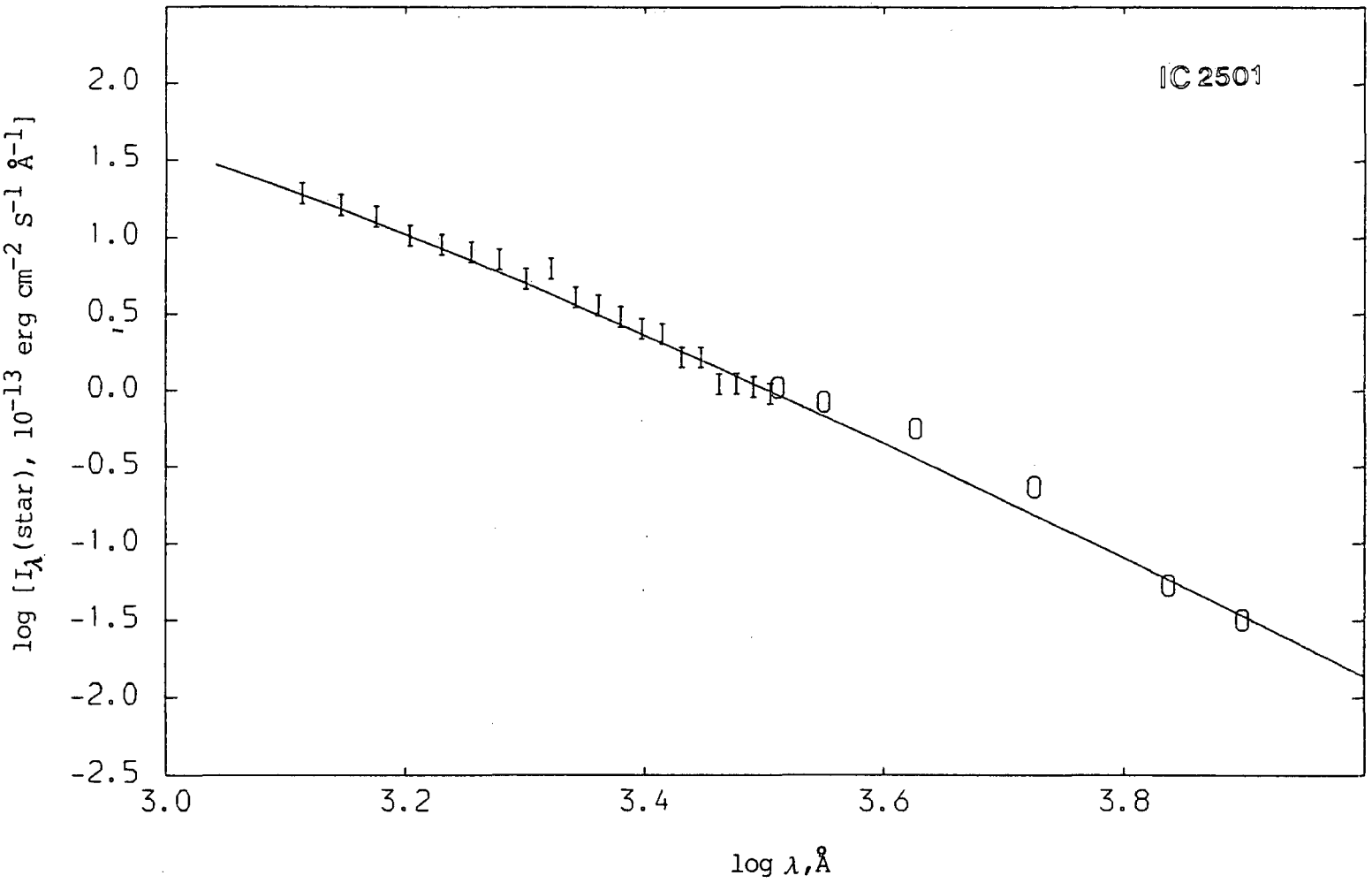

Figure (4-2): Ultraviolet (I) and optical (O) continuum fluxes from the central star of IC2501. The solid curve is the flux for a blackbody star with T_c = 60,000 K and total flux at the distance of the earth normalized such that $\lambda I_\lambda(\text{star}) = 2.13 \times 10^{-9}$ erg cm^{-2} s^{-1} at λ = 1400 Å.

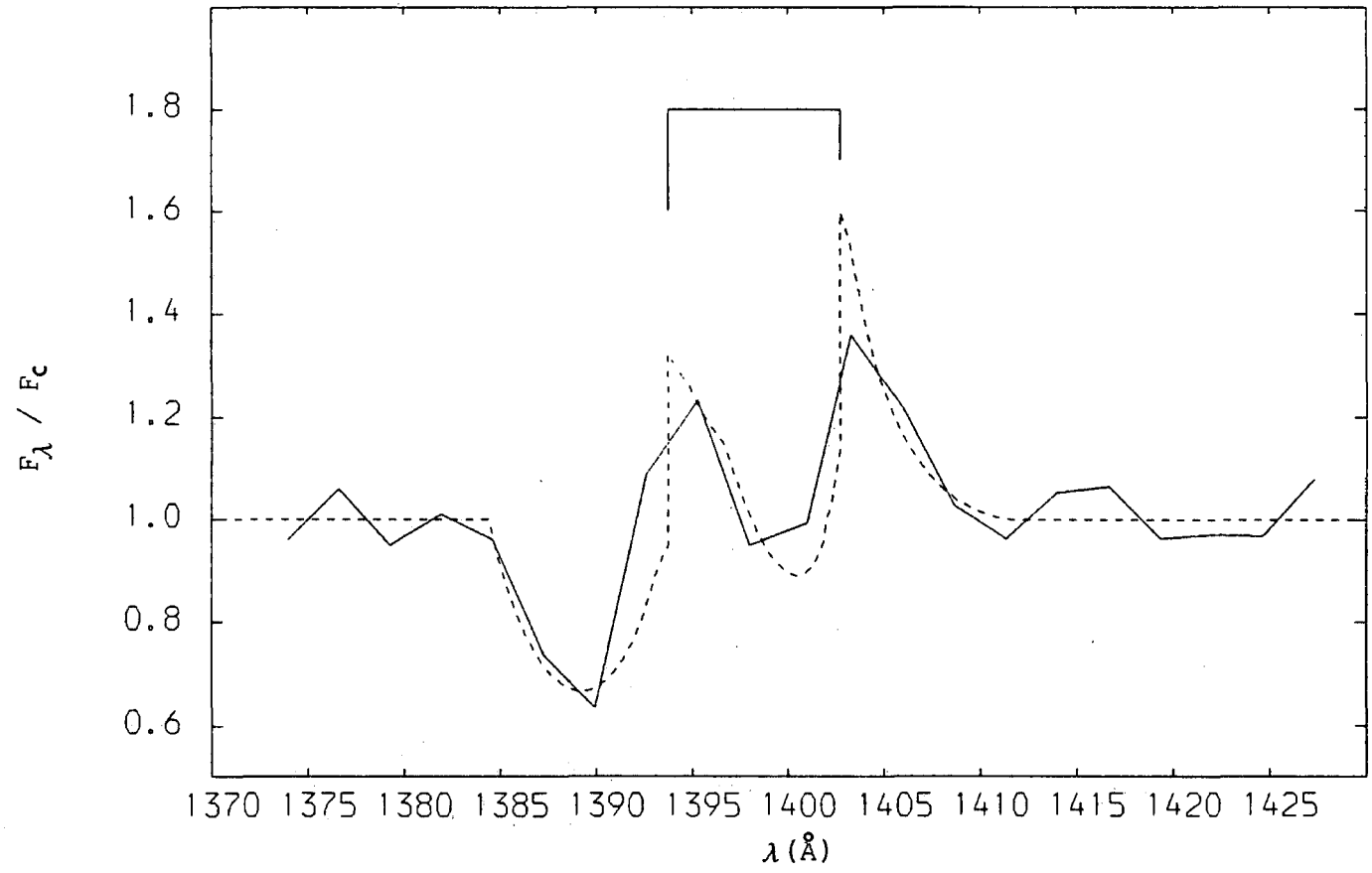

Figure (4-3): The SiIV P Cygni feature observed in the spectrum of SwSt1: F_λ/F_c is plotted against λ, where F_λ is the observed flux and F_c a mean continuum flux in the vicinity of the feature. The feature has a blue component at λ=1393.73Å and a red component at λ=1402.73Å. The positions and relative gf values of these components are indicated. The dashed curve is from the calculation described in section (4.5.2)

CHAPTER (5)

A THEORETICAL MODEL FOR THE PLANETARY NEBULA NGC 4361

5.1 INTRODUCTION

The high-excitation planetary nebula NGC 4361 has been a popular object for detailed observational and theoretical studies. In Chapter 1, we have discussed the observations of NGC 4361, both those which we have obtained in the ultraviolet using IUE satellite and those obtained by other workers at ultraviolet, optical, radio, and infrared wavelengths. In this Chapter, we discuss the interpretation of these observations.

The main feature of the present work is that we have constructed a self-consistent spherically symmetric model of the nebula in which we have attempted to use the most accurate available data for all relevant physical processes. The computer program used is based upon that described by Harrington (1967, 1968) and improved by HSAL. The objectives of this work involved representation of observed nebular continuum and line intensities, including such diagnostic ratios as yield electron temperatures and densities. We believe that the ionization correction factors for the unobserved stages of ionizations are best determined by detailed modelling.

Our study indicates that the observed IUE and optical nebular emission lines are satisfactorily reproduced using a stellar blackbody flux distribution with effective temperature T_{eff} = 140,000 K.

Comparisons between the results of the present model and the models of Aller et al. (1978 ; ARKC) and of Adam and Koppen (1985 ; AK) show that charge exchange and dielectronic recombination processes are, indeed, very important and must be included in the theoretical models of planetary nebulae.

5.2 REDDENING CORRECTION

In the present section we consider the determination of the reddening correction c. We discuss values obtained from the strength of the 2200Å absorption feature, comparison of Hβ and radio fluxes, Balmer decrements, and ratio of He^{+2} line fluxes.

5.2.1 The 2200 Å Feature

The 2200Å absorption feature observed in the ultraviolet continuum of NGC 4361 [see Figure (1-10)] suggests a small interstellar extinction. Figure (5-1) shows the merged SWP 7779 and LWR 6779 spectra, corrected for reddening using $c = 0.05$. It is seen that this value of c, with a deviation of ± 0.05, is sufficient for removing the 2200Å absorption dip in the observed ultraviolet continuum of NGC 4361.

5.2.2 Hβ and Radio Continuum Fluxes

Measurements of F(Hβ) from the whole nebula yield $331 \pm 36 \times 10^{-13}$ erg cm^{-2} s^{-1} [O'Dell (1962)] and $257 \pm 23 \times 10^{-13}$ erg cm^{-2} s^{-1} [Martin (1984)]. These two values are not compatible to within their combined error bars. For the purpose of the present work, we adopt an average value of

$$F(H\beta) = 294 \pm 40 \times 10^{-13} \text{ erg cm}^{-2} \text{ s}^{-1}. \qquad (5.1)$$

On the basis of available radio continuum observations (see Chapter 1), NGC 4361 is optically thin at 5 GHz and has a flux density of

$$F(\text{radio}) = 0.207 \text{ Jy} \quad ; \text{ at 5 GHz}. \qquad (5.2)$$

From (5.1) and (5.2) we obtain, for the entire nebula, $F(H\beta)/F(\text{radio}) = 1420 \pm 200$. The calculated ratio of emitted fluxes, $I(H\beta)/I(\text{radio})$, is dependent on the electron temperature and helium abundance (see eq. 3.32). The ratio from our model is $I(H\beta)/I(\text{radio}) = 1872$. It follows that

$c = 0.12 \pm 0.07$. The previous estimate, $c = 0.29$, by Milne and Aller (1975) was based on incorrect value of F(Hβ).

5.2.3 Balmer Decrements

Using the observed Balmer decrements, TPP derived a value of $c = 0.1$, while Barker (1978) obtained a value of $c = 0.01$. From their own photoelectric measurements of Balmer decrements, Heap et al. (1969) found $c = 0.0$. It is seen that the reddening correction, as derived by this method, is in the range $0.0 \leq c \leq 0.1$. To determine the exact value of c , very accurate measurements of Balmer decrements are required. This is illustrated in Table (5-1) which gives fluxes for Hα, Hγ, and Hδ on the scale of $I(H\beta) = 100$. The theoretical values are from the model. The observed fluxes, corrected for reddening, are the average of values measured by TPP (region a), ARKC, and Barker (1978). It can be seen that the correction for reddening (with $c = 0.0$, 0.05, and 0.1) is very small. However, the theoretical values I(Hα) and I(Hγ) are consistent with the observed fluxes corrected with $c = 0.05$.

5.2.4 Flux Ratios for He II

We consider fluxes in units of 10^{-13} erg cm^{-2} s^{-1} . For the 21 arcsec circular aperture we have $F(\lambda 4686) = 44 \pm 2$ from Table (1-5). From Table (1-15), the values of $F(\lambda 1640)$ are 60 ± 10 from SWP 7779 and 77 ± 18 from SWP 13521. We shall adopt an average value of $F(\lambda 1640) = 69 \pm 20$. Thus:

$$F(\lambda 1640, \text{IUE}) \; / \; F(\lambda 4686, 21") = 1.6 \pm 0.4. \qquad (5.3)$$

From the model we have

$$I(\lambda 1640, \text{IUE}) \; / \; I(\lambda 4686, 21") = 2.0. \qquad (5.4)$$

Using $[f(\lambda 1640) - f(\lambda 4686)] = 1.09$, we obtain $c = 0.09 \pm 0.09$.

5.2.5 Adopted Value For Reddening

All the method used to deduce c have uncertainties associated with them, and we shall adopt $c = 0.05\ (\pm\ 0.05)$. Fortunately, our analysis is not sensitive to the exact value of c, within this range.

5.3 ADOPTED FLUXES IN NEBULAR LINES

Measurements of IUE and optical nebular line fluxes are discussed in Chapter 1.

The IUE measurements give absolute fluxes for He II λ1640, C III] λ1908, C IV λ1549, and [Ne IV] λ2423 nebular emission lines. Projected on to the sky, the sizes of IUE apertures are smaller than the entire size of nebular emission for NGC 4361. We consider measurements for two different regions in the nebula: region A corresponds to an IUE large aperture centered on star; region B corresponds to an IUE large aperture offset 28 arcsec (SE) from star.

Absolute flux measurements of Hβ λ4861, He II λ4686, and [O III] λ5007 nebular emission lines have been made for a variety of circular aperture sizes (10, 21, 40, and 80 arcsec in diameter). Many more lines have been measured for a variety of regtangular aperture sizes.

Table (5-2) gives, for the nebular lines, the extinction function $f(\lambda)$ and adopted fluxes $I(\lambda)$ corrected for extinction using $c = 0.05$. We make some remarks on Table (5-2):

(1) Region A: the values of I(λ1640) and I(λ1549) are the average of values obtained from SWP 7779 (low resolution) and SWP 13521 (high resolution) spectra. The C III] λ1908 line is affected by reseau marks in SWP 7779. The value of I(λ2423) is from LWR 6779.

(2) Region B: the fluxes given for λ1640 and λ1549 are from SWP 7780, while those for λ1908 and λ2423 are from LWR 6780. The C III] λ1908 line is again affected by reseau marks in SWP 7780.

(3) Fluxes through circular apertures: the values of I(Hβ) and I(λ5007) given for the 80 arcsec circular aperture are the average of values measured by O'Dell (1962) and by Martin (1984). All other values are from Martin (1984).

(4) Region C: the fluxes are the average of values obtained by TPP (slit 5.2" × 77.6" offset 3" S of central star) and by Barker (slit 8" × 200" offset 10" N of central star). For [O III] λ5007, the fluxes through circular apertures are included.

(5) The [Ar IV] λ4740 and [Ar V] λ7006 nebular lines which have been measured in NGC 4361 have not been given in Table (5-2), since our model does not contain Ar. This is one of the limitations of the present model.

5.4 CONTINUUM FLUXES

Intermediate band observations of NGC 4361 in the spectral region $1500 \leq \lambda \leq 3300$ Å have been made by Pottasch et al. (1878b ; PWWFD) using the ANS satellite. The observations are made with filters passing bands of width 150 Å centered at five wavelengths (1550, 1800, 2200, 2500, and 3300 Å). The ANS diaphragm is a square , 150" on each side, consequently the light of the central star and the whole nebula are both measured.

Table (5-3) gives, for the wavelengths at which ANS observations have been made :

(1) The nebular continuum flux, I_λ(nebcont), for the whole nebula , calculated using I(Hβ, 80") from Table (5-2) and values of the electron temperatures, electron densities, and relative ion abundances from the model.

(2) The stellar flux, I_λ(star), calculated assuming a blackbody distribution with temperature T_c = 140,000 K and total flux at the distance of the earth normalized such that

$$\lambda\ I_\lambda(\text{star}) = 5.60 \times 10^{-9}\ \text{erg cm}^{-2}\ \text{s}^{-1}\ \text{at}\ \lambda = 1400\ \text{Å}. \qquad (5.5)$$

(these parameters are consistent with IUE and optical continuum measurements of the central star, see section 5.5.3).

(3) The sum of the calculated nebular and stellar fluxes, I_λ(tot).

(4) The total continuum flux , I_λ(tot, ANS), measured in the ANS bands corrected for reddening using c = 0.05.

It is seen from Table (5-3) that our values of I_λ(tot) are in good agreement with the values of I_λ(tot, ANS) obtained by PWWFD. This is not true for λ2500 where the ANS value is larger than our value by a factor of 1.6. Some of this discrepancy could be due to the fact that the ANS bands include some contributions from nebular emission lines (e.g. [Ne IV] λ2423). HSAL have carried out a similar analysis for the planetary nebula NGC 7662 and found that their values of the total flux were systematically smaller than those of PWWFD. They concluded that the errors in the ANS measurements are much larger than the very small errors quoted by PWWFD.

5.5 TEMPERATURE OF THE CENTRAL STAR

5.5.1 Model Atmosphere

Mendez et al. (1981, 1983) have obtained an improved spectral description of six central stars of planetary nebulae using three different observational techniques: (1) the image-tube spectrograms of the CTIO 1-m and 4-m telescopes; (2) the SIT-Vidicon system with the R-C spectrograph of the CTIO 4-m telescope; and (3) the IDS with the

Cassegrain spectrograph of the ESO 3.6-m telescope. They found that the three techniques produce essentially the same results. The spectra of these stars show predominantly absorption line profiles.

Mendez et al. have then constructed non-LTE model atmospheres for the central stars by fitting the observed photospheric H I and He II absorption line profiles. Their aim was to derive the effective temperatures, surface gravities, and He/H abundance ratios for these stars. The model atmospheres have been assumed plane-parallel, in hydrostatic and radiative equilibrium and to be composed of hydrogen and helium only (no metals are included). The profiles have been calculated with non-LTE treatment of hydrogen and helium.

NGC 4361 was one of the six objects which have been analyzed. According to Mendez et al. (1983), the atmospheric parameters which have been used to fit the H I and He II photospheric absorption line profiles observed in the spectrum of NGC 4361 are:

$$\left.\begin{aligned} T_{eff} &= 80{,}000 \pm 10{,}100 \ \ K \ ; \\ \text{Log } [g(\text{cm s}^{-2})] &= 5.5 \pm 0.3 \ ; \\ N(He)/[N(He)+N(H)] &= 0.05 \pm 0.02. \end{aligned}\right\} \qquad (5.6)$$

5.5.2 Zanstra Temperatures

As discussed in Chapter 4, the well known Zanstra method allows the determination of the temperatures of the central stars from observations of the nebular H and He emission lines and the stellar flux at an arbitrary reference wavelength (we use λ = 1400 Å). The stellar flux is given by equation (5.5). The fluxes, corrected for extinction, in the Hβ and He II λ4686 nebular lines are 330 and 325, respectively. Both values are in units of 10^{-13} erg cm^{-2} s^{-1}. The electron temperature is estimated from the I(λ5007)/I(4363) ratio (T_e = 19000 K). Using the relations of

Chapter 4, we obtain G(H I) = 0.181 and G(He II) = 0.102. Assuming a blackbody spectrum for the central star and using the results of Table (4-4), we obtain T_z(H I) = 32,000 K and T_z(He II) = 93,000 K.

These temperatures may be compared with those obtained by Pottasch et al.(1978b) [T_z(H I) = 42,500 K; T_z(He II) = 98,000 K], by Clegg and Seaton (1983) [T_z(H I) = 41,000 K; T_z(He II) = 95,000 K], and by AK [T_z(HI) = 33,000 K; T_z(He II) = 93,000 K]. Our value of T_z(He II] is in excellent agreement with the value obtained by AK. Since we use the same values of T_e and I(He II, λ4686) as AK, this agreement indicates that the stellar continuum flux at 1400Å observed in the low-dispersion spectrum (SWP 7779) is consistent with that observed in the high-dispersion spectrum (SWP 13521).

That T_z(H I) is less than T_z(He II) can be easily explained by the fact that the nebula is optically thin in the H I Lyman continuum. This is indicated by the weakness of the singly ionized spectral lines in the nebular radiation (e.g. [O II], [S II], [N II]) and by the nebular model calculations which show that [O III] and [Ne III] emission extends to the outer edges of the nebula. The model nebula is not optically thick in the He^+ continuum, hence T_z(He II) is also a lower limit on the stellar temperature.

The He II Zanstra temperature depends greatly upon the assumptions made about the stellar flux distribution. If the fluxes given by the plane-parallel LTE model atmospheres of Hummer and Mihalas (1970) are used, then T_z(He II) = 104,000 K. The non-LTE model atmospheres of Husfeld et al. (1984) yield T_z(He II) = 100,000 K. We conclude that the He II Zanstra temperature of the central star of NGC 4361 is

$$93{,}000\ \text{K} \leq T_z(\text{He II}) \leq 104{,}000\ \text{K} \qquad (5.7)$$

5.5.3 Colour Temperature

Figure (5-1) shows log-log plots of flux against wavelength. the plots are:

(a) The observed IUE and optical continuum fluxes, corrected for reddening using c = 0.05. The IUE fluxes are from merged SWP and LWR spectra of region A. The optical continuum measurements are from the narrow band photometric observations of Martin (1984) and from measurements of the UBV magnitudes [see Table (1-6)].

(b) The nebular continuum flux, NEBCONT, calculated using the method of section (5.4). We emphasize that this flux is different from that given in Table (5-3) only in that we now calculate the flux for the IUE aperture.

(c) The stellar continuum flux, STAR, calculated assuming a blackbody distribution with temperature T_c = 140,000 K and total flux at the distance of the earth normalized to (5.5).

(d) The sum of the calculated nebular and stellar fluxes, TOTAL.

It is seen from Figure (5-1) that the total continuum flux observed with IUE is due almost entirely to the star. At optical wavelengths the nebular continuum accounts for no more than about 10% of the total continuum. The agreement between the observed and total calculated continua is good. If T_c is varied by about ± 10,000 K this agreement is still good. We conclude that the colour temperature of the central star of NGC 4361 is

$$T_c = 140{,}000 \pm 10{,}000 \quad K. \tag{5.8}$$

5.6 PREVIOUS MODELS

ARKC have constructed three nebular models of NGC 4361 with the primary aim of determining the elemental abundances. The nebular gas is assumed to be spherically symmetric, motionless, and homogeneous. The

models are material bounded (or truncated models), so that the nebula is optically thin for H ionizing continuum. Charge exchange and dielectronic recombination processes have not been taken into account. Dust in the nebular shell has also been neglected. For the stellar spectrum, ARKC have used a flux distribution of a blackbody of temperature 150,000 K which has been slightly modified to improve the fit between the observed and calculated intensities of He II λ4686 nebular emission line without invoking suspiciously large helium abundances. For comparisons with the present model, we present their stellar flux distribution in Figure (5-2) and the parameters which fix their model 1 in Tables (5-4) - (5-6). With this model, ARKC have achieved a good reproduction of the optical emission lines (ultraviolet emission lines were not available at the time they constructed their models).

Spherically symmetric models of the planetary nebula NGC 4361 have also been constructed by AK. The models have been truncated inside the He^{+2} Stromgron sphere. Therefore, the nebula is optically thin for H and He ionizing continua. In these models, charge exchange reactions of hydrogen with ions of trace elements have been taken into account, but dielectronic recombination processes were not included. Dust has been neglected. For the stellar flux distribution, AK have adopted a non-LTE model atmosphere with T_{eff} = 100,000 K and g = 10^5 cm s^{-2}. This model atmosphere is very similar to the empirical spectrum of ARKC in that it shows the He II Lyman edge in emission [Figure (5-2)]. This effect has been discussed by Husfeld et al.(1984). The parameters corresponding to the nebular model C of AK are given in Tables (5-4) - (5-6). This model seems to reproduce most of the ultraviolet and optical emission lines.

The problem with all of the above nebular models is that they neglect one or two of the most important physical processes in planetary

nebulae. Thus, in addition to the new IUE observations, we need to make a more reliable model of NGC 4361 in which we should include all relevant physical processes.

5.7 THE MODEL OF NGC 4361

5.7.1 The Computer Program

HSAL give an extensive discussion of the computer program which we have used to construct a spherically symmetric model of the planetary nebula NGC 4361. They also give references to the necessary atomic data. These include photoionization cross-sections, radiative and dielectronic recombination coefficients, rates of charge exchange reactions, effective collision strengths, and the corresponding radiative transition probabilites. We have included the new dielectronic recombination rates of Nussbaumer and Storey (1982). All of these parameters are stored in the computer program along with better known data such as spectral line wavelengths, excitation potentials, and ionization potentials.

The program calculates the thermal structure, ionic distribution, emission line intensities, and other observables. A very complete description of the computational procedures is given by HSAL.

Below we discuss the parameters which we have used to fix the nebular model. The results obtained from the model are discussed in section 5.8.

5.7.2 Angular Diameter

The cataloge of galactic planetary nebulae [Perek and Kohoutek (1967)] contains a list of the probable values of the angular diameter of NGC 4361. From these we select the value

$$\Theta = 81 \text{ arc-sec.} \qquad (5.9)$$

which is due to O'Dell (1962) and Kahn and Kaler (1971).

5.7.3 Distance

The distance of NGC 4361 is uncertain. A value of 1400 pc is given by TPP. From proper motions and other statistical data, Gudworth (1974) obtained a distance of 1455 pc. Estimates based on the thin shell hypothesis yield 765 pc [O'Dell (1962)], 797 pc [Higgs (1971)], 900 pc [Cahn and Kaler (1971)], 725 pc [Milne and Aller (1975)], and 910 pc [Daub (1982)].

Since we do not have any improvement over these estimates, we shall adopt the more recent estimate by Daub :

$$D = 910 \text{ pc.} \tag{5.10}$$

The main results of the present work are not very sensitive to the value assumed for the distance.

5.7.4 Outer and Inner Boundaries of the Nebula

The outer radius of the nebular shell is estimated from (5.9) and (5.10). The inner radius was adjusted by reproducing the intensity ratios C IV / C III] and [Ne IV] / [Ne III]. The adopted values are:

$$R_{inner} = 0.01 \text{ pc} \quad ; \quad R_{outer} = 0.179 \text{ pc.} \tag{5.11}$$

5.7.5 The Stellar Flux

Choice of a proper stellar flux poses one of the most difficult problems in the theoretical models of planetary nebulae. The frequency distribution of the stellar radiation at the region shortward of $\lambda = 912$ Å (the H^O ionization limit) is very uncertain. Optical and IUE observations are of limited help. Our main constraints for the central star of the planetary nebula NGC 4361 are as follows:

(1) The stellar flux distribution for $\lambda > 1200$Å should match the observed IUE and optical continuum fluxes of the central star;

(2) The flux at the distance of the earth, at λ = 1400 Å, should be consistent with (5.5);

(3) The stellar flux distribution between 912Å and 228Å must be such as to produce the correct heating or ionization to the gas;

(4) The number of quanta beyond the He^+ ionization limit (λ < 228 Å) must be enough to explain the observed He II λ4686 nebular emission line.

AK have pointed out that a non-LTE model atmosphere with effective temperature T_{eff} = 90,000 K and gravity log [g (cm s^{-2})] = 5.2 should satisfy the above conditions. Unfortuntely, this model atmosphere is not available at the present time. The non-LTE model atmospheres of Husfeld et al. (1984) are not extensive enough for accurate interpolations in T_{eff} and log(g) to be made. The LTE model atmospheres of Hummer and Mihalas (1970) show the He II Lyman edge in absorption and it would not be possible to reproduce the He II λ4686 nebular emission line. In the absence of reliable stellar atmosphere models, we shall adopt the colour temperature of 140,000 K, which reproduces the observed stellar continuum flux [see Figure (5-1)]. The energy emitted beyond the He^+ continuum limit may not be accurately reproduced by this model, but λ < 228 Å accounts for less than 20% of the total stellar luminosity. The low value of the He II Zanstra temperature may arise because the nebula is not very optically thick in the He^+ continuum (see section 5.8.4).

The stellar parameters which we have chosen for our model are summarized in Table (5-4). These parameters imply that λI_λ(star) = 3.6×10^{-9} erg cm^{-2} s^{-1} at λ = 1400 Å, which is a factor of about 1.5 smaller than that given by (5.5). This difference corresponds to a 20% reduction in the adopted value of the distance, but leads to a value which lies between the distances found by O'Dell (1962) and Milne and Aller (1975). Model calculations show that these stellar parameters are satisfactory.

Figure (5-2) shows the stellar flux distributions adopted for our model, model C of AK, and model 1 of ARKC. The ionization thresholds of several ions are indicated in the Figure. For completeness, Table (5-5) lists the adopted ionization thresholds of all ions considered in our model.

5.7.6 The Mean Density Distribution

Since our model is constrained to be spherically symmetric, we can use the measured Hß flux through circular apertures [Table (5-2)] to derive the hydrogen density distribution. Following AK, we consider the nebula to be consists of a series of homogenous shells whose radii correspond to the apertures. The electron temperature, estimated from the [O III] I(λ5007)/I(λ4363) ratio, is assumed to be constant in the whole nebula. With sufficient accuracy for our present purpose, we may let $N(H^+)/N_H = 1$. A mean value of N_e/N_H is calculated allowing for the ionization of helium. Given the distance, we can compute the r.m.s. density of the outermost shell from the difference of the Hß fluxes measured with the largest and second largest aperture. To compute the density in the second largest shell by the analogous difference of fluxes, we must subtract the contribution of those parts of the largest shell that lie within the line of sight. In this way, the density can be calculated going inward shell by shell. This technique produces a histrogram density distribution which can be smoothed by a Gaussian function. Instead, we use a subroutine "SPLINE" included in the computer program to smooth the histrogram. The finally adopted density distribution for the case where the nebular volume is entirely filled with material (filling factor $\xi = 1$) is shown in Figure (5-3). The peak density of $N_H = 317\ cm^{-3}$ occurs at an angular radius of 10.5 arcsec.

Models constructed with the density distribution thus obtained were found to give good agreement with the observed density-sensitive line ratios.

This means that we do not need to consider density fluctuations in the model (the use of $\xi = 1$ is satisfactory in this regard).

5.7.7 Dust

As in all previous models of NGC 4361, we neglect dust in the nebular shell. Infrared observations are in line with this neglect.

5.7.8 Abundances

The nebular gas is assumed to be consists of the nine most abundant elements in planetary nebulae: H, He, C, N, O, Ne, Mg, Si, and S. Table (5-6) lists the chemical abundances which have been adopted for NGC 4361, along with the solar abundances for comparison. These abundances were adjusted by an iterative procedure in such a way as to obtain the best overall agreement between observed and calculated line intensities, with the exception of Si and Mg, which are not constrained by observed lines. The Si abundance, relative to the solar abundance, is assumed to have the lowest value of the other elements, while Mg is assumed to have the same value as in NGC 7662 (HSAL). Although it is quite likely that Si and Mg would be depleted by the formation of solid grains. These abundances will be discussed further in section 5.8.5.

5.8 RESULTS AND COMPARISON WITH OBSERVATIONS

5.8.1 The Emitted Spectrum

The model produces a map of the projected surface brightness in each spectral line. We have integrated the projected brightness of the ultraviolet lines over the 10" × 20" oval aperture which is appropriate for IUE large aperture observations of region A. In Table (5-7), we compare these calculated values with the observed fluxes, which have

been corrected for extinction using c = 0.05. For comparison with previous theoretical work, we have included the fluxes of model C of AK.

Table (5-7) also gives a comparison of calculated and observed fluxes for region B. The observed fluxes are corrected for reddening and on a scale relative to I(He II λ1640) = 100. The theoretical fluxes are obtained by computing the emission in the lines, relative to the emission in He II λ1640, at several radial points within region B and averaging the results. This procedure leads to the error bars given for the predicted fluxes.

It is seen from Table (5-7) that the agreement between our model and IUE observations is good. The brightness distributions of C IV λ1549, C III] λ1908, and [Ne IV] λ2423 emission lines are well reproduced by our model. The strength of He II λ1640 is stronger than that observed by a factor of 1.11, but within the large observational uncertainties. In our model the He abundance was adjusted by reproducing the He II λ4686 flux through circular apertures rather than the He II λ1640 flux. One final note is that model C of AK seems to be satisfactory for C IV λ1549 and C III] λ1908 but gives [Ne IV] λ2423 stronger than observed by a factor of 2.55.

We have integrated the projected brightness of Hβ, He II λ4686, and [O III] λ5007 lines over the 10" × 20" oval aperture as well as over circular apertures whose radii correspond to the apertures used by Martin (1984). The results are given in Table (5-8) along with the observed absolute fluxes, corrected for reddening. The overall agreement between the calculated and observed fluxes is good. The brightness distribution in the model is such that only 7% of the total Hβ flux, 10% of the total He II λ4686 flux, and 4% of the total [O III] λ5007 flux enter the IUE large aperture, centred on the star.

Using a simulated 8" wide, infinitely long aperture, we have calculated the fluxes in the optical lines, relative to Hβ. The centre of the aperture was offset 3" and 10" from the central star. This leads to two sets of results for which the average values should be compared with the average of fluxes measured by Barker (1987) and by TPP (region a). The slit used by TPP is slightly narrower than the simulated aperture but this is not likely to lead to serious errors. In Table (5-9), we compare the observations with our model, model C of AK, and model 1 of ARKC. Except for [Ne V] λ3425, the three nebular models are in good agreement with optical observations. Our model and model C of AK give [Ne V] λ3425 stronger than observed. The production of Ne^{+4} by photoionization of Ne^{+3} requires stellar photons with energies greater than 97 ev. We suggest that a small absorption dip at $h\nu$ = 97 ev in our adopted stellar spectrum could remove the discrepancy between the observed and calculated fluxes of [Ne V] λ3425 without significant changes in the ionization structure of the model.

Fluxes measured in regions other than those mentioned above are reproduced by our model to within a deviation of less than 10%.

The calculated flux density at 5 GHz is 0.180 f.u., compared with an observed value of 0.207 f.u.

5.8.2 Ratios Sensitive to Physical Conditions

In Chapter 3, we have seen that certain ratios of fluxes are sensitive to electron temperature and electron density. For a given element, the ratio of fluxes of different ionization stages depends on the distribution of ionizing stellar flux and the distribution of density in the nebula. A realistic nebular model should reproduce the observed values of such ratios.

In Table (5-10) we compare the calculated and observed values of ratios of fluxes which are sensitive to physical conditions in NGC 4361. The observed values of the C III] λλ1907/1909 and C IV λλ1548/1551 ratios have been taken from AK. Other values are obtained from Tables (5-7) and (5-9). It is seen that there is satisfactory agreement between calculated and observed ratios. The scatter in the measured fluxes by different observers and the uncertainties in the atomic data may explain the small deviations from observations.

5.8.3 Electron Temperatures

The electron temperature in our model is obtained at each radial point by an iterative procedure in which the heating and cooling rates are calculated and the temperature adjusted until equality is achieved. The heating is provided by the energy input from the radiation field $J(\nu) = J^S(\nu) + J^D(\nu)$, where $J^S(\nu)$ is the (attenuated) stellar radiation and $J^D(\nu)$ is the diffuse component produced by the gas. The sources of the diffuse component are: (1) recombinations to the ground states of H^o, He^o, and He^+; (2) recombinations to the n=2 level of He^+; (3) two-photon decays from He^+ 2s and He^o 2 ^1S; (4) single-photon decay of He^o 2 ^3S; and (5) the He^+ Ly-α line and the radiation produced by the degradation of He^+ Ly-α by the Bowen fluorescence mechanism. The cooling processes include free-free emission, recombinations of electrons with ions, and collisional excitation of the low-lying energy levels.

Figure (5-4) shows the run of electron temperature with radius. Near the central star the temperature is very high as there are few coolants. The highest temperature, which occurs at the inner edge, is 30,000 K, but this drops gradually towards the outer region as the cooling effects of ions of O, Ne, C, and N become important. At the outer edge,

the temperature has its minimum value of 16,400 K. The mean value of the electron temperature is $\langle T_e \rangle$ = 17,600 K.

Table (5-11) gives the mean temperatures T_o , defined by equation (3.68), and values of the mean square fluctuation t^2 , defined by equation (3.67), for the first six ionization stages of all elements considered in our model. It can be seen that T_e(O II) ≈ T_e(Ne II) ≦ T_e(C II) , T_e(C III) ≈ T_e(O III) ≧ T_e(Ne III), and T_e(C IV) ≈ T_e(Ne IV) ≦ T_e(O IV).

The calculated electron temperature in the O^{+2} zone , T_e ≈ 17000 K, is well below the value T_e ≈ 19000 K measured by the sensitive line ratio I(λ5007)/I(λ4363). We emphasize that the former value represents the entire nebula, while the latter value corresponds only to regions near the central star. We shall see below that the [O III] ions are concentrated mostly in the outer parts of the nebula. Unfortunately, we do not have any more observationally-determined temperatures for further comparisons with the temperatures of the model.

Since H is everywhere fully ionized, the value t^2(H II) ≈ 0.01 can be considered representative of the nebula. This value of t^2 is significantly smaller than the value t^2 = 0.035 adopted by TPP. We may conclude that there are no large temperature fluctuations in NGC 4361.

5.8.4 The Ionization Structure

Let N_{ij} be the number of ions of element i in ionization stage j (where j = 1 signifies neutral atoms). Define the fractional abundance of the ij ion as

$$\chi(N_{ij}) = N_{ij} \Big/ \sum_k N_{ik} \ , \qquad (5.12)$$

where the summation is over all ionization stages of the element i. The optical depth measured from the inner radius to some point r in the nebula is

$$\tau_\nu(N_{ij}) = \int_{\text{inner radius}}^{r} a(\nu, N_{ij})\ N_{ij}(r, \xi)\ dr \qquad (5.13)$$

where $a(\nu, N_{ij})$ is the photoionization cross-section.

In Table (5-12) we present the calculated values of χ for H^+, He^+, and He^{+2} ions as well as the optical depths due to H^o, He^o, and He^+ at their respective absorption edges ($h\nu$ = 13.60 ev for H^o, $h\nu$ = 24.58 ev for He^o, and $h\nu$ = 54.40 ev for He^+). The threshold optical depths for the whole nebula $\tau(H^o)$ = 0.42 and $\tau(He^+)$ = 0.53 may be comapred with those obtained by model C of AK [$\tau(H^o)$ = 0.50 and $\tau(He^+)$ = 0.55]. The nebular model is not optically thick for H and He ionizing continua.

Values of χ for O, C, and Ne ions are shown graphically in Figures (5-5) to (5-7). We can not be very sure of the ionization equilibrium of N and S ions. Results for Si and Mg are very uncertain.

Table (5-13) gives the average fractional abundances of atoms in various ionization stages, defined as

$$f(N_{ij}) = \langle N_{ij} \rangle \ / \ \sum_k \langle N_{ik} \rangle \ , \qquad (5.14)$$

where the average density of the ij ion over the nebular volume is

$$\langle N_{ij} \rangle = \int N_e\ N_{ij}\ dV \ / \ \int N_e\ dV. \qquad (5.15)$$

The mean hydroden density in the model is $\langle N_H \rangle = 225\ cm^{-3}$. The total hydrogen mass in the nebula is $M_H = 0.13\ M_\odot$.

Because $f(H^o) \geq 0.001$, the ionization structure of the model is complicated by charge exchange reactions with hydrogen. One example is

the reaction $O^{+3} + H^{O} \Longrightarrow O^{+2} + H^{+}$; at electron temperatures found in NGC 4361, the rate coefficient for this charge transfer reaction is very large [$\beta \approx 1.1 \times 10^{-8}$ cm^3 s^{-1}; see Table (2-5)]. Due to this important process, the ratio $f(He^{+2}) / [f(O^{+3}) + f(O^{+4}) + ...]$ from Table (5-13) deviate from unity by about 11%. In all nebular models of NGC 4361, the oxygen-ionization equilibrium is obtained by reproducing only the [O III] emission lines (other O lines are very weak or absent). Hence, the neglect of the strong reaction mentioned above will result in a poor nebular model. We also note that the reactions $C^{+3} + H^{O} \longrightarrow C^{+2} + H^{+}$ ($\beta = 4.2 \times 10^{-9}$ cm^3 s^{-1} at $T_e = 2 \times 10^4$ K) and $Ne^{+3} + H^{O} \longrightarrow Ne^{+2} + H^{+}$ ($\beta = 8.3 \times 10^{-9}$ cm^3 s^{-1} at $T_e = 2 \times 10^4$ K) have important effects on the C^{+3}/ C^{+2} and Ne^{+3}/ Ne^{+2} intensity ratios.

Charge transfer reactions affect greatly the fractional abundances of the singly ionized species of various atoms. A model constructed without charge transfer showed about 45% reduction in the [O II] and [N II] line intensities.

In addition, dielectronic recombination processes are important for some ions in NGC 4361. At temperatures found in this nebula, the rate coefficient for the dielectronic recombination process $C^{+3} + e \rightarrow C^{+2}$ is about 2.5 times the ordinary radiative recombination rate. By neglecting this process in the nebular models of NGC 4361, AK have found it necessary to infer from the photographs of the nebula and expand the central hole to 1/2 of the nebular radius in order to get the observed C^{+3}/ C^{+2} intensity ratio. We do not have such a problem in our model (which is a full sphere) because we include the above process.

It is evident from the above discussion that the inclusion of the charge exchange and dielectronic recombination processes in the nebular model modify strongly the ionization structure of NGC 4361. We may conclude that despite the very few emission lines observed in the spectrum of NGC 4361, our model is able to reproduce the overall ionization and thermal structure of the nebula quite well.

5.8.5 The Chemical Abundances

The He, C, O, and Ne abundances should be well determined. We can not be very sure of the N and S abundances because the [N II] λ6584 and [S II] λ4072 lines are not strong and represent only minor stages of ionization [$f(N^+) = 0.0027$; $f(S^+) = 0.00033$]. The abundances of Si and Mg are very uncertain.

It is seen from Table (5-6) that C, O, and Ne are less abundant in NGC 4361 than in the Sun, but for C we do not see such a large difference as AK or ARKC. The C/O abundance ratio is about 1.2, indicating that NGC 4361 is a carbon rich object.

CHAPTER (5)

Tables and Figures

Table (5-1)

Theoretical and observed Balmer decrements in NGC 4361. The fluxes are expressed relative to Hβ. The observed fluxes are corrected for reddening with c = 0.0, 0.05, and 0.1.

Ion	λ(Å)	f(λ)	Model	Observed		
				c = 0.0	0.05	0.10
Hα	6563	-0.323	302	311	300	289
Hβ	4861	0.0	100	100	100	100
Hγ	4340	0.129	47.0	46.3	47.0	47.7
Hδ	4102	0.172	26.0	26.7:	27.1:	27.8:

Table (5-2)

Adopted fluxes in spectrum lines, corrected for reddening (c = 0.05). The fluxes given for region C are expressed relative to Hβ. Other values are in units of 10^{-13} erg cm^{-2} s^{-1} .

Ion	λ(Å)	f(λ)	Region A	Region B
He II	1640	1.136	88 ± 38	43 ± 3
C III]	1908	1.227	28 ± 5	23 ± 5
C IV	1549	1.184	231 ± 39	109 ± 4
[Ne IV]	2423	1.118	40 ± 4	17 ± 3

			10"	21"	40"	80"
Hβ	4861	0.0	7 ± 3	36 ± 4	123 ± 11	330 ± 40
He II	4686	0.042	11 ± 6	50 ± 2	160 ± 7	325 ± 15
[O III]	5007	-0.034	21 ± 3	91 ± 6	345 ± 16	1100 ± 200

			Region C
Hδ	4102	0.172	28
Hγ	4340	0.129	48
Hβ	4861	0.0	100
Hα	6563	-0.323	288
He I	5876	-0.216	<2.0
He II	4686	0.042	120
[O II]	3728	0.255	6.3:
[O III]	4363	0.124	9.5
[O III]	5007	-0.034	297
[Ne III]	3869	0.223	27
[Ne IV]	4725	0.034	3.0
[Ne V]	3425	0.344	140 ± 70
[N II]	6584	-0.326	1.6:
[S II]	4073	0.178	<2.0

Table (5-3)

Continuum fluxes from the central star and from the whole nebula. The fluxes are in units of 10^{-13} erg cm^{-2} s^{-1} $Å^{-1}$.

λ(Å)	I_λ(nebcont)	I_λ(star)	I_λ(tot)	I_λ(tot; ANS)
1550	4.99	27.70	32.69	32.15 ± 0.23
1800	4.75	16.02	20.77	19.21 ± 0.19
2200	2.74	7.60	10.34	10.75 ± 0.07
2500	2.48	4.69	7.17	11.46 ± 0.15
3300	2.05	1.63	3.68	3.43 ± 0.02

Table (5-4)

Input parameters for the nebular models of NGC 4361.

		Present Model	AK Model C	ARCK Model 1
Angular Diameter	Θ (arc-sec)	81	81	81
Distance	D (pc)	910	1000	1900
Stellar Temperature	T_{eff} (K)	140,000	100,100	150,000
Stellar Radius	$R_s(R_o)$	0.08	0.19	0.11
Luminosity	L (L_o)	2200	3220	5470
Inner Radius	R_{inner}(pc)	0.01	0.062	
Outer Radius	R_{outer}(pc)	0.179	0.131	0.3663
$(R_{outer} - R_{inner})/R_{outer}$		0.94	0.53	
Mean hydrogen Density	$\langle N_H \rangle$ cm^{-3}	225	500	330
Filling Factor	ξ	1	1	1

Table (5-5)

Adopted ionization thresholds (electron volts).

Element	I	II	III	IV	V	VI
H	13.595					
He	24.580	54.403				
C	11.256	24.376	47.426	64.476		
N	14.530	29.593	47.426	77.450	97.863	
O	13.595	35.108	54.886	77.394	113.873	138.08
Ne	21.559	41.000	63.000	97.020	126.300	157.910
S	10.357	23.400	35.100	47.340	72.500	88.029
Si	8.149	16.340	33.460	45.130	166.730	
Mg	7.644	15.031	80.120	109.300	141.200	

Table (5-6)

Abundances in NGC 4361. Numbers in brackets denote adopted values.

Element	Present Model	AK Model c	ARCK Model 1	Solar
H	12.00	12.00	12.00	12.00
He	11.04	11.04	11.096	11.00:
C	8.36	7.60	(7.7)	8.66
N	(7.65)	<6.60	(7.48)	7.98
O	8.30	8.50	8.10	8.91
Ne	7.93	7.90	7.45	8.05
S	(7.18)	(7.20)	(6.18)	7.23
Si	(7.00)			
Mg	(5.85)			
Ar		6.20	6.23	6.57

Table (5-7)

Comparison of calculated and observed IUE fluxes (corrected for reddening with c=0.05).

Ion	λ(Å)	Region A Flux (10^{-13} erg cm^{-2} s^{-1})			Region B I(λ) / I(λ1640)	
		Observed	Present Model	AK Model C	Observed	Present Model
He II	1640	88 ± 38	98	--	100	100
C III]	1908	28 ± 5	28	29	53 ± 17	56 ± 9
C IV	1549	231 ± 39	220	210	253 ± 33	240 ± 11
[Ne IV]	2423	40 ± 4	38	102	40 ± 10	50 ± 2

Table (5-8)

Comparison of calculated and observed fluxes in different apertures. The observed fluxes are corrected for extinction (c = 0.05).

Ion	λ(Å)	Aperture	Absolute flux (10^{-13} erg cm^{-2} s^{-1})		Fraction of total flux	
			Observed	Model	Observed	Model
Hβ	4861	10" circular	7 ± 3	9	0.021	0.027
		IUE large		25		0.074
		21" circular	36 ± 4	42	0.109	0.125
		40" circular	123 ± 11	142	0.373	0.421
		Whole nebula	330 ± 40	337	1.0	1.0
He II	4686	10" circular	11 ± 6	11	0.034	0.028
		IUE large		39		0.100
		21" circular	50 ± 2	49	0.154	0.126
		40" circular	160 ± 7	166	0.492	0.426
		Whole nebula	325 ± 15	390	1.0	1.0
[O III]	5007	10" circular	21 ± 3	18	0.019	0.015
		IUE large		52		0.042
		21" circular	91 ± 6	84	0.083	0.068
		40" circular	345 ± 16	346	0.314	0.279
		Whole nebula	1100 ± 200	1240	1.0	1.0

Table (5-9)

Comparison of calculated and observed optical line fluxes, corrected for reddening (c = 0.05) and expressed relative to Hβ. The observed fluxes are from Barker (1978) and TPP (region a), see Table (1-4).

Ion	λ(Å)	I(λ) / I(Hβ)		Model / Obseved		
		Observed	Present Model	Present	AK	ARCK
Hδ	4102	28	26	0.93		
Hγ	4340	48	47	0.98		
Hβ	4861	100	100	1.0	1.0	1.0
Hα	6563	288	302	1.05		
He I	5876	<2.0	0.5	>0.25	0.0	
He II	6486	120	116	0.97	0.99	0.85
[O II]	3728	6.3	3.0	0.48	0.38	
[O III]	4363	9.5	8.0	0.84	1.08	1.02
[O III]	5007	297	280	0.94	0.99	1.04
[Ne III]	3869	27	24	0.89	1.04	0.86
[Ne IV]	4725	3.0	3.1	1.03	0.87	1.00
[Ne V]	3425	140±70	260	1.86	2.88	0.66
[N II]	6584	1.6:	1.5	0.94	0.02	
[S II]	4072	<2.0	0.1	>0.05		

Table (5-10)

Line ratios sensitive to physical conditions in NGC 4361.

Ratio		Observed	Model	Deviation
C^{+2}	λλ1907/1909	1.44	1.47	2 %
C^{+3}	λλ1548/1551	2.00	1.98	1 %
C^{+3}/ C^{+2}	λλ1549/1908	8.25	7.86	5 %
O^{+2}	λλ5007/4363	32.0	35.0	9 %
Ne^{+3}	λλ2423/4725	13.3	12.3	8 %
Ne^{+3}/ Ne^{+2}	λλ2423/3869	1.48	1.58	6 %

Table (5-11)

Values of T_o (X^{+m}) and , in brackets, t^2 (X^{+m}).

X	I	II	III	IV	V	VI
H	17160(0.0032)	17900(0.0101)				
He	16880(0.0014)	17130(0.0031)	17940(0.0103)			
C	16770(0.0008)	16860(0.0012)	17030(0.0021)	17360(0.0040)	18620(0.0135)	
N	16760(0.0008)	16870(0.0012)	17110(0.0025)	17650(0.0059)	18570(0.0118)	21010(0.0222)
O	16660(0.0004)	16790(0.0009)	17010(0.0021)	17680(0.0062)	18960(0.0154)	21530(0.0250)
Ne	16670(0.0004)	16740(0.0007)	16880(0.0013)	17410(0.0043)	18540(0.0117)	20950(0.0228)
S	16720(0.0006)	16780(0.0008)	16920(0.0014)	17230(0.0030)	17880(0.0070)	18700(0.0115)
Si	16750(0.0008)	16790(0.0009)	16970(0.0017)	17240(0.0035)	18230(0.0113)	20970(0.0291)
Mg	16680(0.0005)	16760(0.0007)	16900(0.0014)	17450(0.0043)	18860(0.0132)	21680(0.0241)

Table (5-12)

Fractional abundances and threshold optical depths in the model.

Radius (pc)	T_e (10^4K)	N_e (cm^{-3})	$\chi(H^+)$	$\chi(He^+)$	$\chi(He^{+2})$	$\tau(H^o)$	$\tau(He^o)$	$\tau(He^+)$
0.010	3.00	320	1.00	1.8(-4)	1.000	0.0	0.0	0.0
0.015	2.85	330	1.00	4.4(-4)	1.000	2.0(-4)	3.9(-9)	2.1(-4)
0.020	2.75	342	1.00	8.2(-4)	0.999	6.2(-4)	2.1(-8)	6.7(-4)
0.022	2.72	346	1.00	1.0(-3)	0.999	8.8(-4)	3.6(-8)	9.6(-4)
0.027	2.61	360	1.00	1.6(-3)	0.998	1.8(-3)	1.1(-7)	2.0(-3)
0.032	2.51	371	1.00	2.4(-3)	0.998	3.3(-3)	3.1(-7)	3.6(-3)
0.037	2.42	379	1.00	3.4(-3)	0.997	5.5(-3)	7.1(-7)	6.0(-3)
0.042	2.33	385	1.00	4.5(-3)	0.995	8.5(-3)	1.5(-6)	9.3(-3)
0.046	2.27	387	1.00	5.6(-3)	0.994	0.012	2.6(-6)	0.013
0.051	2.20	386	1.00	6.9(-3)	0.993	0.017	4.5(-6)	0.018
0.056	2.14	385	1.00	8.5(-3)	0.992	0.023	7.5(-6)	0.025
0.061	2.08	383	1.00	0.010	0.990	0.030	1.2(-5)	0.033
0.066	2.03	380	1.00	0.012	0.988	0.038	1.8(-5)	0.042
0.071	1.99	376	1.00	0.014	0.986	0.047	2.6(-5)	0.052
0.076	1.95	370	1.00	0.016	0.984	0.058	3.7(-5)	0.064
0.081	1.91	363	1.00	0.017	0.982	0.069	5.0(-5)	0.078
0.083	1.90	360	1.00	0.018	0.982	0.074	5.6(-5)	0.083
0.088	1.87	351	1.00	0.020	0.980	0.087	7.4(-5)	0.098
0.093	1.85	341	0.99	0.022	0.978	0.10	9.5(-5)	0.11
0.101	1.81	328	0.99	0.025	0.975	0.12	1.3(-4)	0.14
0.108	1.78	315	0.99	0.029	0.971	0.15	1.8(-4)	0.17
0.116	1.75	300	0.99	0.032	0.968	0.17	2.3(-4)	0.20
0.123	1.73	289	0.99	0.035	0.965	0.20	3.0(-4)	0.23
0.131	1.71	277	0.99	0.039	0.961	0.22	3.7(-4)	0.27
0.138	1.69	266	0.99	0.042	0.958	0.25	4.6(-4)	0.30
0.146	1.68	254	0.99	0.046	0.954	0.28	5.5(-4)	0.34
0.153	1.67	244	0.99	0.050	0.950	0.31	6.6(-4)	0.38
0.161	1.66	234	0.99	0.054	0.946	0.34	7.8(-4)	0.42
0.168	1.65	224	0.99	0.059	0.941	0.37	9.1(-4)	0.46
0.177	1.64	215	0.99	0.065	0.935	0.41	1.0(-3)	0.51
0.179	1.64	214	0.99	0.067	0.933	0.42	1.1(-3)	0.53

Table (5-13)

Average fractional ionic abundances for the model. Numbers in brackets are powers of ten.

Element	I	II	III	IV	V	VI	VII
H	0.1055 (-2)	0.9989					
He	0.2412 (-4)	0.0429	0.9571				
C	0.5451 (-5)	0.4506 (-2)	0.1587	0.3617	0.4750		
N	0.1692 (-5)	0.2695 (-2)	0.2142	0.5141	0.2192	0.0498	
O	0.1177 (-5)	0.1152 (-2)	0.1487	0.6267	0.2090	0.0140	0.5050 (-3)
Ne	0.2154 (-7)	0.1354 (-3)	0.0628	0.5585	0.3382	0.0400	0.3603 (-3)
S	0.1092 (-6)	0.3326 (-3)	0.0526	0.4298	0.2320	0.2342	0.0510
Si	0.6841 (-4)	0.0100	0.0776	0.2472	0.6547	0.0103	
Mg	0.3814 (-4)	0.6348 (-3)	0.1264	0.5397	0.3156	0.0177	

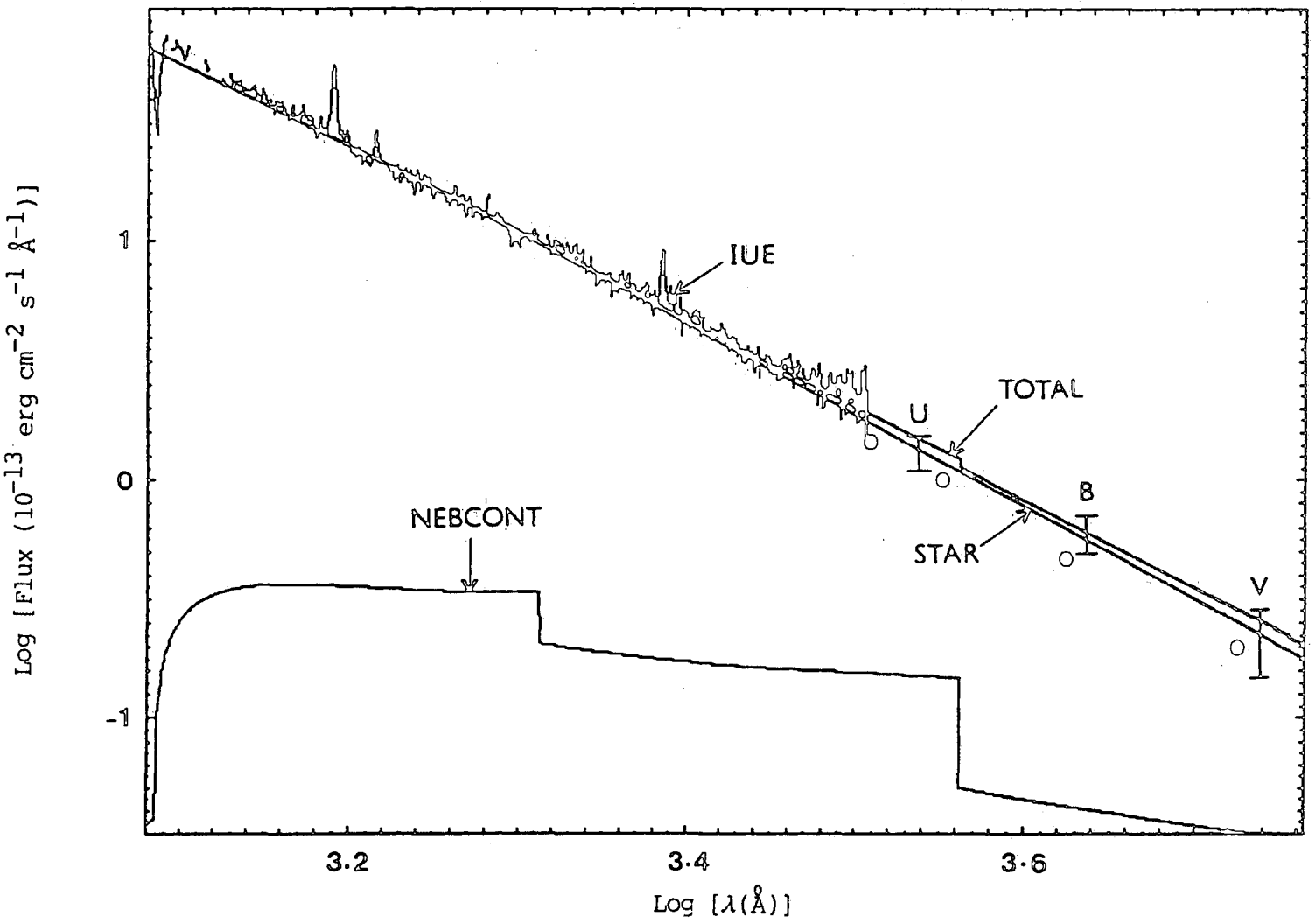

Figure (5-1): The UV spectrum and optical continuum measurements of NGC 4361. The curves shown are: the merged SWP 7779 and LWR 6779 spectra, IUE; the narrow band measurements of Martin (1984),O; the fluxes computed from UBV magnitudes, I; the calculated stellar continuum, STAR; the calculated nebular continuum, NEBCONT; and the sum of the calculated stellar and nebular continua; TOTAL. The observed continuum fluxes are corrected for extinction (c = 0.05).

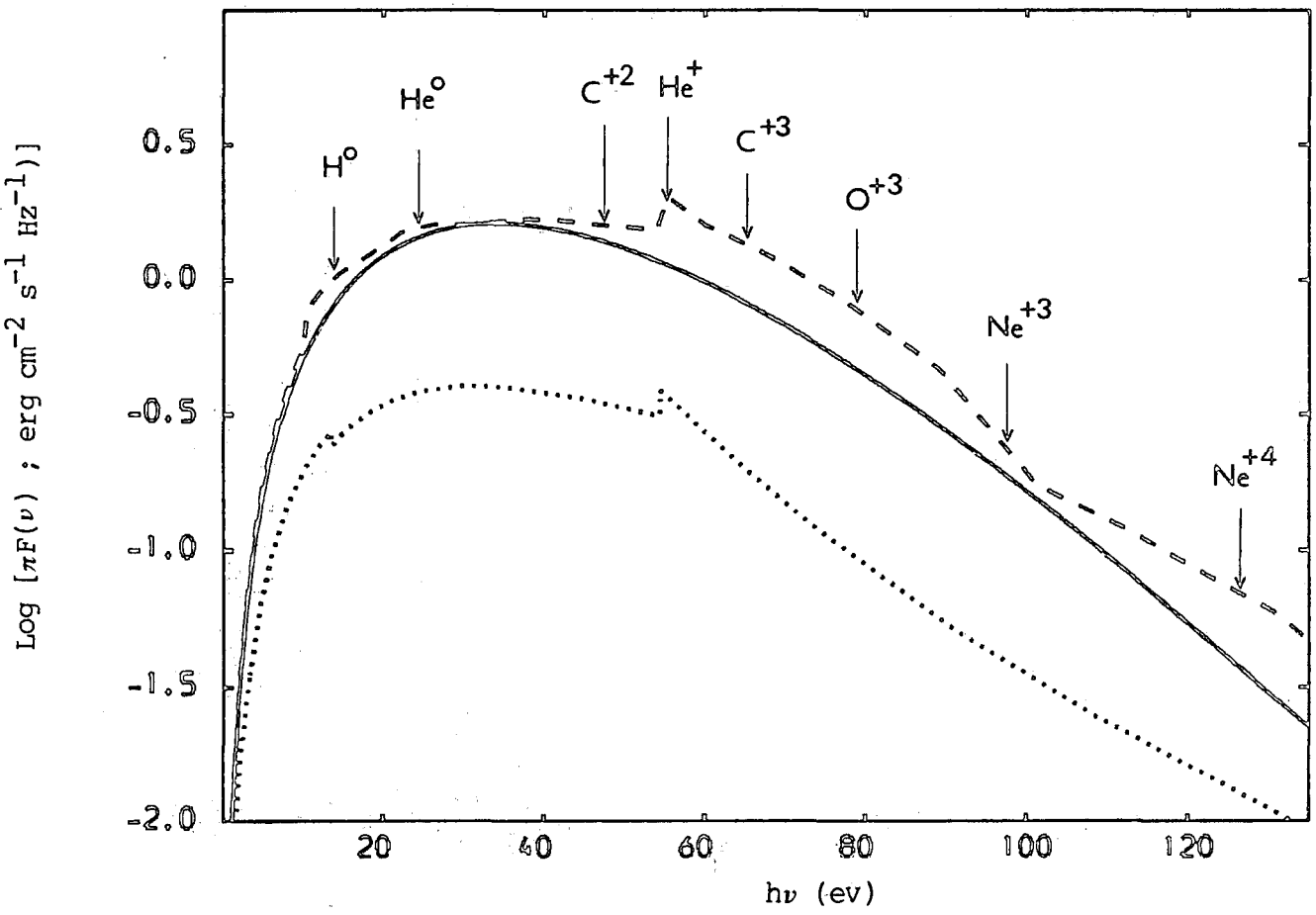

Figure (5-2): The surface flux distributions used for the present model (——— ; blackbody at 140,000 K), model 1 of ARKC (— — —; modified blackbody at 150,000 K), and model C of AK (····· ; non-LTE model atmosphere with effective temperature of 100,000 K and gravity g = 10^5 cm s^{-2}). The ionization thresholds of several ions are indicated.

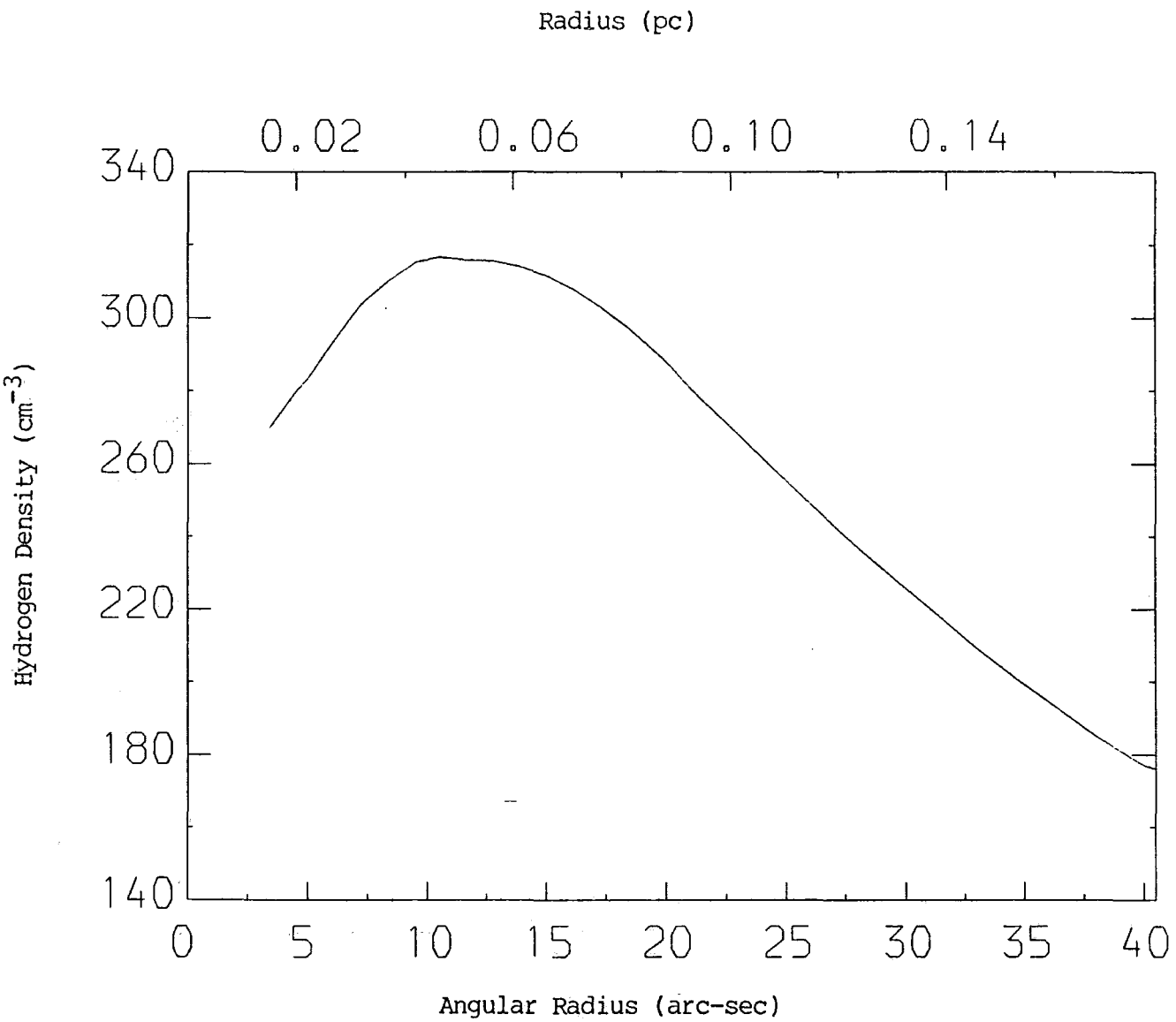

Figure (5-3): The hydrogen density distribution adopted for the model. The radial scale is given both in parsecs and in seconds of arc as seen from the earth.

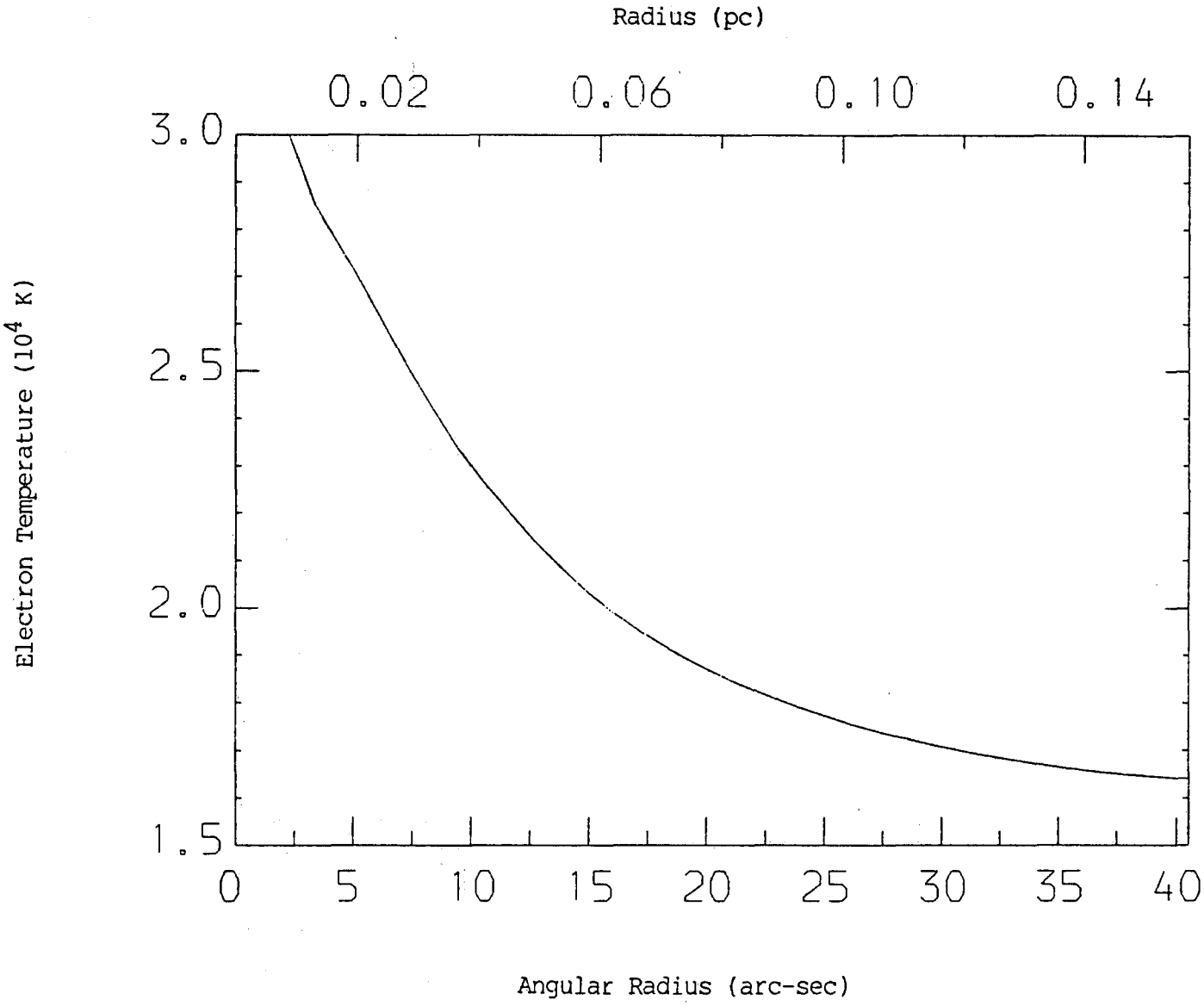

Figure (5-4): The run of electron temperature in the model.

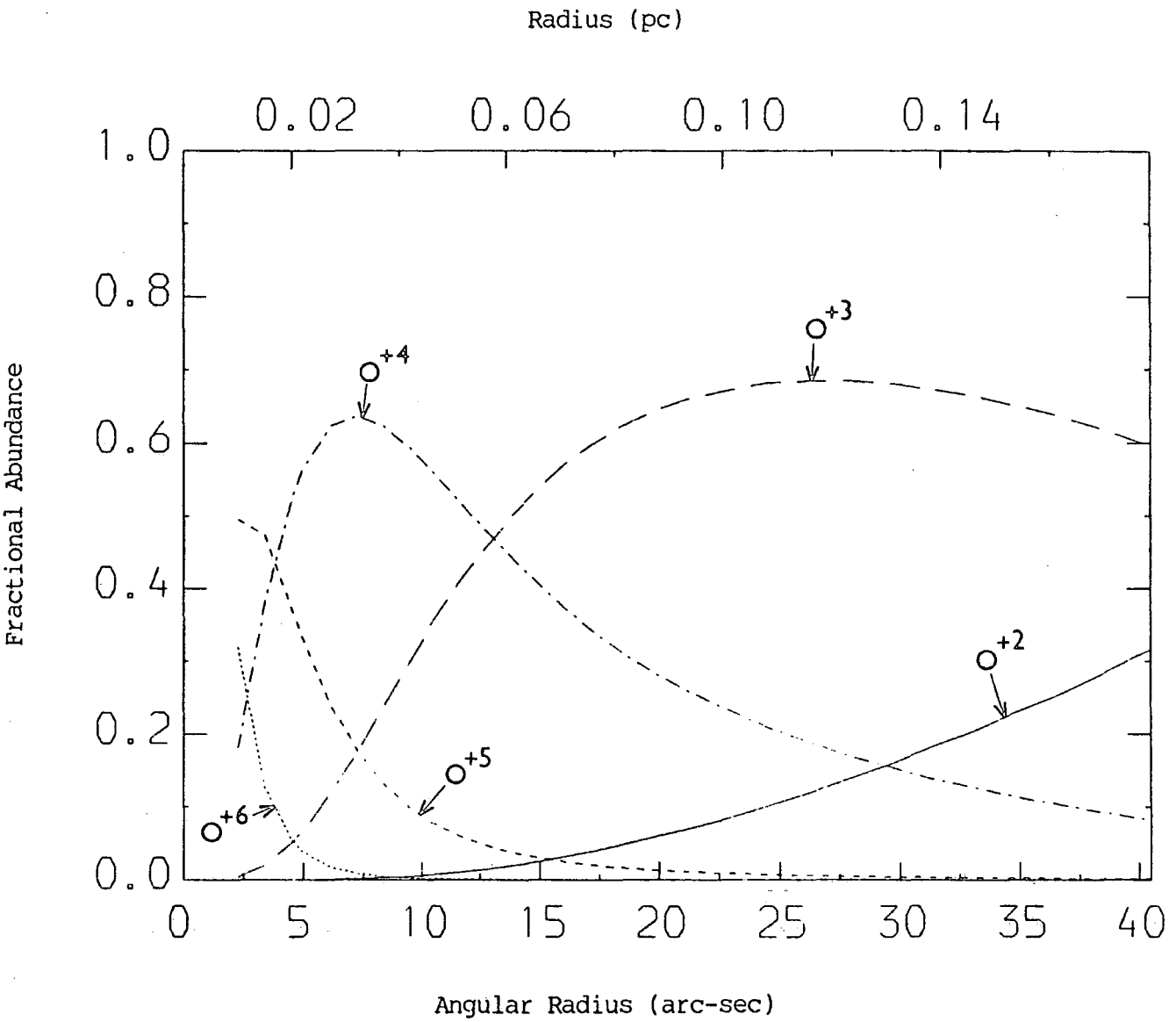

Figure (5-5): The ionization equilibrium for O ions.

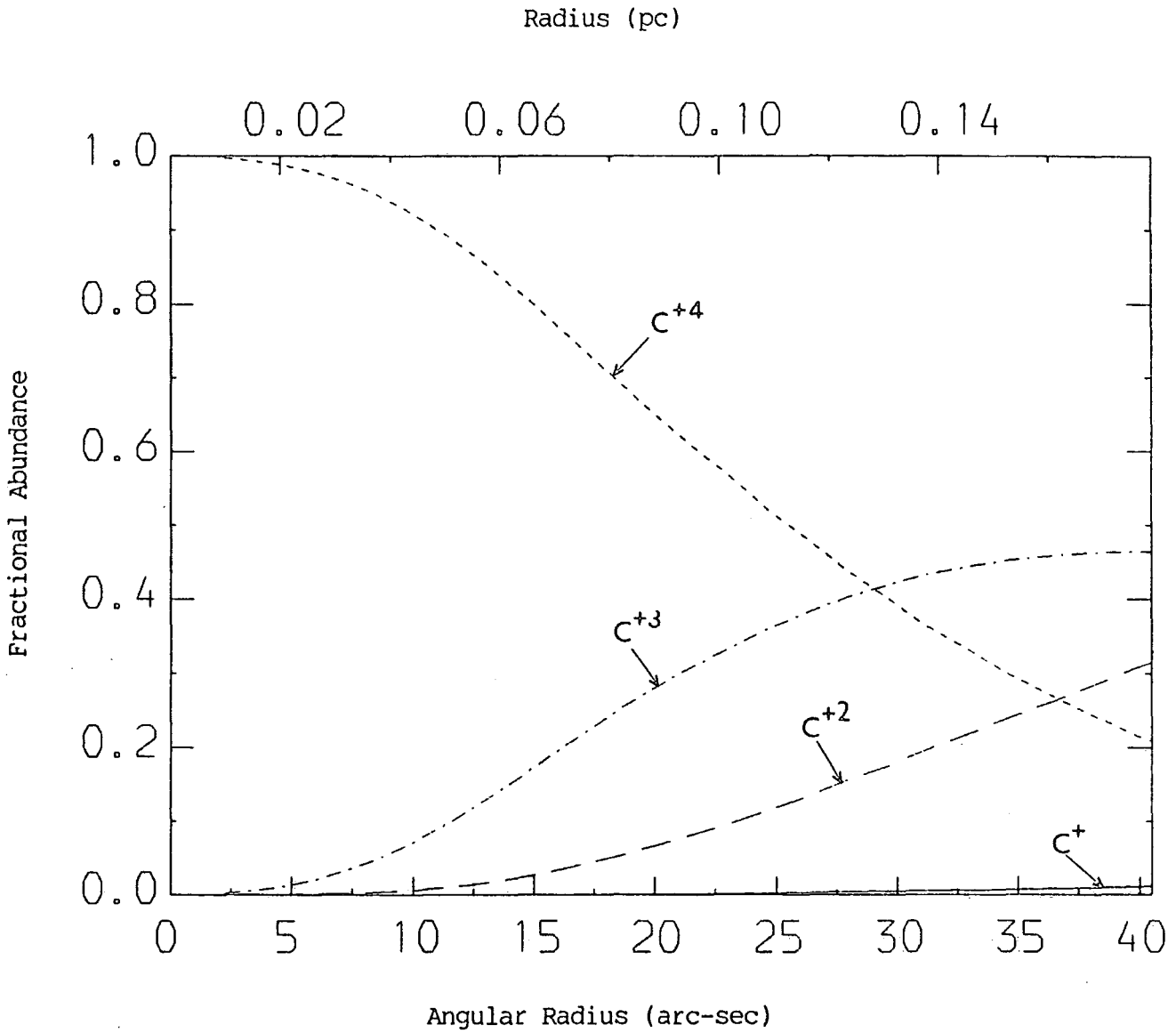

Figure (5-6): The ionization equilibrium for C ions.

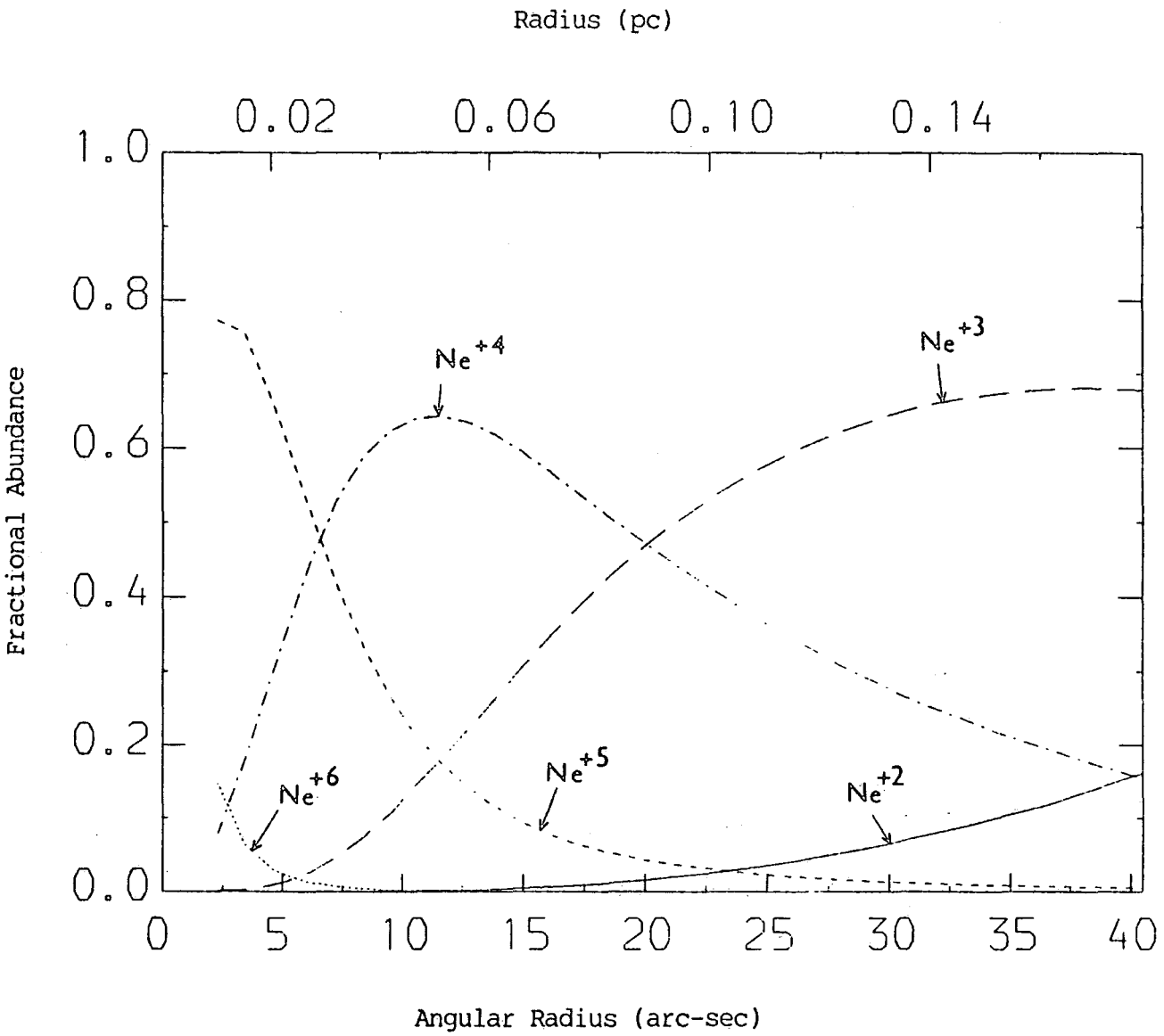

Figure (5-7): The ionization equilibrium for Ne ions.

CHAPTER (6)

SUMMARY AND CONCLUSIONS

6.1 OBSERVATIONS

Observations of planetary nebulae in the ultraviolet, optical, infrared, and radio spectral ranges have been briefly reviewed. Particular attention was given to ultraviolet observations secured with the IUE satellite. Emphasis was placed on the importance of these observations in studies of planetary nebulae, their central stars, and their envelopes.

This thesis concentrates on the planetary nebulae SwSt 1, IC 2501, and NGC 4361. Our own ultraviolet (IUE) observations of these objects were presented and discussed in detail. Results from observations of other workers at optical, infrared, and radio wavelengths were also reported and have been combined with ultraviolet results in order to analyse the physical conditions and abundances in the nebulae.

6.2 PHYSICAL PROCESSES

The atomic scattering processes pertinent to the diagnostics of ionized nebular gases have been discussed. Attention was focused on the most recent atomic parameters, which have been used to obtain numerous diagrams, expressions, and tables so that the observational data can be employed to determine the reddening corrections, electron densities and temperatures, ionic concentrations, and chemical compositions for planetary nebulae.

6.3 REDDENING CORRECTION

The reddening correction c(Hβ) for each object has been determined by several independent methods. In all three cases, the value of c(Hβ)

derived from the λ2200 interstellar absorption feature was less than that obtained from the optically thin radio continuum to Hβ ratio. The discrepancy was particularly large for the case of the very low excitation (VLE) nebula SwSt 1 and it was concluded that, whereas the correction is based on a mean interstellar extinction, variations from object to object may be expected. A similar discrepancy has also been found for the VLE planetary nebula M 1-26 by Adams and Barlow (1983).

6.4 PHYSICAL CONDITIONS IN THE NEBULAE

A detailed analysis of physical conditions and abundances in the three planetary nebulae was based on the combined ultraviolet and optical observations.

The electron density in SwSt 1, determined from the intensity ratio C III λλ1907/1909, is high ($N_e \approx 10^5$ cm^{-3}), consistent with the high emission measure and high critical frequency determined from observations of the thermal radio emission. It would be desirable to make a more reliable determination of the electron temperature in SwSt 1. The value which we derived from the [O III] λλ5007/4363 ratio is subject to some uncertainty owing to the weakness of λ4363. The [O III] λλ5007/1663 ratio gives an inconsistent value of the electron temperature and it was concluded that the feature observed at λ1663 may be attributable entirely to noise. The nebular C/O abundance ratio in this nebula is approximately solar and confirms that the envelope is oxygen-rich, as suggested by infrared spectra which show the silicate emission feature. The carbon-richness of the central star (WC 10) is therefore not reflected in the nebular envelope and may be attributable to a more advanced stage of nucleosynthesis in the core. The hypothesis that SwSt 1 is a young planetary nebula is consistent with current knowledge and available observations.

The electron temperatures and density in the planetary nebula IC 2501 have been determined from the diagnostic forbidden line ratios [O III] λλ5007/4363, [N II] λλ6584/5755, and [O II] λλ3728/2470. It was found that T_e(O III) ≈ 1.04 T_e(N II) ≈ 9400K and N_e(O II) ≈ 2×10^4 cm^{-3}. The electron temperature has also been determined from the intensity ratio of the dielectronic recombination line C II λ1335 to the collisionally excited line C III] λ1908. The derived value was found to be much higher than T_e(O III) and it was concluded that the feature observed at λ1335 is weak and may be attributable entirely to noise. The nebular C/O abundance ratio in IC 2501 was found to be greater than unity, i.e. the envelope is carbon-rich, as suggested by the identification of the SiC feature in the infrared spectrum. It was concluded that Mg^+ is not depleted in IC 2501 and it is possible that much S is tied up in grains.

A spherically symmetric model of the planetary nebula NGC 4361 has been constructed. The density distribution used in the model was obtained from measurements of Hß fluxes through circular apertures. The star was assumed to radiate like a blackbody and absorption by internal dust has been neglected. Abundances were adjusted to reproduce the observed continuum and line fluxes as well as the observed values of ratios which are very sensitive to physical conditions in the nebula. Charge exchange reactions with hydrogen and dielectronic recombination processes were included. The small-scale filamentary structure and dynamical effects, which may be important in planetary nebulae, were not taken into account. Regarding this model, our main conclusions were :

(1) With a 140,000K blackbody flux distribution and suitable adjustment of various parameters, we were able to obtain reasonable agreement with observations for most spectral features. [Ne V] λ3425 was the only line

for which the flux given by the model is significantly larger than that observed. The stellar spectrum which we have used may not be correct at $h\nu > 97$ ev (the ionization limit of Ne^{+3}).

(2) The total energy radiated by the nebula in collisionally excited lines was determined by the slope of the stellar continuum between 912Å and 228Å. This is equivalent to measuring the temperature of the central star by Stoy's method.

(3) The stellar flux for $\lambda < 228$Å which we infer from the He II nebular emission lines is model independent.

(4) The nebular model is optically thin for H and He ionizing continua.

(5) We find that $\langle N_H \rangle = 225$ cm^{-3}, $\langle N_e \rangle = 274$ cm^{-3}, and $\langle T_e \rangle = 17{,}600$ K.

(6) The ionization equilibrium is well determined for H, He, C, O, and Ne ions. Results for other ions are less reliable.

(7) The He, C, O, and Ne abundances should be well determined. There is a possibility, not considered in the model, that the C IV λ1549 line is attenuated by dust internal to NGC 4361. However, even if dust absorption leads to a C^{+3} abundance which is 3 time larger, as in the case of NGC 7662, the abundance of C would increase by only a few per cent.

(8) The present model was compared with previous models of NGC 4361. It was concluded that the inclusion in the model nebula of charge exchange and dielectronic recombination processes greatly improves the ionization and thermal structure of NGC 4361.

6.5 CENTRAL STARS

The stellar ultraviolet and optical continuum of each object was obtained by subtracting the calculated nebular continuum from the total observed continuum. The slope of this stellar continuum was fitted by

a blackbody flux distribution and the colour temperature of the central star, T_C , was derived. The stellar flux at the distance of the earth (at λ1400) was compared with the nebular radio continuum and H or He lines to derive the equivalent blackbody (Zanstra) temperature of the star, T_Z .

A large difference between T_C and T_Z(He II) was found for the central star of NGC 4361, but the nebula is optically thin in the He^+ continuum. This fact may account for T_Z(He II) being so low.

We observed a few P Cygni type line profiles in the UV spectrum of the central star of SwSt 1. The Sobolev approximation was used to analyse the Si IV resonance doublet profile. We find that a stellar wind with terminal velocity V_∞ = 2000 Km s^{-1} and mass-loss rate $\dot{M} = 2.8\times10^{-8}$ ($M_\odot$ yr^{-1}) can explain the observed profiles.

6.6 FUTURE WORK

A paper which summarizes the results obtained from the nebular model of NGC 4361 is in preparation and will be submitted for publication in the near future. I will try to include argon in the computer programme for nebular models, so that future work will lead to further important information. For the sake of model calculations, accurate fits to the most recent atomic data will be made. Future work may also include calculations of atomic parameters.

APPENDIX A

Consider the equations

$$N_e \sum_{j<i}^{i-1} N_j q_{ji} + \sum_{j>i}^{L} N_j [A_{ji} + N_e q_{ji}] = N_i [\sum_{i>j}^{L} A_{ij} + N_e \sum_{j\neq i}^{L} q_{ij}] \quad (3.39)$$

and

$$n_i = N_i / N . \quad (3.41)$$

Assuming a three-level atom (L = 3). Denote the bottom, middle, and top levels by 1, 2, and 3. From the above equations we obtain

$$n_1 N_e q_{13} + n_2 N_e q_{23} = n_3 (N_e q_{32} + N_e q_{31} + A_{32} + A_{31}) \quad (A1)$$

for level 3 , and

$$n_1 N_e q_{12} + n_3 (N_e q_{32} + A_{32}) = n_2 (N_e q_{21} + N_e q_{23} + A_{21}) \quad (A2)$$

for level 2. We can solve (A1) and (A2) for the ratio n_3/n_2. Thus :

$$\frac{n_3}{n_2} = \frac{q_{23}/q_{13} + (q_{21} + q_{23})/q_{12} + A_{21}/(N_e q_{12})}{q_{32}/q_{12} + (q_{32} + q_{31})/q_{13} + A_{32}/(N_e q_{12}) + (A_{32} + A_{31})/(N_e q_{13})} . \quad (A3)$$

Define

$$N_e q_{ij} = C \Omega_{ij} \chi_{ij} / \omega_i \quad ; \quad i < j \quad (A4)$$

$$N_e q_{ji} = C \Omega_{ji} / \omega_j \quad ; \quad j > i \quad (A5)$$

with

$$\chi_{ij} = \exp(-\Delta E_{ij}/KT_e) \quad (A6)$$

and

$$C = 8.63 \times 10^{-4} x , \quad (A7)$$

where

$$x = 10^{-2} N_e / T_e^{1/2} . \quad (A8)$$

Substituting (A4) to (A8) in (A3), we obtain

$$\frac{n_3}{n_2} = \frac{\frac{\omega_1}{\omega_2}\left[\frac{\Omega_{23}\,\chi_{23}}{\Omega_{13}\,\chi_{13}} + \frac{\Omega_{21}}{\Omega_{12}\,\chi_{12}} + \frac{\Omega_{23}\,\chi_{23}}{\Omega_{12}\,\chi_{12}} + \frac{\omega_2\,A_{21}}{C\,\Omega_{12}\,\chi_{12}}\right]}{\frac{\omega_1}{\omega_3}\left[\frac{\Omega_{32}}{\Omega_{13}\,\chi_{13}} + \frac{\Omega_{31}}{\Omega_{13}\,\chi_{13}} + \frac{\Omega_{32}}{\Omega_{12}\,\chi_{12}} + \frac{\omega_3\,A_{32}}{C\,\Omega_{12}\,\chi_{12}} + \frac{\omega_3\,(A_{32}+A_{31})}{C\,\Omega_{13}\,\chi_{13}}\right]} . \quad (A9)$$

Multiplying both sides of (A9) by $\chi_{12}\,\chi_{23}$ and noting that $\chi_{12}\,\chi_{23} = \chi_{13}$ and $\Omega_{ij} = \Omega_{ji}$, we obtain

$$\frac{n_3}{n_2} = \frac{\frac{\omega_3}{\omega_2}\left[1 + \frac{\Omega_{23}}{\Omega_{13}} + \frac{\Omega_{23}\,\chi_{23}}{\Omega_{12}} + \frac{\omega_2\,A_{21}}{C\,\Omega_{12}}\right]\chi_{23}}{\left[1 + \frac{\Omega_{23}}{\Omega_{13}} + \frac{\Omega_{23}\,\chi_{23}}{\Omega_{12}} + \frac{\omega_3\,A_{32}\,\chi_{23}}{C\,\Omega_{12}} + \frac{\omega_3\,(A_{32}+A_{31})}{C\,\Omega_{13}}\right]} . \quad (A10)$$

Dividing both sides of (A10) by $(1 + \Omega_{23} / \Omega_{13})$, we get

$$\frac{n_3}{n_2} = \frac{\omega_3}{\omega_2}\,\frac{b_3}{b_2}\,\exp\left(-\Delta E_{23}/KT_e\right). \quad (A11)$$

where

$$\frac{b_3}{b_2} = \frac{\left[1 + \xi\,\chi_{23} + \frac{\omega_2\,A_{21}}{C\,\Omega_{12}\,(1+\Omega_{23}/\Omega_{13})}\right]}{\left[1 + \xi\,\chi_{23} + \frac{\omega_3\,A_{32}\,\chi_{23}}{C\,\Omega_{12}\,(1+\Omega_{23}/\Omega_{13})} + \frac{\omega_3\,(A_{32}+A_{31})}{C\,\Omega_{13}\,(1+\Omega_{23}/\Omega_{13})}\right]} , \quad (A12)$$

with

$$\xi = \frac{\Omega_{23} / \Omega_{12}}{1 + \Omega_{23} / \Omega_{13}} . \quad (A13)$$

If $b_3 / b_2 = 1$, equation (A11) reduces to Boltzmann's law [equation (2.43) of the text]. Hence, the factor b expresses the deviation of n from its thermodynamic equilibrium value.

APPENDIX B

Consider equations (A11) and (A12). If $A_{32} << A_{31}$ and $\Delta E_{23} << KT_e$ (so that $\chi_{23} \approx 1$), then

$$\frac{n_3}{n_2} = \frac{\omega_3}{\omega_2} \left[\frac{1 + \xi + \dfrac{\omega_2 A_{21}}{C \Omega_{12} (1 + \Omega_{23}/\Omega_{13})}}{1 + \xi + \dfrac{\omega_3 A_{31}}{C \Omega_{13} (1 + \Omega_{23}/\Omega_{13})}} \right] . \qquad \text{(B1)}$$

In the limit of high density (large C), the term involving the A's drops out. Thus ,

$$\frac{n_3}{n_2} = \frac{\omega_3}{\omega_2} \quad ; \qquad \text{(high density)} \qquad \text{(B2)}$$

In the limiting case of low density (small C), the A term dominates. So that

$$\frac{n_3}{n_2} = \frac{A_{21}}{A_{31}} \frac{\Omega_{13}}{\Omega_{12}} \quad ; \quad \text{(low density)} \qquad \text{(B3)}$$

APPENDIX C

Consider equation (A12). If we can neglect the three terms involving χ_{23}, equation (A11) becomes

$$\frac{n_3}{n_2} = \frac{\omega_3}{\omega_2} \left[\frac{1 + \dfrac{\omega_2 A_{21}}{C \Omega_{12} (1 + \Omega_{23}/\Omega_{13})}}{1 + \dfrac{\omega_3 (A_{32} + A_{31})}{C \Omega_{13} (1 + \Omega_{23}/\Omega_{13})}} \right] \chi_{23} \quad . \tag{C1}$$

or, in a general form,

$$\frac{n_3}{n_2} = \frac{\Omega_{13}}{\Omega_{12}} \frac{A_{21}}{A_{32} + A_{31}} \left[\frac{1 + a_1 x}{1 + a_2 x} \right] \exp(-\Delta E_{23}/KT_e). \tag{C2}$$

where

$$a_1 = \frac{8.63 \times 10^{-4} \ \Omega_{12} (1 + \Omega_{23}/\Omega_{13})}{\omega_2 A_{21}}, \tag{C3}$$

and

$$a_2 = \frac{8.63 \times 10^{-4} \ \Omega_{13} (1 + \Omega_{23}/\Omega_{13})}{\omega_3 (A_{32} + A_{31})} . \tag{C4}$$

If we neglect all terms involving Ω_{23} and Ω_{13} in equations (C3) and (C4), equation (C2) becomes

$$\frac{n_3}{n_2} = \frac{\Omega_{13}}{\Omega_{12}} \frac{A_{21}}{A_{32} + A_{31}} \left[1 + \frac{8.63 \times 10^{-4} \ \Omega_{12} x}{\omega_2 A_{21}} \right] \exp(-\Delta E_{23}/KT_e) \quad . \tag{C5}$$

REFERENCES

Abbott, D.C. (1978): Astrophys. J., **225**, 893.
(1982): Astrophys. J., **259**, 282.

Acker, A. (1978): Astron. Astrophys. Suppl., **33**, 367.

Acker, A., Gleizes, F., Chopinet, M., Marcount, J., Ochsenbein, F., & Roques, J.M. (1982): Catalogue of the Central Stars of Planetary Nebulae, Observatoire de Strasbourg.

Adam, J., & Koppen, J. (1985): Astron. Astrophys., **142**, 461 **(AK)**.

Adams, S. (1982): Unpublished, data quoted by Seaton (1983a).

Adams, S., & Seaton, M.J. (1982): Mon. Not. R. astr. Soc., **200**, 7P.

Adams, S., & Barlow, M.J. (1983): IAU Symp. No. **103**, "Planetary Nebulae", ed. Flower, D.R., D. Reidel, Dordrecht, p. 537.

Aitken, D.K., Roche, P.F., Spenser, P.M., & Jones, B. (1979): Astrophys. J., **233**, 925.

Aitken, D.K., & Roche, P.F. (1982): Mon. Not. R. astr. Soc., **200**, 217.

Aldrovandi, S.M.V., & Pequignot, D. (1973): Astron. Astrophys., **25**, 137.
(1974): Revista Brasileiro de Fisica, **4**, 491.

Aller, L.H. (1951): Astrophys. J., **113**, 125.
(1976): Mem. Soc. R. Sci., Liege **9**, 271.
(1983): IAU Symp. No. **103**, p. 1.
(1984): "Physics of Thermal Gaseous Nebulae", Vol. **112**, p. 54, D. Radiel (Dordrecht-Holland).

Aller, L.H., & Liller, W. (1968): Vol. **7** of Stars and Stellar Systems, "Nebulae and Interstellar Matter", eds. Middlehurst, B., & Aller, L.H., Chicago, University of Chicago Press, p. 483.

Aller, L.H., & Milne, D.K. (1972): Aust. J. Phys., **25**, 91.

Aller, L.H., Bowen, I.S., & Minkoowski, R. (1955): Astrophys. J., **122**, 62.

Aller, L.H., Ross, J.E., Keyes, C.D., & Czyzak, S.J. (1979): Astrophys. Space Sci., **64**, 347 **(ARKC)**.

Allen, C.W. (1973): Astrophysical Quantities, 3d ed., London, Athlone.

Allen, D.A., Baines, D.W.T., Blades, J.C., & Whittet, D.C.B. (1982): Mon. Not. R. astr. Soc., **199**, 1017.

Baker, J.G., & Menzel, D.H. (1938): Astrophys. J., **88**, 52.

Barker, T. (1978): Astrophys. J., **219**, 914.
(1982): Astrophys. J., **253**, 167.
(1983): Astrophys. J., **267**, 630.

Baliunas, S.L., & Butler, S.E. (1980): Astrophys. J. Lett., **235**, L45.

Barlow, M.J. (1979): "Mass Loss and Evolution of Early Type Stars, p. 119, ed. Conti, P.S., & De Loore, C.D., D. Reidel, Dordrecht.
(1983): IAU Symp. No. **103**, p. 105.

Becklin, E.E., Neugebauer, G., & Wynn-Williams, C.G. (1973): Astrophys. Lett., **15**, 87.

Beck, S.C., Lacy, J.H., Townes, C.H., Aller, L.H., Geballe, T.R., & Bass, F. (1981): Astrophys. J., **249**, 592.

Beigman, I.L., & Chichkov, B.N. (1980): J. Phys. B.: Atom. Molec. Phys., **13**, 565.

Bell, R.H., & Seaton, M.J. (1985): J. Phys. B., **18**, 1589.

Bell, R.H. (1979): Ph.D. thesis, University of London.

Benvenuti, P., & Perinotto, M. (1981): Astron. Astrophys., **95**, 127.

Bignell, R.C. (1983): IAU Symp. No. **103**, p. 69.

Black, J. (1983): IAU Symb. No. **103**, p. 91.

Boggess, A., Carr, F.A., Evans, D.C., Fischel, D., Freeman, H.R., Fuechsel, C.F., Klinglesmith, A., Krueger, V.L., Longanecker, G.W., Moore, J.V., Pyle, E.J., Rebar, F., Sizemore, K.O., Sparks, W., Underhill, A.B., Vitagliano, H.D., West, D.K., Macchetto, F., Fitton, B., Barker, P.J., Dunford, E., Gondhaleker, P.M., Hall, J.E., Harrison, V.A.W., Oliver, M.B., Sandford, M.C.W., Vaughan, P.A., Ward, A.K., Anderson, B.E., Boksenberg, A., Coleman, C.I., Snijders, M.A.J., & Wilson, R. (1978): Nature **257**, 372.

Bohlin, R.C., Marionni, P.A., & Stecher, I.P. (1975): Astrophys. J., **202**, 415.

Bohlin, R.C., Holm, A.V., Savage, B.D., Snijders, M.A.J., & Sparks, W.M. (1980): Astron. Astrophys., **85**, 1.

Boksenberg, A., Carnochan, D., Cahn, J., & Wyatt, S.P. (1975): Mon. Not. R. astr. Soc., **172**, 395.

Bowen, I.S. (1935): Astrophys. J., **81**, 1.

Bregman, J.D. (1978): Pub. Astron. Soc. Pac., **90**, 548.

Brocklehurst, M. (1970): Mon. Not. R. astr. Soc., **148**, 417.
(1971): Mon. Not. R. astr. Soc., **153**, 471.
(1972): Mon. Not. R. astr. Soc., **157**, 211.

Brown, R.L., & Mathews, W.G. (1970): Astophys. J., **160**, 939.

Burke, P.G., Hibbert, A., & Hobb, W.D. (1971): J. Phys. B., **4**, 153.

Burgess, A. (1958): Mon. Not. R. astr. Soc., **118**, 477.
(1964a): Mem. R. astr. Soc., **69**, 1.
(1964b): Astrophys. J., **139**, 776.
(1965): Astrophys. J., **141**, 1588.

Burgess, A., & Seaton, M.J. (1960a): Mon. Not. R. astr. Soc., **120**, 121
(1960b): Mon. Not. R. astr. Soc., **5**, 34.
(1960c): Mon. Not. R. astr. Soc., **121**, 76.

Butler, S.E. (1979): Phys. Rev. A., **20**, 2317.

Butler, S.E., Heil, T.C., & Dalgarno, A. (1980): Astrophys. J., **241**, 442.

Butler, S.E., & Dalgarno, A. (1979): Astrophys. J., **234**, 765.
(1980): Astrophys. J., **241**, 838.

Butler, S.E., Mendoza, C., & Zeippen, C.J. (1985): Mon. Not. R. astr. Soc., **213**, 345

Cahn, J.H., & Kaler, J.B. (1971): Astrophys. J. Suppl., **22**, 319.

Calabretta, M.R. (1982): Mon. Not. R. astr. Soc., **199**, 141.

Campbell, W.W., & Moore, J.V. (1918): Publ. Lick. Obs., **13**, 75.

Carlson, E.D., & Henize, K.G. (1979): Vistas in Astronomy **21**, 213.

Castor, J.I. (1970): Mon. Not. R. astr. Soc., **149**, 111.

Castor, J.I., & Lamers, H.J. (1979): Astrophys. J. Suppl., **39**, 481.

Castor, J.I., Abbott, D.C., & Klein, R.I. (1975): Astrophys. J., **195**, 157.

Castor, J.I., Lutz, J.H., & Seaton, M.J. (1981): Mon. Not. R. astr. Soc., **194**, 547, **(CLS)**.

Chambaud, G., Launay, J.M., Levy, B., Millie, P., Roueff, E., & Tran Minh, F. (1980): J. Phys. B., **13**, 4205.

Chapman, R.D., & Henry, R.J. (1971): Astrophys. J., **168**, 169.
(1972): Astrophys. J., **173**, 243.

Clavel, J., Flower, D.R., & Seaton, M.J. (1981): Mon. Not. R. astr. Soc., **197**, 301.

Clegg, R.E.S., & Seaton, M.J. (1983): IAU Symp. No. **103**, p. 536.

Code, A.D., Davis, J., Bless, R.C., & Hanbury, B.R. (1976): Astrophys. J., **203**, 417.

Cohen, M., & Barlaw, M.J. (1974): Astrophys. J., **193**, 401.

Cohen, M. (1975): Mon. Not. R. astr. Soc., 173, 489.

Czyzak, S.J. (1968): Vol. 7 of Stars and Stellar Systems, p. 403.

Czyzak, S.J., Aller, L.H., Kaler, J.B., & Faulkner, D.J. (1966): Astrophys. J., 143, 327.

Czyzak, S.J., & Krueger, T.K. (1963): Mon. Not. R. astr. Soc., 126, 177.

Dalgarno, A., & Sternberg, A. (1982): Astrophys. J., 257, L87.

Daub, C.T. (1982): Astrophys. J., 260, 612.

Davies, P.C.W., & Seaton, M.J. (1969): J. Phys. B., 2, 757.

Dinerstein, H.L (1980): Astrophys. J., 237, 486.
(1983): IAU Symp. No. 103, p. 79.

Dopita, M.A., Mason, D.J., & Robb, W.D. (1976): Astrophys.J., 207, 102.

Drummond, J.D. (1980): Thesis, New Mexico State University.

Dubau, J., & Volonte, S. (1980): Rep. Prog. Phys., 43, 199.

Eissner, W., & Seaton, M.J. (1972): J. Phys. B., 5, 2187.

Eissner, W., & Zeippen, C.J. (1981): J. Phys. B., 14, 2125.

Feibelman, W.A., Boggess, A., McCracken, C.W., & Hobbs, R.W. (1981): Astrophys. J., 246, 807.

Field, G.B., & Steigman, G. (1971): Astrophys. J., 166, 59.

Flower, D.R. (1968): IAU Symp. No. 34, Planetary Nebulae, eds. Osterbrock, D.E., & O'Dell, C.R., D. Reidel, Dordrecht, p. 205.
(1969): Mon. Not. R. astr. Soc., 146, 171-185; 243-263.
(1980): Mon. Not. R. astr. Soc., 193, 511.
(1983): "Atoms in Astrophysics", eds. Burke, P.G., Eissner, W.B., Hummer, D.G., & Percival, I.C., Plenum Press, New York, p. 289.

Flower, D.R., & Penn, C.J. (1981): Mon. Not. R. astr. Soc., 194, 13P.
(1983): IAU Symp. No. 103, p. 519.

Flower, D.R., & Seaton, M.J. (1969a): Computer Phys. Comm., 1, 31.
(1969b): Mem. Soc. R. Sci. Liege, Ser. V, 17, 251.

Flower, D.R., Penn, C.J., & Seaton, M.J. (1982): Mon. Not. R. astr. Soc., 201, 39P.

Flower, D.R., Goharji, A., & Cohen, M. (1984): Mon. Not. R. astr. Soc., 206, 293 (Paper I).

Forrest, W.J., Houck, J.R., & McCarthy, J.F. (1981): Astrophys. J., 248, 195.

Gaunt, J.A. (1930): "Continuous Absorption", Phil. Trans. Roy. Soc., London, A229, 163.

Gargaud, M., Hanssen, J., McCarroll, R., & Valiron, P. (1981): J. Phys. B., 14, 2259.

Garstang, R.H. (1968): IAU Symp. No. 34, p. 143.

Gebbie, K.B. (1968): IAU Symp. No. 34, p. 222.

Gillett, F.C., Low, F.J., & Stein, W.A. (1967): Astrophys. J., 149, L97.

Gillett, F.C., Forrest, W.J., & Merrill, K.M. (1973): Astrophys. J., 183, 87.

Goharji, A., & Adams, S. (1984): Mon. Not. R. astr. Soc., 219, 683, **(Paper II)**.

Gordon, W. (1929): Ann. Phys., Paris, 2, 5, 1051.

Gould, R.J. (1978): Astrophys. J., 219, 250.

Grandi, S.A. (1976): Astrophys. J., 206, 658.

Grasdalen, G.L., & Joyce, R.R. (1976): Astropys. J., 205, L11.

Grasdalen, G.L. (1979): Astrophys. J., 229, 587.

Gudworth, K.M. (1974): Astron. J., 79, 1384.

Hall, J.S. (1937): Astrophys. J., 85, 145.

Harrington, J.P. (1967): Ph. D. Thesis, Ohio State University.
(1968): astrophys. J., 152, 943.
(1972): Astrophys. J., 176, 127.

Harrington, J.P., Lutz, J.H., Seaton, M.J., & Stickland, D.J. (1980): Mon. Not. R. astr. Soc., 191, 13 **(HLSS)**.

Harrington, J.P., Seaton, M.J., Adams, S., & Lutz, J.H. (1982): Mon. Not. R. astr. Soc., 199, 517 **(HSAL)**.

Harman, R.J., & Seaton, M.J. (196): Mon. Not. R. astr. Soc., 132, 15.

Hawley, S.A., & Grandi, S.A. (1978): P.A.S.P., 90, 125.

Heap, S., Aller, L.H., & Czyzak, S.J. (1969): Astrophys. J., 157, 607.

Hebb, M.H., Menzel, D.H. (1940): Astrophys. J., 92, 408.

Heil, T.G., & Dalgarno, A. (1979): J. Phys. B., **12**, L557.

Henry, R.J. (1970): Astrophys. J., **161**, 1153.

Hidalgo, M.B. (1968): Astrophys. J., **153**, 981.

Higgs, L.A. (1971): Publ. Astrophys. Branch, Nat. Res. Counc. Canada **1**, 1.

Holm, A.V. (1972): in Scientific Results from OAO-2, ed. Code, A.D., NASA SP-310, p. 229.

Hummer, O.G., & Mihalas, D. (1970): Mon. Not. R. astr. Soc., **147**, 339.

Husfeld, D., Kudritzki, P.P., Simon, K.P., & Clegg, R.E.S. (1984): Astron. Astrophys., **134**, 139.

Johnson, H.L. (1966): Vol. **7** of Stars and Stellar systems, p. 167.

Johnson, H.L., Balick, B., & Thompson, A.R. (1979): Astrophys. J., **233**, 919.

Kaftan-Kassim, M.A. (1966): Astrophys. J., **145**, 658.

Kaler, J.P. (1976a): Astrophys. J. Suppl., **31**, 517.
(1976b): Astrophys. J., **210**, 113.
(1978): Astrophys. J., **226**, 947.
(1979): Astrophys. J., **228**, 163.

Kaler, J.B., Aller, L.H., & Czyzak, S.J., & Epps, H.W. (1976): Astrophys. J. Suppl., **31**, 163.

Kelly, H.P. (1964): Phys. Rev., **136**, B896.

Khromov, G.S., & Moreoz, V.I. (1972): Soviet Astron. J., **15**, 892.

Kohoutek, L., & Martin, W. (1981): Astron. Astophys. Suppl. **44**, 325 **(KM)**.

Koppen, J., & Wehrse, R. (1983): IAU Symp. No. **103**, p. 518.

Krishna Swamy, K.S., & O'Dell, C.R. (1968): Astrophys. J., **151**, L61.

Krueger, T.K., & Czyzak, S.J. (1970): Proc. R. Soc. Lond. A, **318**, 531.

Kwok, S., Purton, C.R., & Keenan, D.W. (1981): Astrophys. J., **250**, 232.

Kwok, S. (1980): Astrophys. J., **236**, 592.

Lambert, D.L., & Luck, R.E. (1978): Mon. Not. R. astr. Soc., **183**, 79.

Lamers, H.J. (1983): Diffuse Matter in Galaxies, ed. Audouze, J. et al., Dordrecht, D. Reidel, p. 53.

Lamers, H.J., & Morton, D.C. (1976): Astrophys. J. Suppl., **32**, 715.

Laughlin, C., & Victor, G.A. (1974): Astrophys. J., **192**, 551.
(1979): Astrophys. J., **234**, 407.

Liller, W., & Shao, C.H. (1968): IAU Symp. No. **34**, p. 320.

Loulergue, M., & Nussbaumer, H. (1976): Astron. Astrophys., **51**, 163.

Lucy, L.B. (1971): Astrophys. J., **163**, 95.

Lutz, J.H., & Carnochan, D.J. (1979): Mon. Not. R. astr. Soc., **189**, 701.

Marsh, K.A., Purton, C.R., & Feldman, P.A. (1976): Astr. Astophys., **49**, 211.

Martin, W. (1984): Unpublished, data quoted by AK

Mathis, J.S., Rump, W., & Nordsieck, K.H. (1977): Astrophys. J., **217**, 425.

Matthews, T.A., & Sandage, A.R. (1963): Astrophys. J., **138**, 30.

McCarroll, R., & Valiron, P. (1976): Astron. Astropys., **53**, 83.

McKim-Malville, J., & Berger, R.A. (1965): Planet. Space Sci., **13**, 1131.

Mendez, R.H., Kudritzki, R.P., Gruschinski, J., & Simon, K.P. (1981): Astron. Astrophys., **101**, 323.

Mendez, R.H., Kudritzki, R.P., & Simon, K.P. (1983): IAU Sump. No. **103**, p. 343.

Mendoza, C., & Zeippen, C.J. (1982): Mon. Not. R. astr. Soc., **198**, 127.

Mendoza, C. (1982): J. Phys. B., **15**, 867.
(1983): IAU Symp. No. **103**, p. 143.

Menzel, D.H., & Pekeris, C.L. (1935): Mon. Not. R. astr. Soc., **96**, 77.

Merrill, K.M., Soifer, B.T., & Russell, R.W. (1975): Astrophys. J., **217**, 425.

Miller, J.S. (1971): Astrophys. J., **165**, L101.

Miller, J.S., Robinson, L.B., & Wampler, E.J. (1976): in "Advances in Electronics and Electron Physics", Academic Press, New York, 40B, p. 693.

Milne, D.K., & Aller, L.H. (1975): Astr. Astrophys., **38**, 183.
(1982): Astr. Astrophys. Suppl., **50**, 209.

Milne, D.K. (1973): Astrophys. J., **78**, 239.
(1979): Astr. Astrophys. Suppl., **36**, 227.

Morgan, W.W. (1938): Astrophys. J., **187**, 460.

Moseley, H. (1980): Astrophys. J., **238**, 892.

Nussbaumer, H. (1980): Proceedings of the Second European IUE Conference ESA SP-157, p. xliii, ESA Scientific and Technical Publications, Noordwijk.

Nussbaumer, H., & Schild, H. (1979): Astron. Astrophys., **75**, L17.

Nussbaumer, H., & Storey, P.J. (1979): Astron. Astrophys., **71**, L5.
(1981): Astron. Astrophys., **99**, 177.
(1983a): Astron. Astrophys., **126**, 75.
(1983b): Atoms in Astrophysics, p. 265.

O'Dell, C.R. (1962): Astrophys. J., **135**, 371.

Oster, L. (1961): Astrophys. J., **134**, 1010.

Paczynski, B. (1971): Acta Astronomica, **21**, 417.

Peach, G. (1967): Mem. R. astr. Soc., **71**, 13.

Peimbert, M. (1971): Bol. Obs. Tanant. Tacub., **6**, 29.
(1967): Astrophys. J., **150**, 825.

(1981): in The Universe at Ultraviolet Wavelengths, ed. Chapman, R.D., NASA CP-2171, p. 557

Peimbert, M., & Costero, R. (1969): Bol. Obs. Tonant. Tacub., **5**, 3.

Peimbert, M., & Torres-Peimbert, S. (1971): Bol. Obs. Tonant. Tacub., **6**, 21.

Pena, M., & Torres-Peimbert, S. (1981): Rev. Mex. Astr. Astrophys., **6**, 309.

Pengelly, R.M., & Seaton, M.J. (1964): Mon. Not. R. astr. Soc., **127**, 165.

Pengelly, R.M. (1963): Ph.D. Thesis, University of London.
(1964): Mon. Not. R. astr. Soc., **127**, 145.

Perek, L., & Kohoutek, L. (1967): Cataloge of Galactic Planetary Nebulae, Czechoslovakian Academy of Scince, Prague.

Perinotto, M. (1977): Astron. Astrophys., **61**, 247.

Pequignot, D., Aldrovandi, S.M.V., & Stasinska, G. (1978): Astr. Astrophys., **63**, 313.

Pequignot, D. (1980a): Astron. Astrophys., **81**, 356.
(1980b): Astron. Astrophys., **83**, 52.

Pottasch, S.R. (1983): IAU Symp. No. **103**, p. 391.

Pottasch, S.R., Wesselius, P.R., Wu, C.C., Fieten, H., & Van Duninen, R.J. (1978a): Astron. Astrophys., **62**, 95 (PWWFD).

Pottasch, S.R., Wesselius, P.R., & Van Dununen, R.J. (1978b): Astron. Astrophys., **70**, 629.

Pradhan, A.K., & Seaton, M.J. (1985): J. Phys. B., **18**, 1631.

Pradhan, A.K. (1976): Mon. Not. R. astr. Soc., **177**, 31.
(1981): Phys. Rev. Lett., **47**, 79.

Preite-Martinez, A., & Pottasch, S.R. (1983): Astron. Astrophys., **126**, 31.

Presnyakov, L.P., & Urnov, A.M. (1974): J. Phys. B., **8**, 1280.

Purke, P.G., & Eissner, W.B. (1983): Atoms in Astrophysics, p. 1.

Purton, C.R., Feldman, P.A., March, K.A., Allen, D.A., & Wright, A.E., (1982): Mon. Not. R. astr. Soc., **198**, 321.

Rank, D.M. (1978): IAU Symp. No. **76**, Planetary Nebulae, ed. Terzian, Y. D. Rediel, Dordrecht, p. 103.

Reay, N.K. (1983): IAU Sump. No. **103**, p. 31.

Reilman, R.F., & Manson, S.T. (1979): Astrophys, J. Suppl., **40**, 815.

Renzini, A. (1979): Stars and Star Systems, ed. Westerlund, B.E., D. Reidel, Dordrecht, p. 155.

Rodriguez, L.F. (1973): Thesis, University Nacional Autonoma de Mexico.

Rubin, R.H. (1968): Astrophys. J., **154**, 391.

Russell, R.W., Soifer, B.T., & Willner, S.P. (1977): Astrophys. J., **217**, L149.

Salem, M. (1974): Mon. Not. R. astr. Soc., **167**, 511.

Saraph, H.E., & Seaton, M.J. (1980): Mon. Not. R. astr. Soc., **193**, 617.

Scott, P.F. (1975): Mon. Not. R. astr. Soc., **170**, 487.
(1983): IAU Symp. No. **103**, p. 61.

Seaton, M.J., & Osterbrock, D.E. (1957): Astrophys. J., **125**, 66.

Seaton, M.J., & Storey, P.J. (1976): Atomic Processes and Applications, eds. Burke, P.G., & Moiseiwitsch (Amsterdam: North-Holland).

Seaton, M.J. (1953): Proc. Roy. Soc., A218, 400.
(1955a): Proc. Roy. Soc., A231, 37.
(1955b): in the Airglow and the Aurora, eds. Armstrong, E.B., & Dalgarno, A., Pergamon Press, Oxford, p. 289.
(1959): Mon. Not. R. astr. Soc., 119, 81.
(1960): Rept. Prog. Phys., 23, 313.
(1966): Mon. Not. R. astr. Soc., 132, 113.
(1968): Mon. Not. R. astr. Soc., 139, 129.
(1974): J. Phys. B., 7, 1817.
(1979): Mon. Not. R. astr. Soc., 187, 73P.
(1983a): IAU Symp. No. 103, p. 129.
(1983b): Rep. Prog. Phys., 46, 167.

Shao, C.Y., & Liller, W. (1982): Unpublished, data quoted by AK.

Shaver, P.A., McGee, R.X., Newton, L.M., Danks, A.C., & Pottasch, S.R. (1983): Mon. Not. R. astr. Soc., 204, 53.

Shklovsky, I.S. (1956): Astr. J. (USSR), 33, 222, 315.

Snijders, M.A.J. (1980): SRC IUE Newsletter, 5, 85.

Smith, E.R., & Henry, R.J.W. (1973): Phys. Rev., A7, 1585.

Stasinska, G. (1978): Astron. Astrophys., 66, 257.

Storey, P.J. (1981): Mon. Not. R. astr. Soc., 195, 27P.
(1983): IAU Symp. No. 103, p. 199.

Stebbins, J., Huffer, C.M., & Whitford, A.E. (1939): Lick Obs. Bull., 90, 209.

Surdej, J. (1982): Astrophysics and Space Seince, 88, 31.

Tarter, C.B. (1971): Astrophys. J., 168, 313.
(1973): Astrophys. J., 181, 607.

Telesco, C.M., & Harper, D.A. (1977): Astrophys. J., 237, 450.

Terzian, Y. (1968): IAU Symp. No. 34, p. 88.
(1978): IAU Symp. No. 76, p. 111.
(1980): Q. J. R. astr. Soc., 21, 82.

Titchmarsh, E.C. (1948): Introduction to the Theory of Fourier Integrals Oxford: Clarendon, pp 13, 42.

Torres-Peimbert, S., Peimbert, M., & Daltabuit, E. (1980): Astrophys. J., 238, 133 (TPPD).

Torres-Peimbert, S., & Peimbert, M. (1977): Rev. Mex. Astr. Astrofis., 2, 278 (TPP).

Trumpler, R.J. (1930): Lick Obs. Bull., 14, 108.

Ulrich, M.H., & Pequignot, D. (1980): Astrophys. J., 238, 45.

Walmsley, C.M., Churchwell, E., & Terzian, Y. (1981): Astr. Astrophys., 96, 278.

Watson, W.D., & Christensen, R.B. (1979): Astrophys. J., 231, 627.

Wesemael, F., Auer, L.H., Van Horn, H.M., & Savedoff, M.P. (1980): Astrophys. J. Suppl., 43, 159.

Weymann, R.J., & Williams, R.E. (1969): Astrophys. J., 157, 12011.

Williams, R.E. (1973): Mon. Not. R. astr. Soc., 164, 111.

Willner, S.P., Jones, B., Puetter, R.C., Russell, R.W., & Soifer, B.T., (1979): Astrophys. J., 234, 496.

Zanstra, H. (1962): Phys. Rev., 2, 27, 644.
(1931): Publs. Dominion Astrophys. Obs., 4, 209.

Zeippen, C.J. (1977): Ph.D. Thesis, University of London.
(1980): J. Phys. B., 13, L485.
(1982): Mon. Not. R. astr. Soc., 198, 111.